JAEA-Conf 2018-001
INDC(JPN)-204
DOI:10.11484/jaea-conf-2018-001

JAEA-Conf

Proceedings of the 2017 Symposium on Nuclear Data November 16-17, 2017, iVil, Tokai-mura, Ibaraki, Japan

(Eds.) Katsuhisa NISHIO, Yutaka UTSUNO, Satoshi CHIBA, Hiroyuki KOURA
Osamu IWAMOTO and Shoji NAKAMURA

Advanced Science Research Center
Sector of Nuclear Science Research

December 2018

Japan Atomic Energy Agency

日本原子力研究開発機構

本レポートは国立研究開発法人日本原子力研究開発機構が不定期に発行する成果報告書です。
本レポートの入手並びに著作権利用に関するお問い合わせは、下記あてにお問い合わせ下さい。
なお、本レポートの全文は日本原子力研究開発機構ホームページ（http://www.jaea.go.jp）
より発信されています。

国立研究開発法人日本原子力研究開発機構 研究連携成果展開部 研究成果管理課
〒319-1195 茨城県那珂郡東海村大字白方 2 番地4
電話 029-282-6387, Fax 029-282-5920, E-mail:ird-support@jaea.go.jp

This report is issued irregularly by Japan Atomic Energy Agency.
Inquiries about availability and/or copyright of this report should be addressed to
Institutional Repository Section,
Intellectual Resources Management and R&D Collaboration Department,
Japan Atomic Energy Agency.
2-4 Shirakata, Tokai-mura, Naka-gun, Ibaraki-ken 319-1195 Japan
Tel +81-29-282-6387, Fax +81-29-282-5920, E-mail:ird-support@jaea.go.jp

JAEA-Conf 2018-001
INDC(JPN)-204

Proceedings of the 2017 Symposium on Nuclear Data November 16-17, 2017, iVil, Tokai-mura, Ibaraki, Japan

(Eds.) Katsuhisa NISHIO, Yutaka UTSUNO, Satoshi CHIBA*,
Hiroyuki KOURA, Osamu IWAMOTO+ and Shoji NAKAMURA+

Advanced Science Research Center, Sector of Nuclear Science Research
Japan Atomic Energy Agency
Tokai-mura, Naka-gun, Ibaraki-ken

(Received September 13, 2018)

The 2017 Symposium on Nuclear Data was held at iVil in Tokai on November 16-17, 2017. The symposium was hosted by the Nuclear Data Division of the Atomic Energy Society of Japan (AESJ) and Advanced Science Research Center of Japan Atomic Energy Agency (JAEA), and co-hosted by Japanese Nuclear Data Committee of AESJ and North Kanto Branch of AESJ. In the symposium, a tutorial was given by Prof. Rykaczewski (ORNL) entitled "New nuclear data from total absorption spectroscopy and beta-delayed neutron measurements", and six oral sessions, "Nuclear Physics and Nuclear Data" (two sessions), "Nuclear Theory and Nuclear Data", "Reactors" and "Nuclear Data and Their Applications" (two sessions) were held. In addition, recent advances in experiment, theory, evaluation, benchmark, and application were presented in the poster session. The symposium had 79 participants, who contributed to very active and fruitful discussions. This report consists of 37 papers, including those of 14 oral and 23 poster presentations.

Keywords: Nuclear Data Symposium 2017, Nuclear Experiment, Nuclear Theory, Nuclear Data Evaluation, Nuclear Data Application, Benchmark Test

---

+ Nuclear Science and Engineering Center
* Tokyo Institute of Technology

Organizers: K. Nishio (JAEA, Chair), S. Chiba (Tokyo Tech, Vice Chair), M. Aikawa (Hokkaido Univ.), O. Iwamoto (JAEA), Y. Utsuno (JAEA), H. Otsu (RIKEN), T. Katabuchi (Tokyo Tech), K. Kino (AIST), S. Kunieda (JAEA), H. Koura (JAEA), T. Sanimi (KEK), N. Shigyo (Kyushu Univ.), S. Nakamura (JAEA), K. Nakajima (Kyoto Univ.), T. Hazama (JAEA), J. Hori (Kyoto Univ.), I. Murata (Osaka Univ.), Y. Watanabe (Kyushu Univ.)

JAEA-Conf 2018-001
INDC(JPN)-204

2017 年度核データ研究会報文集
2017 年 11 月 16 日～17 日
東海村産業・情報プラザ(アイヴィル)

日本原子力研究開発機構　原子力科学研究部門　先端基礎研究センター

（編）　西尾　勝久、宇都野　穣、千葉　敏*、小浦　寛之、岩本　修+、中村　詔司+

(2018 年 9 月 13 日　受理)

2017 年度核データ研究会は、2017 年 11 月 16 日、17 日に、茨城県東海村の東海村産業・情報プラザ(アイヴィル)にて開催された。本研究会は、日本原子力学会核データ部会と日本原子力研究開発機構先端基礎研究センターが主催、日本原子力学会シグマ特別専門委員会と日本原子力学会北関東支部が共催した。今回、チュートリアルとしてオークリッジ国立研究所の Rykaczewski 氏による講演「全エネルギー吸収ガンマ線測定と遅発中性子に関する新しいデータ」を、講演・議論のセッションとして「核物理と核データ」(2 セッション)、「原子核理論と核データ」、「原子炉」、「核データと応用」(2 セッション)の 6 セッションを企画・実施した。さらに、ポスターセッションでは、実験、理論、評価、ベンチマーク、応用など、幅広い研究内容について発表が行われた。参加者総数は 79 名で、それぞれの口頭発表及びポスター発表では活発な質疑応答が行われた。本報告書は、本研究会における口頭発表 14 件、ポスター発表 23 件の論文をまとめている。

キーワード: 2017 年核データ研究会、原子核実験、原子核理論、核データ評価、核データ応用、ベンチマークテスト

+ 原子力基礎工学研究センター
* 東京工業大学

Contents

Papers presented at Poster Session

目次

ポスター発表論文

This is a blank page.

1　Program of the 2017 Symposium on Nuclear Data
11 月 16 日（アイヴィル 多目的ホール他）

講演時間には 5 分（チュートリアルは 10 分）の議論が含まれます。

10:30–10:40　開会式

セッション 1　核物理と核データ　座長：執行 信寛（九大）

10:40–11:10　浅井 雅人（JAEA）
^{254}Es 標的を用いた核分裂・核構造研究

11:10–11:40　静間 俊行（量研機構）
核共鳴蛍光散乱データの現状

11:40–12:10　木村 敦（JAEA）
^{244,246}Cm の中性子捕獲断面積測定の状況

昼食（12:10-13:10）

チュートリアル　ベータ崩壊　座長：西尾 勝久（JAEA）

13:10–14:10　Krzysztof Rykaczewski（ORNL）
全エネルギー吸収ガンマ線測定と遅発中性子に関する新しいデータ

休憩（14:10–14:30）

セッション 2　原子核理論と核データ　座長：宇都野 穣（JAEA）

14:30–15:00　千葉 敏（東工大）
核分裂理論研究の最近の動向

15:00–15:30　西村 信哉（京大基研）
原子核物理の不定性が星の重元素生成に与える影響

15:30–16:00　清水 則孝（東大 CNS）
殻模型計算による核準位密度の微視的記述

ポスターセッション（16:00–17:30、アイヴィル 3 階 301,302 号室）

懇親会（18:00–20:00、東海会館）

11 月 17 日（アイヴィル 多目的ホール）

セッション 3　核物理と核データ　座長：大津 秀暁（理研）

9:10–9:40　今井 伸明（東大 CNS）
OEDO を用いた低エネルギーLLFP の核反応データ取得

9:40–10:10　西原 健司（JAEA）
ADS 核データの現状と積分実験

10:10–10:40　和田 道治（KEK/RIKEN）
MRTOF 質量分光器を用いた重元素の網羅的高精度質量測定

休憩（10:40–11:00）

セッション 4　原子炉　座長：堀 順一（京大炉）

11:00–11:30　竹田 敏（阪大）
軽水炉における水の熱中性子散乱則データの違いによる核計算結果への影響評価

11:30–12:00　奥村 啓介（JAEA）
福島第一原子力発電所の廃炉への核データの応用

写真撮影、昼食（12:00–13:30）

セッション 5　核データと応用　座長：合川 正幸（北大）

13:30–14:00　渡辺 幸信（九大）
半導体ソフトエラー研究の最近の動向

14:00–14:30　田所 孝広（日立製作所）
電子線形加速器を利用した医療用放射性核種の製造

休憩（14:30–14:50）

セッション 6　核データと応用　座長：片渕 竜也（東工大）

14:50–15:20　佐藤 達彦（JAEA）
PHITS を用いた宇宙線挙動解析

15:20–15:50　岩本 修（JAEA）
JENDL の現状と今後の計画

15:50–16:05　ポスター賞授賞式

16:05–16:10　閉会式

ポスター発表

A*はポスター賞審査対象、B*は対象外

A1	核子移行反応による超重核領域の融合分裂過程の研究	宮本 裕也 (近大)
A2	Reaction Study of ^{136}Xe on Proton, Deuteron and Carbon at 168A MeV	Sun Xiaohui (理研)
A3	動力学模型計算によるマルチチャンス核分裂の研究	田中 翔也 (近大)
A4	^{93}Zr に対する 200 MeV/u 陽子・中性子入射反応による同位体生成断面積の測定	川瀬 頌一郎 (九大)
A5	^{nat}Yb への 50 MeV α 粒子入射反応による ^{177}Lu 生成反応断面積測定	齋藤 萌美 (北大)
A6	Survival probability and evaporation residue cross section for synthesizing superheavy nucleus	Nur Liyana Binti Mohd Anuar (近大)
A7	Measurement of the Neutron Capture Cross Section of ^{237}Np Using ANNRI at MLF/J-PARC	ロビラ レベロニ ジェラルド (東工大)
A8	200 MeV 重陽子入射中性子生成反応二重微分断面積の系統的測定	定松 大樹 (九大)
A9	PWR 近傍および強力トリチウム線源にける電気化学的起装置の信号増大の観測	須田 翔哉 (九大)
A10	PHITS コードで計算した検出効率を用いた重粒子入射反応からの中性子エネルギースペクトル	徳元 千隼 (九大)
A11	反対称化分子動力学による核分裂の研究	餌取 篤彦 (東工大)
A12	微視的な摩擦係数とポテンシャルからの核分裂現象解析	西川 崇 (東工大)
A13	殻補正に基づく偶奇性を取り入れた核分裂収率の評価手法について	椿原 康介 (東工大)
A14	炉周期測定のための JENDL-4 を用いた動特パラメータ計算	名内 泰志 (CRIEPI)
A15	^{18}O+^{237}Np の多核子移行反応を用いた核分裂片の質量数分布の測定	マーク・バーミューレン (JAEA)
A16	Fission Probability of Actinide Nuclei Obtained Using ^{18}O-induced Multi-Nucleon Transfer Channels	Kun Ratha Kean (東工大)
B1	鉛冷却高速炉を模擬した臨界集合体 BFS-61 の中性子増倍係数に対する不確かさ評価	千葉 豪 (北大)
B2	ジルコニウム標的を用いた α 粒子入射反応による ^{99}Mo 生成断面積測定	合川 正幸 (北大)
B3	中重核の α クラスター構造研究	伊藤 誠 (関西大)
B4	ボロンタイプ中性子グリッドを用いた中性子イメージングのための透過率測定	原 かおる (北大)

B5	ImPACT プロジェクトで進めている J-PARC MLF ANNRI での中性子捕獲断面積測定の進捗	中村 詔司 (JAEA)
B6	表面電離型質量分析装置を用いた中性子捕獲断面積測定で用いた試料の $^{135}Cs/^{137}Cs$ 同位体比測定	芝原 雄司 (京大炉)
B7	^{90}Sr および ^{88}Kr, ^{89}Rb, ^{91}Y の相互作用断面積測定	親跡 和弥 (新潟大)
B8	重陽子-原子核反応に対する微視的有効反応理論とその応用	蓑茂 工将 (阪大 RCNP)
B9	Studies on Calculations of Prompt Neutron Multiplicities, Fission Product Yields and Isomeric Yields by Hauser-Feshbach Statistical Decay Theory	奥村 森 (東工大)

This is a blank page.

2 Status of nuclear data for nuclear resonance fluorescence

Toshiyuki SHIZUMA
Tokai Quantum Beam Science Center,
National Institutes for Quantum and Radiological Science and Technology
Tokai, Ibaraki 319-1106 Japan
e-mail: shizuma.toshiyuki@qst.go.jp

We have carried out nuclear resonance fluorescence (NRF) experiments using quasi-mono-energetic linearly polarized photon beams at AIST, LASTI, and Duke University to investigate E1 and M1 responses of nuclei such as the spin-flip and scissors M1 resonances as well as the E1 pygmy resonance. In this paper, the techniques applied to the NRF measurements and the examples of the NRF data obtained using the quasi-mono-energetic linearly polarized photon beams are presented.

1. Introduction

Nuclear resonance fluorescence (NRF) is a process of resonant excitation of a nucleus by absorption of a photon and subsequent deexcitation by emission of a photon. Since NRF takes place via electromagnetic interaction, dipole states are selectively excited and transition strength can be extracted from the scattering cross section in a model-independent fashion [1]. In addition, spins of the excited states can be determined from angular correlation measurements. Most of the NRF data were taken by bremsstrahlung beams until 1990s. A breakthrough of NRF measurements came when a quasi-monoenergetic polarized photon beam generated by Compton scattering of laser light with high energy electrons (LCS photons) became available. By using an LCS photon beam, parity quantum numbers can be unambiguously determined [2] and the detection sensitivity increases.

So far, we have carried out NRF measurements using LCS photon beams at National Institute of Advanced Industrial Science and Technology (AIST) [3], Laboratory of Advanced Science and Technology for Industry (LASTI) of University of Hyogo [4], and the High Intensity Gamma-ray Source (HIγS) facility of Duke University [5]. By using NRF, we have investigated electric dipole (E1) and magnetic dipole (M1) responses of nuclei such as the spin-flip and scissors M1 resonances as well as the pygmy dipole resonance. We have also developed techniques of non-destructive isotope-specific identification of nuclear materials for nuclear security purposes. In this paper, the techniques used in the NRF

measurements and some results obtained from the measurements are presented.

2. Experimental techniques and data

The LCS photon beams are generated by collisions between high energy electrons circulating the storage ring and laser quanta. Figure 1 illustrates the LCS photon beam line at the NewSUBARU synchrotron radiation facility of LASTI where the electron energy can be tuned down to 600 MeV to produce LCS photons with an energy of 6 MeV. Since the polarization of the laser photon is approximately conserved in the collision, linearly or circularly LCS photons can be generated. A lead collimator in the 1st hutch is used to form a quasi-monochromatic photon beam with an energy spread of ΔE/E 3 to 10% at full width at half maximum (FWHM). The average intensity on the target is measured using a large volume (8" × 12") NaI(Tl) scintillation detector placed at the downstream of the target. High-purity germanium (HPGe) detectors with relative efficiencies of 120% and 140% are used to measure scattered photons from the target. These detectors are placed in vertical and horizontal planes at a scattering angle of θ=90°. The typical energy resolution of the HPGe detectors is $\Delta E_\gamma/E_\gamma \approx 0.09\%$ at $E_\gamma \approx 7$ MeV. To reduce the background counts originating from bremsstrahlung caused by high-energy electrons in the storage ring, events within 1 μs of laser pulses were stored in a list mode. More details of the experimental techniques are described in Ref. [6].

The intensity asymmetry of the scattered photons with respect to the polarization plane of the incident photon beam can be used for determination of parity quantum. The azimuthal angular distribution of dipole transitions is given in Ref. [2] as

$$W(\theta,\phi) = W(\theta) \pm \frac{3}{4}(1 - cos^2\theta)cos2\phi$$

where θ is the scattering angle with respect to the photon beam, and ϕ is the azimuthal angle between the polarization plane and the reaction plane. W(θ) is the angular correlation function for unpolarized radiation. Here, the minus sign is for E1 transitions and the plus sign is for M1 transitions.

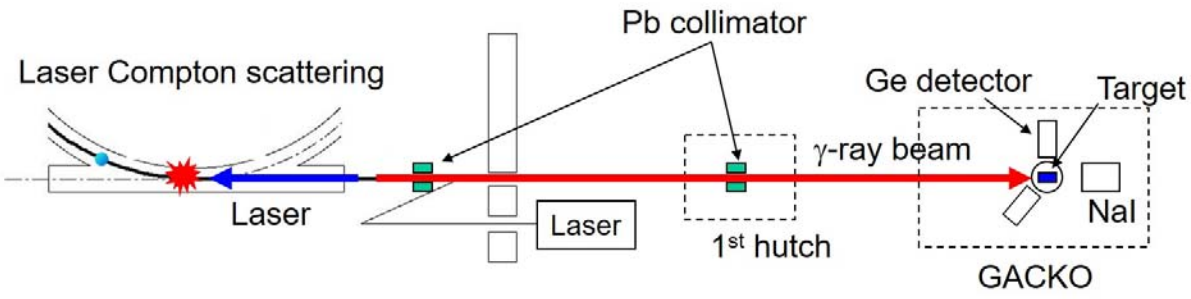

Fig.1. Schematic view of the LCS photon beam line at NewSUBARU.

For the determination of parity quantum numbers, the analyzing power is defined as

$$\Sigma = \frac{W(90^\circ, 0^\circ) - W(90^\circ, 90^\circ)}{W(90^\circ, 0^\circ) + W(90^\circ, 90^\circ)}$$

Under the condition of complete polarization of the incoming photon beam, Σ=+1 is expected for M1 transitions, and Σ=-1 is expected for E1 transitions.

The corresponding azimuthal intensity asymmetry of the scattered photons is given by

$$A = \frac{N_{\parallel} - N_{\perp}}{N_{\parallel} + N_{\parallel}} = q\Sigma$$

where $N_{\parallel}(N_{\perp})$ is the measured intensity of the scattered photons detected at θ=90° in the plane parallel (perpendicular) to the polarization plane. Here, q is the experimental sensitivity, which is less than unity because of the finite solid angle of the HPGe detectors and the spatially extended target.

Figure 2 presents typical energy spectra for the scattered photons at polar and azimuthal angles of (θ , ϕ)=(90°,0°) and (90°,90°) obtained for a ^{52}Cr target using LCS photons at the maximum energy of 9.4 MeV. The parity quantum numbers of the excited states can be determined based on the azimuthal intensity asymmetry described above, as shown in Fig. 3. The intensity asymmetries are well separated depending on the multipolarities of E1 or M1. From Fig. 3, the experimental sensitivity of q is estimated to be 0.8 which is consistent with the result obtained from the numerical simulation. Based on the azimuthal intensity asymmetry, the multipolarity of resonantly scattered transitions can be determined.

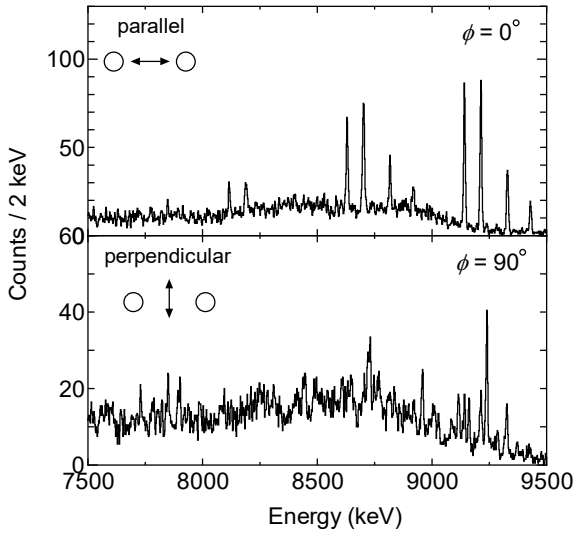

Fig.2. Photon scattering spectra measured at polar and azimuthal angles of (θ, ϕ)=(90°,0°) and (90°,90°) obtained for a ^{52}Cr target using the photon beam with E=9.4 MeV.

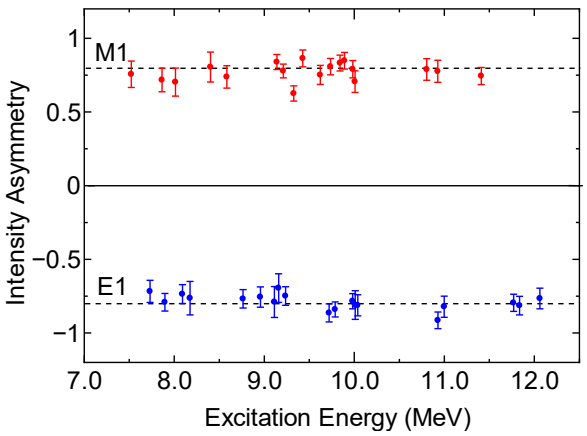

Fig.3. Azimuthal intensity asymmetry obtained for E1 (blue circles) and M1 (red circles) transitions in ^{52}Cr. The experimental sensitivity q(=0.8) deduced from the numerical calculation is indicated by dashed lines.

The scattering strength Γ_0^2/Γ for an excited state at an energy of E_x can be deduced from the measured intensity of the respective transition [1]. Here, Γ and Γ_0 are the total radiative width and the decay width to the ground state, respectively. Γ_0^2/Γ for a dipole state is deduced relative to the known transition:

$$\frac{\Gamma_0^2/\Gamma(E_x)}{\Gamma_0^2/\Gamma(E_{x,ref})} = \frac{I_\gamma E_\gamma^2}{\Phi\lambda} \cdot \frac{\Phi_{\mathrm{ref}}\lambda_{ref}}{I_{\gamma,\mathrm{ref}}E_{\gamma,ref}^2}$$

Here, I_γ denotes the measured intensities of a transition at E_γ. Φ represents the photon fluxe at the energy of the considered. λ is the correction factors of atomic and self-absorption for the level at E_x. The correction factors are determined according to Eq. (19) in Ref. [7].

The reduced transition probabilities, B(E1) and B(M1) can be extracted from the ground state decay width Γ_0 as

$$\mathrm{B}(E1)\uparrow = 2.866\frac{\Gamma_0}{E_\gamma^3}[10^{-3}e^2fm^2]$$

$$\mathrm{B}(M1)\uparrow = 0.2598\frac{\Gamma_0}{E_\gamma^3}[\mu_N^2]$$

where Γ_0 is given in units of meV and E_γ in units of MeV. Figures 4 and 5 show the cumulative E1 and M1 values, respectively, obtained for ^{52}Cr. The gross structure of the measured cumulative strengths are reproduced by the calculations using the random phase approximation model including the 2-particle 2-hole excitation and tensor force [6].

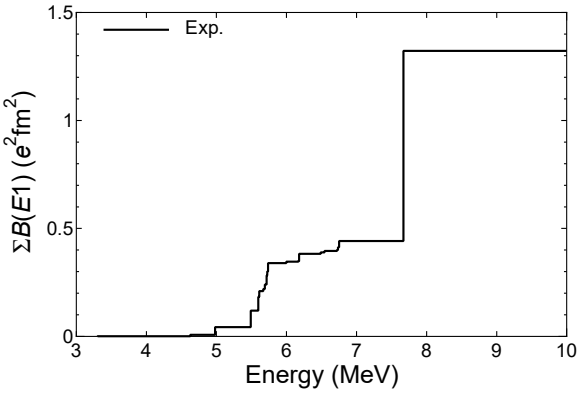

Fig.4. Cumulative E1 strengths measured for ^{52}Cr.

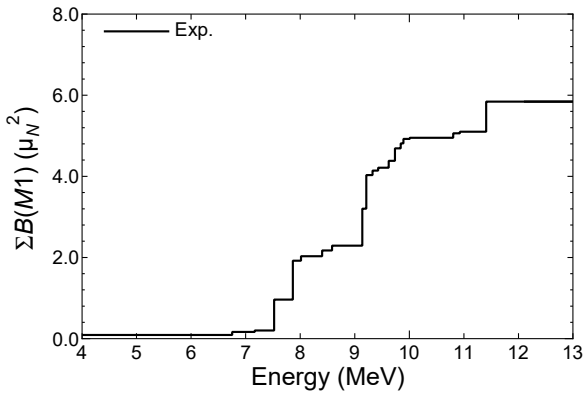

Fig.5. Cumulative M1 strengths measured for ^{52}Cr.

3. Conclusion

A quasi-mono-energetic linearly polarized photon beam generated by backward Compton scattering of laser light with high-energy electrons have been used for nuclear resonance fluorescence measurements. It can be used for determination of parity quantum numbers of resonant states via the analysis of intensity asymmetry with respect to the polarization of

incident photons. This method has an advantage to investigate E1 and M1 responses of nuclei such as the spin-flip and scissors M1 resonances as well as the E1 pygmy resonance in nuclear structure study.

References

[1] U. Kneissl, H.H. Pitz, and A. Zilges: Prog. Part. Nucl. Phys. 37, 349 (1996).
[2] L.W. Fagg and S.S. Hanna: Rev. Mod. Phys. 31, 711 (1959).
[3] H. Ohgaki et al.: IEEE Trans. Nucl. Sci. 38, 386 (1991).
[4] S. Miyamoto et al.: Radiat. Meas. 41, S179 (2006).
[5] H.R. Weller et al.: Prog. Part. Nucl. Phys. 62, 257 (2009).
[6] T. Shizuma et al.: Phys. Rev. C 96, 044316 (2017).
[7] F. Metzger, Progress in Nuclear Physics, edited by O. Frish (Pergamon Press, New York, 1959), Vol. 7. pp. 53-58.

This is a blank page.

3 New nuclear data from total absorption spectroscopy and beta-delayed neutron measurements

K. P. Rykaczewski
Physics Division, Oak Ridge National Laboratory
Oak Ridge, TN 37831, USA
e-mail : rykaczewskik@ornl.gov

The studies contributing to nuclear data on beta decay and performed at ORNL and at RIKEN are presented. The measurements at ORNL were performed with a Modular Total Absorption Spectrometer by means of an on-line mass separator technique. Radioactive nuclei were produced using 40-MeV proton induced fission of ^{238}U target. The experiments focused on the decay heat and reactor anti-neutrino spectrum determination. At RIKEN, fragmentation of ^{238}U beam at 345 MeV/u was used to obtain very neutron nuclei around ^{78}Ni and in heavier mass regions. The decays were studied using ^{3}He detectors enhanced by two Ge-clover detectors as well as the silicon arrays AIDA and mini-WAS3ABi plus a novel YSO scintillator, assembled into the BRIKEN array. The main goal was to measure the beta-delayed 1n and 2n emission rates as well as beta-delayed gamma radiation. On-line analysis points to over one hundred new P_{1n} values measured and many half-lives of neutron rich nuclei determined for the first time. In addition, beta-gamma and beta-neutron-gamma transitions were identified for the first time in decays of many exotic nuclei like ^{78}Ni.

1. Introduction

Nuclear data programs were and are strongly motivated by the science of nuclear reactors. Among the needed information were the decays of fission products contributing around 10% to the total energy release in a fission event. The beta-delayed radiation (decay heat) is the only source of heating after the reactor shutdown, and might have dramatic consequences in case of a Loss-of-Cooling Accident (LOCA). The reliable estimation of the amount and type of released radiation is also important for the understanding of reactor materials response and durability. The priorities for studies of decays of isotopes abundant during the nuclear fuel cycle with the total gamma absorption technique were assessed in 2007 under auspices of the Nuclear Energy Agency (NEA) of the Organization for Economic Cooperation and Development (OECD), see [1].

More recently, the motivation to study beta decay of fission products was enhanced by the need for an improved estimation of the reactor anti-neutrino flux. The re-analysis of integral measurements of beta energy spectra from neutron-irradiated components of nuclear fuel pointed to the deficit of detected anti-neutrinos and led to the concept of “reactor anti-neutrino anomaly” [2,3]. The potential explanation of this anomaly invoked the existence of a fourth sterile neutrino questioning the Standard Model picture of leptons. However, a reliable reference reactor anti-neutrino flux is required to claim the ~ 94(6)% deficit and to understand the observed anti-neutrino energy spectra. Since reactor anti-neutrinos are emitted only from the decays of fission products, it opened up the path to verify and improve substantially existing data by using a total absorption technique to detect beta decays and the following gamma emission.

The decay studies of exotic neutron rich nuclei are motivated by nuclear structure and nuclear astrophysics needs. New information on the beta-delayed gamma lines contributes to the understanding of the evolution of excited states and their origin. The beta-delayed one-neutron and multi-neutron emission modifies the abundance pattern of isotopes produced in the astro-physical rapid-neutron capture process (r-process). Since r-process occurs in a very neutron-rich environment, the decay properties of nuclei very far from stability are critical for understanding the site and mechanism of the potential r-process scenarios.

2. Studies with a Modular Total Absorption Spectrometer (MTAS)

2.1 Experimental Setup

MTAS project was initiated in 2009 [4] profiting from the funding following the American Recovery and Reinvestment Act (ARRA) within DOE Office of Science. Its construction was designed to provide maximum gamma and beta trigger efficiencies and a capability of coincidence radiation analysis through multiple individual modules, see Fig.1. Novel carbon fiber housing having a density below 2 g/cm^3 has been developed on our request by the MTAS manufacturer (Saint Gobain Crystals USA) to minimize the interaction of gamma radiation with non-active detector matter. MTAS was designed to perform experiments by means of on-line mass separation of fission products, with a moving tape transporting collected radioactive samples to the center of the array. Four rings of large NaI(Tl) crystals nicknamed Central (1 module), Middle (6 modules), Inner (6) and Outer (6), the 0.5 inch wide tape running through central module and two silicon detectors can be seen in Fig.1. Custom-modified (Model I-1000) segmented Silicon beta detectors made by Micron Ltd. (UK) were assembled in a very close geometry covering about 96% of the solid angle for beta emission from a radioactive sample. The Si segmentation perpendicular to the tape movement direction allowed us to position the measured samples in the middle of the array and control the accuracy of the sample stopping during long measurements. The GEANT4 simulations of MTAS response function were verified by the measurements using custom-made calibrated sources deposited on tape. The very high peak and total efficiencies of MTAS and its components are also displayed in Fig.1.

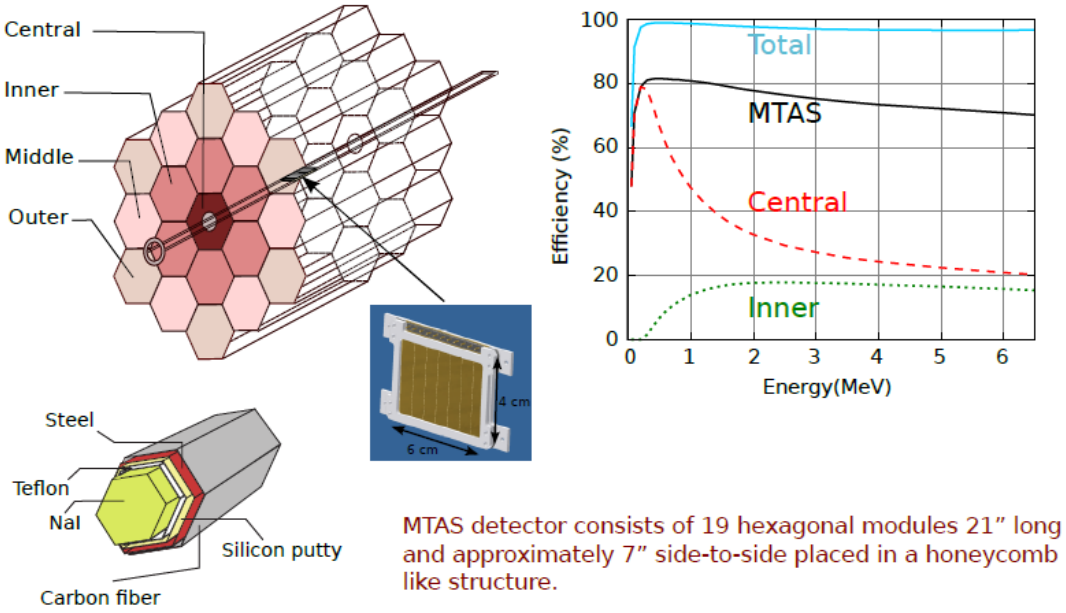

Figure 1. Structure of an individual NaI(Tl) module, rings of MTAS array, silicon counters and the simulation of efficiencies for a single gamma transition. Black solid represents total energy deposit in MTAS and blue line gives the total absorption efficiency, both for a single gamma-line emitted from the center of the array.

MTAS array is very well shielded against laboratory background radiation. There are about five tons of lead around MTAS, in a form of lead plates and lead wool blankets. In addition, two layers of

SWX-244A foam were added to reduce the capture of background neutrons. The measurements at the ORNL on-line isotope-separator, the On-line Test Facility (OLTF) at the Tandem accelerator were performed with different types of ion sources and ^{238}U carbide target. The ion sources used at OLTF included LaB_6 ionizer (releasing negative ions of Br and I) and a hot-plasma ion source optimized to produce molecular ions of metal sulfides to study mass A Sn isotopes at the A+32 OLTF mass setting [5, 6]. The mass separated beams of fission products were collected on the tape viewed by an HPGe detector monitoring sample content and strength. Typically, the initial counting rates were kept well below 10 kHz to reduce the photomultipliers amplification drift. One out of ten measurement cycles was taken without a deposition of radioactive beam, to ensure real background conditions, with some radiation related to the beam on ^{238}U target inside the ion source. The measurement cycles were long enough to measure longer lived daughter activities in addition to the initial short lived isotope. More details on MTAS construction, operation and performance verification is given in [7, 8, 9].

2.2 Results

During several campaigns of MTAS measurements at ORNL's OLTF, the decays of nearly 80 fission products were measured, see Fig. 2 and Fig. 3. Twenty-two decays of high priority nuclei, as established by Nuclear Energy Agency [1] were measured. At the lower mass fission products distribution peak, these measured activities and the respective priorities are ^{86}Br (priority 1), ^{87}Br (1), ^{88}Br (1), ^{89}Kr (1), ^{90}Kr (1), ^{90}Rb (2), ^{92}Rb (2), ^{97}Sr (2), ^{96}Y (2), and ^{98}Nb (1). For the higher mass fission peak, we have obtained MTAS data for ^{132}Sb (1), ^{135}Te (2), ^{136m}I (1), ^{136}I (1), ^{137}I (1), ^{137}Xe (1), ^{139}Xe (1), ^{140}Xe (1), ^{142}Cs (2), ^{145}Ba (2), ^{143}La (2) and for ^{145}La (2). Also, 21 activities out of about 30 listed as the main contributors to the high energy reactor anti-neutrinos [10] were studied. These are ^{86}Br, ^{88}Br, ^{89}Br, ^{91}Kr, ^{90}Rb, ^{92}Rb (identified as #1 contributor), ^{93}Rb, ^{94}Rb, ^{95}Rb, ^{95}Sr, ^{96}Y (#2 contributor), ^{97}Y, ^{98}Y, ^{135}Te, ^{138}I, ^{138}Xe, ^{140}Cs, ^{142}Cs (#3 contributor), ^{143}Cs, ^{143}La and ^{146}La.

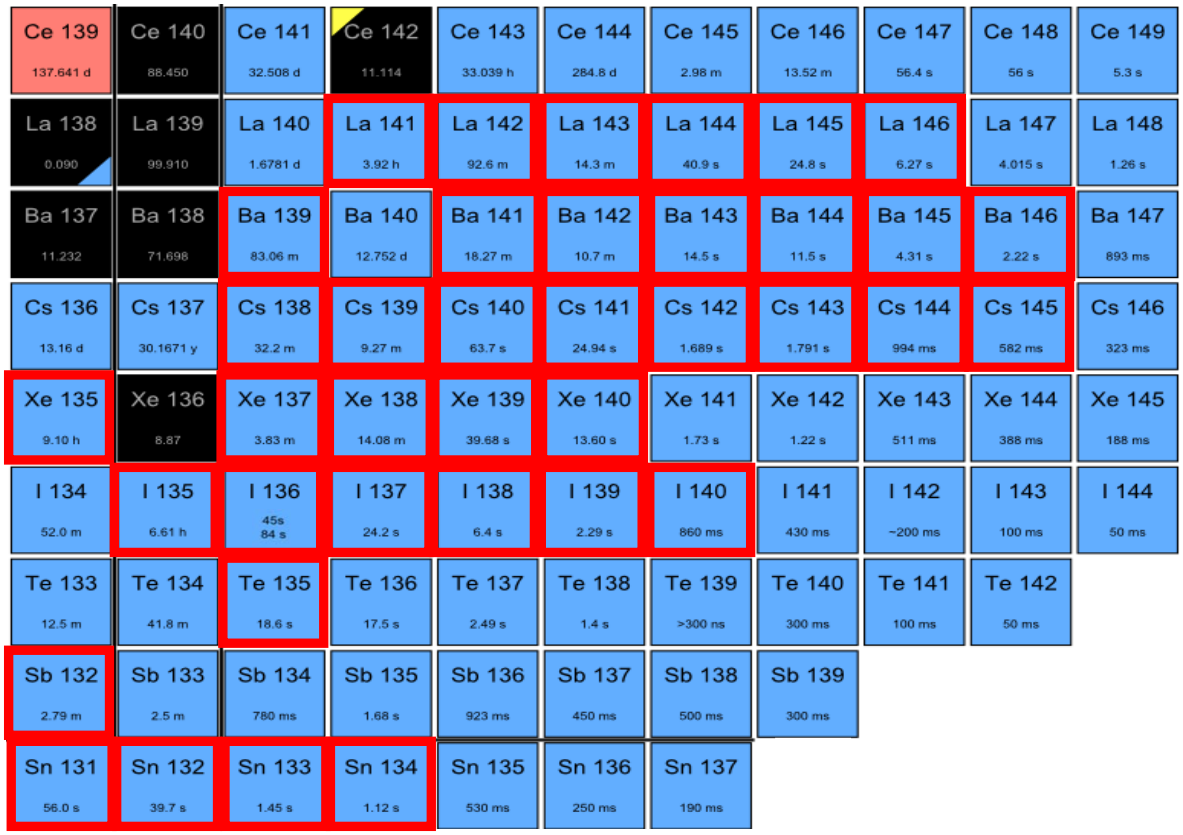

Figure 3. Part of a chart of nuclei displaying the isotopes at the high mass peak of fission product distribution measured with MTAS at the ORNL's OLTF (red squares).

Typically, we were aiming to achieve the statistics of about 10^7 counts in a beta-gated MTAS total absorption spectra. However, not all the measurements were able to collect such high statistics. There are still about 60 decays to be evaluated, perhaps in some cases pointing to the need of a better measurement. This might be the case for the isotopes of the refractory elements, where the activities were obtained as decay products of respective Rb and Sr isobars directly released from the surface ionization ion source, compare Fig.2.

2.3 Impact of MTAS results

Evaluated and interpreted MTAS data were presented in [11, 12, 13, 14]. The impact on the decay heat release during the operation of a nuclear reactor has been demonstrated by comparing decay data from ENDF/B VII.1 to MTAS results for nine activities abundant in nuclear fuel, of ^{86}Br, ^{89}Kr, ^{89}Rb, ^{90}Kr, ^{90gs}Rb, ^{90m}Rb, ^{92}Rb, ^{139}Xe and ^{142}Cs, see Fig. 3 in [9] presenting the changes after a thermal neutron fission of ^{235}U. After including MTAS results, the total decay heat is increased by over 3% in about 2-3 s after fission event, mostly by the modified ^{142}Cs decay ($T_{1/2}$= 1.7s), and it is increased nearly 3% in the 70-100 s after fission. It is a typical change after measuring a complex decay with a total absorption spectrometer. The detection of previously unknown weak beta transitions to highly excited states followed by many gamma lines is increasing the average energy of gamma radiation per decay and decreasing the average energies in beta and anti-neutrino spectra. It also has an impact on the reference anti-neutrino flux encountered during the operation of a nuclear reactor. The respective analysis was performed in [12] for a typical matured nuclear fuel about 600 days after the refueling. The reduction of anti-neutrino flux above the 1.8 MeV energy threshold for the anti-neutrino reaction with a proton was evaluated for all nine activities listed above, per ^{235}U, ^{238}U, ^{239}Pu and ^{241}Pu fuel components. It resulted in a reduced number of interactions of reactor anti-neutrinos with matter, e.g., with anti-neutrino detector matter. The overall change in the number

of anti-neutrino interactions (MTAS/ENSDF) amounted to 0.976, 0.986, 0.983, and 0.984 for ^{235}U, ^{238}U, ^{239}Pu, and ^{241}Pu, respectively [12]. It means that the reference flux used for the comparison with detected anti-neutrinos is lower reducing the effect of "reactor anti-neutrino anomaly" [2, 3]. For the summation calculations, it would yield a result closer to "no anomaly". However, the intriguing detected excess of high energy anti-neutrino gets enhanced by our MTAS results, roughly from 10% to 12%, see [11,12].

3. Measurements of beta-delayed neutron emission with BRIKEN.

BRIKEN array [15] has been constructed by an international collaboration to measure the branching ratios for beta-delayed one- and multi-neutron emission at RIKEN. The world-largest array of ^{3}He counters, a highly segmented array of Silicon detectors AIDA [16] or Wasabi Si-stack [17] enhanced by a novel YSO counter developed at UT Knoxville, and 2 Ge clovers are the main components of this hybrid setup. Over 140 ^{3}He tubes in BRIKEN, with 87% of ^{3}He volume from ORNL, has nearly 70% efficiency for detecting one neutron having energy up to 1 MeV and over 50% efficiency for the 5 MeV neutron [15]. The experiments were performed by means of BigRIPS fragment separator [18] using in most of the runs ^{238}U primary beam at 345 MeV/u and at impressive beam intensity up to 70 part*nanoAmps.

Several experiments with BRIKEN were performed between ^{78}Ni and rare-earth regions yielding over 100 new beta-delayed neutron (βn) branching ratios. Here, some examples of preliminary results achieved for nuclei around ^{78}Ni are presented. The only known beta-delayed two-neutron (β2n) precursor in this region was ^{86}Ga activity measured at ORNL [19]. The values of P_{1n}=60(20)% and P_{2n} of 20(10) % were reported [19]. The β1n and β2n emission from ^{86}Ga was confirmed and measured more precisely. Preliminary evaluated BRIKEN data for ^{86}Ga are yielding 56% for P_{1n} and 16% for P_{2n} values [20], in agreement with ORNL result. There are several new β2n precursors identified in BRIKEN experiments, e.g., ^{87}Ga [20], ^{89}Ge and ^{91}As.

The quality of preliminary analyzed BRIKEN data is illustrated in Fig.4.

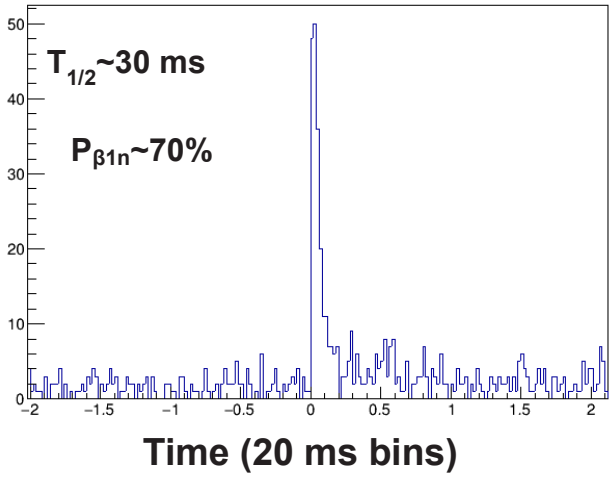

Figure 4 Decay pattern of 1n events recorded in ^{3}He tubes of BRIKEN array in coincidence with β-emission following identified ^{87}Ga ion implantation into AIDA (preliminary analysis N. Brewer, B. Rasco and R. Yokoyama).

In addition to the determination of βxn branching ratios, the BRIKEN is a powerful detector array to measure and identify γ-transitions occurring in β-γ and β-xn-γ decay channels. An example is given in Fig.5 presenting for the first time an identification of γ-radiation following beta-delayed neutron emission from a doubly-magic precursor ^{78}Ni. The individual gamma lines represent most

likely the energies of low-lying states in ^{77}Cu. This result expands our knowledge on the excited states in ^{77}Cu populated directly after beta decay of ^{77}Ni [21]. In particular the 284 keV transition seems to be the best candidate for the lowest 3/2+ state in ^{77}Cu, in addition to the 293 keV state populated in beta decay of ^{77}Ni [21].

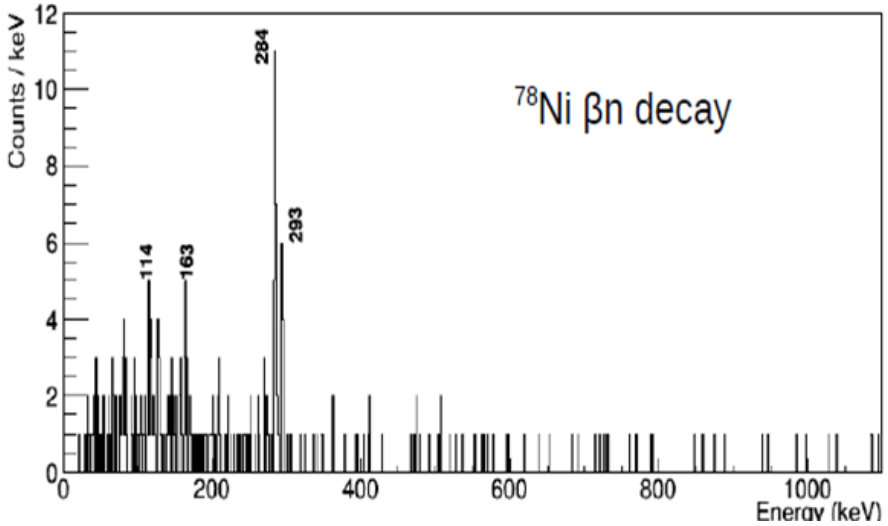

Figure 5. Gamma spectrum recorded in two ORNL HPGe clovers in the BRIKEN array, in correlation with beta-one neutron decay of identified 78Ni ions implanted into the mini-WAS3ABi Si-array (on-line analysis P. Vi and J. Liu).

4. Summary

At the ORNL tandem facility, nuclear data measurements using the Modular Total Absorption Spectrometer have been carried out, to obtain true beta decay properties of nearly 80 fission products most abundant in nuclear fuel. Decay heat values increased by about 3% in the first round of data analysis. MTAS results impact the properties of reactor anti-neutrino energy spectra reducing the number of anti-neutrinos interacting with matter. At RIKEN, a new hybrid detector array BRIKEN dedicated to the studies of new beta-delayed neutron emitters started to take data. Many new βxn precursors have been identified and new β-γ and β-xn-γ decay properties were measured for very neutron-rich nuclei in the ^{78}Ni region and in the rare earth region.

Acknowledgements

Many thanks to the crews of the ORNL-tandem facility and RIKEN accelerator complex for the excellent beams delivered. This work is supported in part by the U.S. DOE Office of Science.

References

[1] “Assessment of Fission Product Decay Data for Decay Heat Calculations,” Nuclear Energy Agency, Organization for Economic Co-operation and Development (coordinator: T. Yoshida, monitor: A.L. Nichols), Nuclear Science NEA/WPEC-25, ISBN 978-92-64-99034-0, NEA No. 6284, OECD 2007, http://www.nea.fr/html/science/wpec/volume25/volume25.pdf.
[2] G. Mention et al., Phys. Rev. D 83, 073006 (2011).
[3] P. Huber, Phys. Rev. C 84, 024617 (2011).
[4] K. P. Rykaczewski and R.K. Grzywacz, Decay studies of fission products with a new Modular Total Absorption Spectrometer (MTAS), ARRA FWP # 22580 (2009).
[5] D.W. Stracener, Nucl. Instr. Meth. Phys. Res. B 204, 42 (2003).

[6] J. R. Beene, et al., Jour. Phys. G, Nucl. Part. Phys. 38, 024002 (2011).
[7] M. Wolińska-Cichocka et al., Nucl. Data Sheets 120, 22 (2014).
[8] B.C. Rasco et al., Nucl. Instr. Meth. Phys. Res. A 788, 137 (2015).
[9] M. Karny et al., Nucl. Instr. Meth. Phys. Res. A 836, 83 (2016).
[10] A.A. Sonzogni et al., Phys. Rev. C 91, 011301(R) (2015).
[11] B.C. Rasco et al., Phys. Rev. Lett.117, 092501 (2016).
[12] A. Fijałkowska et al., Phys. Rev. Lett.119, 052503 (2017).
[13] B.C. Rasco et al., Phys. Rev. C 95, 054328 (2017).
[14] M. Wolińska-Cichocka et al., EPJ Web of Conf. 146, 10005 (2017).
[15] A. Tarifeno-Saldivia et al., J. Instrum. 12, P04006 (2017).
[16] C. J. Griffin et al., POS (NIC-XIII) 097 (2014).
[17] S. Nishimura, Prog. Theor. Exp. Phys. 03C006 (2012).
[18] T. Kubo, Nucl. Instrum. Methods Phys. Res., Sect. B 204, 97 (2003).
[19] K. Miernik et al., Phys. Rev. Lett. 111, 132502 (2013).
[20] R. Yokoyama et al., to be published.
[21] E. Sahin et al. Phys. Rev. Lett. 118, 242502 (2017).

This is a blank page.

4 Recent Progress in Theory of Nuclear Fission

Satoshi CHIBA
Laboratory for Advanced Nuclear Energy, Tokyo Institute of Technology.
e-mail: chiba.satoshi@nr.titech.ac.jp

With the advance of experimental techniques and computational capability, theory of nuclear fission has also advanced in recent years. Especially, those based on quantum mechanics and dynamical models have made a substantial progress. In this paper, a brief review on the recent progress in theory of nuclear fission is given, by emphasizing some results obtained at Tokyo Tech.

1. Introduction

Nuclear fission is the most fundamental physics process dominating properties of nuclear reactors. However, it is still a mysterious phenomenon since it is a unique large-scale collective motion of nuclei which gives rise to a transition from a single to two (or rarely three) nuclear clusters. It is unique indeed in many facets: 1) it is important both in fundamental and application fields, 2) many different observables come out, which must be understood or explained in a consistent manner, such as isotopic and total kinetic energy distributions of fission fragments, emission of prompt neutrons and photons, then weak-decay of the neutron-rich nuclei follows which will emit delayed neutrons, electrons, antineutrinos and photons, 3) quantal effects such as shell and pairing effects, which are tiny addition to the huge macroscopic energy in terms of a macro-micro view, dominate the fission process in many important nuclei such as U and Pu, 4) reactor antineutrino anomaly is offering a challenge to the standard model, 5) it is important to understand the origin of medium to heavy nuclei in astrophysical nucleosynthesis (NS-NS merger scenario), and so forth. In spite of a long history of research, however, understanding of the fission mechanisms, especially the part from the compound nucleus to scission point is still very poor. It is poor also in terms of the fact that predictions of the nuclear theory are not accurate enough to be used in application fields.

We have been doing a comprehensive approach to understand and describe the whole process of nuclear fission, where we use a macro-micro model as well as microscopic theories such as AMD (Antisymmetrized Molecular Dynamics) and TDDFT (time-dependent Density Functional Theory), and a phenomenological statistical decay models. Recent progress of nuclear fission theory including those being developed at other organizations will be explained, and I wish to present and discuss problems we are facing with and possible ways to go.

2. Comparison of various theories

In Table 1, we compare features of various theories of nuclear fission.

Table 1 Comparison of main features of various theories used to describe nuclear fission.

	Quantum	Description	Adiabaticity	Stochasticity	Observable	Computational cost
Scission point model	Half	Static	Yes	N/A	FPY, TKE	Low
Macro-micro (Langevin, random walk)	Half	Static + dynamic	Yes	Yes	Any events	Low
DFT+TDGCM	Full	Static + dynamic	Yes	Half	FPY	Medium
TDDFT	Full	Dynamic	No	No	FPY, TKE	Very high
AMD	Full	Dynamic	No	Yes	Any events	High

Here, all the theories excluding the fScission point model are dynamical theories, which become major tools recently to elucidate dynamics of nuclear fission. The scission point models[1-3] try to describe properties of fragment distributions based on potential energy landscape at the scission point, and are very convenient for many purposes. However, it is now recognized that dynamics is very important, as was shown by the fission of ^{180}Hg[4].

3. Langevin theory

The macro-micro-type theories, like Langevin theory and random-walk model, is based on adiabatic potential energy surfaces (PES) calculated in advance. The PES is normally calculated at zero temperature by two-center shell model or two-center Woods-Saxon model. The shell effect on the PES plays a very important role to account for the 2-peak structure in the mass distribution of fission fragments in the region of U and Pu, and treatment of damping of the shell effect according to the excitation energy is also an important ingredient. Recently, our group has develped a 3D Langevin theory with microscopic transport coefficients[5,6], and a 4D Langevin model based on macroscopic transport coefficients[7].

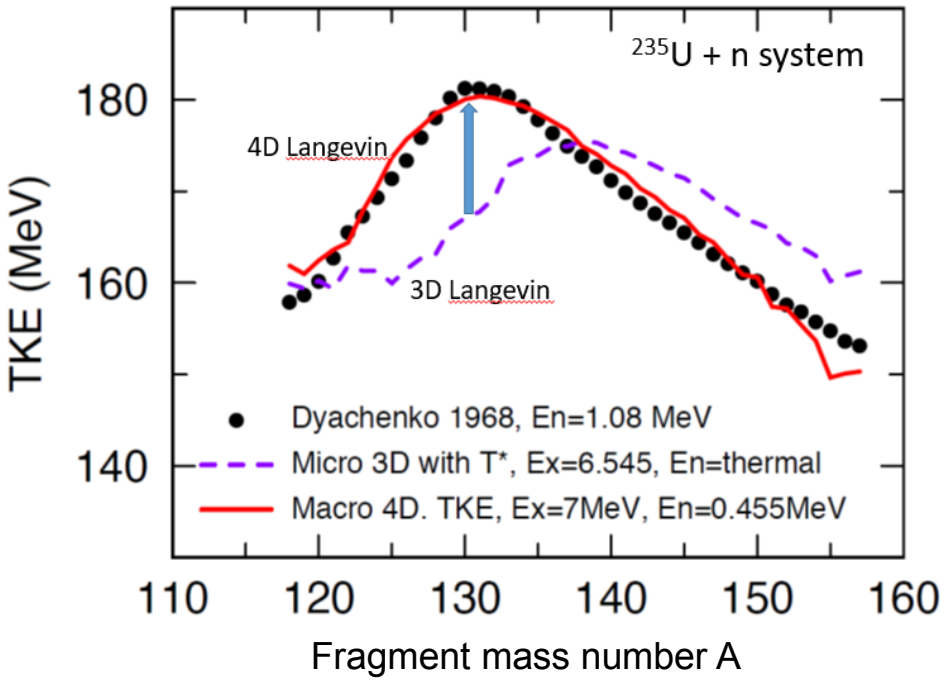

Fig. 1 Comparison of experimental and calculated average total kinetic energy (TKE) of fission fragments from neutorn-induced fission on ^{235}U [7]. The black circles denote expeimentlal data, while 2 lines are those caluclated with 4D (solid line) and 3D (broken line) Langevin theories for excited ^{236}U.

In Fig. 1, we compare average total kinetic energy of fragments at various mass numbers, calculated by 4D and 3D Langevin theories with experimental data. It is evident that 4D Langevin gives a much improved description of the TKE values compared to 3D model. Here we wish to point out the 3D Langevin theory is based on PES calculated by two-center shell-model (TCSM), which is an infinite-depth potential, and can reproduce mass distribution of fission fragments, while that potential calculated as 4D TCSM does not give a good description for the mass distribution in 4D Langevin calculation. Therefore, we had to switch to 4D two-center Woods-Saxon (TCWS) model when we increased the dimensionality from 3D to 4D. Now, we have evidences that 3D Langevin model based on 3D TCSM gives good mass distribution quite accidentally. For example, in Fig.2, we show deformation paramter δ as a function of fragment mass number A. As we can see, the 3D calculation gives symmetric δ around the half of the mass number of compound nucleus, while 4D gives asymmetric distribution, which canot be realized by the 3D calculation. In the 4D calculation, we also understood that about 10% of the TKE arises as a pre-scission kinetic energy. It should be noted that Sierk has develped a 5D Langevin model[9].

In these calculations, we notice that damping of shell effects in the PES as a function of temperature is important, so we have developed recently a way to calculate the temperature-dependent PES, as is shown in Fig. 3. As we can see, the shell structure is washed out as temperature increases, and the potential becomes almost that of liquid-drop model at T=2.0MeV. This change of the potential landscape is shape-dependent, so a simple factor which has been used in previous Langevin-type calcualtion may not be adequate to

realize washing out of the shell effect as excitation energy increases.

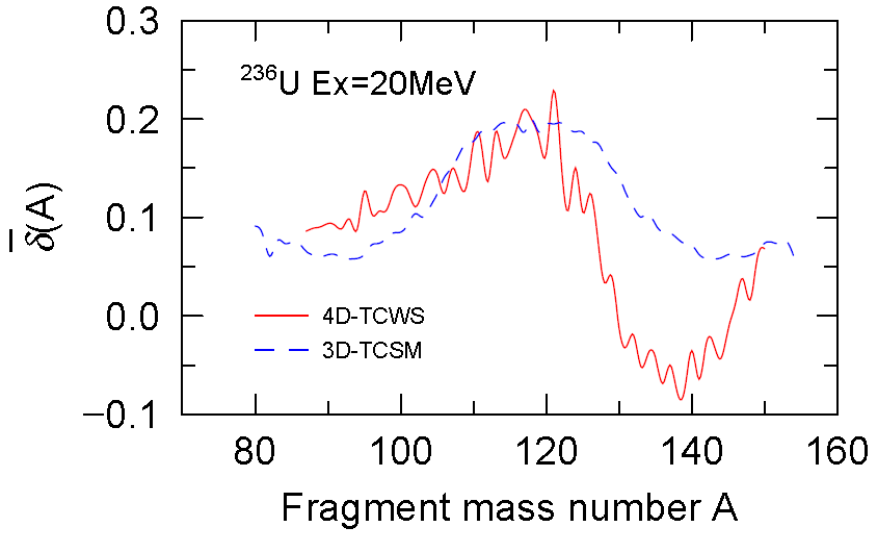

Fig. 2 Comparison of deformation parameter δ obatained by 3D Langevin using two-center shell model (TCSM)-PES and 4D Langevin using two-center Woods-Saxon (TCWS) PES.

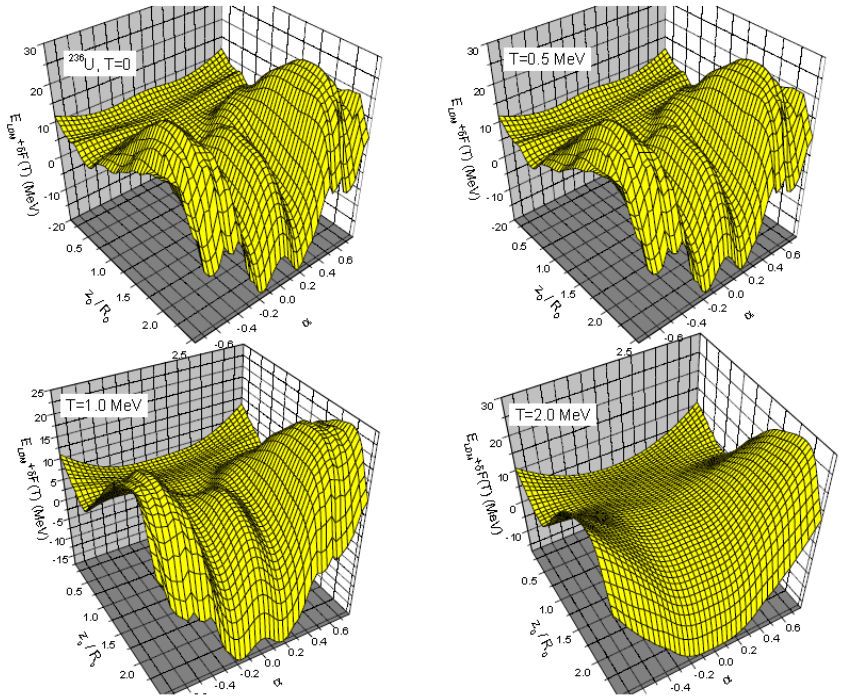

Fig. 3 Temperature-dependent PES of ^{236}U calculated by a 4D finite-temperature two-center Woods-Saxon model [8]. z_0/R_0 denotes elongation, and α denotes mass asymmetry.

4. AMD, TDDFT, TDGCM

AMD (Antisymmetrized Molecular Dynamics)[10], TDDFT (time-dependent density functional theory)[11,12] and DFT-TDGCM (density-functional theory + time-dependent generator coordinate

method)[13] are quantum theories of nuclear fission in different perspectives. In the AMD, the single-particle wave function is constrained to a Gaussian function, but the time-evolution is governed by an equation derived by the time-dependent variational principle supplemented by stochastic NN collision. We have explored a possibility to apply AMD to describe nuclear fission, and the results are quite promising [14]. The TDDFT is a deterministic theory, but effects of pairing is considered in the most up-to-date versions [11], and even a stochasticity is included as an initial condition[12]. The DFT-TDGCM is also an promising theory of nuclear fission, which converts the time-evolution of many-body wave function to that of overlap functions[13] on a superconducting PES, and can derive "distributions" of fission fragments.

5. Conclusion

A brief review is given of the theory of nuclear fission currently used to analyze the data and to understand reaction mechanisms. Dynamical theories are becoming the major methodology for this purpose, and many quantum-mechanical models have been proposed and they all are showing good progress.

Acknowledgements

The authors wish to acknowledge cooperation and valuable information from Drs. F.A. Ivanyuk, J.A. Maruhn, A. Ono, M. Kimura, C. Ishizuka, K. Tsubakihara, S. Okumura, Mrs. M.D. Usang, A. Etori and T. Nishikawa.

References

[1] P. Fong: Phys. Rev. 102, 434 (1956).
[2] B.D. Wilkins, E.P. Steingerg and R.R. Chasman: Phys. Rev. C 14, 1832 (1976).
[3] U. Brosa, S. Grossmann and A. Mueller, Phys. Rep. 197, 167-262(1990).
[4] A. N. Andreyev, K. Nishio and K-H Schmidt, Rep. Prog. Phys. 81, 016301(2018).
[5] M.D. Usang. F.A. Ivanyuk, C. Ishizuka and S. Chiba, Phys. Rev. C 94, 044602(2016).
[6] M.D. Usang. F.A. Ivanyuk, C. Ishizuka and S. Chiba, Phys. Rev. C 96, 064617(2017).
[7] C. Ishizuka, M.D. Usang, F.A. Ivanyuk, J.A. Maruhn, K. Nishio, and S. Chiba: Phys. Rev. C 96, 064616 (2007).
[8] F.A. Ivanyuk et al, to be submitted.
[9] A.J. Sierk, Phys. Rev. C 96, 034603(2017).
[10] A. Ono et al., Prog. Theor. Phys. 87, 1185(1992).
[11] A. Bulgac et al, Phys. Rev. Lett. 116, 122504(2016).
[12] Y. Tanimura et al., Phys. Rev. Lett. 118, 152501(2017).
[13] H. Goutte et al, Phys. Rev. C 71, 024316(2005).
[14] A. Etori et al, this symposium.

This is a blank page.

5 Impacts of nuclear-physics uncertainties in the s-process determined by Monte-Carlo variations

N. Nishimura[1*†], G. Cescutti[2†], R. Hirschi[3,4†], T. Rauscher[5,6†], J. den Hartogh[3†] and A. St. J. Murphy[7†]

[1] Yukawa Institute for Theoretical Physics, Kyoto University, Kyoto 606-8502, Japan
[2] INAF, Osservatorio Astronomico di Trieste, via G.B. Tiepolo 11, I-34131 Trieste, Italy
[3] Astrophysics Group, Keele University, Keele ST5 5BG, UK
[4] Kavli IPMU (WPI), University of Tokyo, Kashiwa 277-8583, Japan
[5] Department of Physics, University of Basel, 4056 Basel, Switzerland
[6] Centre for Astrophysical Research, University of Hertfordshire, Hatfield AL10 9AB, UK
[7] School of Physics and Astronomy, University of Edinburgh, Edinburgh EH9 3FD, UK

Abstract

The s-process, a production mechanism based on slow-neutron capture during stellar evolution, is the origin of about half the elements heavier than iron. Abundance predictions for s-process nucleosynthesis depend strongly on the relevant neutron-capture and β-decay rates, as well as on the details of the stellar model being considered. Here, we have used a Monte-Carlo approach to evaluate the nuclear uncertainty in s-process nucleosynthesis. We considered the helium burning of massive stars for the weak s-process and low-mass asymptotic-giant-branch stars for the main s-process. Our calculations include a realistic and general prescription for the temperature dependent uncertainty for the reaction cross sections. We find that the adopted uncertainty for (n, γ) rates, tens of per cent on average, affects the production of s-process nuclei along the line of β-stability, and that the uncertainties in β-decay from excited state contributions, have the strongest impact on branching points.

1. Introduction

Nucleosynthesis of heavy elements beyond the iron-group peak (mass number $A \sim 60$) is distinctly different from the production process of lighter elements. Neutron-capture is considered to be the primary production mechanism of heavier nuclei, up to $A \sim 200$, facilitated by the neutron having no electric charge, and thus enabling penetration of substantial Coulomb barriers. Two different n eutron-capture p rocesses h ave been proposed [1], *i.e.*, the s- and r-process that are slow and rapid as compared to β-decay half-lives, respectively. The s-process occurs in stellar environments that feature lower neutron densities, while environments with higher neutron densities allow the faster rate of captures that leads to r-process nucleosynthesis.

The slow timescale of the s-process means that it occurs in stellar burning environments that evolve over longer timescale. There are two astronomical sites and corresponding classes of the s-process (see a review [2] and references therein). The *main* s-process occurs in (i) thermal pulses of low-mass asymptotic-giant-branch (AGB) stars producing heavy nuclei up to Pb and Bi, while the *weak* s-process takes place in helium-core and carbon-shell burnings of massive stars and involves lighter nuclei up to $A \approx 90$. In both cases, the primary mechanism is to produce heavier elements due to the neutron capture and β-decay along stable isotopes from seed Fe nuclei over a long-term stellar evolution period. The neutron source reactions for the s-process are

*E-mail: nobuya.nishimura@yukawa.kyoto-u.ac.jp
†BRIDGCE UK Network; www.bridgce.ac.uk, UK

α-capture to different nuclei, where ^{13}C$(\alpha, n)^{16}$O and ^{22}Ne$(\alpha, n)^{15}$Mg are main reactions for the main and weak s-processes, respectively. The impact of these key fusion reactions has been well studied [2].

A major remaining issue is the effect of the uncertainties of the individual (n,γ) and β-decay rates on the final nucleosynthesis products. As there are many reactions involved in the s-process, the overall uncertainty is not as straightforward as for the cases of neutron source and poison reactions, for which key reactions are already well identified. More systematic studies based on the Monte-Carlo (MC) and statistical analysis techniques [3, 4, 5] are necessary for such problems.

In the present paper, we investigate the impact of uncertainty caused by nuclear-physics on the production of s-process elements, using the MC-based nuclear-reaction network (see, [6, 7] for details). Adopting simplified stellar models that reproduce typical s-process nucleosynthesis patterns, we apply realistic temperature-dependent uncertainty of nuclear reaction and decay rates. We evaluate the uncertainty of nucleosynthesis yields and identify key reactions that have significant impact on the final s-process abundances.

2. Methods

For the nucleosynthesis calculations, we use simplified 1-D stellar evolution models with solar metallicity. We follow nucleosynthesis evolution along the temporal history of the temperature and density from the initial abundances. The thermal evolution is treated as the time evolution for a "trajectory" as a single fluid component. We adopt $25M_\odot$ massive star evolution model [8, 9] and $2M_\odot$ AGB star model calculated by the MESA code [10]. We have confirmed that these trajectories reproduce a typical abundance pattern for the main and weak s-process, respectively.

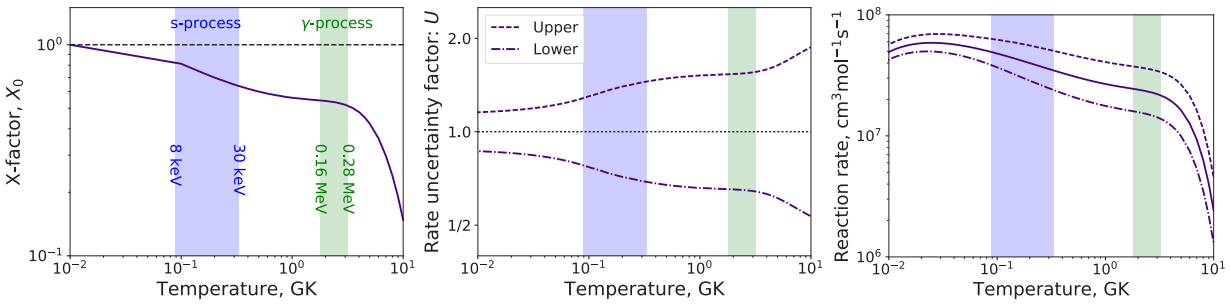

Figure 1: Uncertainty factors for ^{83}Kr$(n,\gamma)^{84}$Kr. (*Left*) X_0 adopted from ref [11]; (*middle*) the upper and lower limits of uncertainty factors; (*right*) the reaction rate [12] with the upper and lower limits. In each panel, the temperature regions for the s-process (8 – 30 keV) and the γ-process (0.16 – 0.28 MeV) are highlighted.

Many nuclear reaction rates of neutron capture relevant to the s-process have been experimentally measured, because the target nuclei are stable (this is not the case for other heavy-element nucleosynthesis, *e.g.*, the r-process, as reactions on the unstable nuclei play a major role). However, these experimental measurements are unable to measure the relevant (n,γ) reaction rates as realized at the high temperatures of the stellar environment due to contributions of excited states [11, 13]. Therefore, we consider that reaction rates have a temperature-dependent uncertainty due to the relative contributions by the ground state and excited states for experimental based cross sections. Following the prescription in refs. [11, 13], we apply the uncertainty factor $u(T)$ for thermonuclear reaction rates as

$$u(T) = X_0(T)u_{\rm exp} + [1 - X_0(T)]\, u_{\rm th} \tag{1}$$

where X_0 is the temperature dependence factor and $u_{\rm exp}$ and $u_{\rm th}$ are uncertainty ranges for experimental and theoretical contributions, respectively. The value of $X_0(T)$ for ^{83}Kr$(n,\gamma)^{84}$Kr is shown in Figure 1 (left panel), which decreases as the temperature increases from 1 at lower temperatures (below ~ 0.01 GK). From Equation 1, therefore, $u(T) \sim u_{\rm exp}$ at lower T, while $u(T)$ reaches $u_{\rm th}$ at higher T.

In this study, experimental uncertainties are used for the ground state contributions to (n,γ) rates, whereas a factor 2 is used for excited state uncertainties (for details, see [13, 6, 5]). As theoretical calculated rates may have large uncertainty, we simply apply a constant value 2. We apply $u(T)$ to determine the upper limit and lower limit for the variation of reaction rates by multiplying $u(T)$ and $1/u(T)$, respectively. The middle panel of Figure 1 shows the adopted uncertainty factor, while the right panel shows the uncertainty range for the ^{83}Kr(n,γ)^{84}Kr reaction.

A similar approach is used for β-decay rates, based on temperature-dependent partition functions $G(T)$ to determine the importance of excited states, *i.e.*, the uncertainty factor of β-decay rates $u_{\rm weak}$ is defined as

$$u_{\rm weak} = \frac{2J_0+1}{G(T)} u_{\rm exp}^{\rm weak} + \left(1 - \frac{2J_0+1}{G(T)}\right) u_{\rm th}^{\rm weak} \ , \tag{2}$$

where $u_{\rm exp}$ and $u_{\rm th}^{\rm weak}$ are experimental and theoretical uncertainty factors, respectively. The uncertainty at lower temperatures ($T < 10^7$ K) corresponds to the measured value at the ground state ($u_{\rm exp}^{\rm weak}$), while the uncertainty becomes larger as the temperature increases. We adopt $u_{\rm th}^{\rm weak} = 1.3$ and $u_{\rm th}^{\rm weak} = 10$, of which the total uncertainty reaches up to ~ 2 in stellar burning temperatures.

3. Results

3.1 Uncertainties of the s-process

Our MC performs many nucleosynthesis simulations, each of which has each nuclear reaction rate sampled from an underlying distribution (*i.e.* applying the variation factor. A uniform random distribution between the upper and lower limit of the reaction rate at a given temperature was used for each variation factor. To identify the separate contributions from uncertainties in (n,γ) and from β-decay rates, we have performed three different cases: `ngbt`, in which all (n,γ) and β-decay rates are varied; `ng` where only (n,γ) rates are varied; and `bt` in which only β-decay rates vary.

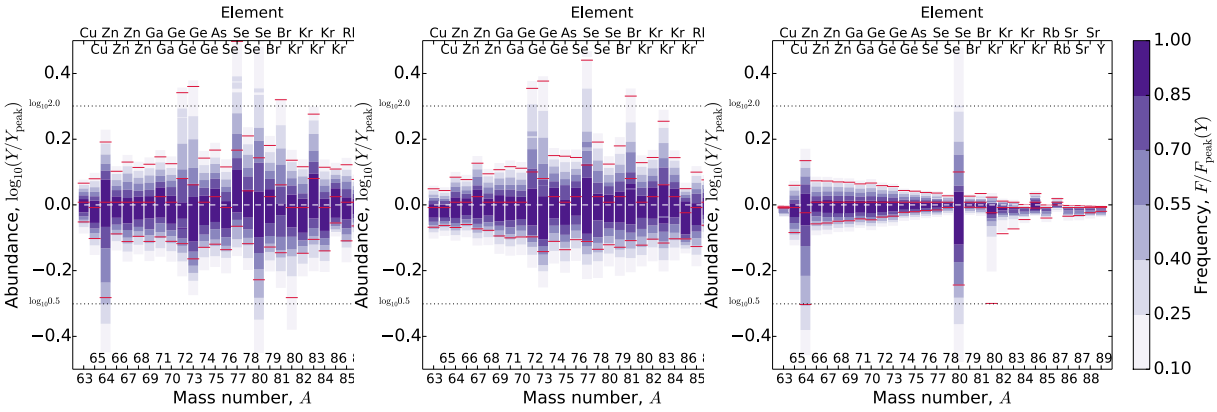

Figure 2: The results of the MC for the weak s-process. The uncertainty range is shown for each isotope with red lines covering 90% from the peak value for variation models of `ngbt` (*left*), `ng` (*middle*) and `bt` (*right*).

Figure 2 shows the resulting production uncertainty for the weak s-process for the cases where we varied all (n,γ) reactions and β-decays. We select abundance uncertainties for stable s-process isotopes up to $A \sim 90$. The colour distribution corresponds to the normalized probability density distribution of the uncertainty in the final abundance.

Considering the `ngbt` case, the 90% uncertainty range of abundances for most nuclides is less than a factor of 1.5 (0.176 in $\log_{10}$) region, while some isotopes show a larger uncertainty that reaches factor 2. Comparison of `ng` and `bt` cases reveals that this is mostly due to (n,γ) reaction. Uncertainties for a few

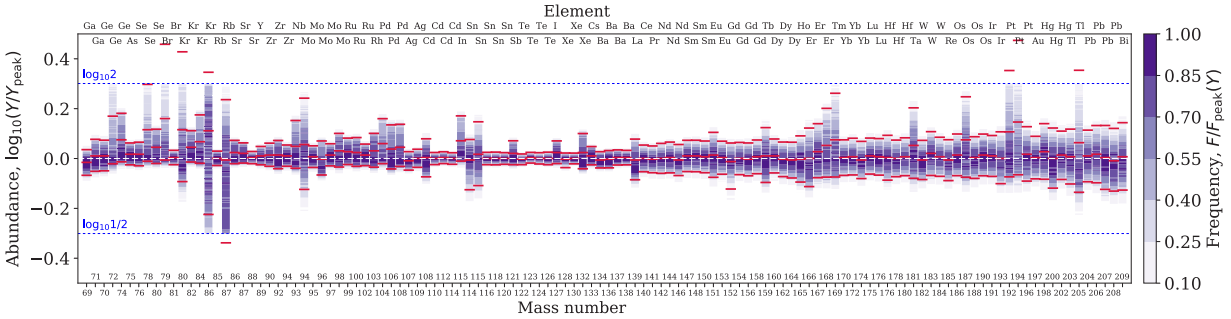

Figure 3: The same as Fig. 2, but the results of main s-process.

isotopes (^{64}Zn and ^{80}Se) are affected by β-decay around branching points, although the effects of β-decay to the global isotopes are minor compared with (n,γ).

The impacts of β-decay uncertainties on the s-process appear only around s-process branchings. This is seen in the results of `bt` (in Figs. 2 and 3), where a few β-decays cause larger uncertainties in nucleosynthesis. Our technique allows one to quantitatively analyze the MC result to identify the correlation between decay rate and final abundance (see, [6]). We find that ^{64}Cu(β^+)^{64}Zn and ^{80}Br(β^+)^{80}Kr have the dominant impact on the production of ^{64}Zn and ^{80}Se for the weak s-process, respectively. These β-decay rates are around the s-process branching points as indicated in previous investigations (in Fig. 2).

These features are also pronounced for the case of main s-process, as the primaly physical mechanism is the same as in the weak s-process. The overall uncertainty of final abundances, shown in Figure 3, shows that they mostly caused by uncertainty of (n,γ) reactions except at branching points (see [7] for more details). The impacts of β-decay uncertainties on the s-process appear only around s-process branchings.

3.2 Key neutron-capture reactions

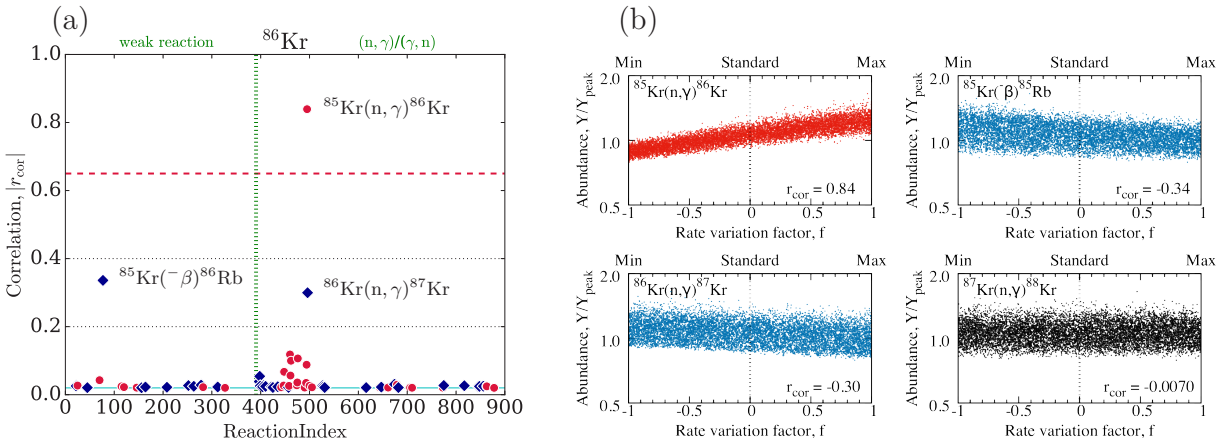

Figure 4: The results of the MC for the weak s-process, focusing on ^{85}Kr production. (a) The values of correlation factor, $|r_{\rm cor}|$, for all varied rates. (b) The distribution of uncertainty factor vs $|r_{\rm cor}|$ for selected reactions:.

Based on the MC calculations, we selected reactions & decays that had a significant impact on the final abundance uncertainties. As shown in Fig. 4, we calculated the Pearson's product-moment correlation coefficient, $r_{\rm cor}$, between variation factors and calculated abundances. In this study, we assume $|r_{\rm cor}| \geq 0.65$ as the significant value. Thus, ^{85}Kr(n,γ)^{86}Kr is the key reaction for the production of ^{86}Kr as shown in

Fig. 4. We also find two cases (*i.e.*, ^{85}Kr(β^-)^{85}Rb and ^{86}Kr(n, γ)^{86}Kr) with $|r_{\rm cor}| > 0.2$, which are possibly key reactions if the uncertainty involving ^{85}Kr(n, γ)^{86}Kr were to become significantly reduced due to future work. They are actually the key reactions for ^{86}Kr when we perform the MC run omitting the uncertainty of ^{85}Kr(n, γ)^{86}Kr, as shown in [6]. Figure 4(b) presents the distribution of uncertainty factors and obtained abundances. This confirms the basic features of $r_{\rm cor}$ that a positive $r_{\rm cor}$ results in a positive correlation of the two parameters, and vice versa, and that a larger $|r_{\rm cor}|$ results in a stronger correlation.

We calculated correlation factors for all possible combinations of varied reaction rate and s-process products. As the full lists of these key rates are summarized in our papers [6, 7], here, we only highlight "Level 1" key rates with highest priorities for the weak and main s-processes. In Tables 1 and 2, we list key (n, γ) reactions, of which $|r_{\rm cor}| >= 0.65$, for the weak s-process and main s-process, respectively. Here, only the target nucleus is listed for (n, γ) reactions, e.g. the (n, γ)-target nucleus "^{67}Zn" indicates ^{67}Zn(n, γ)^{68}Zn.

We note that there are a few cases that the key nucleus is not the target-nucleus of the key (n, γ) reaction. This is due to the propagation of large uncertainties from "upstream" to "downstream" through the s-process nucleosynthesis flow. Besides the reactions listed in the tables, there are still some reactions that show the non-negligible value of $r_{\rm cor}$. These will become important reactions if the relevant first-priority reactions become well determined (*e.g.* through future experimental work). Refs [6, 7] provide further details.

Table 1: The key neutron-capture reactions for the weak s-process. Key (n, γ) reactions are listed with their correlation factors $r_{\rm cor,0}$ for each key "product" nucleus. Only the target nucleus for the involving neutron capture is shown in the column of "(n, γ)-target".

Product	^{67}Zn	^{72}Ge	^{73}Ge	^{77}Se	^{78}Se	^{81}Kr	^{83}Kr	^{85}Kr
(n, γ)-target	^{67}Zn	^{72}Ge	^{73}Ge	^{77}Se	^{78}Se	^{81}Br	^{83}Kr	^{86}Kr
$r_{\rm cor,0}$	−0.67	−0.85	−0.84	−0.86	−0.71	−0.80	−0.76	0.84

Table 2: Key neutron-capture reactions for the main s-process. The columns are the same as Table 1.

Product	^{69}Ga	^{71}Ga	^{70}Ge	^{72}Ge	^{74}Ge	^{75}As	^{76}Se	^{78}Se	^{79}Se	^{79}Se	^{80}Se	^{81}Br
(n, γ)-target	^{69}Ga	^{71}Ga	^{70}Ge	^{72}Ge	^{74}Ge	^{75}As	^{76}Se	^{78}Se	^{79}Br	^{80}Kr	^{80}Se	^{81}Br
$r_{\rm cor,0}$	−0.78	−0.89	−0.87	−0.93	−0.97	−0.86	−0.89	−0.97	−0.94	−0.90	−0.96	−0.74
Product	^{84}Kr	^{85}Kr	^{85}Kr	^{85}Rb	^{86}Sr	^{87}Sr	^{88}Sr	^{89}Y	^{90}Zr	^{92}Zr	^{93}Zr	^{94}Zr
(n, γ)-target	^{84}Kr	^{86}Kr	^{87}Rb	^{85}Rb	^{86}Sr	^{87}Sr	^{88}Sr	^{89}Y	^{90}Zr	^{92}Zr	^{93}Nb	^{94}Zr
$r_{\rm cor,0}$	−0.98	0.88	0.86	−0.86	−0.94	−0.92	−0.65	−0.83	−0.88	−0.92	−0.97	−0.85
Product	^{96}Mo	^{97}Mo	^{98}Mo	^{99}Tc	^{100}Ru	^{102}Ru	^{103}Rh	^{104}Pd	^{106}Pd	^{107}Pd	^{108}Pd	^{109}Ag
(n, γ)-target	^{96}Mo	^{97}Mo	^{98}Mo	^{99}Ru	^{100}Ru	^{102}Ru	^{103}Rh	^{104}Pd	^{106}Pd	^{107}Ag	^{108}Pd	^{109}Ag
$r_{\rm cor,0}$	−0.94	−0.87	−0.94	−0.91	−0.92	−0.86	−0.95	−0.97	−0.96	−0.80	−0.96	−0.79
Product	^{115}In	^{115}In	^{121}Sb	^{126}Te	^{127}I	^{132}Xe	^{133}Cs	^{134}Ba	^{136}Ba	^{137}Ba	^{138}Ba	^{139}La
(n, γ)-target	^{115}In	^{115}Sn	^{121}Sb	^{126}Te	^{127}I	^{132}Xe	^{133}Cs	^{134}Ba	^{136}Ba	^{137}Ba	^{138}Ba	^{139}La
$r_{\rm cor,0}$	−0.97	−0.65	−0.92	−0.68	−0.92	−0.97	−0.89	−0.85	−0.88	−0.84	−0.65	−0.88
Product	^{159}Tb	^{165}Ho	^{166}Er	^{167}Er	^{168}Er	^{169}Tm	^{181}Ta	^{187}Os	^{192}Pt	^{194}Pt	^{200}Hg	^{205}Pb
(n, γ)-target	^{159}Tb	^{165}Ho	^{166}Er	^{167}Er	^{168}Er	^{169}Tm	^{181}Ta	^{187}Os	^{192}Pt	^{194}Pt	^{200}Hg	^{205}Tl
$r_{\rm cor,0}$	−0.80	−0.68	−0.81	−0.78	−0.86	−0.90	−0.84	−0.86	−0.89	−0.90	−0.67	−0.87

4. Conclusion

We have evaluated the impact on s-process nucleosynthesis in massive stars and low mass AGB stars of nuclear physics uncertainties using a Monte Carlo driven variational technique. We find that (n,γ) reactions dominate the total uncertainty, with a few important contributions from β-decays around branching points. We have then identified individual key reactions in a rigorous and robust way, to guide and support further investigations in nuclear astrophysics regarding the s-process.

Acknowledgements

This project has been financially supported by the ERC (EU-FP7-ERC-2012-St Grant 306901-SHYNE, EU-FP7 Adv Grant GA321263-FISH), the UK STFC (ST/M000958/1), "ChETEC" COST Action (CA16117) and MEXT as "Priority Issue on Post-K computer" (Elucidation of the Fundamental Laws and Evolution of the Universe) and JICFuS. Parts of computations presented in the paper were carried out by computer facilities at the University of Cambridge (COSMOS at DAMPT, STFC DiRAC Facility), University of Edinburgh (Eddie mark 3), CfCA in National Astronomical Observatory of Japan and YITP at Kyoto University.

References

[1] E. M. Burbidge, G. R. Burbidge, W. A. Fowler, and F. Hoyle: Reviews of Modern Physics **29** (1957) 547.

[2] F. Käppeler, R. Gallino, S. Bisterzo, and W. Aoki: Reviews of Modern Physics **83** (2011) 157.

[3] C. Iliadis, R. Longland, A. Coc, F. X. Timmes, and A. E. Champagne: Journal of Physics G Nuclear Physics **42** (2015) 034007.

[4] T. Rauscher, N. Nishimura, R. Hirschi, G. Cescutti, A. S. J. Murphy, and A. Heger: Mon. Not. R. Astron. Soc. **463** (2016) 4153.

[5] N. Nishimura, T. Rauscher, R. Hirschi, A. S. J. Murphy, G. Cescutti, and C. Travaglio: Mon. Not. R. Astron. Soc. **474** (2018) 3133.

[6] N. Nishimura, R. Hirschi, T. Rauscher, A. St. J. Murphy, and G. Cescutti: Mon. Not. R. Astron. Soc. **469** (2017) 1752.

[7] G. Cescutti, R. Hirschi, N. Nishimura, T. Rauscher, A. St. J. Murphy, and S. Cristallo: submitted to Mon. Not. R. Astron. Soc. (2018).

[8] R. Hirschi, G. Meynet, and A. Maeder: Astron. Astrophys. **425** (2004) 649.

[9] R. Hirschi, U. Frischknecht, F.-K. Thielemann, M. Pignatari, C. Chiappini, S. Ekström, G. Meynet, and A. Maeder: In L. K. Hunt, S. C. Madden, and R. Schneider (eds), *IAU Symposium*, Vol. 255 of *IAU Symposium*, December 2008, pp. 297–304.

[10] B. Paxton, L. Bildsten, A. Dotter, F. Herwig, P. Lesaffre, and F. Timmes: Astrophys. J. Suppl. **192** (2011) 3.

[11] T. Rauscher, P. Mohr, I. Dillmann, and R. Plag: Astrophys. J. **738** (2011) 143.

[12] I. Dillmann, M. Heil, F. Käppeler, R. Plag, T. Rauscher, and F.-K. Thielemann: In A. Woehr and A. Aprahamian (eds), *Capture Gamma-Ray Spectroscopy and Related Topics*, Vol. 819 of *American Institute of Physics Conference Series*, March 2006, pp. 123–127.

[13] T. Rauscher: Astrophys. J. Suppl. **201** (2012) 26.

6 Microscopic description of nuclear level density in shell-model calculations

Noritaka Shimizu[1)] and Yutaka Utsuno[2)]

1) Center for Nuclear Study, The University of Tokyo,
Hongo 7-3-1, Bunkyo-ku, Tokyo, 113-0033, Japan
e-mail: shimizu@cns.s.u-tokyo.ac.jp

2) Advanced Science Research Center, Japan Atomic Energy Agency,
Tokai, Ibaraki 319-1195, Japan

Abstract

We report a recent development of nuclear level-density study in terms of shell model calculations. In order to calculate the level density efficiently, we introduced a novel stochastic estimation method into the shell-model framework and demonstrated that it works quite well in pf-shell nuclei. The present work is mainly based on Refs. [1, 2].

1. Introduction

The nuclear level density is one of the most important nuclear data to understand neutron capture processes under astrophysical conditions (e.g. [3]). Nuclear shell-model calculation is one of the most powerful tools to describe the nuclear structure especially in low-lying excitation spectra. However, in medium-heavy nuclei, it is difficult to compute all highly excited states directly and its applicability is quite limited [4], since in the highly-excited region the level density becomes large and the resulting computational demands increase rapidly. In such a case, the Lanczos strength function method is a good tool to obtain the excitation strength distribution from the ground state [5, 7]. Recent progresses in supercomputer and theoretical developments enable us to study giant dipole resonances in the around E_x=20 MeV region utilizing the Lanczos strength function method. Other kinds of giant resonances, e.g. Gamow-Teller resonance [8], attract much attention. However, the Lanczos strength function method cannot provide us with the level density.

Thus, an efficient method to estimate the level density in nuclear shell-model calculations has been demanded. Various methods have been suggested to obtain the level density in the shell-model calculation [9, 10]. Among them, the application of the auxiliary-field quantum Monte Carlo method to shell-model calculations is a powerful method to overcome this difficulty [11], while the negative sign problem in quantum Monte Carlo methods prevents us from using a realistic effective interaction which can describe spectroscopic information of the low-lying states precisely. In the present study we introduce a stochastic estimation combined with a conjugate gradient method.

In section 2, the computational aspect of the large-scale shell-model calculation is summarized. The theoretical framework of the stochastic estimation method is described in section 3. The shell-model result and discussion of the level-density study are given in section 4.

2. Large-Scale Shell-Model Calculations

In shell model calculations, the nuclear wave function is described as a superposition of configurations, which represent various ways of the occupation of active particles in the valence orbits. Namely, the wave function is a linear combination of a vast number of Slater determinants, which are the antisymmetrized products of the single-particle wave functions. The simplest representation for the Slater determinant is called "M-scheme" basis state,

$$|M_i\rangle = \prod_{\alpha=1}^{A} c^{\dagger}_{M_i^{(\alpha)}}|-\rangle, \tag{1}$$

where A and $|-\rangle$ are the number of the active nucleons and an inert core, respectively. $M_i^{(\alpha)}$ represents that the single-particle state i is occupied by the α-th active nucleon.
$M_i = \{M_i^{(1)}, M_i^{(2)}, ..., M_i^{(A)}\}$ is called "configuration" and represents that 1st, 2nd, ..., A-th particles occupy $M_i^{(1)}, M_i^{(2)}, ..., M_i^{(A)}$ single-particle states, respectively.

A Hamiltonian in nuclear shell-model calculations is defined as

$$\hat{H} = \sum_i t_i c_i^{\dagger} c_i + \sum_{i<j,k<l} v_{ijkl} c_i^{\dagger} c_j^{\dagger} c_l c_k, \tag{2}$$

where c_i and $c_i^{\dagger}$ denote the annihilation and creation operators of the single particle state i. From the Schrödinger equation we deduce

$$\sum_j \langle M_i|\hat{H}|M_j\rangle f_j = E f_i, \quad |\Phi\rangle = \sum_i f_i |M_i\rangle \tag{3}$$

where E and $|\Phi\rangle$ is the eigenenergy and its corresponding nuclear wave function, respectively. The subspace $\{|M_i\rangle\}$ is spanned with the the configurations with a fixed z-component of angular momentum and parity quantum number. The number of the configurations corresponds the dimension of the Hamiltonian matrix $\langle M_i|\hat{H}|M_j\rangle$ and called M-scheme dimension. Since this Hamiltonian matrix tends to be large but sparse, the Lanczos algorithm is advantageous to solve the eigenvalue problem. Recent supercomputers enable us to perform the computation of the yrast (lowest) eigenenergy of the $O(10^{11})$-dimensional matrix. However, it is much more difficult to compute the highly-excited states than the yrast states in the Lanczos method. We introduce an efficient way to obtain nuclear level densities without computing each eigenvalue in the next section.

3. Stochastic Estimation of Level Density

In this section, we describe the theoretical framework to obtain level densities in the large-scale shell-model calculation. Since each state corresponds to the eigenvalue of the Hamiltonian matrix, we estimate the number of eigenvalues in a given energy range stochastically using the method presented in Ref. [12] and firstly introduced to the nuclear shell model calculations in Refs. [1, 2].

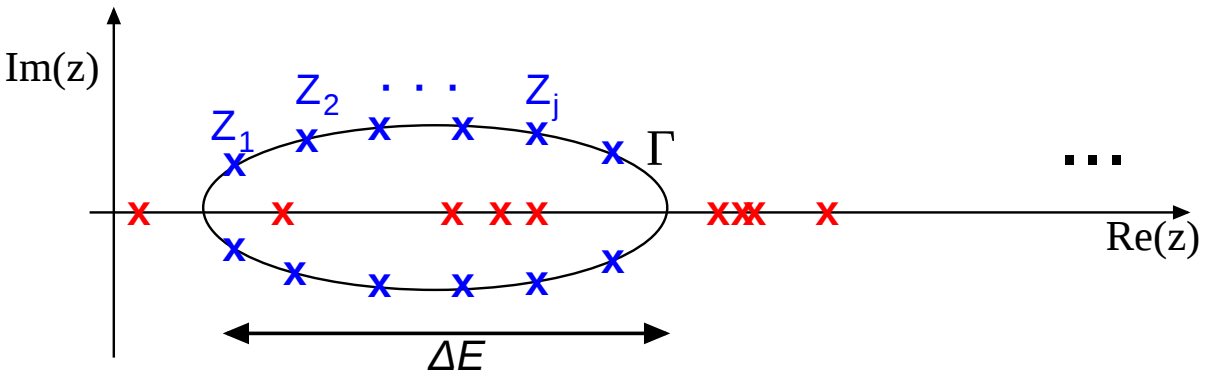

Figure 1: (Color Online) Schematic view of the contour integral to count the eigenvalues (red crosses). The blue crosses denote the discretized mesh points z_j along the integral contour Γ.

In order to evaluate the number of eigenvalues in an arbitrary energy range, we consider the Cauchy integral in the complex plane of z in Fig. 1. The number of eigenstates surrounded by the contour Γ is stochastically estimated as

$$\rho^{\Gamma} = \frac{1}{2\pi i}\oint_{\Gamma} dz \mathrm{Tr}\left(\frac{1}{z-H}\right) \simeq \sum_j w_j \mathrm{Tr}\left((z_j - H)^{-1}\right), \tag{4}$$

where $H = \langle M_i|\hat{H}|M_j\rangle$ is a shell-model Hamiltonian matrix. The contour integral is approximated by a summation of the discretized points z_j shown as blue symbols in Fig. 1 with the corresponding weights w_j. The trace of the matrix $\mathrm{Tr}\left((z_j - H)^{-1}\right)$ is stochastically estimated by Hutchinson's estimator [13] as

$$\mathrm{Tr}\left((z_j - H)^{-1}\right) \simeq \frac{1}{N_s}\sum_{s=1}^{N_s} v_s^T (z_j - H)^{-1} v_s, \tag{5}$$

where v_s is a sample vector whose elements are taken as 1 or -1 randomly. N_s is the number of the sample vectors, and it is known that even a small value of N_s gives a reasonable estimation. The product of the inverse matrix and the vector in Eq.(5) is obtained by solving the linear equation $v_s = (z_j - H)x$ by the block complex orthogonal conjugate gradient (COCG) method. The shift algorithm enables us to solve the equations for various z_j's simultaneously [12]. The procedure is summarized as follows. Further details can be found in Refs. [1, 2].

1. Prepare mesh points z_j for the contour integral which surrounds a certain energy range of interest.
2. Prepare random vectors v_s to stochastically estimate the trace of the matrix by Hutchinson's estimator.
3. Solve $v_s = (z_j - H)x$ by shifted Block COCG method and obtain $v_s^T (z_j - H)^{-1} v_s$.

4. Calculate the number of eigenvalues inside Γ with Eqs.(4) and (5).

The computational implementation for the present method was developed combining the KSHELL code [14] and the z-Pares library [15] to utilize supercomputers efficiently. We demonstrated how the present method works well in Refs.[1, 2].

4. Numerical Results

In this section we discuss the level density of ^{57}Fe as an example. The experimental level density is shown in Fig. 7(b) of [16], the shell-model level density is also presented for comparison. However, this shell-model calculation was performed in the pf-shell model space with allowing 1-particle 1-hole truncation from the $0f_{7/2}$ orbit possibly due to the restriction of computational resources. Such a strict truncation causes the underestimation of the level density by about 40% in the $E_x \sim 5$ MeV region. The stochastic estimation discussed in section 3 enables us to obtain the level density by shell-model calculations without any truncation.

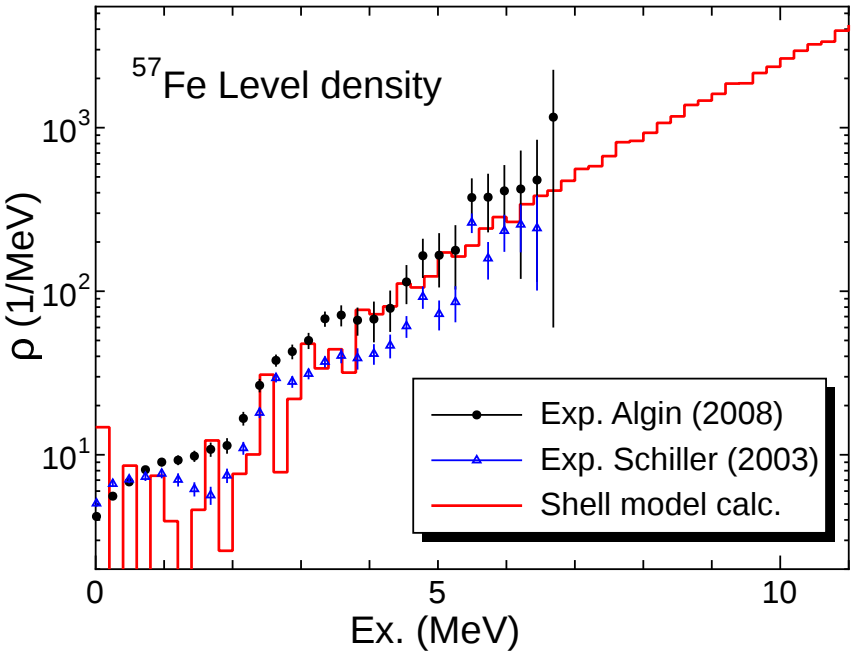

Figure 2: Nuclear level density of ^{57}Fe. The black circles (blue triangles) with the error bars show the experimental values taken from Ref. [18] (Ref. [17]). The red line shows the shell-model results obtained by the stochastic estimation ($N_b = 8$) using the GXPF1A interaction [19].

Figure 2 shows the level density obtained by the present method. The model space taken is the pf shell with the ^{40}Ca inert core and any particle-hole truncation is allowed inside pf shell. The M-scheme dimension of the full pf-shell model space reaches 455,078,565. The

GXPF1A interaction is adopted for the Hamiltonian [19]. The shell-model result successfully reproduces the experimental values well up to 5 MeV. However, the shell-model only provides us with the negative parity states since the model space taken is the $0\hbar\omega$ space. We still possibly underestimate the latest experimental value [17] at $E_x > 5$ MeV, and this can be due to the contribution of positive parity states.

In Ref. [1], we enlarge the model space so that 1-particle 1-hole excitation is allowed from the *sd* shell to the *pf* shell, or the *pf* shell to *sdg* shell in order to obtain the level density of unnatural parity states. We demonstrated that the present method works well even with the 1.5×10^{10} dimensional problem and successfully described both the low-lying spectroscopy and the level density at $E_x \sim 10$ MeV in a unified manner. Especially, experimentally observed parity equilibration of $J^\pi = 2^+$ and 2^- states in ^{58}Ni was described microscopically.

5. Summary

It has been a challenge to obtain nuclear level densities microscopically based on the nuclear shell model. We applied the stochastic estimation of the eigenvalue density to shell model calculations and successfully obtained the level density of medium-heavy nuclei. The developments of such a methodological framework and progress in supercomputers open a new era of microscopic description of the nuclear shell model calculations.

Acknowlegements

We acknowledge Drs. Y. Futamura, T. Sakurai, T. Mizusaki, and T. Otsuka for our valuable collaborations. This work has been supported by the HPCI Strategic Program and Priority Issue 9 to be tackled by using Post-K computer from MEXT, CREST from JST, the CNS-RIKEN joint project for large-scale nuclear structure calculations, and KAKENHI grants (25870168, 23244049, 15K05094) from JSPS, Japan. The numerical calculations were performed on K computer at RIKEN AICS (hp140210, hp150224) and COMA supercomputer at the University of Tsukuba.

References

[1] N. Shimizu, Y. Utsuno, Y. Futamura, T. Sakurai, T. Mizusaki and T. Otsuka: Phys. Lett. B **753**, 13 (2016).

[2] N. Shimizu, Y. Utsuno, Y. Futamura, T. Sakurai, T. Mizusaki and T. Otsuka: EPJ Web of Conference **122**, 02003 (2016).

[3] T. Rauscher, F.-K. Thielemann, and K.-L. Kratz, Phys. Rev. C **56**, 1613 (1997).

[4] K. Sieja, Phys. Rev. Lett. **119**, 052502 (2017).

[5] E. Caurier, G. Martinez-Pinedo, F. Nowacki, A. Poves, and A. P. Zuker, Rev. Mod. Phys. **77** 427 (2005).

[6] W. Hauser and H. Feshbach, Phys. Rev. **87**, 366 (1952).

[7] Y. Utsuno, N. Shimizu, T. Otsuka, S. Ebata and M. Honma, Prog. Nucl. Ener. **82**, 102 (2015).

[8] S. Yoshida, Y. Utsuno, N. Shimizu and T. Otsuka, Phys. Rev. C, **97**, 054321 (2018).

[9] R. A. Sen'kov and V. Zelevinsky, arXiv:1508.03683 [nucl-th]; R. A. Sen'kov and M. Horoi, Phys. Rev. C **82** 024304 (2010).

[10] E. Teran and C. W. Johnson, Phys. Rev. C **73** 024303 (2006).

[11] C. Ozen, Y. Alhassid, and H. Nakada, Phys. Rev. Lett. **110**, 042502 (2013).

[12] Y. Maeda, Y. Futamura and T. Sakurai, JSIAM Lett. **3**, 61 (2010).

[13] M. F. Hutchinson, Commun. Stat., Simulation Comput., **19** 433, (1990).

[14] N. Shimizu, arXiv:1310.5431 [nucl-th].

[15] Y. Futamura and S. Sakurai, http://zpares.cs.tsukuba.ac.jp/ (accessed 2018-04-01).

[16] B. A. Brown and A. C. Larsen, Phys. Rev. Lett. **113**, 252502 (2014).

[17] E. Algin *et al.*, Phys. Rev. C **78**, 054321 (2008).

[18] A. Schiller *et al.*, Phys. Rev. C **68**, 054326 (2003).

[19] M. Honma, T. Otsuka, B. A. Brown, and T. Mizusaki, Eur. Phys. J. A **25**, Suppl. 1, 499 (2005).

7 Nuclear reaction data of low-energy LLFP produced by OEDO

N. Imai
Center for Nuclear Study, University of Tokyo
Hirosawa 2-1, Wako city, Saitama 351-0198, Japan
email: n.imai@cns.s.u-tokyo.ac.jp

Abstract

The energy degraded beam line of radioactive isotope beam, named OEDO, has been newly developed at RIKEN RI beam Factory. The key parts of the OEDO are the RF deflector and two superconducting quadrupole magnets. OEDO would squeeze the beam spot size of the RI beam to carry out experiments in the inverse kinematics. The commissioning of the OEDO was successfully conducted to provide ^{79}Se and ^{107}Pd beams in June 2017. Two experiments, the proton or deuteron induced reaction measurement with ^{93}Zr and ^{107}Pd beams and the surrogate reaction measurement of $^{79}\mathrm{Se}(d,p)^{80}\mathrm{Se}$ for $^{79}\mathrm{Se}(n,\gamma)^{80}\mathrm{Se}$ were successfully performed at around 20-30 MeV/nucleon as nuclear data of these long-lived fission products.

1. Introduction

The nuclear power plants had been operated since 1963 in Japan. After the Great East Japan Earthquake of March 11, 2011, though only a few nuclear power plants are working, the nuclear wastes of the power plant have been left over since the first operation. The high-level radioactive waste from the reprocessing of the spent fuel is determined to be disposed in the underground deeper than 300 meters. However, some of them have long lives as long as 10^6 years. In parallel with preparing for the geological disposal, a way of decommissioning such long lived fission products (LLFPs) must be studied to avoid the inheritance of the waste in the future.

The ImPACT program [1] aims to propose a facility to mutate the LLFP to the shorter-lived or stable nucleus. Several nuclear reactions of LLFPs have been so far studied from 50 to 200 MeV/nucleon produced by the BigRIPS in RIBF and with a few targets, such as proton, deuteron, carbon [2, 3, 4]. The LLFP beams were produced from the in-flight-fission of ^{238}U at 345 MeV/nucleon. The lower beam energy was obtained by slowing down the energy of the beam with the material. When the beam energy is lowered further by the material, the beam spot size would be more deteriorated due to the straggling. The device to squeeze the beam spot needs to be developed for performing experiments at below 50 MeV/nucleon.

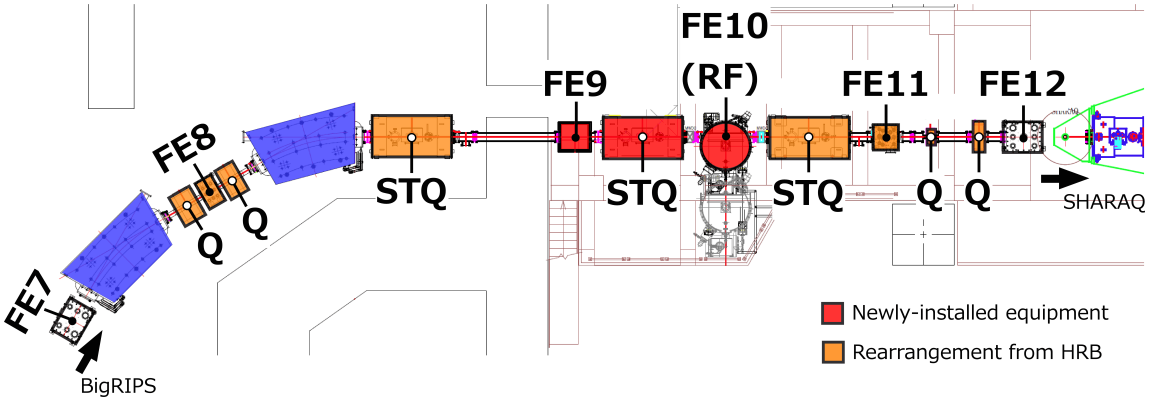

Figure 1: The overview of the energy degraded beam line, OEDO. The focal plances upstream of FE7 which belong to the BigRIPS beamline are not shown here.

2. OEDO beam line

A new technique to squeeze the beam spot has been introduced at RIBF to obtain the LLFP beam of around 20-30 MeV/nucleon. Because the new beam line uses the "Optimized Energy Degrading Optics for RI beams", it is called as the OEDO beam line.

A schematic figure of the OEDO beam line is presented in Fig. 1. The radioactive ion (RI) beams produced by the BigRIPS are transported via FE7 and FE8. In this experiment, the energy degrader was installed at F5 in the BigRIPS beam line to produce the RI beam of 26 MeV/nucleon. The first super conducting triplet quadrupole magnet (STQ) of OEDO is used to make a point to parallel beam independent of the beam momentum at FE10, where the RF deflector is installed. Due to the momentum difference caused by the energy straggling at F5 degrader, the arrival time from F5 to FE10 depends on the beam velocity after the degrader. The faster beam flux reaches FE10 earlier than the slower beam. After the tuning of the optics of the beam line, the faster beam is mapped to the outer trajectory at the dipole magnets while the slower beam pass through the inner. Then, the RF deflector changes the trajectory of the beam depending on the arrival time. As a result, the horizontal angles of the beam is aligned and the correlation between the momentum and the horizontal angle is canceled. The second STQ focuses the parallel beam to the point.

The commissioning experiment was conducted with ^{107}Pd and ^{79}Se beams. In the case of the ^{107}Pd beam, the last energy degrader placed at F5 made the beam energy of 33 $\pm$ 0.5 MeV/nucleon. Whereas for ^{79}Se beam, the last was located at FE9, which made the beam energy of 45 $\pm$ 2 MeV/nucleon. The beam energy was determined by measuring the time of flight between FE9 and FE12. Figure 2 compares the beam spot size with and without the RF for ^{79}Se beam. The beam spot size was successfully reduced to be 15 mm (FWHM) from 25 mm.

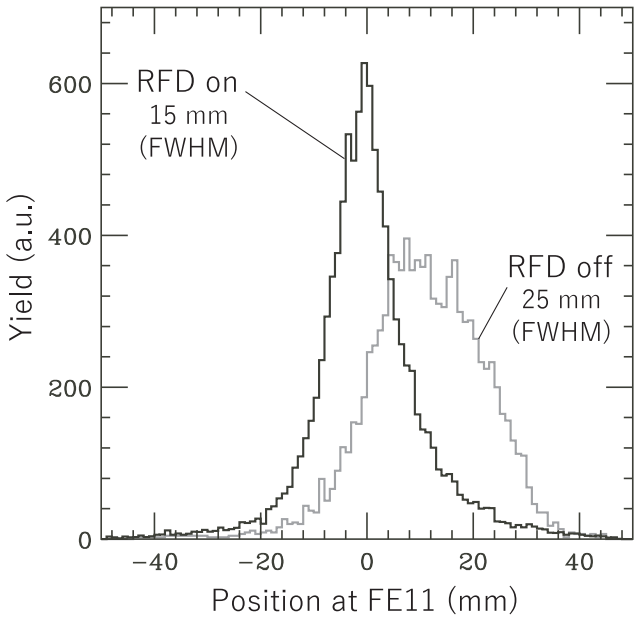

Figure 2: The horizontal distribution of the ^{79}Se beam at FE11. The beam spot size with the RF on was smaller than that without.

3. Two experiments

After the successful commissioning, two experiments were conducted. One is for the proton or deuteron induced reaction with ^{93}Zr and ^{107}Pd beams at 20-30 MeV/nucleon to study the fusion or pre-equilibrium reaction. The other one is the measurement of ^{77,79}Se(d,p)^{78,80}Se reactions in inverse kinematics as a surrogate for ^{79}Se(n, γ)^{80}Se reaction.

In both experiments, the secondary beams were produced by the ^{238}U beam with a ^{9}Be target. The thickness was optimized to get a high purity of the beam of around 40%. The secondary beams were purified with the thick Al degrader at the first focal plane (F1) of BigRIPS. The secondary beams were identified only by measuring the time of flight (TOF) between two focal plances, the thrid (F3) and fifth focal planes (F5), with the diamond detectors. Thanks to the high purity of the beam, the Bρ measurement was not needed. By changing the thickness of the energy degrader at F5 the beam energy was adjusted. The beam spot at a secondary target position S0 was squeezed to be around 30 mm in FWHM by using the OEDO [5].

3.1 Proton or deuteron induced reaction with ^{107}Pd and ^{93}Zr

The theoretical calculation with the Talys code [6] estimates the fusion evaporation reaction cross section of ^{107}Pd with protons as 1 b around 20-30 MeV, which means that the total reaction cross section is almost exhausted by one channel. From the point of view to make a clean nuclear transmutation, meaning that the mutation will not make the other long-lived isotopes, the low-energy nuclear reaction look promising.

To evaluate the cross sections experimentally, the energy degraded ^{93}Zr or ^{107}Pd beams impinged on a cryogenic gas target of 40 K of hydrogen or deuterium. The pressure was adjusted as the thickness to be 7.5 mg/cm^2 for hydrogen and 15 mg/cm^2 for deuterium.

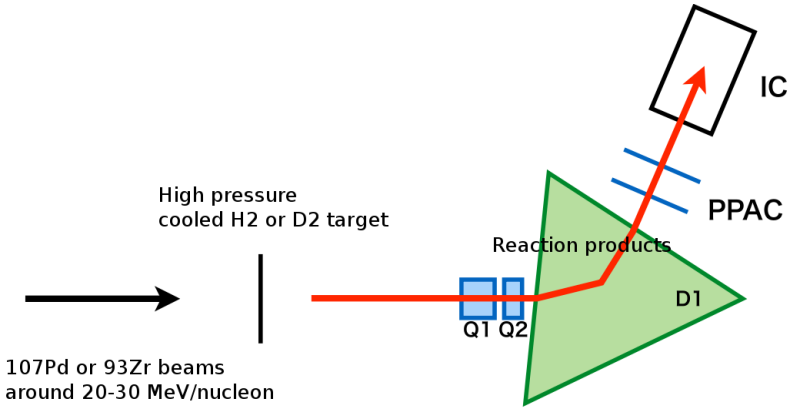

Figure 3: A schematic picture of the experimental setup around the secondary target. The ^{107}Pd beam was directed onto the hydrogen gas target. The reaction products were momentum analyzed by a dipole magnet of SHARAQ. The outgoing particles were detected by a pair of PPACs and the ionization chamber.

Because the reaction took place in the inverse kinematics, the reaction products were scattered in the forward angles. They were momentum-analyzed by a dipole magnet. At the focal plane of the magnet located about 7 m downstream of the secondary target, a pair of parallel plate avalanche counters (PPACs) and an ionization chamber (IC) were placed. The mass-to-charge ratio (A/Q) were deduced from the Bρ value and the TOF between the target and PPACs. The schematic view of the experiment is presented in Fig. 3. Because the velocity of the ions is not enough to be fully stripped, the charge states after the secondary beam are widely distributed. The magnetic rigidity of the S1 magnet were changed by the five steps from -10% to +10% to map the distribution. It is found that that the most intensive charge state was hydrogen-like ions among four charge states. Concerning the beam energies, in the case of the ^{93}Zr case, the beam energy was 26-30 MeV/nucleon at the secondary target while for the ^{107}Pd two beam energies, 25-30 and 21-24 MeV/nucleon were produced to measure the energy dependence of the cross sections.

The correlation of the energy loss of ionization chamber and the A/Q value is presented in Fig. 4. In addition to the beam-like particles of ^{107}Pd the silver isotopes were successfully measured. This is the first measurement of the fusion reaction of RIB with the proton target in the inverse kinematics.

3.2 Surrogate reaction of ^{79}Se$(n, \gamma)^{80}$Se

The neutron induced reactions also offer a promising opportunity. Because of the longer mean free path, the transmutation can be applied more efficiently. This requires a neutron facility, in addition to enriched radioactive targets. Instead, the reaction cross section can also be determined in an indirect way of employing a surrogate reaction.

It is generally assumed that the (n, γ) cross section separates into two parts, the formation of a compound nucleus and its subsequent decay. The first part can be calculated using optical model potentials with global parameters [7]. On the other hand,

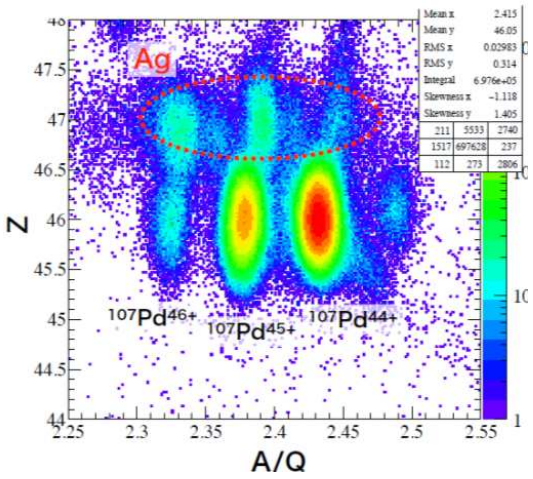

Figure 4: Correlation of the energy loss in the IC and the A/Q ratio determined with the position at the focal plane and the TOF. Three loci along $Z = 46$ presents the ^{107}Pd with the different charge states of 46^+, 45^+, 44^+, 43^+. Above the Pd isotopes, silver isotopes synthesized with the proton were clearly observed.

the theoretical estimates of the second process are uncertain and need to be validated by experiment. The present work aims to determine the γ emission probability from the unbound state of ^{80}Se by using the (d, p) reaction as a surrogate for ^{79}Se$(n, \gamma)^{80}$Se reaction. The method will be tested by measuring the ^{77}Se$(d,p)^{78}$Se reaction which is the surrogate for ^{77}Se$(n, \gamma)^{78}$Se whose cross section was already measured [8].

The experimental setup is almost the same as that for the fusion experiment. The cryogenic target was replaced with a CD_2 target of 4 mg/cm^2. A SSD-CsI(Tl) array which was newly developed and named as TiNA was placed upstream of the target. The TiNA consists of six Micron YY1 type sector-shape SSD detectors and two CsI detectors on each back of the SSD. Each telescope covered 100 to 150 degrees in the laboratory frame. The front side of SSD has 16 electrodes to determine the scattering angles of the recoiled particles. The excitation energy of the populated state in ^{78}Se (^{80}Se) was deduced based on the momenta of the protons and the incident beams.

The outgoing particles were identified with ΔE-E-Bρ method by employing the S1 spectrometer of the SHARAQ coupled with the focal plane detectors. Figure 5 presents the mass-to-charge (A/Q) ratio of the outgoing particles measured with the S1 detector. By identifying the nucleus at S1, the γ emission probability P_γ will be determined.

4. Summary

In the framework of ImPACT program, the new energy degraded beam line for RI beams, OEDO, were constructed. The OEDO can provide around 20 MeV/nucleon LLFP beams for the first time in the world. By employing a special optics produced by two STQ magnets and the RF deflector, the small beam spot of around 30 mm (FWHM) was achieved.

Two experiments were successfully conducted to obtain the nuclear reaction data with

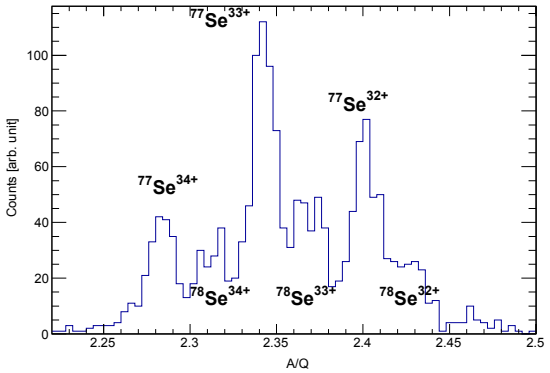

Figure 5: A/Q spectrum measured with the S1 spectrometer with the focal plane detectors for the ^{77}Se(d,p)^{78}Se reaction. ^{77}Se and ^{78}Se were clearly separated.

energy-degraded beams of ^{79}Se, ^{93}Zr and ^{107}Pd. The proton or deuteron induced reaction with ^{93}Zr were measured at 30 MeV/nucleon. For ^{107}Pd beams, the experiments were conducted at 25 and 30 MeV/nucleon with the proton and deuteron targets. For the ^{79}Se, the ^{77,79}Se(d,p)^{78,80}Se reactions were measured to determine the ^{79}Se$(n,\gamma)^{80}$Se reaction.

Acknowledgments

The work was funded by ImPACT Program of Council for Science, Technology and Innovation (Cabinet Office, Government of Japan).

References

[1] http://www.jst.go.jp/impact/en/program/08.html, (accessed 2018-04-01).

[2] Wang H. et al., Spallation reaction study for fission products in nuclear waste: Cross section measurement for ^{137}Cs and ^{90}Sr on proton and deuteron, Phys. Lett. B 754, 104 (2016).

[3] Wang H. et al., Spallation reaction study for the ling-lived fission product of ^{107}Pd, Prog. Theo. Exp. Phys. 021, D01 (2017).

[4] Kawase S. et al., Study of proton- and deuteron-induced spallation reactions on the long-lived fission product ^{93}Zr at 105 MeV/nucleon in inverse kinematics, Prog. Theo. Exp. Phys. 093, D03 (2016).

[5] Michimasa S. et al., Commissioning of the OEDO beamline, RIKEN Accel. Prog. Rep. 51 (2018).

[6] http://www.talys.eu/ (accessed 2018-04-01).

[7] Escher J.E. et al., Compound-nuclear reaction cross sections from surrogate measurement, Rev. Mod. Phys. 84 353 (2012).

[8] Kamada S, Igashira M., Katabuchi T., Mizumoto M., Measurements of keV- Neutron Capture Cross Sections and Capture Gamma-Ray Spectra of ^{77}Se, J. Nucl. Sci. Tech. 47, 634 (2010).

8 Status of Nuclear Data for ADS and Integral Experiments

Kenji NISHIHARA, Takanori SUGAWARA and Masahiro FUKUSHIMA
Nuclear Science and Engineering Center, Japan Atomic Energy Agency
Tokai-mura, Naka-gun, Ibaraki-ken 319-1195 Japan
e-mail: nishihara.kenji@jaea.go.jp

The first result of a benchmark problem proposed in the International Atomic Energy Agency (IAEA) Coordinated Research Project (CRP) is shown. Main issues for the problem are accuracy of nuclear data for MA and novel materials such as lead-bismuth and nitrogen-15. Also, introduced is a series of experiment using a critical assembly for nuclear data of lead, where replacement reactivities of lead was measured in various neutron spectrum.

1. Introduction

Japan Atomic Energy Agency (JAEA) has been proceeding with the research and development on the accelerator-driven subcritical system (ADS) cooled by lead-bismuth eutectic with a thermal output of 800 MW[1], whose fuel contains significant amount of minor actinide (MA). Such reactors with large amount of MA have never been operated and examined by using critical assembly; therefore, accuracy of MA nuclear data is concerned.

From above respect, a benchmark problem is proposed as one of problems discussed in the IAEA Coordinated Research Project (CRP) on “Accelerator Driven System (ADS) Applications and use of Low-Enriched Uranium in ADS”. Purpose of the benchmark problem is to obtain fundamental knowledge of calculation accuracy at the present time for the commercial grade ADS. Main issues for the calculation are accuracy of nuclear data for MA and novel materials such as lead-bismuth and nitrogen-15. In the present paper, calculation results obtained in the IAEA CRP activity are shown.

JAEA is also conducting a series of experiment using a critical assembly for nuclear data of lead, where replacement reactivities of lead was measured in various neutron spectrum[2]. The result shows considerable discrepancy between experiment and analysis, although further investigation is necessary.

2. Benchmark in IAEA CRP

2.1 Description of problem

As a primary option, JAEA is proposing a lead-bismuth eutectic (LBE) cooled ADS to transmute MA. In this concept, LBE is able to be used simultaneously as the coolant and a spallation target. The core layout of dedicated ADS is shown in Fig. 1. The benchmark calculation is carried out for a cylindrical R-Z model

with the dimension given in Fig. 1. The core is radially divided into two zones with different initial Pu loading to smooth the radial power distribution. Surrounding the core, LBE reflector, stainless steel shielding, and B_4C shielding are loaded.

Main parameters of the ADS are summarized in Table 1. The core thermal power is 800 MW and burnup period is 600 effective full power days (EFPD). The proton LINAC with proton energy of 1.5 GeV is used for the accelerator to operate the ADS. The fuel assembly is hexagonal duct-less type and the pitch is 134.5 mm. Total number of fuel assemblies is 276. The cladding tube is T91 steel of 0.5 mm in thickness and 7.65 mm in diameter.

For the core fuel, mixture of mono-nitride of MA and plutonium (Pu) is used with a pellet density of 95%TD and a smear density of 85%TD. As the inert matrix, zirconium-nitride (ZrN) is used with the fuel. Nitrogen with N-15 (assumed as100% enrichment) is used for both (MA,Pu)-nitride and ZrN. The spent PWR fuel of 45 GWd/t burnup is reprocessed after 7 years cooling, and MA and Pu are recovered. For the calculation model, details are presented in Ref. [1].

Requested results in the benchmark are following items; (a) k-eff value at BOC (Beginning of Cycle) and EOC (End of Cycle), (b) radial fission reaction distributions (z=170 cm), axial fission reaction distributions (r= 30.78 cm and 77.68 cm) at BOC and EOC and (c) fuel isotopic composition at EOC.

2.2 Result

Table 2 lists contributors to the benchmark and their methods. JAEA used ADS3D code system[2] which contains PHITS code for transport of high energy particles and PARTISN code for transport of low energy neutrons below 20 MeV. JAEA adopted three major nuclear data library and made comparison among them. Kyoto University (KU) used MVP/MVP-BURN codes which is Monte-Carlo code and employed JENDL-4.0 and ENDF/B-VII.0. KIT used ERANOS code system with JEFF-3.1.

Figure 2 shows the result of k-eff at BOC and EOC. As the preliminary results, results calculated by JAEA and KU are presented in this paper. It was found that there was 1365 pcm difference at BOC in JAEA's result. The main cause of this discrepancy was the cross section data of Am-241. It was also observed that the burnup tendency was different between JAEA/JENDL-4.0 and JAEA/JEFF-3.2 or KU's results. The cause of this difference is under investigation.

Figure 3 presents the radial distribution of fission reaction rate at BOC and EOC. Due to the difference of the k-eff value, shapes of JAEA/JENDL-4.0 at BOC and KU/JENDL-4.0 at EOC were different from other results. For other results, good agreement was observed.

The axial distributions of fission reaction rate at BOC are plotted in Fig. 4. KU/ENDF-VII at r=30.78 cm was different from other results. The cause of this difference is not clear but it is supposed that the cause may be the statistical precision in Monte-Carlo (MC) calculation or the data of external neutron source.

Figures 5 and 6 show the change of isotopic composition by the burnup. In Fig. 5, the results calculated by the deterministic method (JAEA) and the MC method (KU) with the same nuclear data library (JENDL-4.0) are compared. Figure 6 compares with the results calculated by the same code with

JENDL-4.0 and ENDF/B-VII.1. In Fig. 5, it was confirmed that the consumptions of Np-237 and Am-241 and production of Pu-238 in KU are larger than those of JAEA's one at the inner core. It is supposed that the main cause of this difference will be the difference of neutron spectrum or flux distribution. In Fig. 6, although the consumptions of Np-237 and Am-241 in ENDF/B-VII.1 are larger than those in JENDL-4.0, the difference was small and good agreement was observed.

These results are preliminary one and the causes of these differences are under investigation. Sensitivity and uncertainty analyses will be performed to understand the causes of these differences.

Table 1 Parameters of ADS

Thermal power	800 MWt
Maximum k_{eff}	0.98
Spallation target/coolant	LBE
Proton beam energy	1.5 GeV
Maximum proton current [mA]	15mA
Operation time [EFPD]	600 EFPD
Cooling time [year]	4 year
Fuel composition	(MA+Pu)N + ZrN
Pitch of fuel assembly [mm]	134.5 mm
Number of fuel assembly	276

Table 2 Contributors to the benchmark and methods

Participant	Calculation code (method)	Nuclear data library
JAEA	ADS3D (deterministic)	JENDL-4.0 ENDF/B-VII.1 JEFF-3.2
Kyoto univ. (KU)	MVP/MVP-BURN (Monte-Carlo)	JENDL-4.0 ENDF/B-VII.0
KIT	ERANOS (BISTRO/VARIANT) (deterministic)	JEFF-3.1

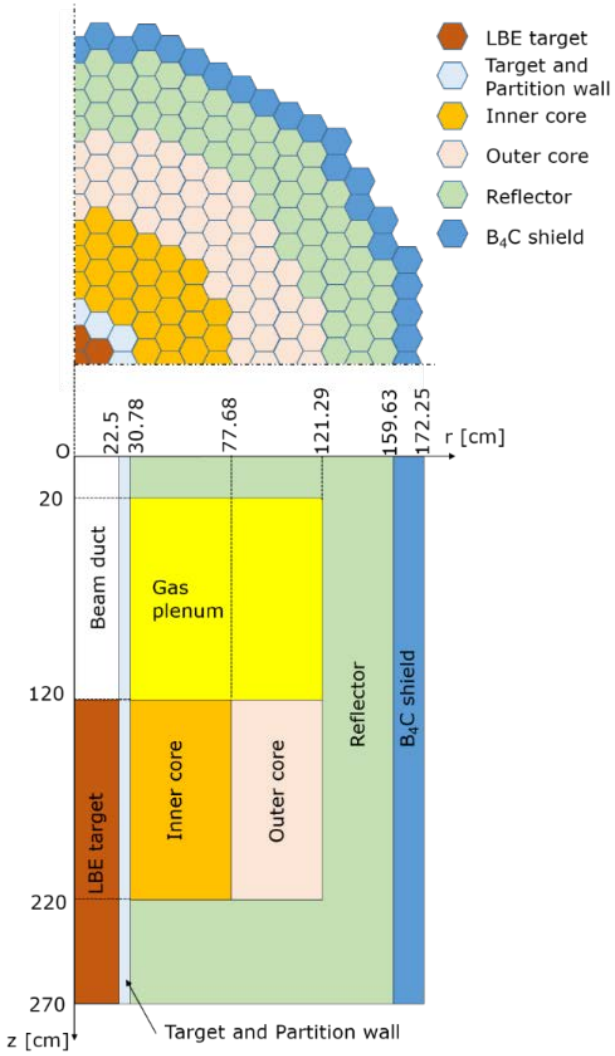

Fig. 1 R-Z calculation model of ADS core

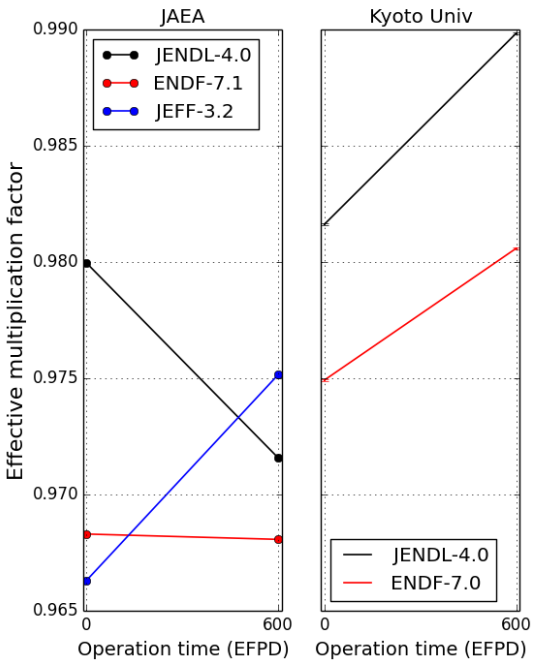

Fig. 2 Result of k-effective with different libraries (Left: JAEA, Right: KU)

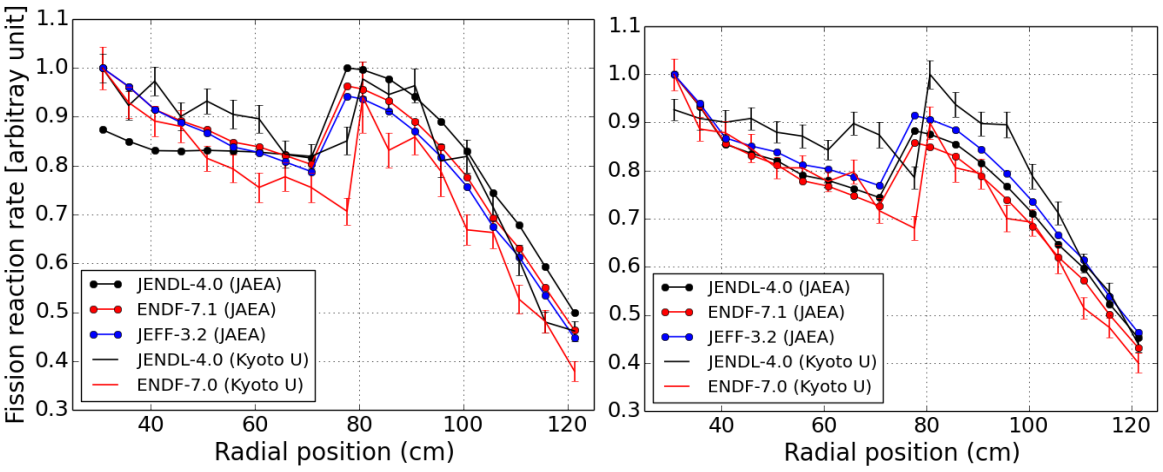

Fig. 3 Result of radial distribution at axial center (Left: BOC, Right: EOC)

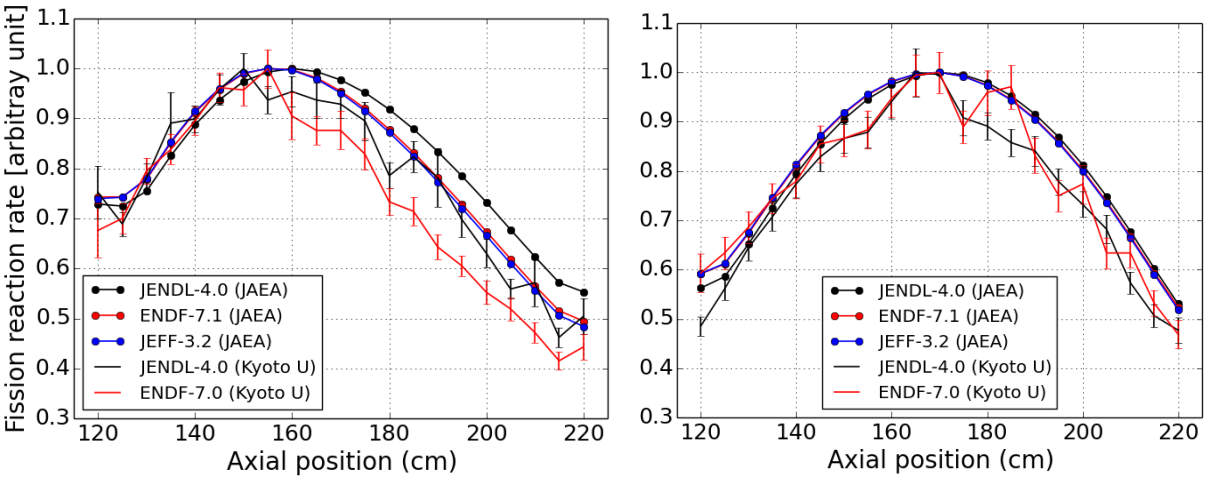

Fig. 4 Result of axial distribution at BOC (Left: r=30.78cm, Right: r=77.68cm)

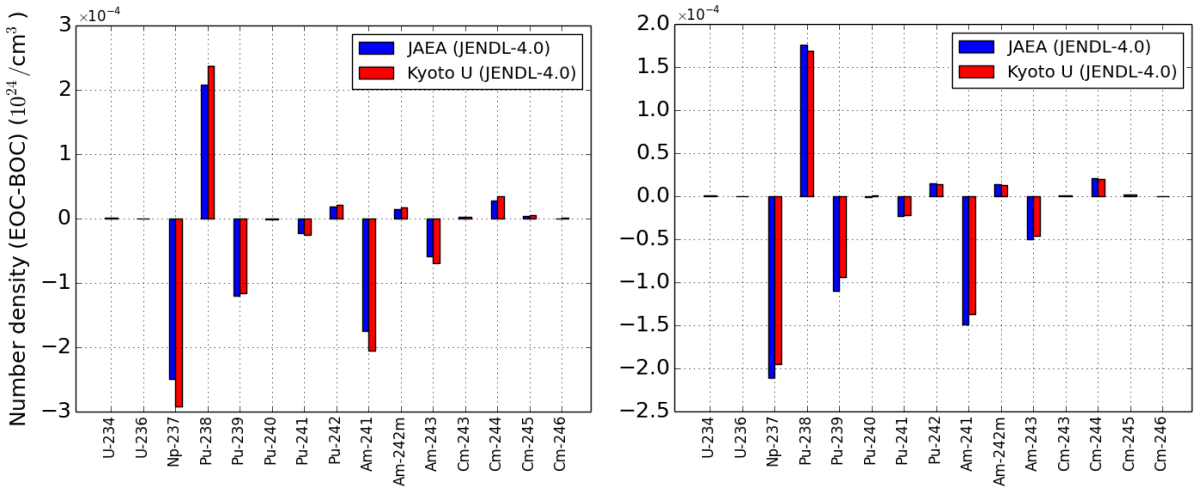

Fig. 5 Result of isotopic change after burn-up, JAEA vs. Kyoto univ.

(Left: inner core, Right: outer core)

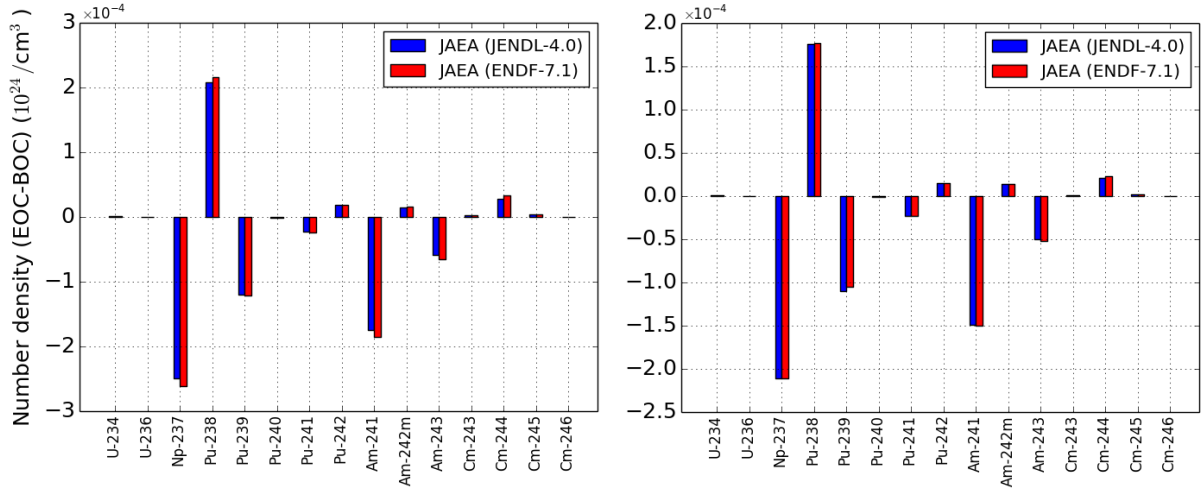

Fig. 6 Result of isotopic change after burn-up, JENDL-4.0 vs. ENDF-VII.1

(Left: inner core, Right: outer core)

3. Integral experiment

JAEA and LANL is conducting a series of integral experiments to measure lead void reactivity worths to validate lead (Pb) nuclear cross sections. Because detail of the experimental conditions and result is described in Ref. [2], summary of result is introduced in this section.

Lead void reactivity measurements have been completed in two uranium/Pb cores with different uranium enrichments: a high-enriched uranium (HEU)/Pb core and a low-enriched uranium (LEU)/Pb core. The series of experiments provides complementary data sets having different sensitivities to scattering cross sections of Pb depending on their inherent importance for higher energy neutrons.

The experimental analyses were performed using MCNP6.1 with use of the two major libraries JENDL-4.0 and ENDF/B-VII.1. The results show that the calculations by both the libraries overestimates the measurements for the HEU/Pb core while being consistent for the LEU/Pb core.

A similar series of experiments using a plutonium (Pu)/Pb system using the ZPPR plutonium fuels is currently under investigation and further studies are planned for the benchmark evaluations, detailed analyses and sensitivity analyses with other nuclear data libraries to clarify the cause of the discrepancies between calculation and experimental values.

4. Conclusion

A preliminary result of a benchmark problem in IAEA CRP was obtained for the purpose of understanding the current calculation accuracy for ADS design. It was found that there was 1365 pcm difference at beginning of burnup among three major nuclear data libraries. The discrepancy is very large comparing to the design subcriticality of ADS, 2000 pcm. It was also observed that the burnup tendency was different between JAEA/JENDL-4.0 and JAEA/JEFF-3.2 or KU's results. The cause of these discrepancy will be revealed by sensitivity and uncertainty analysis planned in the CRP.

Because nuclear data of lead is recognized as one of causes of such discrepancy, JAEA and LANL is conducting a series of integral experiments to measure lead void reactivity worths. The results show that the calculations overestimates the measurements for the HEU/Pb core while being consistent for the LEU/Pb core. Such inconsistency between two cores is valuable for validation of nuclear data of lead because common perturbation to the experimental result can be cancelled. Further experiments using Pu/Pb core and studies are planned for the benchmark evaluations, detailed analyses, and sensitivity analyses with other nuclear data libraries to clarify the cause of the discrepancies between calculation and experimental values.

References

[1] T. Sugawara, R. Katano, K. Tsujimoto, Annals of Nuclear Energy **111**, 449-459 (2018).

[2] M. Fukushima, et al., Nucl. Sci. Eng. **189**, 93-99 (2018).

[3] T. Sugawara, K. Nishihara, H. Iwamoto, et al., J. of Nucl. Sci. Tech. **53**, 12, 2018-2027 (2016).

9 Comprehensive mass measurements of heavy elements with a multi-reflection time-of-flight mass spectrograph

Michiharu Wada for the SHE-Mass-II Collaboration
Wako Nuclear Science Center, institute of Particle and Nuclear Studies, High Energy Accelerator Research Organization
&
Nishina Center for Accelerator-based Science, RIKEN
e-mail: miciharu.wada@kek.jp

A research project for comprehensive mass measurement of heavy elements using a novel mass spectrograph, MRTOF, at various low-energy RI-beam facilities of RIKEN RIBF is discussed.

1. Introduction

The atomic mass is a fundamental quantity in nuclear physics. The mass defect, the difference between the atomic mass and the sum of the masses of the individual constituents, is representative of the total binding energy of the atom that determines the existence of the atom, whether it is stable and the decay mode and decay energy if it is unstable. Systematic comparisons of the atomic masses can indicate nuclear deformation, nuclear shell effects, the particle drip lines, and key information for the origin of heavy elements, such as gold or uranium, in the universe. Up to now, the masses of ≈2300 nuclides have been determined experimentally with a relative precision of better than 1 ppm [1,2]. However, more than 600 of them were determined indirectly by reaction Q-values or decay energies which are known to have sizeable ambiguities. Approximately 1000 nuclides were experimentally identified but their masses are still not known as indicated in Fig. 1. The half-lives of these nuclides are distributed in a few orders of magnitude, however, dominantly in a range of 10-100 ms. Typical mass spectrometers for short-lived nuclei are summarized in Fig. 2. The Penning trap mass spectrometer (PTMS) is a state-of-the-art device for the most precise and accurate mass measurements, however, it requires an ion cyclotron resonance time of one second or longer if a mass resolving power of one million is needed. Furthermore, PTMS does not make allowance

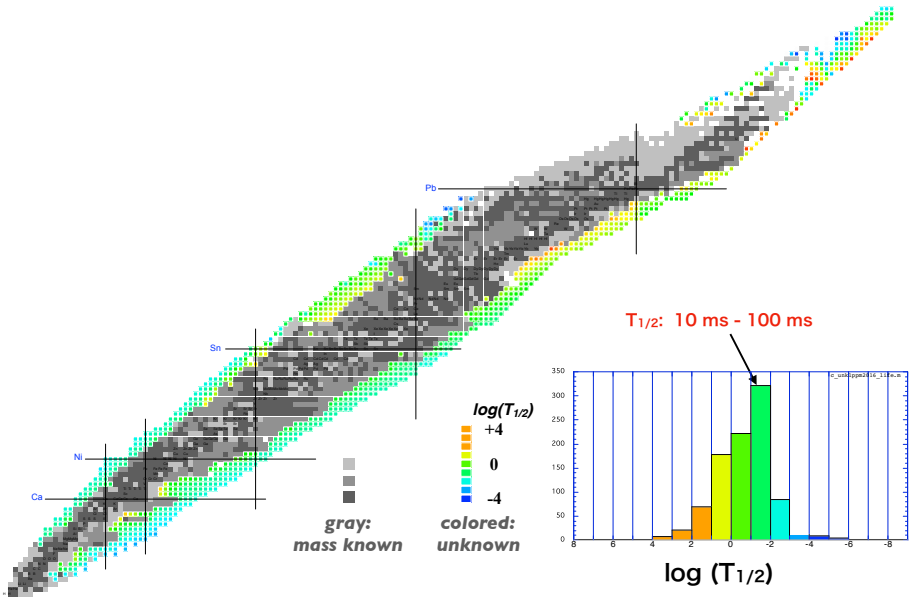

Fig. 1 Chart of nuclides showing mass known nuclides (gray boxes) and unknown nuclides (colored boxes). The color codes indicate the nuclear half-lives. The light gray boxes indicate their masses were determined by indirect methods. The insert shows distribution of half-life for mass unknown nuclides.

for any impurities. Consequently, only one species can be measured at a time. Large storage rings at GSI and Lanzhou and in-flight mass spectrometers such as TOFI and SPEG have also played important roles in mass measurements of unstable nuclei. The most urgently needed nuclear data at present requires relative mass precisions of 10^{-7} for nuclei with half-lives of 10-100 ms. This represents a "blank zone" because no appropriate devices exist to measure such nuclei with the desired precision (Fig. 3).

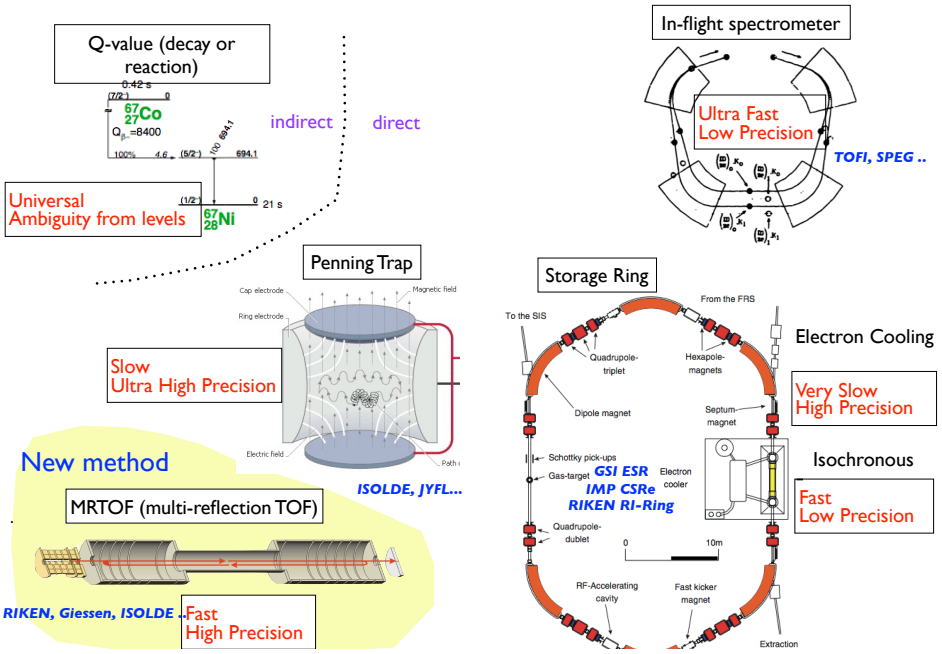

Fig. 2 Typical methods for mass measurement of unstable nuclei

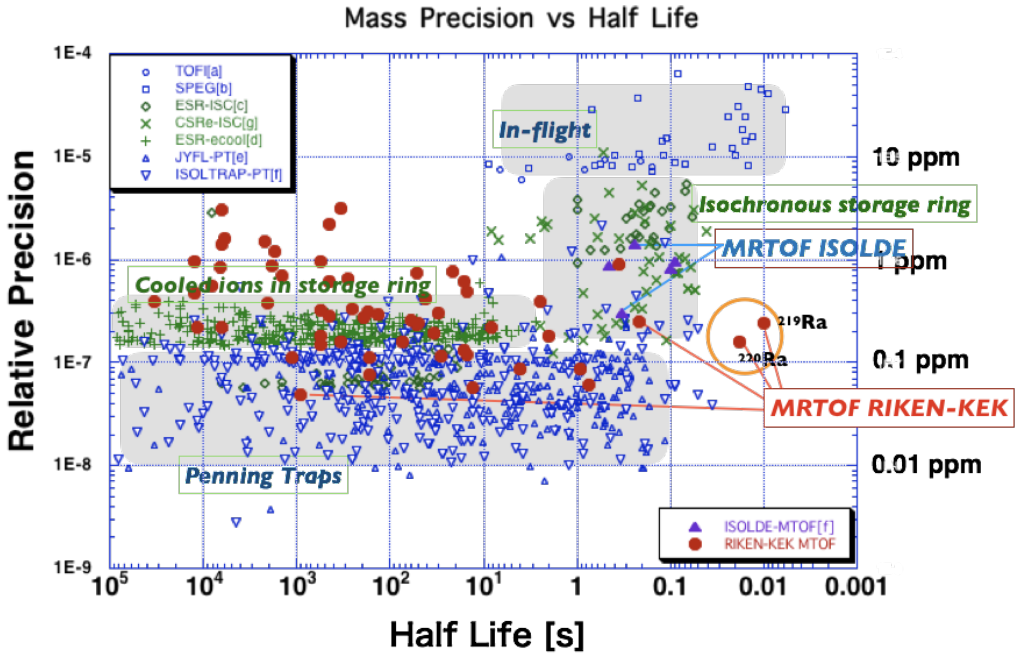

Fig. 3 Plots of relative mass precision vs. half-life with typical mass spectrometers [3-15].

2. Multi-reflection time-of-flight mass spectrograph

We developed a novel mass spectrograph, MRTOF (multi-reflection time-of-flight) mass spectrograph to cover the "blank zone". It is a time-of-flight mass spectrograph built to extend the flight path. Bunched ions between a pair of electronic ion mirrors. A small kinetic energy spread among the ions can be compensated for in the mirrors; higher energy ions go deeper and are reflected later than lower energy ones that go shallower and are reflected earlier, resulting in the desired energy isochroous condition. A typical flight time is 10 ms with a width of 25 ns, corresponding to a mass resolving power of 200,000. This is compatible with short-lived nuclei with half-lives of ≈10 ms. We determined the mass of $^{219}Ra^{++}$ (half-life of 10 ms) with a relative precision of 4.1×10^{-7} from ≈100 events [3].

A great advantage of the MRTOF is that it can measure multiple ion species at once without scanning. Figure 4 shows a TOF spectrum for A = 204 and 205 isobars that includes nine nuclides [4]. Occasionally, contaminant ions having a different number of

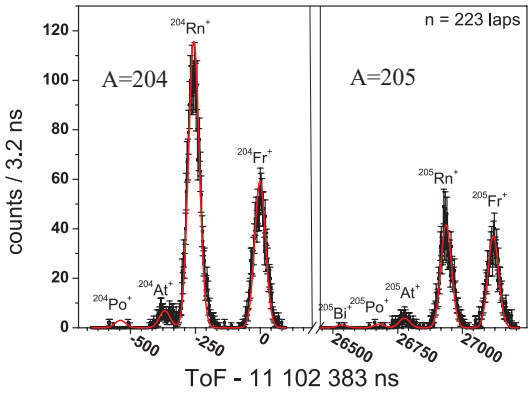

Fig. 4 ToF spectrum for A=204, 205 isobars

laps may appear in a spectrum. To discriminate such intruder peaks, we always take two or more spectra with different numbers of laps. The highest precision MRTOF mass measurement was demonstrated for $^{65}Ga^{+}$ using an isobaric reference of stable $^{65}Cu^{+}$ [5]. The mass was determined with a relative precision of 3.5 x 10^{-8} using more than 10,000 events. The result agrees with the data measured by a PTMS. Such high accuracy was achieved because the isobaric reference ions, $^{65}Cu^{+}$, were simultaneously measured with high statistics. Using the TOF of the reference ions, the temporal drifts in the measured TOF, which arise from voltage or thermal fluctuations, were compensated. However, suitable reference ions are not always available. To remedy this, we developed a universal referencing method, named the "concomitant" method, which takes advantages of our novel trap geometry that can accept ions from two directions. Reference ions from any sources can be supplied to one side of the ion trap, while radioactive ions are supplied to the other side, alternating one shot after the other in each (typically 15 ms) flight cycle.

This new mass spectrograph has performed well and have demonstrated that it is ideal for the mass measurement of very rare, short-lived, heavy nuclides. At first, we installed it in the GARIS at RIKEN RIBF for the SHE-Mass project, to perform high precision mass measurements of trans-uranium elements. During the first phase of the project, masses of ≈80 nuclides were measured, six of which (^{246,247,248}Es, ^{249,250,252}Md) were measured for the first time [6], and more than 30 masses were directly measured for the first time [7]. Our measurements agree significantly with PTMS data for known nuclides. However, a few measured masses, including the stable ^{81}Br, disagreed with the values given in the literature. This showed possible inaccuracy of the indirectly measured masses and suggests that it is worth re-measuring the nuclides whose masses were determined by indirect methods.

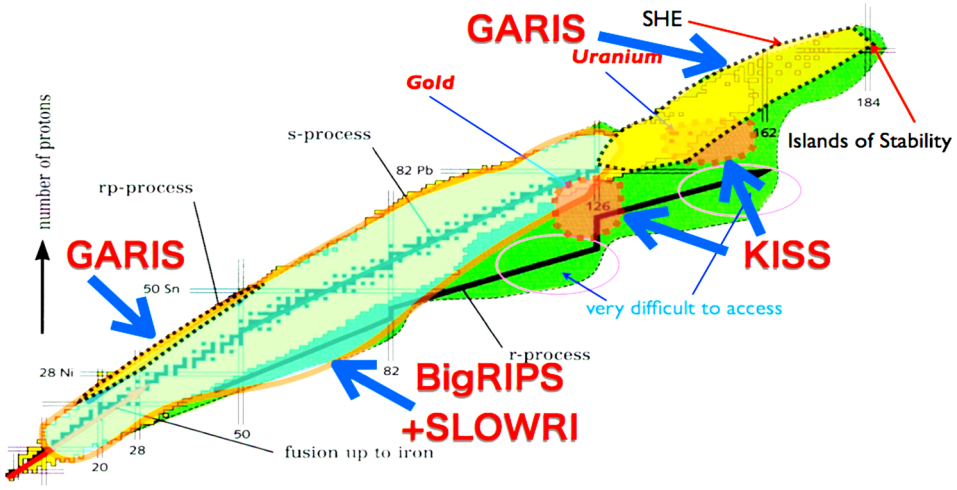

Fig. 5 Expected regions of nuclides to be measured at different facilities of RIBF

3. The ongoing mass measurement project with multiple MRTOF

In the next phase of the SHE-Mass project, we will place several MRTOF setups at three different RI-beam facilities of RIKEN RIBF in order to cover all available nuclides at RIBF and to measure >1000 masses within coming five years. Figure 5 shows the regions of nuclides that will be measured at GARIS-II, KISS, and BigRIPS+SLOWRI. The GARIS-II will be continuously used for superheavy elements but the device has moved to the new location in the Ring Cyclotron facility. An advantage of the new location is that we can place the MRTOF in the vicinity of the focal plane chamber of the GARIS-II. As shown in Fig. 6, the total efficiency of the new setup is expected to be more than 10% level by directly coupling the MRTOF to the first triplet ion trap of the gas cell in the focal plane chamber of the GARIS-II. This improvement will allow us to measure the hot-fusion superheavy elements such as Mc and Nh. The KISS facility provides some particular neutron rich nuclides synthesized by multi-nucleon transfer reactions which are difficult to be obtained with other facilities. The BigRIPS provides universal radioactive ion beams by in-flight fission and projectile fragmentation reactions. The beams from the BigRIPS are not only high energy (≈100 MeV/u) but contain ≈30 nuclides in the vicinity of the anticipated nuclide. Combining the rf-carpet gas catcher and the MRTOF, very efficient mass measurements of nuclides far from the stability can be performed. Thanks to the "spectrographic" feature of MRTOF, multiple nuclides can be measured simultaneously. When we aim at very exotic nuclide, such as ^{80}Ni, it takes long measurement time, however, many neighborhood nuclides can be seen in the same spectrum with very high statistics. One symbolic MRTOF setup, z-MRTOF, will be placed at the end of the ZeroDegree Spectrometer, where we can obtain many exotic nuclei with parasitic mode.

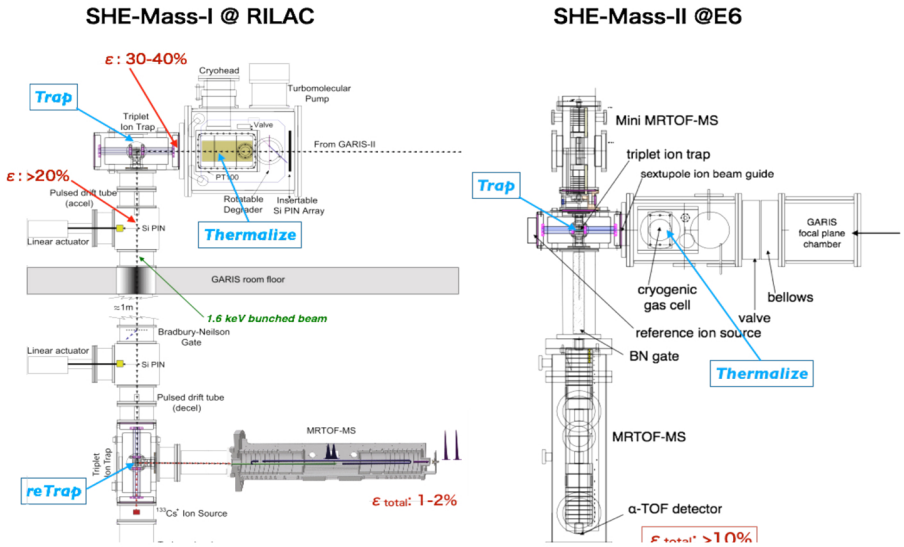

Fig. 6 Previous and new MRTOF setup for superheavy elements

4. Conclusion

The MRTOF mass spectrograph is a powerful device for comprehensive mass measurements of short-lived nuclei. Multiple MRTOF devices at RIKEN RIBF will provide hundreds of important mass data for various scientific studies.

Acknowledgements

The SHE-Mass-II project members are: W. Wada, P. Schury, Y. Ito, M. Rosenbusch, S. Kimura, D. Kaji, H. Haba, K. Morimoto, S. Ishizawa, A. Niwase, J.Y. Moon, H. Miyatake, X.Y. Watanabe, Y. Hirayama, A. Takamine, T. Tanaka, H. Koura, T. Sonoda, H. Ueno, S. Nishimura, and H. Wollnik. The experiments will be performed at RIKEN RI-beam factory. We express gratitude to the RIKEN Nishina Center for Accelerator-based Science, the Center for Nuclear Science at the University of Tokyo, and KEK Wako Nuclear Science Center for their support for the project. This project is supported by the Japan Society for the Promotion of Science KAKENHI, Grant Numbers 23224008, 15H02096, 15K05116, and 17H06090.

References

[1] W. Huang, G. Audi, M. Wang, F. Kondev, S. Naimi, X. Xu, Chi. Phys. C 41 (2017) 030002.
[2] M. Wang, G. Audi, F. Kondev, W. Huang, S. Naimi, X. Xu, Chi. Phys. C 41 (2017) 030003.
[3] Y. Ito et al., to be submitted.
[4] P. Schury et al., Phys. Rev. C 95 (2017) 011305R.
[5] S. Kimura et al., arXiv: 1706.00186.
[6] Y. Ito et al., arXiv: 1709.06468.
[7] M. Rosenbusch et al., arXiv: 1801.02823.
[8] Y. Bai et al., AIP Conf. Proc. 455 (1998) 90.
[9] F. Sarazin et al., Phys. Rev. Lett., 84 (2000) 5062.
[10] R. Knöbel et al., Eur. Phys. J. A 52 (2016) 138.
[11] L. Chen et al., Nucl. Phys. A 882 (2012) 71.
[12] Yu. A. Litovinov et al., Nucl. Phys. A 756 (2005) 3.
[13] http://research.jyu.fi/igisol/JYFLTRAP masses/ (accessed 2018-04-01).
[14] https://isoltrap.web.cern.ch/isoltrap/database/isodb.asp (accessed 2018-04-01).
[15] H.S. Xu et al., Int. J. Mass Spectrom. 349 (2013) 162.

10 Impact of Changing Thermal Scattering Law Data of H in H_2O on Nuclear Properties for LWR

Satoshi TAKEDA[1], Mikihiko MUTA[1], Hikaru YAMAGUCHI[1], Takanori KITADA[1], Yasunori OHOKA[2], Shogo MATSUOKA[2], Hiroaki NAGANO[2]

[1]Osaka University
2-1, Yamadaoka, Suita, Osaka 565-0871, Japan
[2]Nuclear Fuel Industries, Ltd.
950-1, Asashironishi, Kumatori-cho, Sennan-gun, Osaka 590-0481, Japan
e-mail: takeda@see.eng.osaka-u.ac.jp

Thermal scattering law data of hydrogen in H_2O is important nuclear data for the analysis of Light Water Reactor (LWR). In the present study, the impact of changing thermal scattering law data on nuclear calculation is evaluated. The processing of thermal scattering law data files was performed with the NJOY code. At the processing, three cross-sections of H_2O are obtained by thermal scattering law data files of JENDL-4.0, ENDF/B-VII.0 and Abe. The calculation results using these cross-sections are compared in pin cell geometry and assembly geometry. The results show that the results of ENDF/B-VII.0 and Abe have a good agreement in both geometries. The multiplication factor obtained by JENDL-4.0 is slightly larger than that of other cross sections in the model which contains Gd-bearing fuel. It seemed that JENDL-4.0 relatively suppressed the capture reaction of Gd since the cross section of JENDL-4.0 makes neutron spectrum relatively hard.

1. Introduction

For accurate analysis of LWR, several thermal scattering law data of hydrogen in H_2O have been generated. Thermal scattering law data used in the latest JENDL library is from ENDF/B-VI.8 and was originally generated for ENDF/B-VI.2 in 1994 [1]. The thermal scattering law data was revised for ENDF/VII.0 by adopting a rigorous model [2]. On the other hand, Abe generated new thermal scattering law data based on molecular dynamics by including the details of the molecular motions such as intermolecular vibration [3]. Although there are several thermal scattering law data, the impact on nuclear calculation is not well discussed. Therefore, the impact of changing thermal scattering law data is evaluated in the present study.

2. Process of cross sections

The neutron scattering of hydrogen in H_2O is dominated by incoherent scattering. Thus, the double differential thermal scattering cross section of hydrogen in H_2O can be written as:

$$\frac{\partial^2\sigma}{\partial\Omega\partial E} = \frac{\sigma_b}{4\pi kT}\sqrt{\frac{E'}{E}}\,\mathrm{e}^{-\frac{\beta}{2}}S(\alpha,\beta), \tag{1}$$

where E and E' are the energies of the incident and scattered neutrons, respectively and Ω is the scattering angle and σ_b is the characteristic bound cross section and k is the Boltzman constant and T is the temperature and $S(\alpha,\beta)$ is thermal scattering law data. $S(\alpha,\beta)$ is a function of the change of the momentum α and the change of energy β as described in the following equations:

$$\alpha = \frac{E' + E - 2\sqrt{E'E}\cos(\theta)}{AkT}, \tag{2}$$

$$\beta = \frac{E' - E}{kT}, \tag{3}$$

where $\cos(\theta)$ is the cosine of the scattering angle in the laboratory system and A is the ratio of the target mass to the neutron mass.

The cross section is processed by THERMR module of NJOY[4]. For the comparison of the impact of thermal scattering law data of hydrogen in H_2O, four sets of the cross section are produced for H_2O by using thermal scattering law data of Abe, JENDL-4.0[5], ENDF/B-VII.0. These cross sections are based on the cross section of JENDL-4.0 and only different in thermal scattering law data as shown in Figure 1. For convenience, these cross sections and their results are simply referred to as “Abe”, “JENDL-4.0”, “ENDF/B-VII.0” in this paper. The other cross sections such as the fuel are produced by Pij module of SRAC2006[6].

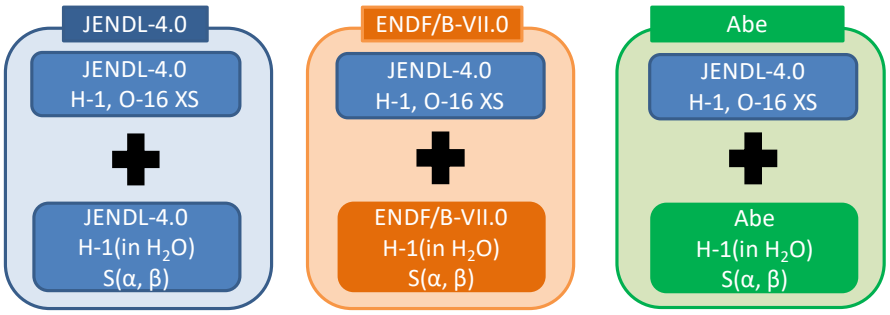

Figure 1. Three sets of cross sections for H_2O.

3. Calculation of assembly model

The calculation is performed for BWR assembly model by a multi-group Monte Carlo code GMVP[7]. The assembly model is shown in Figure 2. The calculation condition is summarized in Table 1. The number of histories is defined in order to suppress the statistical error of the flux of each energy groups less than 1 %. The 107 group structure of SRAC code system is used for the pin cell calculation[6].

Table 1. Calculation condition

Temperature of Moderator [K]	600
Temperature of fuel [K]	900
Void ratio [%]	40
Number of energy groups	107
Max order of neutron scattering	3
Total history	0.25 billion

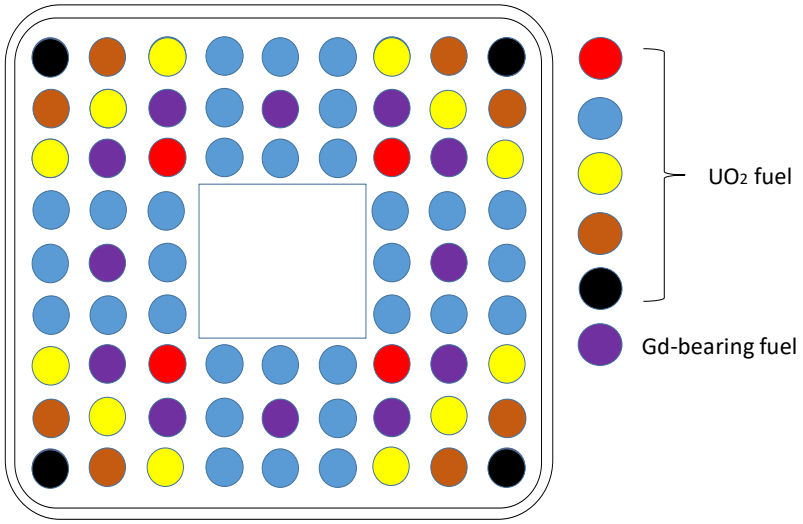

Figure 2. BWR assembly model.

Multiplication factors and their comparison for assembly calculation are summarized in Table 2. While ENDF/B-VII.0 shows good agreement with Abe, the difference in the multiplication factor between JENDL-4.0 and Abe is about 70 pcm. The maximum difference in pin-wise fission rate distribution between Abe and other cross sections is less than 1 % and the root mean squares are less than 0.5 %.

Table 2. Comparison of multiplication factors for assembly model.

	Abe	ENDF/B-VII.0	JENDL-4.0
K-infinity	1.00828	1.00823	1.00900
Relative difference in K-infinity compared with Abe (%)	-	-0.005	0.071

4. Discussion by pin cell calculation

In the previous section, the multiplication factor evaluated by JENDL-4.0 is relatively large compared with results of other cross sections. In order to investigate the difference, the pin cell calculation is performed. The pin cell model is shown in Figure 3. The calculation condition is

same as the assembly calculation.

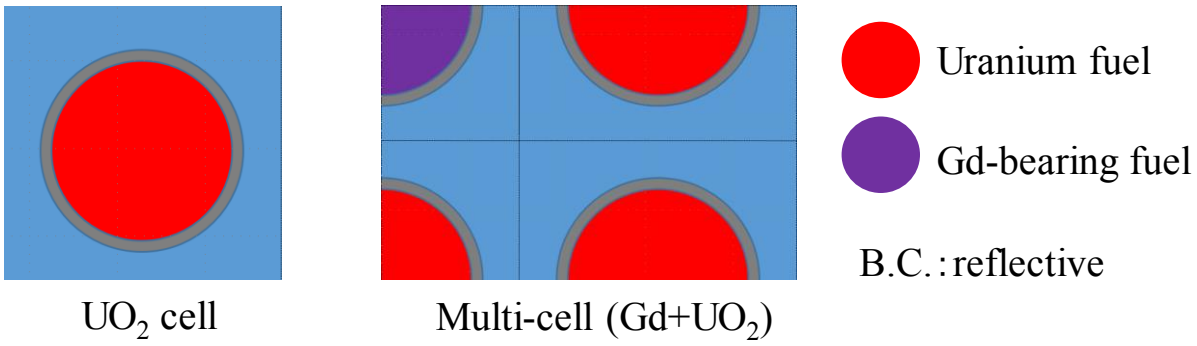

Figure 3. Pin cell model.

Multiplication factors and their comparison for UO_2 fuel cell calculation are shown in Table 3. The result shows that the difference between Abe and ENDF/B-VII.0 is small, and the multiplication factor of JENDL-4.0 is slightly smaller than that of Abe unlike the calculation result of BWR assembly model. Multiplication factors and their comparison for multi-cell calculation are shown in Table 4. As well as other calculation results, the difference between Abe and ENDF/B-VII.0 is small in the model. The multiplication factor evaluated by JENDL-4.0 is larger than that of Abe in the model. The results of these pin cell models indicate that the multiplication factor evaluated by JENDL-4.0 is relatively large in the case that Gd-bearing fuel exists.

Table 3. Comparison of multiplication factors for UO_2 fuel cell model.

	Abe	ENDF/B-VII.0	JENDL-4.0
K-infinity	1.25177	1.25175	1.25146
Relative difference in K-infinity compared with Abe (%)	-	-0.002	-0.025

Table 4. Comparison of multiplication factors for multi-cell model.

	Abe	ENDF/B-VII.0	JENDL-4.0
K-infinity	0.92258	0.92263	0.92298
Relative difference in K-infinity compared with Abe (%)	-	0.005	0.043

The difference in the neutron spectrum (Abe – ENDF/B-VII.0 or Abe – JENDL-4.0) at water region of UO_2 cell model is shown in Figure 4. The neutron spectrum is normalized at 1 eV to obtain the difference of the neutron spectrum. As shown in Figure 4, the neutron spectrum of JENDL-4.0 is smaller at 0.01 ~ 0.1 eV. Thus, it is considered that absorption reaction of Gd is

suppressed in the case of JENDL-4.0 since the neutron is mainly absorbed in Gd at lower energy region.

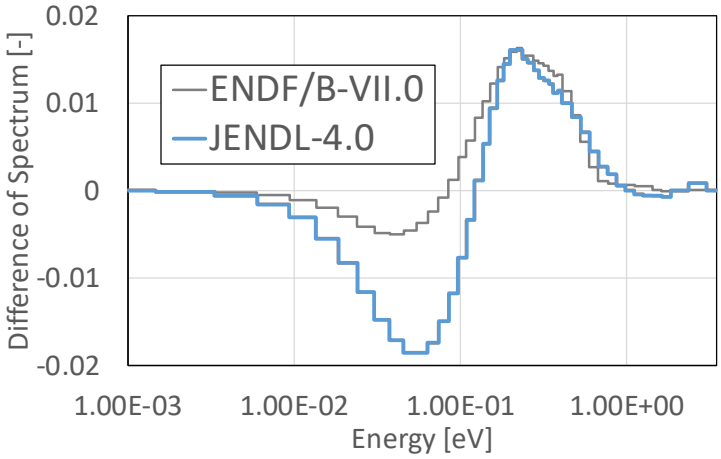

Figure 4. Difference in neutron spectrum between Abe and others

Figure 5 shows the relative difference in scattering cross section between Abe and JENDL-4.0. As shown in Figure 5, up-scattering cross section obtained by JENDL-4.0 is relatively large around 0.1eV, and down-scattering cross section of JENDL-4.0 is relatively small around 0.1eV. These tendencies of JENDL-4.0 makes the neutron spectrum hard.

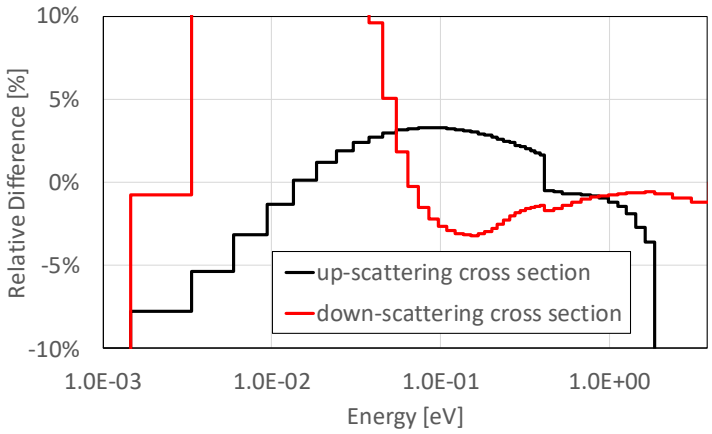

Figure 5. Relative difference in scattering cross section between Abe and JENDL-4.0. The difference is evaluated by (JENDL-4.0 − Abe) / Abe.

5. Summary

The impact of changing thermal scattering data on the multiplication factor was evaluated for the assembly and the pin cell calculations. The difference in the multiplication factor between Abe and ENDF/B-VII.0 is less than 10 pcm in these models. The multiplication factor of JENDL-4.0 is about 70 pcm larger than that of Abe in the assembly. From calculation results

of UO_2 fuel cell model and multi-cell model which contains Gd-bearing fuel, the multiplication factor evaluated by JENDL-4.0 is relatively large in the case that Gd-bearing fuel is exist.

References

[1] Macfarlane RE, New thermal neutron scattering files for ENDF/B-VI release 2. New Mexico: Los Alamos National Laboratory; 1994. LA-12639-MS.
[2] Mattes M, Keinert J, Thermal neutron scattering data for the moderator materials H2O, D2O, and ZrHx in ENDF-6 format and as ACE library for MCNP(X) codes. Austria: International Atomic Energy Agency; 2005. INDC(NDS)-0470.
[3] Abe Y, Tsuboi T, Tasaki S, Evaluation of the neutron scattering cross-section for light water by molecular dynamics. Nucl. Instrum. Methods Phys. Res. A. 2014; 735: 568-573.
[4] MacFarlane RE, Muir DW. The NJOY nuclear data processing system, version 91. New Mexico: Los Alamos National Laboratory; 1994. LA-12740-M.
[5] Shibata K, Iwamoto O, Nakagawa T, et al., JENDL-4.0: A new library for nuclear science and technology. J. Nucl. Sci. Technol. 2011; 48: 1-30.
[6] Okumura K, Kugo T, Kaneko K, Tsuchihashi K, SRAC2006 : A Comprehensive Neutronics Calculation Code System. Japan: Japan Atomic Energy Research Institute; 2007, JAEA-Data/Code 2007-004.
[7] Nagaya Y, Okumura K, Mori T, et al., MVP/GMVP II: General Purpose Monte Carlo Codes for Neutron and Photon Transport Calculations Based on Continuous Energy and Multigroup Methods. Japan: Japan Atomic Energy Research Institute; 2005. JAERI 1348.

11 Application of nuclear data to the decommissioning of the Fukushima Daiichi Nuclear Power Station

Keisuke Okumura, Eka Sapta Ruyana
Accident Progression Evaluation and Fuel Debris Characterization Division, Collaborative Laboratories for Advanced Decommissioning Science (CLADS), Japan Atomic Energy Agency (JAEA)
Tomioka-machi, Futaba-gun, Fukushima-ken, 979-1151 Japan

The decommissioning of the Fukushima Daiichi nuclear power station (1F) is an unexplored field. Although the investigations for inside primary containment vessel (PCV) by robots have been underway, actual situation inside the PCV and the characteristics of fuel debris have not been sufficiently clarified yet. Under such circumstances, the computational simulation with reliable data is an effective means for solving many problems for the 1F decommissioning. Here, as application examples using nuclear data such as JENDL-4.0, we will introduce two R&Ds on the prediction of dose rate distribution in PCV, and on the non-destructive assay of nuclear fuel materials in a fuel debris canister.

1. Prediction of Dose Rate Distribution in PCV

In order to predict the dose rate distribution in PCV of 1F, a series of calculations were carried out [1],[2] in the following way: 1) burnup calculation to obtain fuel composition at the time of accident, 2) activation calculation for the structural materials including impurities, 3) estimation of Cs contamination in PCV based on the 1F accident progression analysis by International Research Institute for Nuclear Decommissioning (IRID)[3], 4) decay calculation of radioactive nuclides, 5) photon transport calculation to obtain dose rate distribution.

For the burnup calculation, the JENDL-4.0[4] library was used to assume the radioactive isotope composition of fuel debris, because it is well validated for the spent fuel composition of LWRs [5]. As for the activation calculation, we used a multi-group activation cross library MAX2015[6] generated from JENDL-4.0 and JEFF-3.0/A[7] which covers nuclear data not evaluated in JENDL-4.0. For the decay and photon source calculations, JENDL Decay Data File 2015 [8] was employed.

Figure 1 shows the three-dimensional model of the unit-1 of 1F (1F1) for the photon transport calculation by PHITS [9]. Figure 2 shows the calculated dose rate distribution at the end of 2021, when the retrieval of fuel debris is scheduled to begin. The predicted dose rate at the lower part of PCV out of the pedestal is reliable, because the Cs contamination sources around there were determined based on the dose rate measurements in the three times of PCV investigations carried out from 2012 to 2017. On the while, uncertainty is large for the dose rate inside the reactor pressure vessel (RPV) and pedestal, because radiation sources are strongly depending on the accuracy of calculations.

In the PCV investigation so far, the position of the fuel debris has not been confirmed by the dose rate

measurements. The dose rate has been measured by a sensor using a small scintillator. However, as shown in Fig.2, the dose rate in PCV is dominantly determined by the Cs contamination sources rather than the fuel debris, in which most of Cs are released at the accident. In this study, we assumed 84 % as Cs release fraction from fuel debris on the basis of the measured one in the FP release experiment PHEBUS-FPT4 [10].

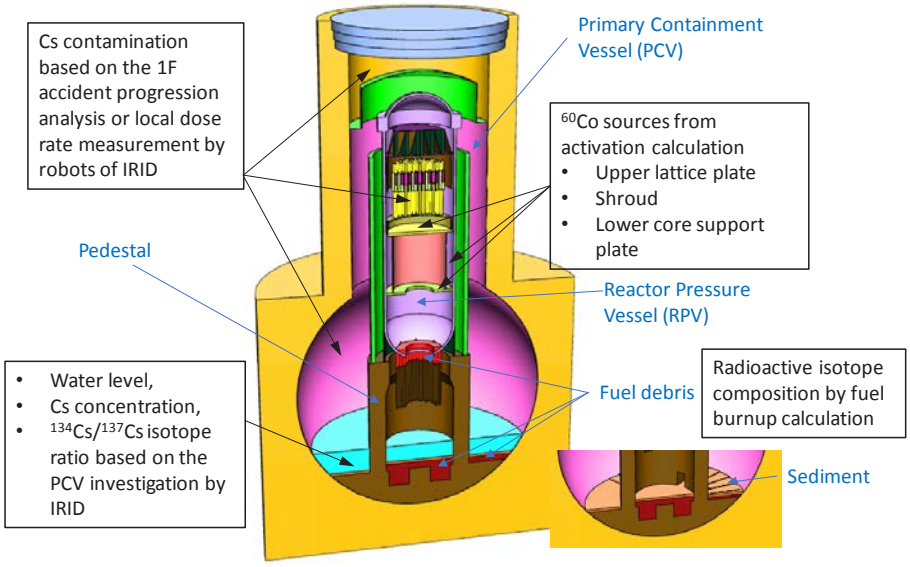

Fig. 1 Photon transport calculated model by PHITS (PCV of 1F1)

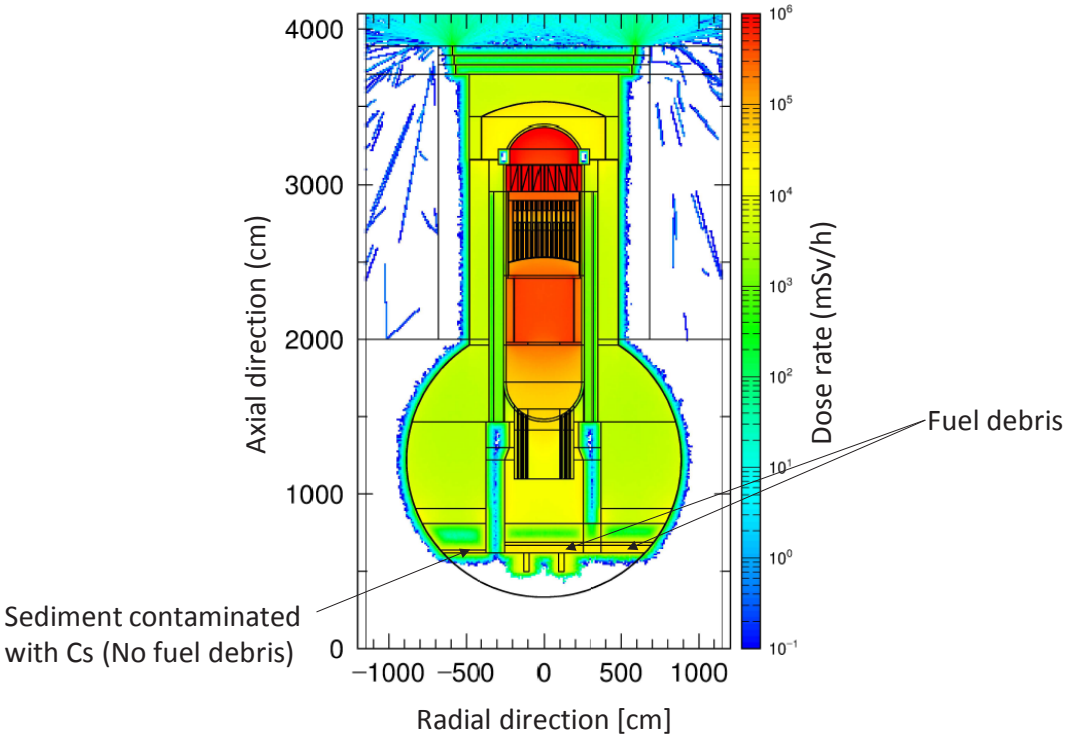

Fig. 2 Predicted dose rate distribution in PCV of 1F(unit-1) at the end of 2021

Fig. 3 shows the γ-ray sources from fuel debris in March 2018. It seems difficult to find fuel debris by measurement of the dose rate integrated over all γ-ray energy, because the dose rate is affected by γ-ray of Cs contamination sources and Compton scatterings. The alternative effective ways to find the fuel debris are:

- To detect γ-rays unique to fuel debris by using a sensor which has an energy resolution capability. For example, target nuclides are ^{154}Eu, ^{144}Ce(^{144}Pr), and ^{60}Co, which are expected to coexist with actinides and emit γ-rays whose energies are higher (>1MeV) than those of ^{134}Cs and ^{137}Cs.
- To detect any neutrons due to the spontaneous fissions of ^{244}Cm or ^{240}Pu, induced fissions, and (α,n) reactions in the fuel debris.
- To detect prompt γ-ray with relatively higher energy by (n,γ) or (n,f) reactions. For example, γ-ray with 2.2 MeV by H(n,γ) is expected for the submerged fuel debris (See Fig. 4).
- To get count rates of γ-ray summed over 1 MeV, if individual γ-ray cannot be identified.

The above detection technologies are not easy because of so high dose rate in PCV as shown in Fig. 2 and limitations on detector size and weight to mount the detector on robots. These approaches are under study by detector simulations in the PCV on the computer.

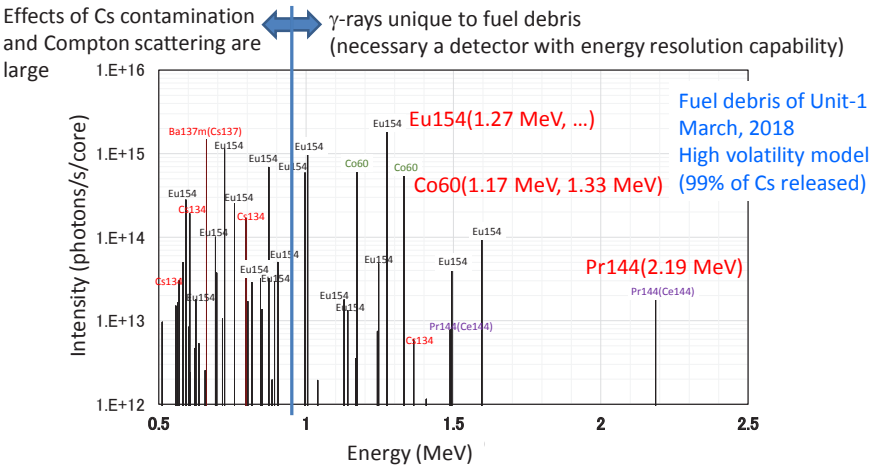

Fig. 3 γ-ray sources of fuel debris (March 2018, case for 99% of Cs released)

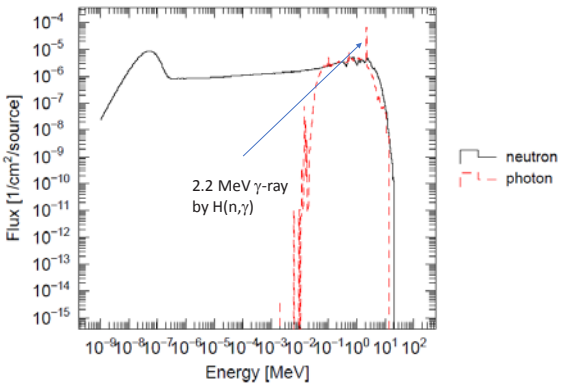

Fig. 4 Neutron and γ spectra near the fuel debris in water

2. Non-Destructive Assay for Nuclear Material Quantification in Fuel Debris

To determine the amount of nuclear material in fuel debris is important for proper management of retrieved fuel debris. However, the Non-Destructive Assay (NDA) technology for the 1F fuel debris is quite challenging because of the following reasons:

- The 1F fuel debris contain unknown amounts of actinides, FPs, neutron absorber (B, Gd), metals (Zr, Fe, Cr, Ni, etc.), water (H, O) and concrete elements (Ca, Si, Al, etc.).
- Conventional NDA methods can use accurate composition ratios obtained by another destructive assay (DA) in the routine sampling, but such DA cannot be expected for the 1F fuel debris in a canister.
- It is not easy to make a calibration curve to determine the amount of target nuclide from the count rate of detector, because there is no standard of fuel debris.
- Characterization (mixed elements, density, uranium contents, etc.) of 1F fuel debris are various and heterogeneous.
- Long-term applicability is necessary (at least 40 years), and passive measurement of radioactivity of nuclides with relatively short half-life (e.g. ^{144}Ce(^{144}Pr), ^{134}Cs, etc.) will not be available in long future.
- The correlation for the isotope ratio of key nuclides (e.g. ^{134}Cs/^{137}Cs, ^{154}Eu/Pu) by burnup calculations cannot be always used. The effectiveness of the correlation is unknown until destructive analyses are performed for the 1F fuel debris samples.
- Range of isotope ratio is widely changed depending on burnup degree of fuel debris (about 5 GWd/t - 50 GWd/t).
- Details of the fuel debris retrieval method and the specification of fuel debris canister are not decided yet. In some cases, neutron absorber may be added into the fuel debris in PCV or into the canister to prevent criticality.

Therefore, accurate quantification of nuclear materials would be difficult by applying a single measurement technology. To develop an integrated measurement system that combined several measurement technologies, Japan Atomic Energy Agency (JAEA) and Central Research Institute of Electric Power Industry (CRIEPI) have carried out a characterization study to investigate the applicability of four candidate technologies in Fig. 5 to the 1F fuel debris in a canister [11-15]. They are, 1) passive neutron method with the differential die-away self-interrogation (DDSI) method aiming to measure ^{244}Cm effective mass, 2) passive γ method to measure mass of ^{154}Eu that coexists with actinides in fuel debris, 3) active neutron method (Fast Neutron Direct Interrogation: FNDI) to measure mass of fissile nuclides directly, and 4) active γ method (Neutron Induced γ Spectrometry, NIGS) to measure mass ratio of ^{240}Pu/^{238}U and so on.

This study has been carried out by using several Monte Carlo calculation codes (MCNP[16], MVP[17], PHITS) with the Ace library based on JENDL-4.0. Currently it is difficult to conduct experiments to verify the NDA techniques for 1F fuel debris, accurate neutrons, photons and electron transport calculation is essential to grasp the detector response.

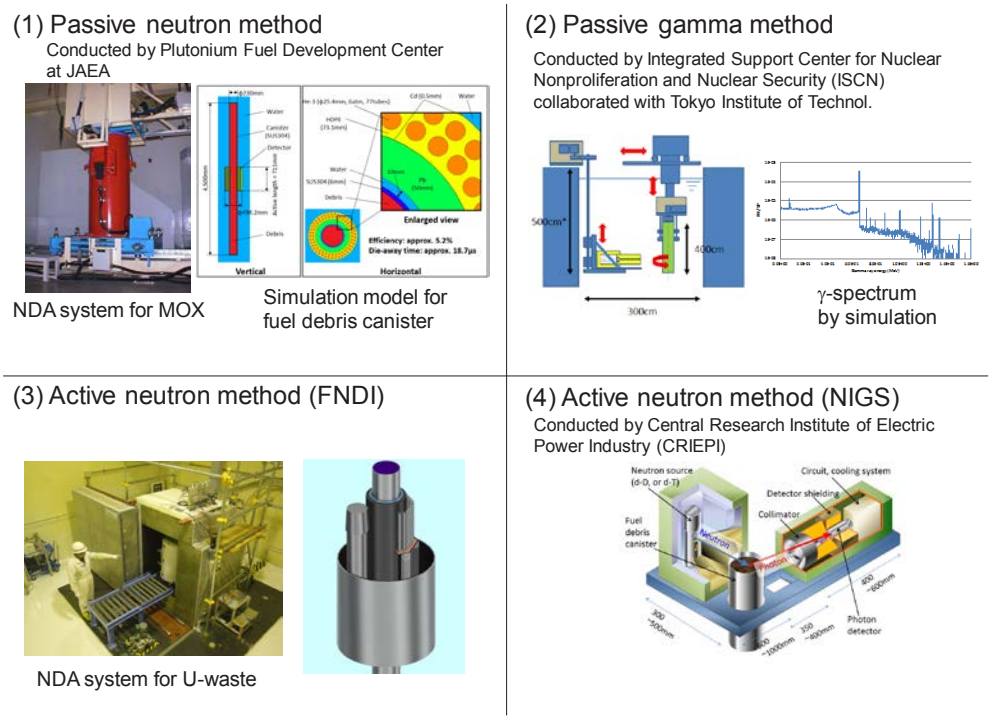

Fig. 5 Four candidate NDA methods for fuel debris in canister

3. Afterword

We introduced two R&Ds for the 1F decommissioning: prediction of dose rate distribution in PCV, and NDA for nuclear material quantification in fuel debris. The studies to realize the 1F decommissioning is a field that has not been experienced so far and quite challenging. Currently it is difficult to carry out experiments to use actual fuel debris, various case studies based on numerical calculations are very effective. Therefore, we expect reliable nuclear data and simulation codes with state-of-the-art functions, V&V, and their timely distribution.

References

[1] K. Okumura, E. S. Riyana, S. Sato, et al., "A Method for the Prediction of the Dose Rate Distribution in a Primary Containment Vessel of the Fukushima Daiichi Nuclear Power Station," 9th Int. Symposium on Radiation Safety and Detection Technology (ISORD-9), July 10-14, 2017, Nagoya, Japan, (accepted for Prog. Nuc. Sci. Tech. in 2018).

[2] K. Okumura, "Preliminary Calculation with JENDL-4.0 for Evaluation of Dose Rate Distribution in the Primary Containment Vessel of the Fukushima Daiichi Nuclear Power Station," JAEA-Conf 2016-004, pp.123-128 (2016).

[3] International Research Institute for Nuclear Decommissioning (IRID), http://irid.or.jp/en/ (accessed 2018-04-01).

[4] K. Shibata, O. Iwamoto, T. Nakagawa, et al., "JENDL-4.0: A New Library for Nuclear Science and

Engineering," J. Nucl. Sci. Technol. 48[1], pp.1-30 (2011).
[5] K. Okumura, "Nuclear Data for Prediction of Isotope Generation and Depletion," JAEA-Conf 2012-001, pp.39-44 (2012).
[6] K. Okumura, K. Kojima, K. Tanaka, "Development of multi-group neutron activation cross-section library for decommissioning of nuclear facilities", JAEA-Conf 2015-003, pp.43-47 (2016).
[7] J-Ch. Sublet, A. J. Koning, R.A. Forrest, J. Kopecky, "The JEFF-3.0/A Neutron Activation File -EAF-2003 into ENDF-6 format -," JEFDOC-982, OECD/NEA (2003).
[8] J. Katakura and F. Minato "JENDL Decay Data File 2015", JAEA-Data/Code 2015-030 (2016).
[9] T. Sato, Y. Iwamoto, S. Hashimoto, et al., "Features of Particle and Heavy Ion Transport code System (PHITS) version 3.02," J. Nucl. Sci. Technol., 55, pp.684-690 (2018).
[10] P.D.W Bottomley, A-C Gregoire, P. Carbol, et al., "Fission Product and Actinide Release from the Debris Bed Test PHEBUS FPT4: Synthesis of the Post Test Analyses and of the Revaporisation Testing of the Plenum Samples," Nucl. Eng. and Technol., 38, pp.163-174 (2006).
[11] T. Nagatani, M. Komeda, T. Shibata, Y. Nauchi, et al., "Characterization Study of Four Candidate Technologies for Nuclear Material Quantification in Fuel Debris at Fukushima Daiichi Nuclear Power Station (1) - General Outline -," Proc. of International Nuclear Fuel Cycle Conference (GLOBAL 2017), EA-236 (USB memory), Sept. 24-29, 2017, Seoul, Korea (2017).
[12] T. Nohmi, T. Nagatani, T. Kosuge, et. al., "Characterization study of four candidate technologies for nuclear material quantification in fuel debris at Fukushima Daiichi Nuclear Power Station, 2; Numerical simulations for passive neutron technique," ibid., EA-242 (2017).
[13] T. Shiba, H. Sagara, H. Tomikawa, "Characterization Study of Four Candidate Technologies for Nuclear Material Quantification in Fuel Debris at Fukushima Daiichi Nuclear Power Station (3) - Numerical Simulation of Passive Gamma Technique -," ibid., EA-286 (2017).
[14] M. Komeda, A. Ohzu, M. Kureta, et al., "Characterization Study of Four Candidate Technologies for Nuclear Material Quantification in Fuel Debris at Fukushima Daiichi Nuclear Power Station (4) - Numerical Simulations for Active Neutron Technique -," ibid., EA-310 (2017).
[15] Y. Nauchi, "Characterization Study of Four Candidate Technologies for Nuclear Material Quantification in Fuel Debris at Fukushima Daiichi Nuclear Power Station (5) - Numerical Simulations for Active Gamma Technique -," ibid., EA-247 (2017).
[16] T. Goorley, et al., "Initial MCNP6 Release Overview," Nuclear Technology, 180, pp.298-315 (2012).
[17] Y. Nagaya, K. Okumura, T. Sakurai, T. Mori, "MVP/GMVP Version 3 : General Purpose Monte Carlo Codes for Neutron and Photon Transport Calculations Based on Continuous Energy and Multigroup Methods," JAEA-Data/Code 2016-018 (2017).

12 Recent progress in the study of soft errors in semiconductor devices

Yukinobu WATANABE
Department of Advanced Energy Engineering Science, Kyushu University,
6-1 Kasuga, Fukuoka 816-8580, Japan
Email: watanabe@aees.kyushu-u.ac.jp

Recent progress in the study of cosmic-ray induced soft errors in semiconductor devices is outlined with focus on the single event upsets (SEUs) caused by neutrons and muons resulting in soft errors. For neutron-induced SEUs, we have developed a multi-scale Monte Carlo simulator PHYSERD, and applied it successfully to the analysis of terrestrial neutron-induced SEUs in 25-nm to 65-nm design rule MOSFETs. For muon-induced SEUs, we have conducted a new measurement of SEU cross sections by irradiation of low-energy positive and negative muons on 65-nm SOTB and Bulk SRAMs at J-PARC MUSE, and found that the negative muon SEU cross sections are much larger than the positive muon ones in the case where the muons stop near the sensitive volume of the SRAMs.

Keyword : Semiconductor devices, Soft errors, Neutron, Muon, Single event upset, Measurement

1. Introduction

Modern advanced information society is supported by a huge number of high-performance and multifunctional electric equipment in which semiconductor devices, e.g., VLSI (very-large-scale integration), are embedded. Increasing improvement of semiconductor devices has been driving the advancement of information systems. People and society, in the meantime, have been more and more dependent on the services provided by the information systems. Accordingly, it becomes a social requirement to guarantee the reliability of semiconductor devices. In recent years, the problem of soft errors in the semiconductor devices subjected to terrestrial radiation environment has been recognized as a major threat for electronics used in terrestrial environment [1]. The radiation-induced soft errors indicate a transient malfunction due to single-event upset (SEU) caused by the transient signal induced by a single energetic particle strike as illustrated schematically in Fig.1, *e.g.*, resulting in upset of memory information in static random access memories (SRAMs) .

Until recently, the effect of cosmic-ray neutrons has been the major subject of a large number of investigations on radiation-induced soft errors at ground level [2]. Secondary ions such as alpha and heavy ions generated by nuclear reactions in the memory devices cause the transient signal which results in SEUs. So far, many experimental and simulation works on cosmic-ray neutron induced soft errors in modern CMOS SRAMs, have been conducted, *e.g.*, irradiation tests using high-energy spallation neutrons at RCNP, Osaka University [3].

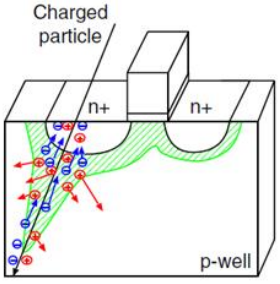

Fig.1 Schematic drawing of single event effects in SRAM memory

A major component of secondary cosmic-rays at ground level is known to be muon, and its fraction is about three-quarter of the total cosmic-ray flux. Recently, a progressive reduction in radiation tolerance on soft errors has become evident because the critical charge, i.e., the minimum charge incident at memory node that causes a bit flip, decreases by the miniaturization and low-power consumption of circuits. Thus, the possibility of muon-induced soft errors has been reported and discussed in some recent investigations [4-8].

Hereafter, our recent progress in the study of cosmic-rays induced soft errors will be described with particular attention to neutron- and muon-induced soft errors.

2. Neutron-induced soft errors

We have conducted many acceleration tests on cosmic-ray neutron induced soft errors in modern CMOS SRAMs using high-energy neutrons from the W(p,xn) spallation reaction at RCNP [9,10], because the energy spectrum of the spallation neutrons is well comparable to that of cosmic-ray neutrons at ground level at energies below 400 MeV. It should be noted that this facility is widely used for acceleration tests in industry as well.

Physics-based simulation tools of soft errors play an important role in the analysis of experimental data for acceleration tests and the estimation of soft error rates (SERs) in practical use. So far, we have developed a multi-scale Monte Carlo simulation code system called PHYSERD (PHits-HYenexss integrated code System for Effects of Radiation on Devices) [11-13] by combining the particle transport code PHITS [14] and the 3-D TCAD simulator HyENEXSS [15]. The schematic overview of PHYSERD is illustrated in Fig. 2. We have successfully applied PHYSERD to analyses of cosmic-ray neutron-induced SERs for 65-nm to 25-nm design rule MOSFETs [11,12]. In Ref. [13], the nuclear reaction models implemented in PHITS were validated by comparisons with experimental data.

Furthermore, we calculated neutron-induced SEU cross sections for a 25-nm MOSFET as a function of incident energy up to 1 GeV using PHYSERD [16]. The calculation result showed that the secondary H and He ions dominate SEUs above the threshold energies of (n,p) and (n,α) reactions, although the production cross sections of H and He ions are sufficiently smaller than the elastic scattering cross sections at neutron energies below 20MeV. From the viewpoint of nuclear data, this indicates that accurate production cross-section data of secondary protons and alphas from neutron-induced reactions are required for the simulation of SEU occurrence caused by neutrons in semiconductor devices.

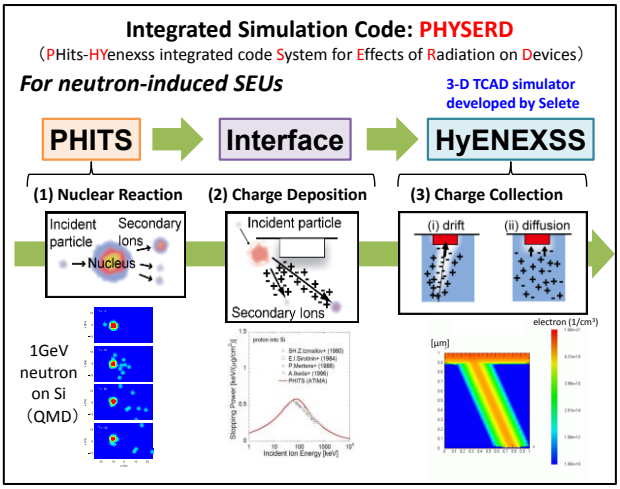

Fig.2. Schematic overview of PHYSERD

3. Muon-induced soft errors

In recent years, Sierawski et al. have carried out irradiation experiments using low-energy positive muon beams at TRIUMF and the Rutherford Appleton ISIS facility [4,5,6]. They demonstrated and qualified that the effects of muon direct ionization on different bulk SRAMs of different technology nodes (65, 55, 45, and 40 nm). Also, similar SEU experiments with low-energy positive muon beam were conducted at TRIUMF [7,8]. The experimental results showed the advantage of FDSOI and 3D Tri-Gate technologies with respect to the tolerance on muon-induced SEUs. However, no irradiation experiment with negative muons has so far been reported. Recent numerical simulation on 65-nm SRAMs by Serre et al. [17] have indicated that a residual heavy nucleus and light particles generated by negative muon capture reactions cause SEUs significantly if muons are stopped and captured near the sensitive drain region. Thus, irradiation testing with negative muons had been strongly required to verify their simulation result.

Under these circumstances, we have conducted the first irradiation experiment with both "positive" and "negative" muon beams using the D2 experimental area at J-PARC Muon Facility, MUSE [18,19]. The SEU cross sections for 65-nm Silicon on thin buried oxide (SOTB) and Bulk SRAMs were measured as a function of incident muon momentum and operating supply voltage. The major purpose of this work was to clarify the effect of negative muon capture reactions on the SEUs by comparison with the SEUs induced by positive muons.

The details of the experimental procedure and data analysis will be described in Ref.[20]. Here only the results of the irradiation test of SOTB SRAMs are shown. The measurements with negative and positive muons were performed in the momentum range from 34 MeV/c to 44 MeV/c, which corresponds to the kinetic energy range from 5.3 MeV to 8.8 MeV. As one of the results, the measured SEU cross sections for SOTB SRAM with supply voltage of 0.5 V are plotted as a function of momentum in Fig. 3. The error bars indicate the statistical uncertainties. Both the negative and positive muon SEU cross sections have the peaks around 38 MeV/c. Our preliminary simulation with the PHITS code [21] shows that the 38-MeV/c muon can stop near the sensitive volume. This suggests that the muon deposits the maximum charge in the region localized at the end of its path and the deposited charge leads to high probability of SEU occurrence. Next, it is found that the negative muon SEU cross sections are approximately two to four times higher than the positive muon SEU ones in the momentum range from 35 MeV/c to 39 MeV/c. From this result, the secondary ions generated from negative muon capture reaction are expected to cause SEUs more significantly than the direct ionization of muons. As the muon momentum is higher than 40 MeV/c, the difference between the positive and negative muon SEU cross sections is smaller and smaller, and both are almost the same over 42 MeV/c. Most of the muons with momentum over 42 MeV/c pass through the device board, and negative muon capture reaction seldom happens near the sensitive volume. Only the direct ionization contributes mainly to the occurrence of SEUs. Therefore, the difference between the positive and negative muon SEU cross sections is approximately equivalent to the contribution from secondary heavy

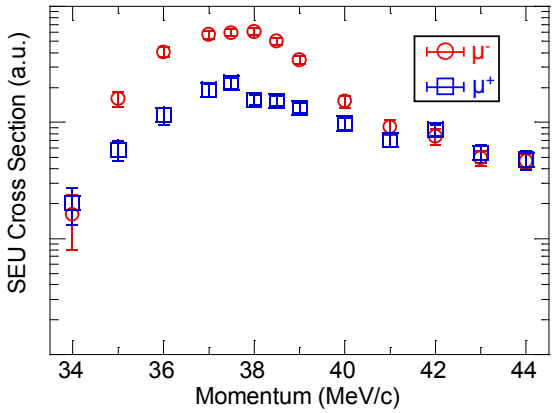

Fig.3. Measured cross sections of SEUs induced by negative and positive muons for SOTB SRAM with supply voltage of 0.5 V as a function of momentum.

and light ions generated by negative muon capture reactions in the device.

Analysis of the experimental results with advanced radiation transport codes is necessary for quantitative understanding of muon-induced SEUs. Recently, well-established muon interaction models have been implemented in the PHITS code [21] and the transport of muons in matter including the negative muon capture reaction can be predicted with high accuracy. The overall behavior of the observed momentum dependence of SEUs was reproduced generally well by the simplified simulation method in which the charge deposition process is described by PHITS simulation and the charge collection process is approximated by the sensitive volume model [22]. The detail of the result will be reported in Ref. [20].

4. Summary and future perspectives

Recent progress in the study of neutron- and muon-induced soft errors which has been conducted by our research group was outlined.

Firstly, we have developed the multi-scale Monte Carlo simulator PHYSERD, and applied it to the analysis of terrestrial neutron-induced soft errors in MOSFETs from a 65 nm down to a 25 nm design. As one of the results, it was indicated that secondary He and H ions generated by neutron-induced reactions have a major impact on soft errors with decreasing critical charge. In the future, we plan to apply PHYSERD simulation to the latest devices based on modern FDSOI and 3D Tri-Gate technologies and conduct new irradiation tests using quasi mono-energetic neutrons at CYRIC, Tohoku University, towards development of a reliable prediction tool of terrestrial neutron-induced soft errors.

Secondly, the measurement of muon-induced SEU cross sections for 65-nm SRAMs (SOTB and Bulk) was performed by irradiation of low-energy negative and positive muon beams at J-PARC MUSE. It was found that the negative muon SEU cross sections are much larger than the positive muon ones in the case where the muons stop completely in the test device. The preliminary simulation with PHITS showed that the charged particles and secondary ions generated by negative muon capture reaction influence significantly on SEUs. We are planning on further systematic measurements with advanced devices at J-PARC MUSE and RCNP MuSIC and more realistic simulations with PHYSERD for further understanding of the SEU mechanism induced by muons.

Acknowledgements

The author wishes to thank all the co-workers for their kind cooperation and fruitful discussions: S. Abe, M. Hashimoto, S. Manabe, W. Liao, K. Nakano, H. Sato, T. Kin, K. Hamada, M. Tampo, and Y. Miyake. The work on muon-induced soft errors was supported by Grant-in-Aid for Scientific Research (B) (No.16H03906) from the Japan Society for the Promotion of Science (JSPS). The muon experiment was performed at the Materials and Life Science Experimental Facility of the J-PARC under user programs Nos. 2016B0046 and 2017A0139.

References

[1] Austran JL, Munteanu D, Soft Errors, CRC Press, 2015.

[2] Nakamura T, Baba M, Ibe E, et al., Terrestrial Neutron-Induced Soft-Error in Advanced Memory Devices, World Scientific, 2008.

[3] Ibe EH, Terrestrial Radiation Effects in ULSI Devices and Electronic Systems, IEEE Press, John Wiley and Sons Singapore Pte. Ltd., 2015: 90.

[4] Sierawski BD, Mendenhall MH, Reed RA, et al., Muon-Induced Single Event Upsets in Deep-Submicron Technology, IEEE Trans. on Nucl. Sci., 2010; 57(6): 3273-3278.

[5] Sierawski BD, Reed RA, Mendenhall MH, et al., Effects of Scaling on Muon-Induced Soft Errors, Proceedings of IRPS2011, 2011: 3C.3.1-3C.3.6 .

[6] Sierawski BD, Bhuva B, Reed RA, et al., Bias Dependence of Muon-Induced Single Event Upsets in 28 nm Static Random Access Memories, Proceedings of IRPS2014, 2014: 2B.2.1-2B.2.5 .

[7] Gasiot G, Soussan D, Autran JL, Malherbe V, Roche P, Muons and thermal neutrons SEU characterization of 28nm UTBB FD-SOI and Bulk eSRAMs, Proceedings of IRPS2015, 2015: 2C.2.1-2C.2.5.

[8] Seifert N, Jahinuzzaman S, Velamala J, Patel N, Susceptibility of Planar and 3D Tri-Gate Technologies to Muon-induced Single Event Upsets, Proceedings of IRPS2015, 2015:2C.1.1-2C.1.6.

[9] Harada R, Abe S, Fuketa H, Uemura T, Hashimoto M, Watanabe Y, Angular Dependency of Neutron-Induced Multiple Cell Upsets in 65-nm 10T Subthreshold SRAM, IEEE Trans. on Nucl. Sci., 2012; 59(6): 2791-2795.

[10] Hirokawa S, Harada R, Hashimoto M, Onoye T, Characterizing Alpha- and Neutron-Induced SEU and MCU on SOTB and Bulk 0.4-V SRAMs, IEEE Trans. on Nucl. Sci., 2015; 62(2): 420-427.

[11] Abe S, Watanabe Y, Shibano N, Sano N, et al., Multi-Scale Monte Carlo Simulation of Soft Errors Using PHITS-HyENEXSS Code System, IEEE Trans. on Nucl. Sci., 2012; 59(4): 965-970.

[12] Abe S, Watanabe Y, Shibano N, Sano N, et al., Neutron-Induced Soft Error Analysis in MOSFETs from a 65 nm to a 25 nm Design Rule using Multi-Scale Monte Carlo Simulation Method, Proceedings of IRPS2012, 2012: SE.3.1-SE.3.6.

[13] Watanabe Y, Abe S, Nuclear Reaction Models Responsible for Simulation of Neutron-induced Soft Errors in Microelectronics, Nuclear Data Sheets, 2014;120: 254-257.

[14] Sato T, Niita K, Matsuda N, et al., Particle and Heavy Ion Transport Code System PHITS, Version 2.52, J. Nucl. Sci. Technol., 2013;50(9):913-923.

[15] Semiconductor Leading Edge Technologies Inc.,Yokohama-shi, Kanagawa, Japan, “3-D TCAD Simulator HyENEXSS, Developed by Selete,” , 1996.

[16] Abe S, Ogata R, Watanabe Y, Impact of Nuclear Reaction Models on Neutron-Induced Soft Error Rate Analysis, IEEE Trans. on Nucl. Sci.,2014; 61(4):1806-1812.

[17] Serre S, Semikh S, Autran JL, et al., Effects of Low Energy Muons on Electronics: Physical Insights and Geant4 Simulation, Proceedings of RADECS2012, 2012.

[18] Miyake Y, Nishiyama K, Kawamura N, et al., J-PARC muon source, MUSE, Nucl. Instrum. Methods A, 2009; 600:22-24.

[19] Miyake Y, Shimomura K, Kawamura N, et al., J-PARC Muon Facility, MUSE, Physics Procedia, 2012; 30:46-49.

[20] Manabe S, Watanabe Y, Liao W, Hashimoto M, et al., Negative and Positive Muon-Induced Single Event Upsets in 65-nm UTBB SOI SRAMs, to be published in IEEE Trans. on Nucl. Sci., 2018.

[21] Abe S, Sato T, Implementation of Muon Interaction Models in PHITS, J. Nucl. Sci. Technol., 2017; 54(1):101-110.

[22] Tosaka Y, Kanata H, Satoh S, Itakura T, Simple Method for Estimating Neutron-Induced Soft Error Rates Based on Modified BGR Model, IEEE Electron Device Lett., 1999; 20(2): 89-91.

This is a blank page.

13 Production of medical radioactive nuclides using an electron linear accelerator

Takahiro TADOKORO[1]*, Yuichiro UENO[1], Yuko KANI[1]
Shun SEKIMOTO[2], Tsutomu OHTSUKI[2]
[1]Center of Technology Innovation - Energy, Research & Development Group, Hitachi, Ltd.
7-2-1 Omika-cho, Hitachi-shi, Ibaraki-ken 319-1221 Japan
[2]Research Reactor Institute, Kyoto University
2, Asashiro-nishi, Kumatori-cho, Sennan-gun, Osaka-fu 590-0494, Japan
*E-mail: takahiro.tadokoro.wr@hitachi.com

An electron linear accelerator based Mo-99 production system has many advantages in comparison with other accelerator systems: the size of the system is relatively small, a high beam current is easily achieved and the cross section of the Mo-99 production reaction, Mo-100(γ,n)Mo-99, is relatively high. These advantages can lead to a cost-effective system. With the final goal of implementing such a system, we have been evaluating the Mo-99 production amount in a real-scale system. To provide even more cost-effectiveness, we have been considering production of other medical nuclides using the same Mo-99 production system. Hence, we also have carried out the evaluation of Cu-67, Ge-68 and Ga-68 production amounts which are recently being studied as nuclides for diagnostic and treatment agents. We focus on evaluation of Mo-99, Cu-67, Ge-68 and Ga-68 production amounts in the present paper.

1. Introduction

Mo-99 is a parent nuclide of Tc-99m and used in nuclear medicine. Mo-99 is produced in research reactors by the fission of U-235, and Japan imports 100% of the Mo-99 that is medically used [1]. However, with aging of these overseas reactors, their closedowns are planned, and the demand for Mo-99 is assumed to become tight [1]. Consequently, a variety of production methods of Mo-99 using accelerators have been proposed [2], but none of the production methods have been realized presently. The main reason for this situation is the high production cost of Mo-99. An electron linear accelerator based Mo-99 production system has some possibilities to become a cost-effective system, because the system size can be made relatively small, a high beam current is easily achieved and the cross section of the Mo-99 production reaction, Mo-100(γ,n)Mo-99, is relatively high. Moreover, the production amounts of impurity nuclides are very small. To produce Mo-99 effectively, one-stage approach (based on using a molybdenum as a photon converter and also photoneutron target) have been investigated [3].

When other medical nuclides are produced using the same Mo-99 production system with only the target nuclides being changed, the system ought to become more cost-effective. Thus, we have stated examination of the medical nuclide production system using an electron linear accelerator ad have estimated production of some medical nuclides in the real-scale system.

2. Medical radionuclide production method using an electron linear accelerator

When high-energy electrons are irradiated onto a heavy metal such as Pt or W, a continuous spectrum of bremsstrahlung photons is generated. The bremsstrahlung photons subsequently interact with the nucleus of the target material, resulting in the emission of neutrons or protons. This reaction is known as a photonuclear reaction. Neutrons or protons are bound to the nucleus by a binding energy of 5-15 MeV, thus a photonuclear reaction can be caused by using the photons with an energy above this value. When Mo-100 is used as a target material with the photonuclear reaction of Mo-100(γ,n)Mo-99, Mo-99 can be produced. When Zn-68 and Ge-70 are used as target materials with the photonuclear reactions of Zn-68(γ,p)Cu-67 and Ge-70(γ,2n)Ge-68, Cu-67 and Ge-68 can be produced; these nuclides have been recently studied as diagnostic and treatment agents.

3. Evaluation of medical radionuclide production amounts

3.1 Mo-99 and Tc-99m

We carried out a basic examination of Mo-99 production using the electron linear accelerator of the Kyoto University Research Reactor Institute. A schematic view of the basic experiment for Mo-99 mass production is shown in Figure 1. We used nat-Mo (isotope ratio of Mo-100, 9.6 %) as a target nuclide, and the energy of the electron beam was 35 MeV and the current was 80 μA. To facilitate dissolution after irradiation of bremsstrahlung photons, we used molybdenum trioxide (nat-Mo･O_3). Ten columnar samples of nat-Mo･O_3 (diameter ,10 mm; thickness, 10 mm) were set parallel to each other in the direction of the electron beam radiation. The bremsstrahlung photon production material was Pt (diameter, 60 mm; thickness, 2 mm).

We also carried out a Mo-99 production calculation. We derived the bremsstrahlung radiation distribution using the Monte Carlo radiation transport calculation code PHITS [4], and we also derived the production rate of Mo-99 using the above-derived bremsstrahlung radiation distribution and the reaction cross section of the Mo-100(γ,n)Mo-99 nuclear reaction which had been evaluated by a Mo-99 production experiment [5].

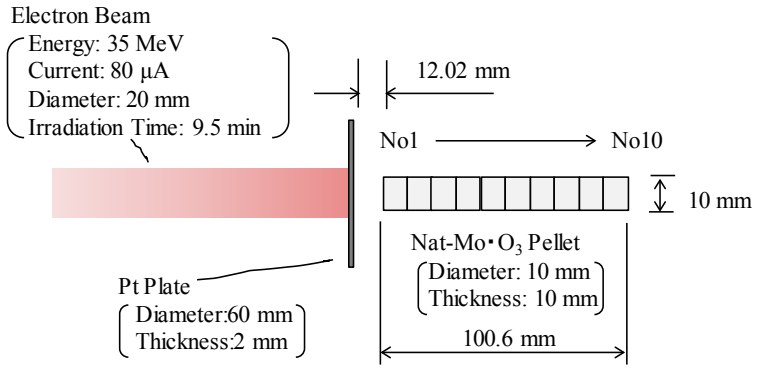

Fig.1 Schematic view of the basic experiment of Mo-99 mass production

A comparison between calculation and experimental values of Mo-99 production amount is shown in Figure 2. The calculation results that were obtained using the Monte Carlo simulation accorded with the results of the

basic examination of Mo-99 mass production within 30%. Thus, we carried out the estimation of Mo-99 production amount in the real-scale system (electron beam energy, 35 MeV; current, 1 mA; irradiation time, 20 h) using the same calculation method.

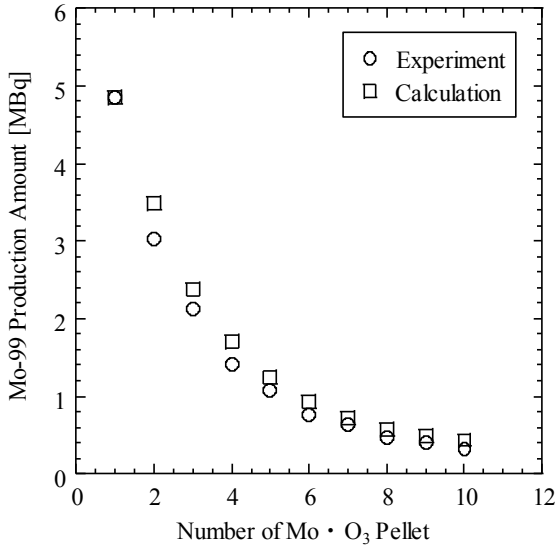

Fig.2 Comparison between calculation and experimental values of Mo-99 production amount

Evaluation results of the Mo-99 and Tc-99m production amounts in a real-scale production system are shown in Figure 3. Tc-99m (half-life, 6.0 h) is the descendant nuclide of Mo-99 (half-life, 66 h). Tc-99m is produced according to the decay of Mo-99 during and after production of Mo-99, and then Tc-99m and Mo-99 are in a transit equilibrium. The estimated Mo-99 production amount was 1340 GBq and that of Tc-99m was 1003 GBq. If this system were operating 20 hours per day, 200 days per year, the annual production of Mo-99 would be 268 TBq. Three systems producing this amount would be able to cover the demand in Japan for nuclear medicine use [6].

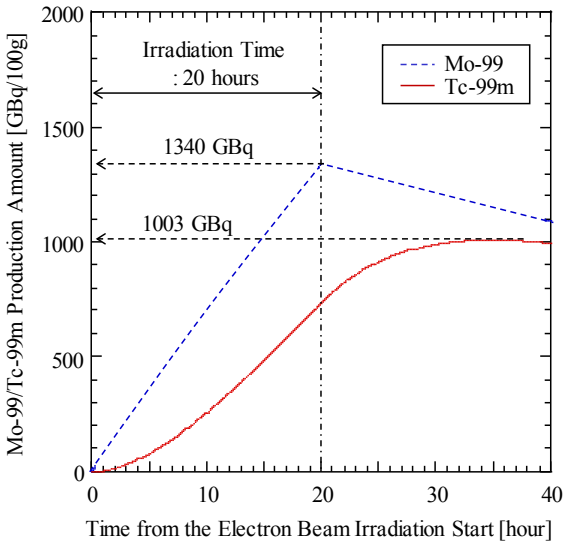

Fig.3 Evaluation results of Mo-99 and Tc-99m production amounts in a real-scale production system

3.2 Cu-67

We carried out a Cu-67 production calculation for the the same production system as used for Mo-99 production, the only change as substitution of Zn-68 as the target. We derived the bremsstrahlung radiation distribution for a Zn-68 target (diameter, 20 mm; thickness, 45 mm) using PHITS, and we also obtained the production rate of Cu-67 using the derived bremsstrahlung radiation distribution and the evaluated reaction cross section of the Zn-68(γ,p)Cu-67 nuclear reaction [7].

Evaluation result of Cu-67 production amount is shown in Figure 4. The estimated Cu-67 production amount was 150 GBq. The consumption of Cu-67 in treatment agents per person would likely be 3.7 to 7.4 GBq based on the fact that this is the amount of I-131 consumed as a treatment agent [8], thus the production amount for treatment of 20 to 40 persons per day could be obtained.

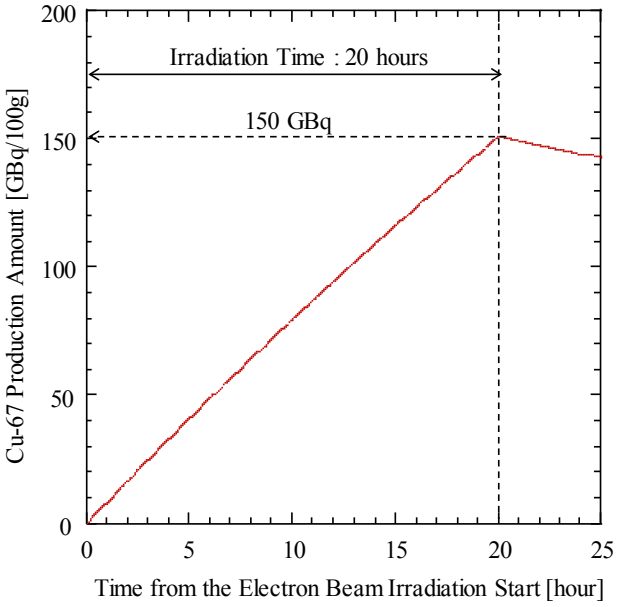

Fig.4 Evaluation result of Cu-67 production amount

3.3 Ge-68 and Ga-68

We carried out a Ge-68 and Ga-68 production calculation for the same production system as used for Mo-99 production; the only change was the substitution of Ge-70 as the target. We derived the bremsstrahlung radiation distribution for the Ge-70 target (diameter, 10 mm; thickness, 24 mm) using PHITS, and we also obtained the production rate of Ge-68 using the derived bremsstrahlung radiation distribution and the evaluated reaction cross section of the Ge-70(γ,2n)Ge-68 nuclear reaction [9].

Evaluation results of Ge-68 and Ga-68 production amounts are shown in Figure 5. Ga-68 (half-life, 68 min) is the descendant nuclide of Ge-68 (half-life, 288 days). Ga-68 is produced according to decay of Ge-68 during and after production of Ge-68, and then Ga-68 and Ge-68 are in a secular equilibrium. The estimated Ga-68 production amount was 540 MBq. The consumption of Ga-68 in a PET examination using Ga-68-DOTATOC is

132 to 222 MBq per person [10], so the production amount for approximately 2 to 4 persons could be produced in a 20-h irradiation. If Ge-68 were milked as a generator of Ga-68 twice a day and used for 250 days per year, it would be possible to produce Ga-68 for PET examinations of 750 to 1500 persons per year.

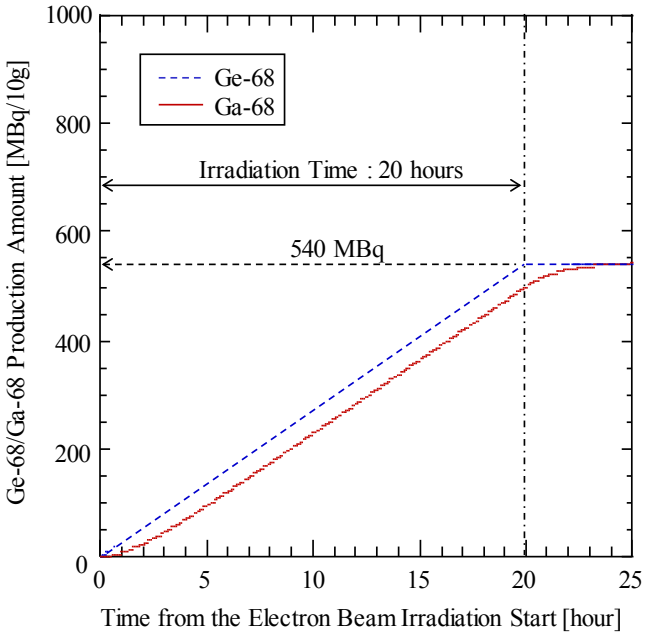

Fig.5 Evaluation results of Ge-68 and Ga-68 production amounts

4. Summary

An electron linear accelerator based Mo-99 production system has many advantages in comparison with other accelerators. The size of the system can be relatively small, a high current is easily achieved and the reaction cross section of the Mo-100(γ,n)Mo-99 nuclear reaction is relatively high. Thus, we chose an electron linear accelerator based system and carried out an evaluation of Mo-99 production amount.We derived the bremsstrahlung radiation distribution using the Monte Carlo radiation transport calculation code PHITS, and we also obtained the production amount of Mo-99 using the above-derived bremsstrahlung radiation distribution and the reaction cross section of the Mo-100(γ,n)Mo-99 nuclear reaction. The estimated Mo-99 production amount was 1340 GBq in a real-scale system (electron beam energy, 35 MeV; current, 1 mA; irradiation time, 20 h). Three systems producing this amount would be able to cover the demand in Japan for nuclear medicine use.

The estimated Cu-67 production amount was 150 GBq using the same production system as for Mo-99. The consumption of Cu-67 in treatment agents per person would likely be 3.7 to 7.4 GBq, thus the production amount for treatment of 20 to 40 persons per day could be obtained. We also evaluated Ge-68 and Ga-68 production amounts. Ge-68 and Ga-68 have been used for PET examinations in Europe and the US. The estimated Ga-68 production amount we 540 MBq, also for the same Mo-99 production system. The consumption of Ga-68 in the PET examination using Ga-68-DOTATOC is 132 to 222 MBq per person, thus the production amount for approximately 2 to 4 persons can be produced by the 20-h irradiation. If Ge-68 were milked as a

generator of Ga-68 twice a day and used for 250 days per year, it would be possible to produce Ga-68 for PET examinations of 750 to 1500 persons per year.

References

[1] Science Council of Japan. Considerations on maintaining a steady supply system of radioisotopes in Japan. 2008. [cited 2016 Dec 20]. Available from: http://www.scj.go.jp/ja/info/kohyo/pdf/kohyo-20-t60-5.pdf [in Japanese].

[2] OECD/NEA. Review of potential Mo-99/ Tc-99m production technologies. 2010. [cited 2015 Dec 10]. Available from: http://www.oecd-nea.org/med-radio/reports/Med-Radio-99Mo-Prod-Tech.pdf.

[3] A. Tsechanski, et al. Electron accelerator-based production of molybdenum-99: Bremsstrahlung and photoneutron generation from molybdenum vs. tungsten. Nuclear Instrument and Methods in Physics Research. Section B. 2016;366:124.

[4] JAEA. PHITS: Particle and Heavy Ion Transport code System. 2007. [cited 2016 May 10]. Available from: http://phits.jaea.go.jp/.

[5] H. Beil, et al. A Study of the Photoneutron Contribution to the Giant Dipole Resonance in Doubly Even Mo Isotopes. Nucl. Phys A. 1974;227:427.

[6] Japan Radioisotope Association. Statistics on the Distribution of Radioisotopes in Japan. 2017. [cited 2017 Dec 20]. Available from: https://www.jrias.or.jp/report/pdf/ryutsutoukei2017.pdf.

[7] A. I. Blokhin, et al. Handbook on photonuclear data for applications, Cross-sections and spectra. IAEA-TECDOC-1178. 2000:160.

[8] Japanese Society of Nuclear Medicine. Guidelines for private business engaged in radioiodine therapy for thyroid cancer (n.d.). [cited 2016 May 20]. Available from: http://oncology.jsnm.org/files/pdf/thyroid-guideline09.pdf [in Japanese].

[9] J. J. McCarthy, et al. Systematic study of the photodisintegration of Ge-70, Ge-72, Ge-74, and Ge-76. Phys. Rev C. 1975;11:772.

[10] P. Pankaj, et al. Role of 68-Ga Labelled PSMA PET CT Scan in the Evaluation of Prostate Cancer and its Correlation with Histopathology Findings - Preliminary Analysis. International Conference on Clinical PET-CT and Molecular Imaging (IPET 2015). IAEA-CN-232/92. 2015.

14 Features and applications of PARMA: PHITS-based analytical radiation model in the atmosphere

Tatsuhiko SATO

Nuclear Science and Engineering Center, Japan Atomic Energy Agency (JAEA),
Tokai, Ibaraki 319-1195, Japan
E-mail: sato.tatsuhiko@jaea.go.jp

Abstract

Estimation of terrestrial cosmic-ray fluxes is of great importance not only for particle physics and astrophysics but also for geosciences and radiation research. We therefore developed an analytical model for calculating the terrestrial cosmic-ray fluxes anytime and anywhere in the atmosphere, based on the results of the extensive air shower simulation performed by Particle and Heavy Ion Transport code System (PHITS). The model was named PARMA: PHITS-based Analytical Radiation Model in the Atmosphere, and was released to public together with its associated software EXPACS: EXcel-based Program for calculating Atmospheric Cosmic-ray Spectrum. They have been used for various purposes such as evaluation of the cosmic-ray doses for aircrew and public, estimation of the production rates of cosmogenic nuclides, and calculation of the soft-error rates of semi-conductor devices. This paper summarizes the features and applications of PARMA and EXPACS.

1. Introduction

Galactic cosmic rays are continuously incident on the Earth, and they induce extensive air shower (EAS) by successively causing nuclear and atomic interactions in the atmosphere. Simulation of EAS over a wide energy range is essential not only for particle physics and astrophysics but also for geosciences and radiation research. For example, evaluation of the temporal and locational variations of cosmic ray fluxes generated through EAS is very important for estimating cosmogenic nuclide yields, radiation doses for aircrews, and soft-error rates of semi-conductor devices.

We therefore performed the EAS simulation using the Particle and Heavy Ion Transport code System PHITS [1]. The selection of the total reaction cross section models is the key issue to determine the accuracy of the EAS simulation. When we employed a cross section model specially developed for cosmic-ray transport simulation [2] instead of the default model in PHITS, excellent agreements can be observed between the measured and calculated cosmic-ray fluxes for various conditions [2, 3]. Examples of the EAS simulation results in comparison with the corresponding experimental data are shown in Figs. 1 and 2. By fitting the results of the EAS simulation, we developed an analytical model for instantaneously estimating the cosmic-ray fluxes nearly anytime and anywhere in the Earth's atmosphere. The model and the associated software are named PHITS-based Analytical Radiation Model in the Atmosphere, PARMA, and Excel-based Program for calculating Atmospheric Cosmic-ray Spectrum, EXPACS, respectively. They are opened to public via EXPACS website [4].

The details of the simulation procedure together with the verification of the results are described in our previous papers [2, 3]. Thus, this paper focuses on describing the features and applications of PARMA and EXPACS.

2. Features of PARMA and EXPACS

Fig. 3 shows a screenshot of EXPACS version 4.02. It is an Excel file without using any macro program, and thus, it can be used in any computer with Microsoft Excel installed. Five parameters must be specified in EXPACS, which are: 1. Altitude (km) or atmospheric depth (g/cm^2), 2. Geographic coordinate (latitude and longitude) or vertical cut-off rigidity (GV), 3. Date of interest (year, month, and day) or solar activity (W-index), 4. Surrounding environment (in the atmosphere, on ground with water density, or inside aircraft with its mass), 5. Calculated dose type (Effective dose, ambient dose equivalent, or absorbed dose in dry air). When these parameters are changed by a user, EXPACS interactively calculates the terrestrial cosmic ray fluxes of neutrons, protons, ions with charge up to 28 (Ni), muons, electrons, positrons, and photons as well as their corresponding dose rates for the condition. The calculated fluxes are plotted in a graph as shown in Fig. 3. After EXPACS version 4.0, the angular differential fluxes for a certain zenith angle can be also calculated except for ions with charge greater than 2.

We also developed software for visualizing the cosmic-ray dose rates calculated by EXPACS on the map of Google Earth, and named it as EXPACS-V. It can be downloaded from EXPACS website, though the registration is required for the download. Fig. 4 shows a screenshot of EXPACS-V together with Google Earth. The input data are basically the same as those for EXPACS except for altitude, where the "ground level" mode can be selected in addition to the "fixed altitude" mode. When the former is selected, the elevation of each location on the map is determined from a database developed based on ETOPO v2 [5]. EXPACS-V has been used as an educational tool for better understanding of natural background radiation in several countries.

In addition, a Fortran program package of the PARMA model itself can be downloaded from EXPACS website. It is particularly useful when the cosmic-ray fluxes for various conditions must be evaluated, such as dose calculation on a flight route. A sample user-defined source program of PHITS based on PARMA is also provided from the website, which determines energy and direction of each source particle using random number. Using this program, the motions of terrestrial cosmic-rays in certain objects can be easily analyzed by PHITS, such as the cases of the designs of cosmic-ray detectors and muon radiography.

3. Applications of PARMA

One of the most important applications of PARMA (or EXPACS) is the cosmic-ray dose estimation for aircrews and public. For aircrew dosimetry, PARMA was implemented in Japanese Internet System for Calculation of Aviation Route Doses, JISCARD [6], which is used for the dose evaluation of aircrews of Japanese airline companies. For public dosimetry, PARMA was used for estimating the population weighted annual effective doses and their probability densities for the enter world as well as for 230 individual nations, in tandem with detailed grid population and elevation databases [7]. The resulting world population-weighted annual effective dose was determined to be 0.32 mSv, which is smaller than the

UNSCEAR's evaluation by 16%.

Geosciences is another important application field of PARMA. A scaling model for in situ cosmogenic nuclide production rates was developed based on PARMA [8], which was employed as a key model in the Cosmic-Ray Produced Nuclide Systematics on Earth, CRONUS-Earth, project [9]. Note that the precise evaluation of the production rates of cosmogenic nuclides with a long half-life such as ^{10}Be and ^{26}Al is essential in the surface exposure dating. PARMA was also used in the evaluation of footprint characteristics for soil moisture monitoring with cosmic-ray neutrons [10], in the analysis on the relation between volcano explosion and the solar activity [11], and in the discussion on the possible link between the encounters with nebulae and environmental catastrophes on the Earth, such as the snowball Earth, mass extinctions, and explosive evolution [12]. In addition, a new climate theory that cosmic-rays impact global temperatures due to the influence on cloud formation via ionization was recently proposed [13]. PARMA has a potential to contribute to the quantitative discussion for verifying this theory owing to its capability of calculating the cosmic-ray induced ionization densities anywhere in the atmosphere.

PARMA is also used in the engineering fields, particularly for the estimation of the soft-error rates of semi-conductor devices. For example, the building shielding effect of stacked servers were analyzed by calculating the neutron-induced soft-error rates inside and outside a building using PHITS coupled with PARMA [14]. Not only neutrons but also muons can induce the soft error, and simulation using PARMA suggested an increasing role of muons in the soft-error rates for smaller technologies [15].

4. Conclusions

We developed an analytical model PARMA and its associated software EXPACS for calculating the terrestrial cosmic-ray fluxes anytime and anywhere in the atmosphere by fitting the results of the EAS simulation performed by PHITS. They have been used for various purposes such as evaluation of the cosmic-ray doses for aircrew and public, estimation of the production rates of cosmogenic nuclides, and calculation of the soft-error rates of semi-conductor devices. This implies the importance of the studies of nuclear technologies for a wide research area because reliable nuclear data libraries and nuclear reaction models are indispensable for accurate simulation of the EAS.

References

[1]. Sato T, Iwamoto Y, Hashimoto S, Ogawa T, Furuta T, Abe S, Kai T, Tsai PE, Matsuda N, Iwase H, Shigyo N, Sihver L, and Niita K, Features of particle and heavy ion transport code system PHITS Version 3.02, J. Nucl. Sci. Technol. 2018; DOI:10.1080/00223131.2017.1419890.

[2]. Sato T, Analytical Model for Estimating Terrestrial Cosmic Ray Fluxes Nearly Anytime and Anywhere in the World: Extension of PARMA/EXPACS, PLOS ONE 2015; 10: e0144679.

[3]. Sato T, Analytical Model for Estimating the Zenith Angle Dependence of Terrestrial Cosmic Ray Fluxes, PLOS ONE 2016; 11: e0160390.

[4]. *EXPACS: EXcel-based Program for calculating Atmospheric Cosmic-ray Spectrum*. 2016 [cited 2018 Jan. 4]; Available from: http://phits.jaea.go.jp/expacs/.

[5]. *2-minute Gridded Global Relief Data (ETOPO2) v2*. 2006 [cited 2018 Jan. 4]; Available from: https://www.ngdc.noaa.gov/mgg/global/etopo2.html.

[6]. Yasuda H, Sato T, Yonehara H, Kosako T, Fujitaka K, and Sasaki Y, Management of Cosmic Radiation Exposure for Aircraft Crew in Japan, Radiat. Prot. Dosim. 2011; 146: 123-125.

[7]. Sato T, Evaluation of World Population-Weighted Effective Dose due to Cosmic Ray Exposure, Sci Rep 2016; 6: 33932.

[8]. Lifton N, Sato T, and Dunai TJ, Scaling in situ cosmogenic nuclide production rates using analytical approximations to atmospheric cosmic-ray fluxes, Earth Planet Sc Lett 2014; 386: 149-160.

[9]. Borchers B, Marrero S, Balco G, Caffee M, Goehring B, Lifton N, Nishiizumi K, Phillips F, Schaefer J, and Stone J, Geological calibration of spallation production rates in the CRONUS-Earth project, Quat. Geochronol. 2016; 31: 188-198.

[10]. Kohli M, Schron M, Zreda M, Schmidt U, Dietrich P, and Zacharias S, Footprint characteristics revised for field-scale soil moisture monitoring with cosmic-ray neutrons, Water Resour Res 2015; 51: 5772-5790.

[11]. Ebisuzaki T, Miyahara H, Kataoka R, Sato T, and Ishimine Y, Explosive volcanic eruptions triggered by cosmic rays: Volcano as a bubble chamber, Gondwana Res 2011; 19: 1054-1061.

[12]. Kataoka R, Ebisuzaki T, Miyahara H, Nimura T, Tomida T, Sato T, and Maruyama S, The Nebula Winter: The united view of the snowball Earth, mass extinctions, and explosive evolution in the late Neoproterozoic and Cambrian periods, Gondwana Res 2014; 25: 1153-1163.

[13]. Svensmark H, Cosmoclimatology: a new theory emerges, Astron Geophys 2007; 48: 18-24.

[14]. Kato T, Akano R, Uemura T, Watanabe Y, and Matsuyama H, Neutron Shielding Effect of Stacked Servers and Its Impact on Reduction of Soft Error Rate, IEEE Trans. Nucl. Sci. 2014; 61: 3408-3415.

[15]. Sierawski BD, Reed RA, Mendenhall MH, Weller RA, Schrimpf RD, Wen SJ, Wong R, Tam N, and Baumann RC, Effects of scaling on muon-induced soft errors, in *Reliability Physics Symposium (IRPS)*. 2011, 2011 IEEE International: Monterey, CA, USA, DOI: 10.1109/IRPS.2011.5784484.

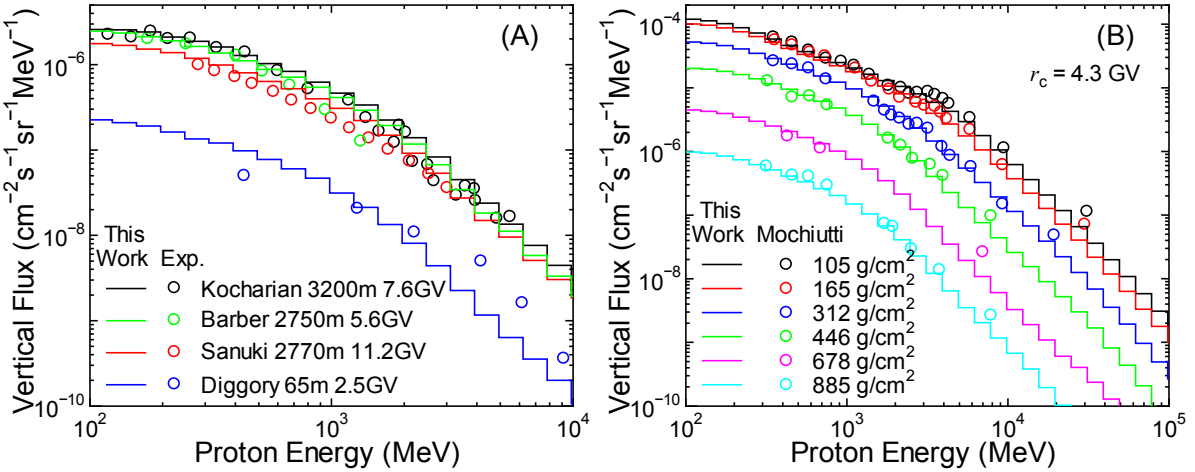

Fig. 1. Cosmic-ray proton fluxes calculated by our EAS simulation in comparison with the corresponding experimental data. The detailed calculation conditions together with the references are given in our previous paper [2].

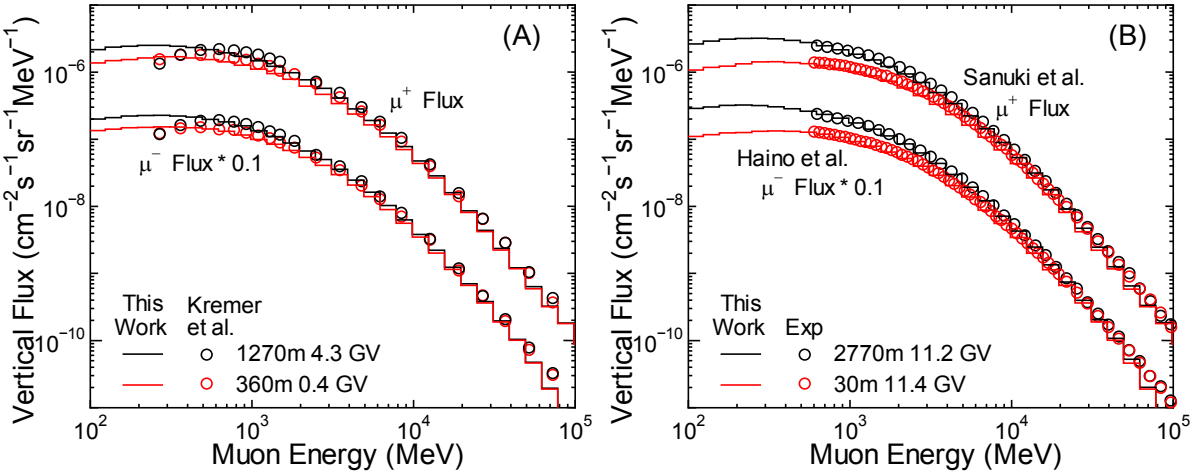

Fig. 2. Cosmic-ray muon fluxes calculated by our EAS simulation in comparison with the corresponding experimental data. The detailed calculation conditions together with the references are given in our previous paper [2].

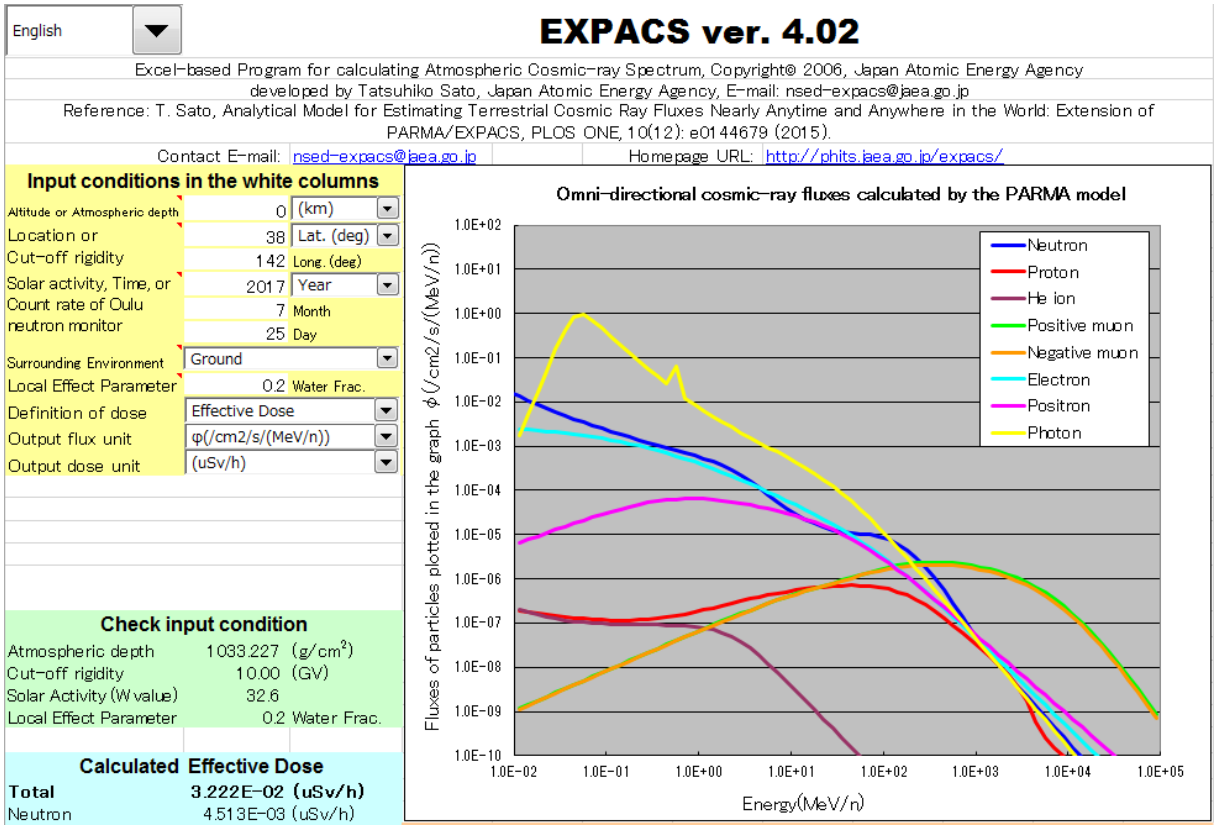

Fig. 3. Screenshot of EXPACS version 4.02

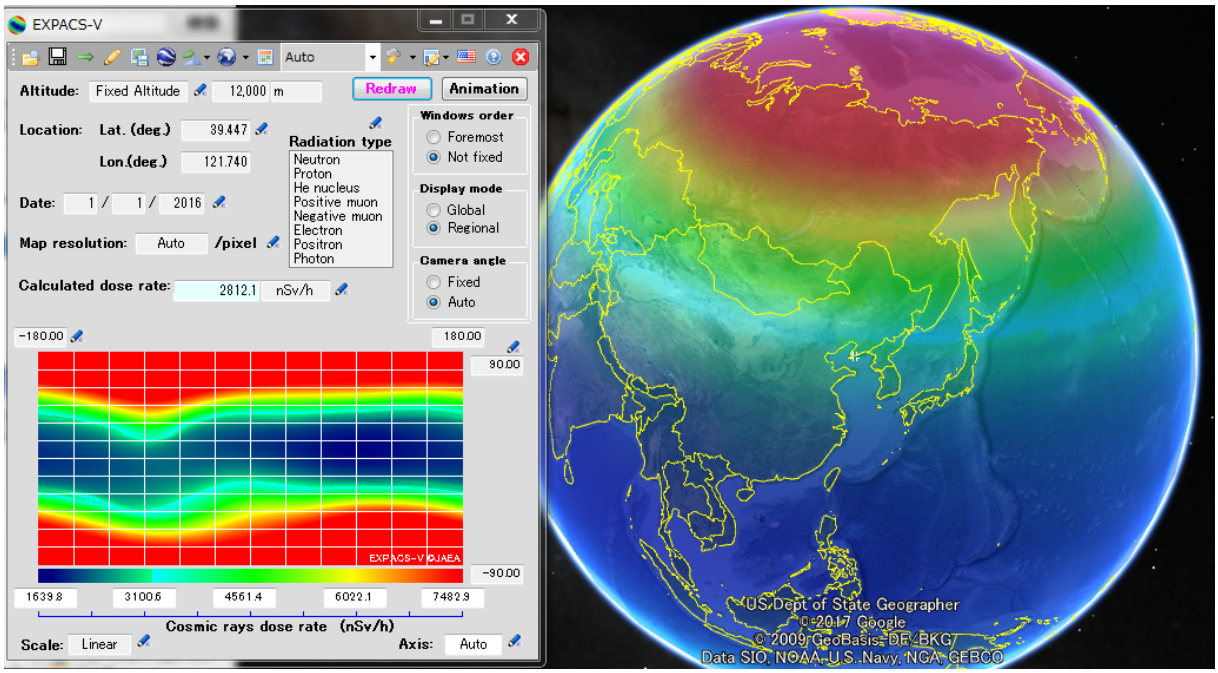

Fig. 4. Screenshot of EXPACS-V and Google Earth

15 Present Status and Future Plan of JENDL

Osamu IWAMOTO
Nuclear Data Center, Japan Atomic Energy Agency
Tokai-mura, Naka-gun, Ibaraki-ken 319-1195 Japan
e-mail: iwamoto.osamu@jaea.go.jp

Present status and future plan of JENDL special- and general-purpose files are briefly described. Regarding the special purpose files, three files of JENDL-4.0/HE, JENDL/PD-2016 and JENDL/AD-2017, which have released recently or will be released near future, are summarized. Concerning the general-purpose files, two topics of JENDL-4.0u, which is prepared for maintenance, and JENDL-5, which is the next version of JENDL-4.0, are mentioned.

1. Introduction

After the release of JENDL-4.0 in 2010 [1], six special purpose files have been developed. Five of them were already released and one is under preparation for the release. New decay and yield data for fission products were released as JENDL/FPD-2011 and JENDL/FPY-2011 [2] in 2011, respectively, accounting for new measured decay data. JENDL-4.0/HE released in 2015 [3] includes proton and neutron induced reaction data on 130 and 133 nuclei, respectively, up to 200 MeV. Comprehensive decay data JENDL/DDF-2015 [4] were released in 2015. It contains data for 3,237 nuclides from atomic number 1 to 104 including neutron. The new photonuclear reaction data file JENDL/PD-2016 [5] was released in 2017 and the activation file for decommissioning of nuclear facility JENDL/AD-2017 [6] is under preparation for release.

Regarding general purpose files, two activities are in progress. One is JENL-4.0u [7] which was created for maintenance of JENDL-4.0 and the other is development of next version of JENDL. JENDL-4.0u contains data updated by correcting errors found in JENDL-4.0. For evaluation on light nuclei for the next JENDL, a new R-matrix resonance analysis code AMUR [8] has been developed. Evaluations on structure materials are in progress by using nuclear model calculation code CCONE [9,10].

Status of JENDL project [11] regarding development of special- and general-purpose files is briefly described below.

2. Special purpose file

2.1 JENDL-4.0/HE

JENDL-4.0 High Energy File (JENDL-4.0/HE) was developed to meet expanding needs from wide application areas of accelerators such as accelerator driven system for transmutation of minor actinides and medical RI productions. JENDL-4.0/HE was released in 2015. It includes neutron and proton induced nuclear reaction data on 130 and 133 nuclei, respectively, up to 200 MeV. The data consist of residual nucleus production cross sections and emission spectra of gamma-ray and light particles *i.e.* proton, neutron, alpha particles etc.

A nuclear reaction model code CCONE, which had been developed for JENDL-4.0, was upgraded to improve prediction accuracy of reaction cross sections above 20 MeV. The revision mainly consists of three parts. The first is extension of the exciton model to allow multiple particle emission. The second is transformation of emission spectrum from center of mass system to laboratory system taking account of changes of velocities of compound nuclei by particle emissions. The last is composite particle emission in preequilibrium process which was done by introducing the Iwamoto-Harada model with modification by Kunieda *et al*. Significant improvements was achieved in calculation of emission spectra of nucleon and light ions *i.e.* deuteron, triton, He-3 nucleus, alpha-particles as seen in references [12, 13]. With state-of-the-art global optical model potential of Kunieda et al. [14], the improved CCONE code was applied to systematical evaluations for isotopes of Si, P, Cl, Ca, Ti, V, Cr, Mn, Fe, Co, Ni, Cu, Zn, Ga, Ge, As, Se, Zr, Nb, Mo, In, Sn, I, Cs, Ta, W, Au, Hg, Pb and Bi. The evaluation with CCONE improves not only emission spectra but also residual nucleus productions as shown in Fig. 1 for example. They would be important to estimate amounts of activation of structural material and transmutation of radioactive wastes.

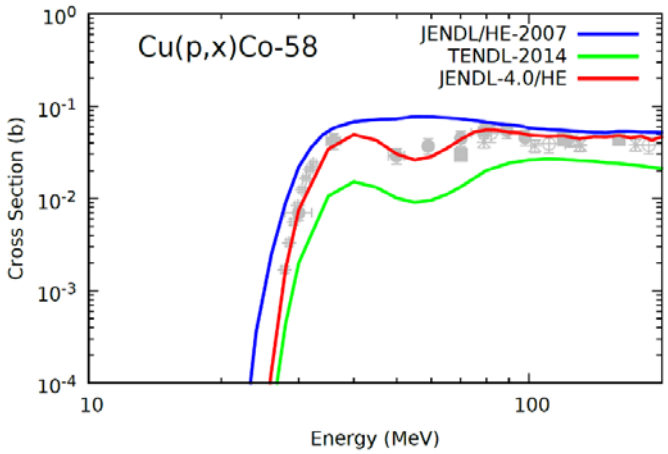

Fig. 1 Production cross section of Co-58 via Cu(p,x) reaction

2.2 JENDL/PD-2016

A new photonuclear data file JENDL/PD-2016 was published in December 2017. It contains cross sections of various reactions, emission spectra of light particles and gamma-rays, and production cross sections of residual nucleus for photon induced reactions in the energy range from 1 MeV to 140 MeV. JENDL/PD-2016 is provided as two sets of standard and expanded versions. The standard version consists

of 181 nuclides along the beta-stability line. On the other hand, the expanded one comprise 2681 nuclides covering unstable nuclei of short half-lives based on systematic nuclear model calculation.

Fine resonant structures of cross sections appearing on light nuclei in low energy region were obtained by fitting to available experimental data or nuclear structure data. Evaluations for heavier nuclei were performed mainly with two nuclear reaction model codes of CCONE [10] and ALICE-F [15] taking account of giant resonance and quasi-deuteron processes. The CCONE code were mainly used for evaluation of heavier nuclei with atomic number equal or larger than 30 in the standard version of JENDL/PD-2016. ALICE-F were mainly used for the lighter ones with Z < 30 in the standard version and most of the extended version. The nuclear model calculations allow to deduce emission spectra for gamma-ray, neutron, proton, deuteron, triton, He-3 nucleus, and alpha-particle as well as residual nucleus production cross sections. Fission cross sections were given for not only for actinides but also for non-actinide heavy nuclei such as Pb, Bi etc.

2.3 JENDL/AD-2017

An activation cross section file for decommissioning of nuclear facility JENDL/AD-2017 is under preparation for release. It is targeted for estimation of amounts of 239 radioactive nuclei having half-lives longer than 30 days possibly produced in light water reactors. After release of JENDL-4.0, new evaluations were performed to obtain activation cross sections including isomer productions for more than 220 nuclides taking account of available experimental data. Cross sections of JENDL-4.0 and JENDL/A-96 [16] were adopted for some nucleus with modification if necessary. More than 300 nuclides from H-2 to Es-254 will be included in the JENDL/AD-2017. Point-wise cross sections will be given for the new file in spite of group-wise ones were stored in the JENDL/A-96 to give fine structures of cross sections in resonance regions at temperatures of 0 and 293.6 K. It is planned to be released in FY of 2017.

3. General purpose file

3.1 JENDL-4.0u

JENL-4.0u is attempted to provide updated data with correcting errors found in JENDL-4.0. Addition of covariance data lacked in JENDL-4.0 is also within the scope of JENDL-4.0u. Version number of JENDL-4.0u is given for each nuclide. The first update for some nuclides was released as JENDL-4.0u1, the second one of the same nuclides become JENDL-4.0u2, and so on.

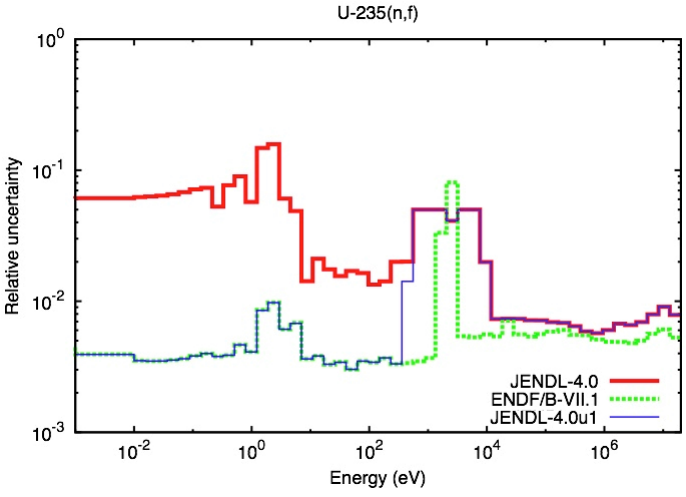

Fig. 2 Uncertainty of U-235(n,f) cross section

Up to now 38 files were released as JENDL-4.0u. Among those files, 14 nuclides of Cr-52, 53, U-233, 235, 238, Pu-239, U-234, Np-237, Pu-238, Pu-242, Pb-204, 206, 207, 208 in released order were related to covariance data including new evaluation, revision of data, or correction of format errors. Figure 2 shows uncertainties of U-235 fission cross section of JENDL-4.0u. In JENDL-4.0, the covariance matrix obtained by resonance analysis was truncated to reduce the size of covariance data, but it caused unacceptable large uncertainty in fission cross section. Instead of the resonance parameter covariance, JENDL-4.0u adopts the cross-section covariance calculated with full covariance matrix, which should be identical to ENDF/B-VII.1. Fully new evaluation of covariance data for Pb isotopes was performed to meet the needs from accelerator driven system (ADS). They were also released as JENDL-4.0u.

3.2 JENDL-5

Concerning development of the next general-purpose file JENDL-5, evaluations for light nuclei and structure material are in progress. To improve nuclear data of light nuclei, a new R-matrix resonance analysis code AMUR has been developed and applied for several isotopes of O and F. The nuclear model calculation code CCONE has been used for evaluation for structure materials such as Cu, Nb and Zr. JENDL-5 is planned to complete data for the nuclei with natural abundance. Addition of covariance data will be one of the main targets of JENDL-5. The covariance data for light nuclei and structure material, which are deficient in JENDL-4.0, will be added as possible. As for the light nuclei, the AMUR code will be used for the covariance evaluation as well as cross section evaluation in the resonance region.

4. Conclusion

After the release of JENDL-4.0, we have developed several special purpose files. Among them, three nuclear reaction data files of JENDL-4.0/HE, JENDL/PD-2016 and JENDL/AD-2017 have been created to meet needs of nuclear data from various fields such as accelerator application and decommissioning of nuclear facilities. To correct errors and to feed covariance data in JENDL-4.0, JENDL-4.0u was created and 38 files have been released. As the next version of JENDL-4.0, development of JENDL-5 is in progress. JENDL-5 is planned to be released in FY 2021. It will include new evaluated data for light nuclei and structure materials with covariance data. Data of the fission products and the actinides will be revised as well.

References

[1] K. Shibata, O. Iwamoto, T. Nakagawa, N. Iwamoto, A. Ichihara, S. Kunieda, S. Chiba, K. Furutaka, N. Otuka, T. Ohsawa, T. Murata, H. Matsunobu, A. Zukeran, S. Kamada, and J. Katakura, "JENDL-4.0: A New Library for Nuclear Science and Engineering," *J. Nucl. Sci. Technol.*, **48**(1), 1-30 (2011).

[2] J. Katakura, "JENDL FP Decay Data File 2011 and Fission Yields Data File 2011", JAEA-Data/Code 2011-025 (2012).

[3] S. Kunieda et al., "Overview of JENDL-4.0/HE and benchmark calculation", JAEA-Conf 2016-004,

pp. 41-46 (2016).

[4] J. Katakura and F. Minato, “JENDL Decay Data File 2015”, JAEA-Data/Code 2015-030 (2016).

[5] N. Iwamoto, K. Kosako, T. Murata, “Photonuclear Data File”, JAEA-Conf 2016-004, pp. 53-58 (2016).

[6] K. Shibata, N. Iwamoto, S. Kunieda, F. Minato, O. Iwamoto, “Activation Cross-section File for Decommissioning of LWRs”, JAEA-Conf 2016-004, pp. 47-52 (2016).

[7] https://wwwndc.jaea.go.jp/jendl/j40/update/ (accessed 2018-04-01).

[8] S. Kunieda, “Status of the R-matrix Code AMUR toward a consistent cross-section evaluation and covariance analysis for the light nuclei”, *EPJ Web of Conferences,* 146, 12029 (2017).

[9] O. Iwamoto, “Development of a Comprehensive Code for Nuclear Data Evaluation, CCONE, and Validation Using Neutron-Induced Cross Sections for Uranium Isotopes”, *J. Nucl. Sci. Technol.*, **44**(5), pp. 687-698 (2007).

[10] O. Iwamoto, N. Iwamoto, S. Kunieda, F. Minato, K. Shibata, “The CCONE Code System and its Application to Nuclear Data Evaluation for Fission and Other Reactions”, *Nucl. Data Sheets,* 131, 259 (2016).

[11] O. Iwamoto, K. Shibata, N. Iwamoto, S. Kunieda, F. Minato, A. Ichihara and S. Nakayama, “Status of the JENDL project”, *EPJ Web of Conferences*, 146, 02005 (2017).

[12] O. Iwamoto, “Extension of a nuclear reaction calculation code CCONE toward higher incident energies — multiple preequilibrium emission, and spectrum in laboratory system”, *J. Nucl. Sci. Technol.*, **50**(4), pp. 409-418 (2013).

[13] O. Iwamoto, “Progress in Developing Nuclear Reaction Calculation Code CCONE for High Energy Nuclear Data Evaluation”, *Nucl. Data Sheets,* 118, 204 (2014).

[14] S. Kunieda, S. Chiba, K. Shibata, A. Ichihara, E. Sh. Sukhovitskii, “Coupled-channels Optical Model Analyses of Nucleon-induced Reactions for Medium and Heavy Nuclei in the Energy Region from 1 keV to 200 MeV”, *J. Nucl. Sci. Technol.*, **44**(6), pp. 838-852 (2007).

[15] T. Fukahori, “ALICE-F Calculation of Nuclear Data up to 1 GeV”, JAERI-M 92-039, pp.114–122 (1992).

[16] https://wwwndc.jaea.go.jp/ftpnd/jendl/jact10.html (accessed 2018-04-01).

This is a blank page.

16 Nuclear fission properties of actinide isotopes investigated by Langevin equation

Y. Miyamoto[1], Y. Aritomo[1], S. Tanaka[1], K. Hirose[2] and K. Nishio[2]

[1]*Faculty of Science and Engineering, Kindai University Higashiosaka 577-8502, Japan*

[2]*Advanced Science Research Center, Japan Atomic Energy Agency (JAEA), Tokai, Ibaraki 319-1195, Japan*

Contact e-mail: yuuya.miyamoto.kindai@gmail.com

Abstract

Fission fragment mass distributions (FFMDs) for actinide nuclides at low excitation energies were investigated using the dynamical model (3D Langevin) with the potential energy surface obtained by two center shell model. The FFMDs for several actinide nuclides (U, Np, Pu, Cm, Bk, Cf), taken at the JAEA tandem facility, are well reproduced only by adjusting the neck parameter. The systematics of the neck parameter was adopted to calculate the FFMDs of fermium isotopes.

1. Introduction

The mass-asymmetry shape of fission fragment mass distribution (FFMD) has been observed for the fission in the light actinide nuclides like uranium. It is clear we can explain only mass symmetric fission from the liquid drop model (LDM) [3], hence the mass-asymmetric fission is thought to be associated with the shell effect [9]. However, in the heavy actinide region like fermium, transition from asymmetric fission to the sharp symmetric fission is found. A possible qualitative interpretation is that two identical nuclei around the doubly magic nuclei ^{132}Sn having nearly the spherical shape are generated in the fission process.

In this study, we analyzed isotope dependence of fission properties in fermium isotopes. We calculated the FFMDs for $^{250\text{-}260}$Fm from the low excited states with the calculation model developed in Ref [21], and we studied neck parameter dependence for calculating FFMDs in Fm isotopes.

2. Framework

We use the fluctuation-dissipation model and employ the Langevin equations to investigate the dynamics of the fission process. The nuclear shape is defined by the two-center parametrization, which has three deformation parameters, z_0, δ, and α to serve as collective coordinates: z_0 is the distance between two potential centers, while $\alpha = (A_1 - A_2)/(A_1 + A_2)$ is the mass asymmetry of the two fragments, where A_1 and A_2 denote the mass numbers of heavy and light fragments [19,23], respectively. The symbol δ denotes the deformation of the fragments.

The detail of the definition is explained as $\delta = 3(a - b)/(2a + b)$, where a and b are the half length of axes of an ellipse in the z_0 and directions of the cylindrical coordinate. We assume in this work that each fragment has the same deformation.

To reduce the computational time, we employ the coordinate z defined as $z = z_0/(R_{CN}B)$, where R_{CN} denotes the radius of a spherical compound nucleus and B is defined as $B = (3 + \delta)/(3 - 2\delta)$. It is argued that the neck parameter $\varepsilon = 0.35$ can account for the fission of actinide nucleus [24]. The neck parameter ε is the ratio of smoothed potential height to the original one where two harmonic oscillator potentials cross each other.

In the present work, however, it was found that the parameter should change with mass of fissioning nuclides as explained below.

The potential energy is defined as a sum of the liquid-drop part V_{LD} and microscopic shell-energy correction E^0_{shell}, where smearing of the shells as a function of temperature of the system was considered. The multidimensional Langevin equations [19] are given as,

$$\frac{\partial q_i}{\partial t} = m^{-1}_{ij} p_j$$

$$\frac{\partial q_i}{\partial t} = -\frac{\partial V}{\partial q_i} - \frac{1}{2}\frac{\partial}{\partial q_i} m^{-1}_{jk} p_j p_k - \gamma_{ij} m^{-1}_{jk} p_k + g_{ij} R_j(t) \qquad (1)$$

where $i = \{z, \delta, \alpha\}$ and $p_i = m_{ij} dq_j/dt$ is a momentum conjugate to coordinate q_i. The sum is taken over repeated indices. In the Langevin equation, m_{ij} and γ_{ij} are the shape-dependent collective inertia and the friction tensors, respectively. The wall-and-window one-body dissipation [26-28] is adopted for the friction tensor. A hydrodynamical inertia tensor is adopted with the Werner-Wheeler approximation for the velocity field [29]. The normalized random force $R_i(t)$ is assumed to be that of white noise, i.e., $R_i(t) = 0$ and $R_i(t_1)R_j(t_2) = 2\delta_{ij}\delta(t_1 - t_2)$. The strength of the random force gij is given by the Einstein relation $\gamma_{ij}\mathrm{T} = \sum_k g_{ij} g_{jk}$. The fission events are determined in our model calculation by identifying the different trajectories in the deformation space.

3. Results

First, we investigated the FFMDs of nuclides ranging from uranium to californium, in order to see the predictive power of the present model. The calculation using the neck parameter $\varepsilon = 0.35$ reasonably explains the FFMDs for Th, Pa, and U isotopes [29,30].

The results for heavier element isotopes (U, Pu, Am, Cm, Bk, and Cf), however, do not reproduce the data. To give a reasonable agreement, the neck parameter ε must be increased with the mass of fissioning nucleus. Examples of the parameters dependence of the FFMD are shown in Fig.1, where the calculated results with different parameters are compared with the measured FFMDs at excitation energy of ~15MeV.

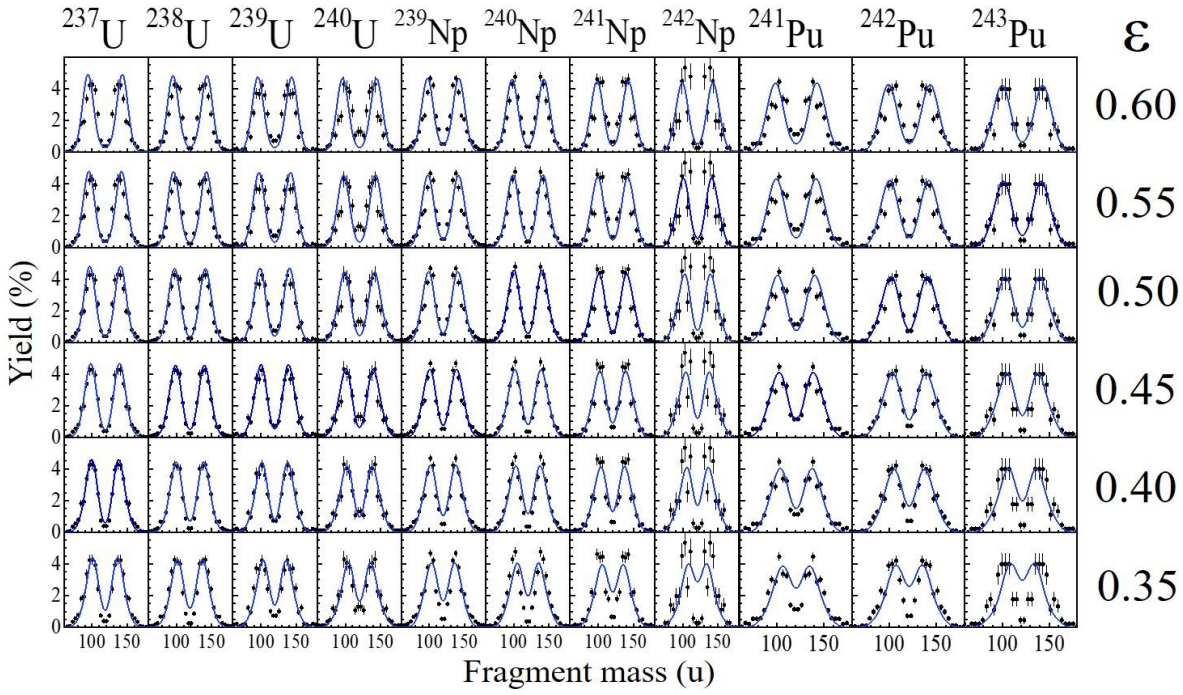

Fig. 1. Experimental FFMDs (points and error bars) of the U, Np, Pu isotopes and excitation energy om the range of 10-20MeV [30]. The experimental FFMDs are compared with Langevin calculations (color online) and their dependence on neck parameter ε in the range of $\varepsilon = 0.35$-0.60 (U, Np, Pu) is investigated.

From the comparison between calculated and experimental mass distributions, we found the optimum ε value to reproduce the experimental results. It was investigated by using the chi-squared method.

The chi-squared value is defined as,

$$\chi^2 = \frac{\sum_1^N (\frac{Y_{ex} - Y_{cal}}{\sigma_{ex}})^2}{N} \quad (2)$$

where Y_{ex} and Y_{cal} are each experiment and calculated yield values, respectively. The σ_{ex} is the uncertainty in the experimental value. N is the number of data. The χ^2 values as a function of ε can be expressed as,

$$\chi^2 = C\varepsilon^2 + B\varepsilon + A. \quad (3)$$

The ε value was chosen to give minimum value in (3).

We found that the optimum ε value to reproduce experimental data is proportional to mass of nuclei. Following the systematics for ε values, the calculation was extended to the fission of fermium isotopes, $^{250\text{-}260}$Fm, from low excitation energies.

While this calculation cannot be directory compared to spontaneous fission data, we found two interesting results in the calculation.

One is isotope dependence. Focusing on $E^* = 7.0\text{MeV}$, in this range, sharp drastic transition from asymmetric to symmetric fission occurs in between ^{254}Fm and ^{256}Fm. Next, calculated FFMDs results of Fm isotopes are very sensitive to excitation energy, which forms large difference from the fission of lighter-element actinide nuclides.

4. Summary and Outlook

In this work, we studied different fission modes of Fm isotopes. We successfully reproduced experimental data of fission fragment mass distribution (U, Np, Pu, Cm, Bk, Cf isotopes) by incorporating the mass dependence of the neck parameter in the calculations. Our future works are the following:

(i) Detailed analysis of the change of FFMDs in the region of Fm.
(ii) Extending the calculation to heavier-element and neutron-rich isotopes.

Furthermore, we are planning to extend this calculation to total kinetic energy distribution, deformation distribution of fission fragment, time dependent parameter trajectory on potential energy surface. We think that this procedure contributes to understanding the nuclear fission mechanism more realistically.

Acknowledgments

The authors are grateful to Prof. M. Ohta of Konan University, and Dr. A. Iwamoto, Dr. M. Asai, Dr. R. Orlandi, Dr. M.J. Vermeulen, Dr. H. Koura and Dr. Y. Nagame of JAEA for fruitful discussions. The Langevin calculations have been done using the cluster computer system (Kindai-VOSTOK) which is supported by "Research funds for External Fund Introduction (2015-16)" by Kindai University.

References

[1] O. Hahn and F. Straßmann, Naturwissenschaften 27, 11 (1939).
[2] L. Meitner and O.R. Frisch, Nature (London) 143, 239 (1939).
[3] N. Bohr and J. A. Wheeler, Phys. Rev. 56, 426(1939).
[4] D.C. Hoffman and M.R. Lane, Radiochamica Acta 70/71, 135 (1995).
[5] E.K. Hulet et al., Phys. Rev. C 40, 770 (1989).
[6] V.F. Apalin et al., Nucl. Phys. 71, 553 (1965).
[7] K. Nishio et al., Nucl. Phys. A 632, 540 (1998).
[8] T. Ohsawa, J. Nucl. Radiochem. Sci. 9, 19 (2008).
[9] V. M. Strutinsky, Nucl. Phys. 3, 449 (1966); Nucl. Phys. A95, 420 (1967); Nucl. Phys. A122, 1 (1968).
[10] P. Moller, J.R. Nix and W.J. Swiatecki, Nucl. Phys. A469, 1 (1987).
[11] U. Brosa, S. Großmann, and A. Muller, Phys. Rep. 197, 167 (1990).
[12] P. Moller, D.G. Madland, A.J. Sierk and A. Iwamoto, Nature (London) 409, 785 (2001).
[13] P. Moller, A.J. Sierk, T. Ichikawa, A. Iwamoto, R. Bengtsson, H. Uhrenholt and S. Aberg, Phys. Rev. C 79, 064304 (2009).
[14] Y. Abe, C. Gregoire and H. Delagrange, J. de. Physique C47, 4 (1986).
[15] I.I. Gontchar, G.I. Kosenko, N.I. Pischasov and O.I. Serdyuk, Yad. Fiz. 55, 920 (1992).
[16] T. Wada, Y. Abe and N. Carjen, Phys. Rev. Lett. 7, 3538 (1993).
[17] P. Frobrich and I.I. Gontchar, Nucl. Phys. A563, 326 (1993).
[18] T. Asano, T. Wada, M. Ohta, T. Ichikawa, S. Yamaji, and H. Nakahara, J. Nucl. Radiochem. Sci. 5, 1 (2004).
[19] Y. Aritomo and M. Ohta, Nucl. Phys. A 744, 3 (2004).
[20] Y. Aritomo, K. Hagino, K. Nishio, and S. Chiba, Phys. Rev. C 85, 044614 (2012).
[21] Y. Aritomo and S. Chiba, Phys. Rev. C 88, 044614 (2013).
[22] Y. Aritomo, S. Chiba and F. Ivanyuk, Phys. Rev. C 90, 054609 (2014).
[23] J. Maruhn and W. Greiner, Z. Phys. 251, 431 (1972).

[24] K. Sato, A. Iwamoto, K. Harada, S. Yamaji, and S. Yoshida, Z. Phys. A 288, 383 (1978).
[25] H.J. Krappe, J.R. Nix, and A.J. Sierk, Phys. Rev. C 20, 992 (1979).
[26] J. Blocki, Y. Boneh, J.R. Nix, J. Randrup, M. Robel, A.J. Sierk, and W.J. Swiatecki, Ann. Phys. 113, 330 (1978).
[27] J.R. Nix and A.J. Sierk, Nucl. Phys. A 428, 161c (1984).
[28] H. Feldmeier, Rep. Prog. Phys. 50, 915 (1987).
[29] R. Leguillon, K. Nishio, K. Hirose, H. Makii, I. Nishinaka, R. Orlandi, K. Tsukada, J. Smallcombe, S. Chiba, Y. Aritomo, T. Ohtsuki, R. Tatsuzawa, N. Takaki, N. Tamura, S. Goto, I. Tsekhanovich, C. M. Petrache, and A. N. Andreyev, Phys. Lett. B 761, 125 (2016).
[30] K. Hirose, K. Nishio, S. Tanaka, R. Leguillion, H. Makii, I. Nishinaka, R. Orlandi, K. Tsukada, J. Smallcombe, M.J. Vermeulen, S. Chiba, Y. Aritomo, T. Ohtsuki, K. Nakano, S. Araki, Y. Watanabe, R. Tatsuzawa, N. Takaki, N. Tamura, S. Goto, I. Tsekhanovich, and A. N. Andreyev, Phys. Rev. Lett. 119, 222501 (2017).
[31] K.T.R. Davies, A.J. Sierk, and J.R. Nix, Phys. Rev. C 13, 2385 (1976).

17 Reaction study of ^{136}Xe on proton, deuteron and carbon at 168 *A*MeV

X. Sun [a], H. Wang [a] , H. Otsu [a], H. Sakurai [a], D.S. Ahn [a], M. Aikawa [b], P. Doornenbal [a], N. Fukuda [a], T. Isobe [a], S. Kawakami [c], S. Koyama [d], T. Kubo [a], S. Kubono [a], G. Lorusso [a], Y. Maeda [c], A. Makinaga [e], S. Momiyama [d], K. Nakano [f], M. Niikura [d], Y. Shiga [g, a], P.-A. Söderström [a], H. Suzuki [a], H. Takeda [a], S. Takeuchi [a], R. Taniuchi [d, a], Ya. Watanabe [a], Yu. Watanabe [f], H. Yamasaki [d], K. Yoshida [a]

[a] *RIKEN Nishina Center, 2-1 Hirosawa, Wako, Saitama 351-0198, Japan*

[b] *Faculty of Science, Hokkaido University, Sapporo 060-0810, Japan*

[c] *Department of Applied Physics, University of Miyazaki, Miyazaki 889-2192, Japan*

[d] *Department of Physics, University of Tokyo, 7-3-1 Hongo, Bunkyo, Tokyo 113-0033, Japan*

[e] *Graduate School of Medicine, Hokkaido University, North-14, West-5, Kita-ku, Sapporo 060-8648, Japan*

[f] *Department of Advanced Energy Engineering Science, Kyushu University, Kasuga, Fukuoka 816-8580, Japan*

[g] *Department of Physics, Rikkyo University, 3-34-1 Nishi-Ikebukuro, Toshima, Tokyo 171-8501, Japan*

Email: xiaohui.sun@riken.jp

Cross sections of ^{136}Xe on proton, deuteron and carbon were measured at 168 *A*MeV in inverse kinematics at the RIKEN Radioactive Isotope Beam Factory. The target dependence was investigated systematically. Our experiment data are compared with the reactions of ^{136}Xe + *p* at energies of 200 *A*MeV, 500 *A*MeV and 1000 *A*MeV in order to investigate the energy dependence of the cross sections on proton. The experimental results are also compared with semi-empirical parameterization SPACS and EPAX formula.

Keyword: spallation reaction, ^{136}Xe, target dependence, energy dependence

1. Introduction

Spallation reactions have been attracting much interest both for fundamental research and applications. In fundamental research, spallation reactions have been employed worldwide to produce unstable nuclei [1,2]. In the field of applications, spallation reactions are one of the possible mechanisms for nuclear waste transmutation in accelerator-driven systems [3]. In particular, it has been suggested that spallation could be utilized to transmute long-lived fission products (LLFP) to stable or short lived isotopes [4-6]. For both aspects, their systematic interpretation based on nuclear reaction theory of spallation reaction mechanism is critical.

Spallation and/or fragmentation of ^{136}Xe is essential to address these two questions. This is because ^{136}Xe is used as a primary beam worldwide to produce unstable beams in heavy ion accelerator facilities. For transmutation, ^{136}Xe is a stable isotope, neighboring with the LLFP ^{137}Cs, of which the experiment studies are quite scarce. Therefore, comparison between these two isotopes is critical to clarify the reaction mechanism and will be a good benchmark for checking the validity of theoretical calculations, which were performed for LLFP ^{137}Cs, ^{90}Sr [4], ^{107}Pd [5] and ^{93}Zr [6]. Several experiments have been performed for spallation reactions of ^{136}Xe [7-10]. Aiming at a comprehensive understanding of spallation of ^{136}Xe, we have studied proton-, deuteron- and carbon-induced reactions at 168 *A*MeV for target dependence. Together with previous studies at high energies [7-9], energy dependence has also been investigated in the present work.

2. Experiment

The experiment was performed at the RIKEN Radioactive Isotope Beam Factory operated by RIKEN Nishina Center and the Center for Nuclear Study, University of Tokyo. The secondary beams were produced by in-flight fission of ^{238}U beam at 345 *A*MeV incident on a 1-mm-thick ^{9}Be target. The particles in the secondary beams were identified event by event by measuring the time of flight (TOF), the magnetic rigidity ($B\rho$), and the energy loss (ΔE) [11]. The atomic number Z and the mass-to-charge ration A/Q were deduced from the TOF-ΔE and $B\rho$-TOF correlations, respectively. Three targets, CH_2 (179.2 mg/cm^2), CD_2 (217.8 mg/cm^2) [12], and C (226.0 mg/cm^2) were used to induce secondary reactions. An empty target (frame without target material) run was measured in order to subtract the background contribution. The energy of the ^{136}Xe beam was 168 *A*MeV at the center of secondary targets. The average intensity of the ^{136}Xe beam was 2.6×10^3 particles per second. The reaction products were analyzed by the ZeroDegree spectrometer and particles were identified event by event using $B\rho$-TOF-ΔE method in a similar way to BigRIPS. In order to cover a wide range of fragments, several different $B\rho$ settings were applied to the ZeroDegree spectrometer: -9%, -6%, -3%, 0%, and +3% relative to the $B\rho$ value of the secondary beam.

A particle identification plot of the reaction products produced from ^{136}Xe on CH_2 target for -6% $B\rho$ setting is shown in Fig. 1. In this setting, the transport of ^{128}Xe was optimized for the ZeroDegree spectrometer. The typical A/Q and Z resolutions were 6.1×10^{-3} (FWHM) and 0.52 (FWHM), respectively. For the reaction products, the fraction of the fully stripped ($Q = Z$) ions was about 66.5% for Xe isotope through ZeroDegree spectrometer.

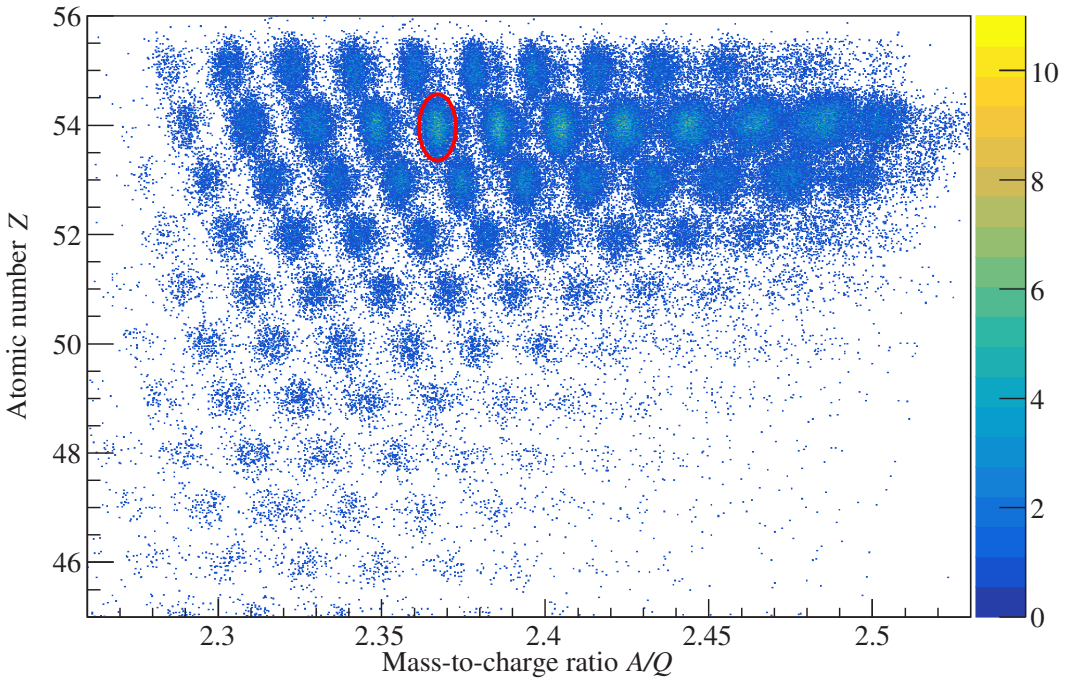

Fig. 1. Two-dimensional particle identification plot of Z versus A/Q for the reaction residues produced from ^{136}Xe and detected by the ZeroDegree spectrometer. The red circle indicates ^{128}Xe to guide the eye.

3. Results and discussion

The isotopic distributions of cross sections obtained in the present work for the ^{136}Xe + p, ^{136}Xe + d and ^{136}Xe + C reactions at 168 *A*MeV are plotted in Fig. 2. The cross sections on proton and deuteron were deduced from the respective CH_2 and CD_2 targets after subtracting contributions from carbon (using data from the C target run) and beam-line materials (using

data from the empty-target run). The cross sections on carbon target were deduced from the carbon target after subtracting the background from empty-target runs.

The distribution of cross sections on carbon and deuteron are agree with each other for the four elements shown in Fig. 2. The Cs isotopes in Fig. 2 (a) are produced by the charge-exchange reactions $\Delta Z = +1$. For this reaction channel, the value of the reaction cross sections on carbon (σ_C) are similar to those for deuteron (σ_d), while proton-induced ones (σ_p) are larger than both σ_C and σ_d. Such target dependence of the cross sections in charge-exchange reactions is also reported in the studies of ^{137}Cs and ^{90}Sr at 185 *A*MeV [4] and ^{136}Xe at 500 *A*MeV [10]. For Xe isotopes, σ_d is similar to σ_p, and both of them are larger than σ_C in general. For I and Te isotopes, σ_p becomes smaller than both σ_d and σ_C. In addition, the difference between σ_p and σ_d (σ_C) is getting larger towards neutron-deficient side within the same isotopic chain. This is because the excitation energy gained by pre-fragments on deuteron is higher, resulting in more nucleons emitted compared to the reaction on proton. This kind of behavior is in agreement with ^{136}Xe at 500 *A*MeV [10]. The difference between σ_p and σ_d is relatively smallsa compared with that at 168 *A*MeV.

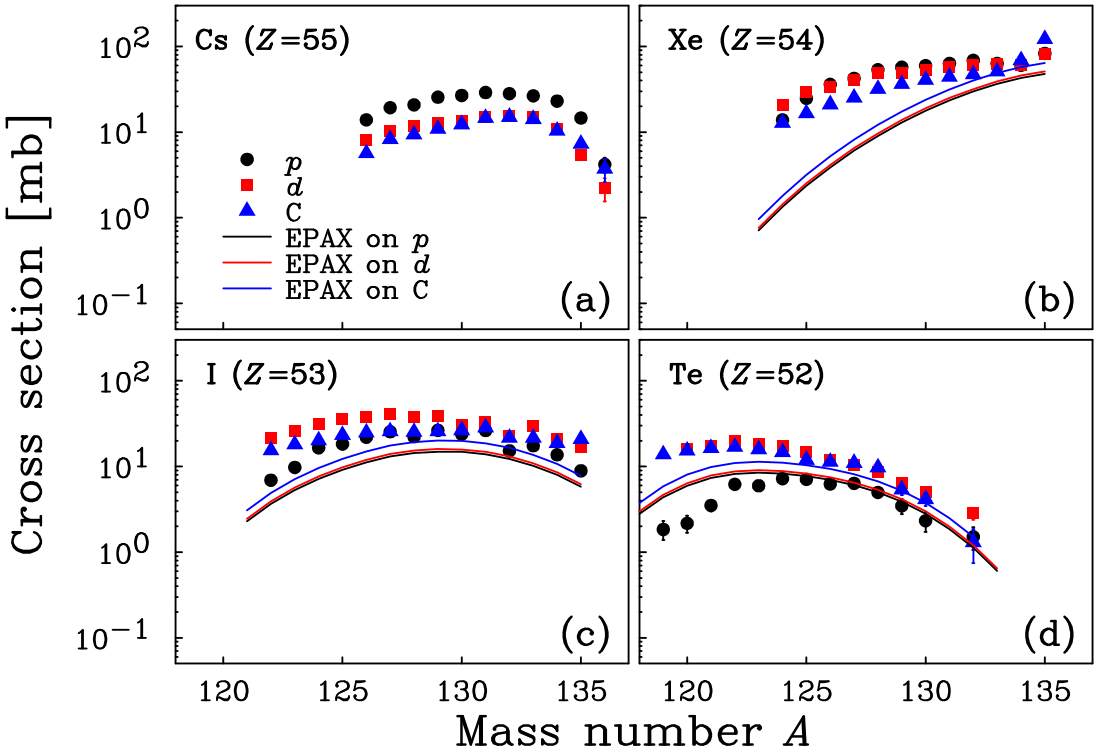

Fig. 2. Isotopic distribution of the cross sections for products from cesium element to tellurium element produced in the reaction ^{136}Xe + *p* (circle), ^{136}Xe + *d* (square) and ^{136}Xe + C (triangle) at 168 *A*MeV. The dot-dashed line represents the calculations of parameterization SPACS on proton. The solid blue, black and red lines represent the calculations of EPAX formula on carbon, proton and deuteron target, respectively. The error bar in the figure shows the statistical uncertainties.

The calculations of the semi-empirical parameterization SPACS [13] and EPAX formula [14] are also plotted in Fig. 2 to compare with the experimental results. For proton-induced reactions, the SPACS calculation reproduced the overall shape of isotopic distribution. It overestimates the cross sections on the neutron-rich side for the I, Te and Sb isotopes, and underestimates the cross sections on the neutron-deficient side for the Cs and Xe isotopes. Such

overestimation was also found in the reactions of ^{137}Cs and ^{90}Sr on proton at 185 *A*MeV [4]. The EPAX calculation on proton underestimates the cross sections for Xe and I isotopes, which is also found in Ref. [4]. EPAX calculations on carbon underestimated the cross sections, especially in the neutron-deficient side. Similar behavior has been observed for ^{86}Kr on ^{9}Be and ^{181}Ta target as reported in Ref. [15]

The isotopic cross sections of the reaction ^{136}Xe + *p* at different reaction energies are shown in Fig. 3 to investigate the energy dependence. For charge exchange reactions in Fig. 3 (a), the cross sections decrease when the reaction energy increases. Such behavior for charge-exchange reactions has also been observed in the studies for ^{197}Au [16] and ^{72}Ge [17]. In panels (b) - (d) in Fig. 3, the coverage of isotopic distribution is wider at higher reaction energy. For the Xe isotopes, for the products with mass number close to the projectile, the cross sections increase when the reaction energy decreases. For the I and Te isotopes, on the neutron-deficient side, the cross sections become larger at high reaction energy. This is because more energy is deposited in the pre-fragment, resulting in a large production of products in the neutron-deficient side by evaporating more nucleons.

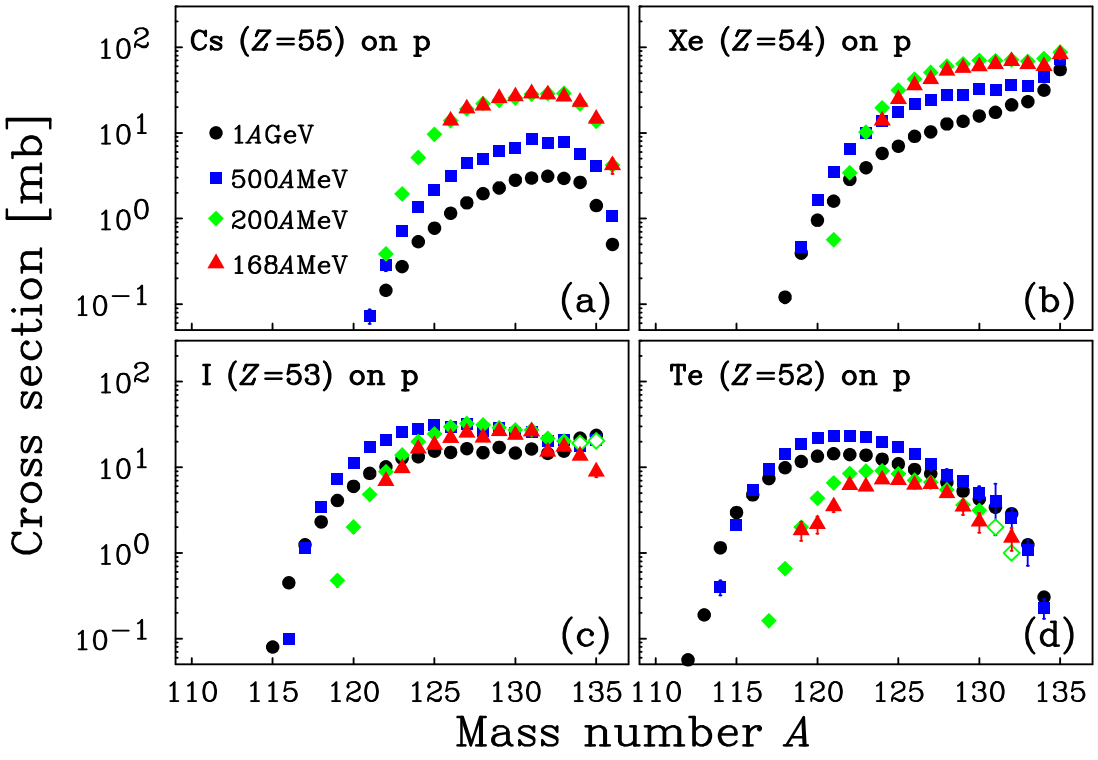

Fig.3. Isotopic distributions of the cross sections measured in the reaction of ^{136}Xe + *p* at 1000 *A*MeV [7] (black), 500 *A*MeV [8] (blue), 200 *A*MeV [9] (green) and 168 *A*MeV (red). Empty diamonds at 200 *A*MeV represent extrapolated values.

4. Summary

Cross sections for ^{136}Xe on proton, deuteron and carbon at 168 *A*MeV have been measured in inverse kinematics technique. It was found that the shape of isotopic cross sections on deuteron and carbon are similar. In case of the charge exchange reaction channel, the cross sections decrease when the reaction energy increases. The cross sections are larger at high reaction energy for light products because of the high excitation energy of pre-fragments. The experimental results have been compared with SPACS and EPAX calculations, and SPACS calculation reproduced the overall tendency of the isotopic cross sections. In future, our

experimental results will be compared with the model calculations of PHITS [18] which was widely used to describe the spallation reaction of LLFP nuclei [4-6]. Such a comparison will be very useful to check the validity of PHITS for both stable nuclei and LLFP.

Acknowledgements

We express our gratitude to the accelerator staff of the RIKEN Nishina Center for providing the ^{238}U beam. This work was supported by ImPACT Program of Council for Science, Technology and Innovation (Cabinet Office, Government of Japan).

References

[1] H. Suzuki, T. Kubo, N. Fukuda, N. Inabe, D. Kameda, H. Takeda, K. Yoshida, K. Kusaka, Y. Yanagisawa, M. Ohtake, H. Sato, Y. Shimizu, H. Baba, M. Kurokawa, T. Ohnishi, K. Tanaka, O. B. Tarasov, D. Bazin, D. J. Morrissey, B. M. Sherrill, K. Ieki, D. Murai, N. Iwasa, A. Chiba, Y. Ohkoda, E. Ideguchi, S. Go, R. Yokoyama, T. Fujii, D. Nishimura, H. Nishibata, S. Momota, M. Lewitowicz, G. DeFrance, I. Celikovic, K. Steiger. Production cross section measurements of radioactive isotopes by BigRIPS separator at RIKEN RI Beam Factory. 2013. Nov. 317:756-768.

[2] J. Benlliure, M. Fernández Ordóñez, L. Audouin, A. Boudard, E. Casarejos, J. E. Ducret, T. Enqvist, A. Heinz, D. Henzlova, V. Henzl, A. Kelic, S. Leray, P. Napolitani, J. Pereira, F. Rejmund, M. V. Ricciardi, K.-H. Schmidt, C. Schmitt, C. Stéphan, L. Tassan-Got, C. Volant, C. Villagrasa, and O. Yordanov. Production of medium-mass neutron-rich nuclei in reactions induced by ^{136}Xe projectiles at 1 *A*GeV on a beryllium target. Phys. Rev. C. 2008 Nov. 78: 054605.

[3] C.D. Bowman, E.D. Arthur, P.W. Lisowski, G.P. Lawrence, R.J. Jensen, J.L. Anderson, B. Blind, M. Cappiello, J.W. Davidson, T.R. England, L.N. Engel, R.C. Haight, H.G. Hughes III, J.R. Ireland, R.A. Krakowski, R.J. LaBauve, B.C. Letellier, R.T. Perry, G.J. Russell, K.P. Staudhammer, G. Versamis and W.B. Wilson. Nuclear energy generation and waste transmutation using an accelerator-driven intense thermal neutron source. Nucl. Instrum. Methods Phys. Res. A. 1992 Jan. 320:336-367.

[4] H. Wang, H. Otsu, H. Sakurai, D.S. Ahn, M. Aikawa, P. Doornenbal, N. Fukuda, T. Isobe, S. Kawakami, S. Koyama, T. Kubo, S. Kubono, G. Lorusso, Y. Maeda, A. Makinaga, S. Momiyama, K. Nakano, M. Niikura, Y. Shiga, P.-A. Söderström, H. Suzuki, H. Takeda, S. Takeuchi, R. Taniuchi, Ya. Watanabe, Yu. Watanabe, H. Yamasaki, K. Yoshida. Spallation reaction study for fission products in nuclear waste: Cross sections measurements fro ^{137}Cs and ^{90}Sr on proton and deuteron. Phys. Lett. B. 2016 Jan; 754: 104-108.

[5] He Wang, Hideaki Otsu, Hiroyoshi Sakurai, DeukSoon Ahn, Masayuki Aikawa, Takashi Ando, Shouhei Araki, Sidong Chen, Nobuyuki Chiga, Pieter Doornenbal, NaokiFukuda1, Tadaaki Isobe, ShunsukeKawakami, ShoichiroKawase, TadahiroKin, Yosuke Kondo, Shunpei Koyama, Shigeru Kubono, Yukie Maeda, Ayano Makinaga, Masafumi Matsushita, Teiichiro Matsuzaki, Shin'ichiro Michimasa, Satoru Momiyama, Shunsuke Nagamine, Takashi Nakamura, Keita Nakano, Megumi Niikura, Tomoyuki Ozaki, Atsumi Saito, Takeshi Saito,Yoshiaki Shiga, Mizuki Shikata, YoheiShimizu, Susumu Shimoura, Toshiyuki Sumikama, Pär-Anders Söderström, HiroshiSuzuki, Hiroyuki Takeda, Satoshi Takeuchi, Ryo Taniuchi, Yasuhiro Togano, JunichiTsubota, Meiko Uesaka,YasushiWatanabe,YukinobuWatanabe, KathrinWimmer, TatsuyaYamamoto. Spallation reaction study for the long-lived fission product ^{107}Pd. Prog. Theor. Exp. Phys. 2017 Apr, 021D01.

[6] Shoichiro Kawase, Keita Nakano, Yukinobu Watanabe, He Wang, Hideaki Otsu, Hiroyoshi Sakurai, Deuk SoonAhn, Masayuki Aikawa, TakashiAndo, Shouhei Araki, Sidong Chen, Nobuyuki Chiga, Pieter Doornenbal, Naoki Fukuda, Tadaaki Isobe, Shunsuke Kawakami, Tadahiro Kin,Yosuke Kondo, Shunpei Koyama, Shigeru Kubono,Yukie Maeda, Ayano Makinaga, Masafumi Matsushita, Teiichiro Matsuzaki, Shin'ichiro Michimasa, Satoru Momiyama, Shunsuke Nagamine, Takashi Nakamura, Megumi Niikura, Tomoyuki Ozaki, Atsumi Saito, Takeshi Saito, Yoshiaki Shiga, Mizuki Shikata, Yohei Shimizu, Susumu Shimoura, Toshiyuki Sumikama, Pär-Anders Söderström, Hiroshi Suzuki, Hiroyuki Takeda, Satoshi Takeuchi, Ryo Taniuchi, Yasuhiro Togano, Jun'ichi Tsubota, Meiko Uesaka, YasushiWatanabe, KathrinWimmer, TatsuyaYamamoto and KoichiYoshida. Study of proton- and deuteron-induced spallation reactions on the long-lived fission product 93Zr at 105 MeV/nucleon in inverse kinematics. Prog. Theor. Exp. Phys. 2017 Sep, 093D03.

[7] P. Napolitani, K.-H. Schmidt, L. Tassan-Got, P. Armbruster, T. Enqvist, A. Heinz, V. Henzl, D. Henzlova, A. Kelíc, R. Pleskač, M. V. Ricciardi, C. Schmitt, O. Yordanov, L. Audouin, M. Bernas, A. Lafriaskh, F. Rejmund, C. Stéphan, J. Benlliure, E. Casarejos, M. Fernandez Ordonez, J. Pereira, A. Boudard, B. Fernandez, S. Leray, C. Villagrasa, and C. Volant. Measurement of the complete nuclide production and

kinetic energies of the system ^{136}Xe+hydrogen at 1 GeV per nucleon. Phys. Rev. C.2007 Dec. 76: 064609.
[8] L. Giot, J.A. Alcántara-Núñez, J. Benlliure, D. Pérez-Loureiro, L. Audouin, A. Boudard, E. Casarejo, T. Enqvist, J.E. Ducret, B. Fernández-Domínguez, M. Fernández Ordóñez, F. Farget, A. Heinz, V. Henzl, D. Henzlova, A. Kelíc-Heil, A. Lafriaskh, S. Leray, P. Napolitani, C. Paradela, J. Pereira, M.V. Ricciardi, C. Stéphan, K.-H. Schmidt, C. Schmitt, L. Tassan-Got, C. Villagrasa, C.Volant, O. Yordanov. Isotopic production cross sections of the residual nuclei in spallation reactions induced by ^{136}Xe projectiles on proton at 500 *A*MeV. Nucl. Phys. A. 2013, Jan. 899: 116-132.
[9] C. Paradela, L. Tassan-Got, J. Benlliure, J. L. Rodríguez-Sánchez, L. Audouin, A. Boudard, E. Casarejos, T. Enqvist, J. E. Ducret, F. Farget, B. Fernández-Domínguez, M. Fernández Ordóñez, L. Giot, A. Heinz, V. Henzl, D. Henzlova, A. Kelíc-Heil, A. Lafriaskh, S. Leray, P. Napolitani, J. Pereira, D. Pérez-Loureiro, M. V. Ricciardi, C. Stéphan, K.-H. Schmidt, C. Schmitt, C. Villagrasa, C. Volant, and O. Yordanov. Isotopic production cross sections of residual nuclei in the spallation reaction ^{136}Xe (200*A* MeV) + *p*. Phys. Rev. C. 2017 Apr; 95: 044606;
[10] J. Alcántara-Núñez, J. Benlliure, C. Paradela, C. Pérez-Loureiro, J. L. Rodíguez-Sánchez, L. Audouin, A. Boudard, E. Casarejos, T. Enqvist, F. Farget, M. Fernández-Ordóñez,1 A. Heinz, V. Henzl, D. Henzlova, A. Kelíc-Heil, A. Lafriaskh, S. Leray, P. Napolitani, J. Pereira, M. V. Ricciardi, C. Stéphan, K.-H. Schmidt, C. Schmitt, L. Tassan-Got, C. Villagrasa, C. Volant, and O. Yordanov. Isotopic yields of spallation residues produced in 136Xe-induced reactions on deuterium at 500 *A*MeV. Phys. Rev. C. 2015 Aug; 92: 024607.
[11] N. Fukuda, T. Kubo, T. Ohnishi, N. Inabe, H. Takeda, D. Kameda, H. Suzuki. Nucl. Instrum. Methods B. 2013 Nov. 317: 323-332.
[12] Y. Maeda, H. Sakai, K. Hatanaka, A. Tamii. Production of thick and highly uniform CD_2 targets for n + d measurements. Nucl. Instrum. Methods A. 2002 Apr. 490: 518-521.
[13] C. Schmitt, K.-H. Schmidt and A. Kelíc-Heil. SPACS: A semi-empirical parameterization for isotopic spallation cross sections. Phys. Rev. C. 2014 Dec. 90: 064605.
[14] K. Sümmerer and B. Blank. Modified empirical parametrization of fragmentation cross sections. Phys. Rev. C. 2000 Dec. 61: 034607
[15] M. Mocko, M. B. Tsang, Z. Y. Sun, N. Aoi, J. M. Cook, F. Delaunay, M. A. Famiano, H. Hui, N. Imai, H. Iwasaki, W. G. Lynch, T. Motobayashi, M. Niikura, T. Onishi, A. M. Rogers, H. Sakurai, A. Stolz, H. Suzuki, E. Takeshita, S. Takeuchi, and M. S. Wallace. Projectile fragmentation of ^{86}Kr at 64 MeV/nucleon. Phys. Rev. C. 2007 July. 76: 014609.
[16] S. B. Kaufman and E. P. Steinberg. Cross-section measurements of nuclides formed by the reaction of 0.20 — 6.0 Gev protons. Phys. Rev. C. 1980. Feb. 22: 167-178.
[17] LARRY B. CavzCa et al., LARRY B. CavzCa and ALBERT A. CARETTO, JR. Study of (*p*, *xn*) Reactions at 400 MeV*. Phys. Rev. 1969 Feb. 178: 1732-1742.
[18] Tatsuhiko Satoa, Koji Niita, Norihiro Matsuda, Shintaro Hashimoto, Yosuke Iwamoto, Shusaku Noda, Tatsuhiko Ogawa, Hiroshi Iwase, Hiroshi Nakashima, Tokio Fukahori, Keisuke Okumura, Tetsuya Kai, Satoshi Chiba, Takuya Furuta and Lembit Sihver. Particle and Heavy Ion Transport code System, PHITS, version 2.52. J.Nucl. Sci. Technol. 2013 Jul. 50: 913.

18 Study of Multi-chance Fission in Dynamical Model calculation

Shoya TANAKA[1], Kentaro HIROSE[2], Katsuhisa NISHIO[2], Yoshihiro ARITOMO[1]

[1]Faculty of Science and Engineering, Kindai University
Higashi-Osaka, Osaka 577-8502, Japan
[2]Advanced Science Research Center, Japan Atomic Energy Agency
Tokai, Ibaraki 319-1195, Japan
e-mail: tanaka.shoya9071@gmail.com

Fission-fragment mass distributions (FFMDs) have not been explained at high excitation energy. It was found that the mass distributions for all studied nuclides maintain a double-humped shape up to the highest measured energy in contrast to experiments of predominantly symmetric fission due to the washing out of nuclear shell effects. To understand this behavior, the fluctuation-dissipation model was used. The result showed that this behavior of the FFMDs was unambiguously attributed to the effect of multi-chance fission.

1. Introduction

The fission process is usually described as an evolution of a nuclear shape on a potential-energy surface, resulting from the interplay of macroscopic nuclear properties and microscopic shell effects. The shape of fission-fragment mass distributions (FFMDs) is directly influenced by nuclear shell effects, a well-known example being the asymmetric FFMD in the thermal-neutron-induced fission of ^{235}U, whereby the compound nucleus ^{236}U fissions at the excitation energy of 6.55 MeV. The asymmetric FFMD, in this case, is attributed to the influence of strong shell effects in the fission fragments in the vicinity of doubly magic ^{132}Sn. With increasing excitation energy, two competing processes are expected to occur. First of all, due to a reduced importance of shell effects, the transition to predominantly symmetric (liquid-drop) type fission should occur, which is indeed demonstrated by many experiments [1]. The other process is multi-chance fission (MCF), or fission after consecutive neutron evaporations, where the fissioning nuclei with less neutrons will have lower excitation energy, thus showing stronger shell effects than in the initial compound nucleus. The latter effect is then supposed to favor the asymmetric fission of typical actinides after neutron evaporation. The MCF concept itself is well known from studies of the fission probability in high-energy neutron-induced reactions, whereby steplike behavior is observed in the fission cross sections at the energies corresponding

to 1n, 2n, … neutron emission (see, for example, Fig. 17 in [2]). It was also reported that the effects of MCF can be seen in the average total kinetic energy [3,4], and in the average energy of the prompt fission neutrons [5], as a function of the excitation energy of the compound nuclei. In contrast to these fission observables, to our knowledge, no experimental study of the effects of MCF on mass distributions has been reported to date. It was only recently that the effect of MCF on mass distributions was introduced in theoretical studies [6–9]. However, the validity of the calculated FFMDs for each fission chance was not shown because of the lack of experimental data. The purpose of this study is an estimation of FFMDs by dynamical model calculation including MCF effects.

2. Model

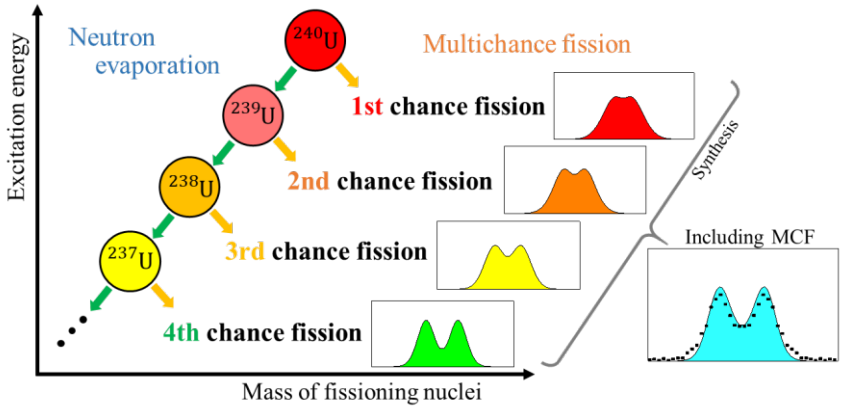

Fig. 1 Schematic diagram of multi-chance fission process.

A calculation procedure of FFMDs with MCF effects can be divided into two steps based on MCF concept, as shown in Fig. 1. At first step, FFMD for each fission chance is calculated by the fluctuation dissipation model. At second step, fraction for each fission chance is calculated by the statistical model using the GEF Model code [7]. FFMDs for each fission chance which multiplied by the fraction are summed to obtain the distribution to be compared with the experimental data.

We use the fluctuation-dissipation model and employ Langevin equations [10] to investigate the dynamics of the fission process. The nuclear shape is defined by the two-center parametrization [11,12], which has three deformation parameters, z_0, δ, and α to serve as collective coordinates: z_0 is the distance between two potential centers, while $\alpha = (A_1 - A_2)/(A_1 + A_2)$ is the mass asymmetry of the two fragments, where A_1 and A_2 denote the mass numbers of heavy and light fragments [10]. The symbol δ denotes the deformation of the fragments, and is defined as $\delta = 3(R_{\parallel} - R_{\perp})/(2R_{\parallel} + R_{\perp})$, where $R_{\parallel}$ and $R_{\perp}$ are the half length of the axes of an ellipse in the z_0 and ρ directions of the cylindrical coordinate, respectively. We use the neck parameter $\varepsilon = 0.35$, which is recommended in Ref. [11] for the

fission process. The three collective coordinates may be abbreviated as q, $q = \{z, \delta, \alpha\}$.

For a given value of a temperature of a system T, the potential energy is defined as a sum of the liquid-drop (LD) part, a rotational energy and a microscopic (SH) part:

$$V(q, l, T) = V_{\mathrm{LD}}(q) + \frac{\hbar^2 l(l+1)}{2I(q)} + V_{\mathrm{SH}}(q, T), \tag{1}$$

$$V_{\mathrm{LD}}(q) = E_{\mathrm{S}}(q) + E_{\mathrm{C}}(q), \tag{2}$$

$$V_{\mathrm{SH}}(q, T) = E^0_{\mathrm{shell}}(q)\Phi(T), \tag{3}$$

$$\Phi(T) = \exp\left(-\frac{aT^2}{E_{\mathrm{d}}}\right). \tag{4}$$

Here, the potential energy V_{LD} is calculated with the finite-range liquid drop model, given as a sum of the surface energy E_{s} [13] and the Coulomb energy E_{c}. The shell correction energy V_{SH} is evaluated by the Strutinski method from the single-particle level of the two-center shell model. The shell correction energy has a temperature dependence expressed by a factor $\Phi(T)$ in which the shell damping energy E_{d} is chosen as 20 MeV [14] and a is the level density parameter. At the zero temperature ($T = 0$), the shell correction energy reduces to that of the two-center shell model values E^0_{shell}. The second term on the right-hand side of Eq. (1) is the rotational energy for an angular momentum l [10], with a moment of inertia at q, $I(q)$.

The multidimensional Langevin equations [10] are given as

$$\frac{dq_i}{dt} = (m^{-1})_{ij} p_j,$$

$$\frac{dp_i}{dt} = -\frac{\partial \mathrm{V}}{\partial q_i} - \frac{1}{2}\frac{\partial}{\partial q_i}(m^{-1})_{jk} p_j p_k - \gamma_{ij}(m^{-1})_{jk} p_k + g_{ij} R_j(t), \tag{5}$$

where $i = \{z, \delta, \alpha\}$ and $p_i = m_{ij} dq_j/dt$ is a momentum conjugate to coordinate q_i. The summation is performed over repeated indices. In the Langevin equation, m_{ij} and γ_{ij} are the shape-dependent collective inertia and the friction tensors, respectively. The wall-and-window one-body dissipation [15] is adopted for the friction tensor which can describe pre-scission neutron multiplicities and total kinetic energy of fragments [16]. A hydrodynamical inertia tensor is adopted with the Werner-Wheeler approximation for the velocity field [17]. The normalized random force $R_i(t)$ is assumed to be that of white noise, i.e., $\langle R_i(t) \rangle = 0$ and $\langle R_i(t_1) R_j(t_2) \rangle = 2\delta_{ij}\delta(\mathrm{t}_1 - \mathrm{t}_2)$. The strength of the random force g_{ij} is given by the Einstein relation $\gamma_{ij} T = \sum_k g_{ij} g_{jk}$.

The fission events are determined in our model calculation by identifying the different trajectories in the deformation space. Fission from a compound nucleus is defined as the case that a trajectory overcomes the scission point on the potential energy surface.

The reduction of the excitation energy of the compound nucleus due to neutron emission was calculated from neutron binding energies [18] and a mean energy for the emitted neutron, ~1.9 MeV, obtained by the PACE2 code [19].

3. Results and discussion

As a summary of all the calculation results, Fig. 2 shows the FFMDs for the twenty-three compound nuclides $^{231\text{-}234}$Th, $^{233\text{-}236}$Pa, $^{234\text{-}240}$U, $^{239\text{-}242}$Np and $^{241\text{-}244}$Pu with the excitation energy range of E^* = 15-55 MeV. A 10 MeV interval of the excitation energy was chosen as a compromise between the available statistics and a reasonable increment of E^*. To understand these trends, the calculation results compared with the experimental FFMDs as [20,21].
At Fig. 2, there are several blanks of experimental data, because the experimental data does not have enough statics.

The calculation taking into account the MCF (red curves in Fig. 2) reproduced the experimental data, and peak position and peak-to-valley (P/V) ratio agree well for all the measured excitation-energy range by including MCF. Isotope dependence of the FFMDs (large P/V ratio for small atomic-number elements) can be also explained. However, the calculation gives a smaller P/V ratio for heavier neptunium (^{241,242}Np) and plutonium ($^{241\text{-}244}$Pu) isotopes in Fig. 2. This is seemed that calculation accuracy of potential energy surface is low. One of the possible reasons for this deviation could be in the treatment of the neck parameter ($0 < \varepsilon < 1$), which denes the depth of the potential at the neck of the dumbbell-shaped nucleus, used in our two-center shell calculation. In this work, we adopted $\varepsilon = 0.35$ derived as an optimal value in to explain the FFMDs of compound nuclei with mass of 234-240. For heavier nuclei, this value could thus be slightly different. This deviation, however, does not influence our conclusion which was drawn from the discussion on the excitation-energy dependence of the FFMDs. The evolution of the ε parameter in heavier nuclei will be the topic of a future investigation.

The calculation without the MCF (blue curves in Fig. 2) can explain data only for low-energy data. The curve is considered as the FFMD of the first-chance fission component for each initial excitation energy.

In this study, shell damping energy is used as conventional 20 MeV. It is seemed that shell damping energy value can be changed for every nucleus. However, we use specific value for shell damping energy, and the calculation is good agreement with experiment. Therefore, this value has a certain precision.

A persistence of predominantly asymmetric FFMDs at high excitation energy is not signatures of survival of shell effects in the initial compound. This behavior shows by MCF effect in this study. The apparent asymmetric shape of FFMDs for a given initial excitation energy originates from fission of less excited lighter isotopes produced via a chain of MCF. It was shown that a reliable understanding of the observed FFMDs can be obtained only by invoking MCF.

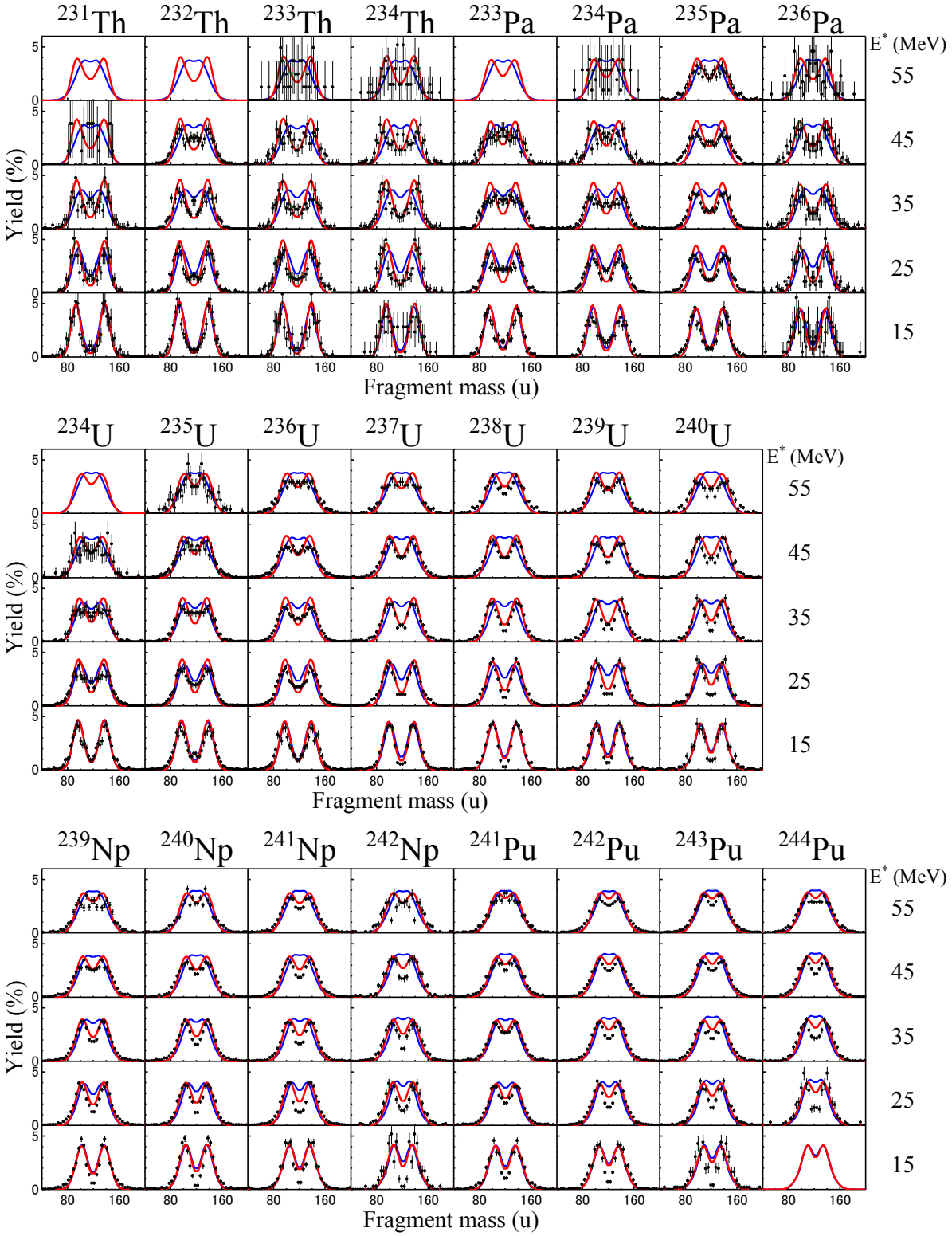

Fig. 2 Experimental FFMDs (points with error bars) of the Th, U, Np and Pu isotopes and their dependence on excitation energy in the range of E^*=15-55 MeV. The experimental FFMDs are compared with Langevin calculations respectively without (blue curves) and with (red curves) the inclusion of multi-chance fission.

4. Conclusion

Nuclear fission is an extremely complex reaction, and still not understood completely. Especially, the behavior at high excitation energy has not been explained. In this study, calculation results maintain a double-humped shape, as well as the experimental data, at high excitation energy by including MCF. Moreover, we explain that various FFMDs of each chance fission compose the calculation result. Thus, it presents that experiment data is similarly mixed by various FFMDs as MCF. In conclusion, FFMDs are affected by MCF, and this shape changes significantly. This result suggests that the consideration of MCF is essential to interpret and evaluate fission observables.

References

[1] *The Nuclear Fission Process*, edited by C. Wagemans (CRC Press, Boca Raton, FL, 1991).
[2] K. Shibata, O. Iwamoto, T. Nakagawa, et al., J. Nucl. Sci. Technol. **48**, 1 (2011).
[3] J. Lestone and T. Strother, Nucl. Data Sheets **118**, 208 (2014).
[4] D. L. Duke, F. Tovesson, A. B. Laptev, S. Mosby, F.-J. Hambsch, T. Bryś, and M. Vidali, Phys. Rev. C **94**, 054604 (2016).
[5] T. Ethvignot, M. Devlin, H. Duarte, T. Granier, R. C. Haight, B. Morillon, R. O. Nelson, J. M. O'Donnell, and D. Rochman, Phys. Rev. Lett. **94**, 052701 (2005).
[6] M. C. Duijvestijn, A. J. Koning, and F.-J. Hambsch, Phys. Rev. C **64**, 014607 (2001).
[7] K.-H. Schmidt, B. Jurado, C. Amouroux, and C. Schmitt, Nucl. Data Sheets **131**, 107 (2016), Special Issue on Nuclear Reaction Data.
[8] M. D. Usang, F. A. Ivanyuk, C. Ishizuka, and S. Chiba, Phys. Rev. C **94**, 044602 (2016).
[9] P. Möller and C. Schmitt, Eur. Phys. J. A **53**, 7 (2017).
[10] Y. Aritomo and M. Ohta, Nucl. Phys. A **744**, 3 (2004).
[11] J. Maruhn and W. Greiner, Z. Phys. **251**, 431 (1972).
[12] K. Sato, A. Iwamoto, K. Harada, S. Yamaji, and S. Yoshida, Z. Phys. A **288**, 383 (1978).
[13] H. J. Krappe, J. R. Nix, and A.J. Sierk, Phys. Rev. C **20**, 992 (1979).
[14] A.V. Ignatyuk, G. N. Smirenkin, and A. S. Tishin, Sov. J. Nucl. Phys. **21**, 255 (1975).
[15] J. Blocki, Y. Boneh, J. R. Nix, J. Randrup, M. Robel, A. J. Sierk, and W. J. Swiatecki, Ann. Phys. **113**, 330 (1978).
[16] T. Wada, Y. Abe and N. Carjen, Phys. Rev. Lett. **7**, 3538 (1993).
[17] K. T. R. Davies, A. J. Sierk, and J. R. Nix, Phys. Rev. C **13**, 2385 (1976).
[18] P. Möller, A. J. Sierk, T. Ichikawa, H. Sagawa, Atomic Data and Nuclear Data Tables **109–110**, 1–204 (2016).
[19] A. Gavron, Phys. Rev. C **21**, 230 (1980).
[20] R. Léguillon, et al., Phys. Lett. B **761**, 12 (2016).
[21] K. Hirose, K. Nishio, S. Tanaka, et al., Phys. Rev. Lett. **119**, 222501 (2017).

19 Measurement of isotopic production cross sections of proton- and deuteron-induced reactions on ^{93}Zr at 200 MeV/nucleon

Shoichiro KAWASE[1], Yukinobu WATANABE[1], Keita NAKANO[1,2], Junki SUWA[1,2], He WANG[2], Nobuyuki CHIGA[2], Hideaki OTSU[2], Hiroyoshi SAKURAI[2], Satoshi TAKEUCHI[3], and Takashi NAKAMURA[3] for ImPACT-RIBF collaboration

[1]*Department of Advanced Energy Engineering Science, Kyushu University, Japan*

[2]*RIKEN Nishina Center for Accelerator-based Science, Japan*

[3]*Department of Physics, Tokyo Institute of Technology, Japan*

E-mail: kawase@aees.kyushu-u.ac.jp

Isotopic production cross sections of proton- and deuteron-induced spallation reactions on ^{93}Zr at 200 MeV/nucleon were measured by using the inverse kinematics method. The experimental results were compared to PHITS calculations describing the intra-nuclear cascade and evaporation processes. PHITS calculations show a generally good agreement with the experimental cross sections, but some discrepancies were observed especially in charge-exchange and few-nucleon removal channels as well as in the preceding measurement at 105 MeV/nucleon.

Keyword : Spallation reaction, Zirconium-93, Inverse kinematics method

1. Introduction

The long-lived fission products (LLFPs), which are produced in nuclear reactors, have been an important issue because of the difficulty of disposal due to their remarkably long lifetimes. Therefore some treatment methods to transform the LLFPs into short-lived and/or low-toxic materials are strongly desired. For that purpose, nuclear transmutation technology that makes use of spallation reactions is expected to be one of the candidate processes to address this issue. However, the reaction data on LLFPs required for the design of an optimum pathway of the transmutation process are currently quite scarce. In our former study of the proton- and deuteron-induced reactions on ^{93}Zr at 105 MeV/nucleon [1], the isotopic production cross sections in few-nucleon removal channels were largely overestimated by the PHITS calculations [2], which describe the spallation reaction as a two-step process composed of the cascade and the evaporation processes. To improve the reliability of the reaction model calculations, further systematic experimental data are required for a wide range of reaction energies. In this study, the isotopic production cross sections of the proton- and deuteron-induced spallation reactions on ^{93}Zr at 200 MeV/nucleon were measured in inverse kinematics.

2. Experiment

The experiment was carried out at the RIKEN RI Beam Factory (RIBF) [2] operated by the RIKEN Nishina Center and the Center for Nuclear Study (CNS), University of Tokyo. A primary ^{238}U beam at 345 MeV/nucleon bombarded a ^{9}Be production target and secondary beams including ^{93}Zr were generated via inflight fission of ^{238}U.

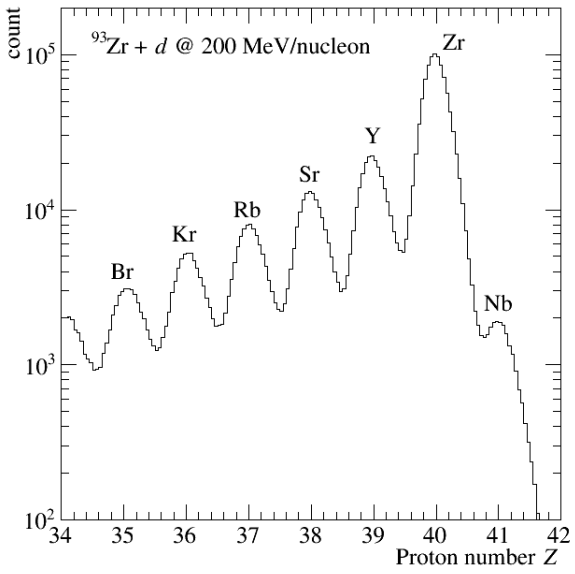

Fig. 1 Proton number distribution of reaction products in ^{93}Zr + d runs.

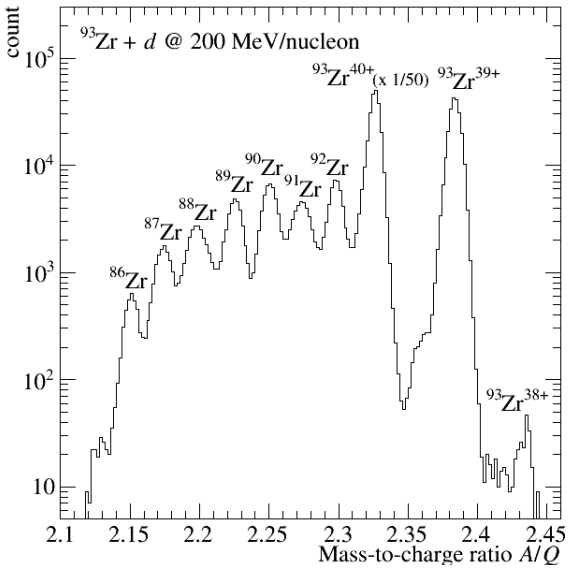

Fig. 2 Mass-to-charge ratio distribution of Zr isotopes in reaction products in ^{93}Zr + d runs.

The generated secondary ^{93}Zr beam was separated and identified by using the BigRIPS particle separator [3] on an event-by-event basis. Then the secondary beam bombarded a liquid hydrogen and a liquid deuterium target located at the entrance of the SAMURAI spectrometer [4]. The liquid targets were prepared using the CRYPTA target system [5]. The reaction products were momentum analyzed and identified using the SAMURAI spectrometer. Figures 1 and 2 show the proton number (Z) distribution and the mass-to-charge ratio (A/Q) distribution of zirconium isotopes (Z = 40) of the reaction products for the liquid D_2 target runs. The A and Z resolution for ^{90}Zr were 0.59 (FWHM) and 0.45 (FWHM), respectively. Finally, the isotopic production cross sections were derived from the numbers of incident ^{93}Zr beams and that of generated isotopes. In this experiment, the scattering angle and the energy of neutrons emitted in the evaporation process were also simultaneously measured with the neutron detector array NEBULA [5,6] and NeuLAND [7]. In this report, the analysis of these neutrons will not be discussed.

3. Results and discussion

The isotopic production cross sections of the proton- and deuteron-induced reactions on ^{93}Zr at 200 MeV/nucleon using the liquid hydrogen and deuterium targets are shown in Fig. 3. The circles and the diamonds indicate proton-induced cross sections (σ_p) and deuteron-induced cross sections (σ_d), respectively. The error bars indicate only the statistical uncertainties.

The niobium production shown in Fig. 3 (a) corresponds to charge-increasing reactions. In this channel, σ_p is approximately twice as large as σ_d. This ratio is consistent with the existing experimental data (see, for example, Ref. [8] for ^{137}Cs and ^{90}Sr at 185 MeV/nucleon). With decreasing proton number, σ_p becomes smaller than σ_d. This can be understood by the difference in excitation energy of the reaction residues generated after direct processes. In this experiment, deuterons have twice as large kinetic energy as protons and are likely to transfer more energy to the reaction residue. As a result, the deuteron-induced case emits more protons on average than the proton-induced case.

An enhancement of the cross sections for ^{90}Zr and ^{89}Y, which have neutron magic number N = 50, was

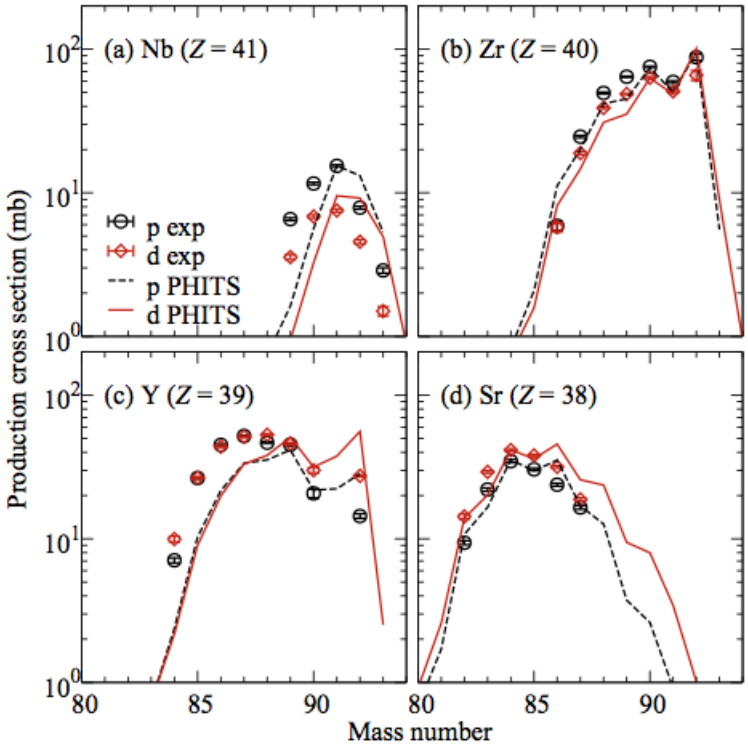

Fig. 3 Isotopic production cross sections of the proton- and deuteron-induced reactions on ^{93}Zr at 200 MeV/nucleon.

observed, and it is also the case for the 105 MeV/nucleon measurement [1]. The effect of the shell closure is still important in the interpretation of the spallation reaction cross sections at 200 MeV/nucleon despite the high reaction energy compared to the nucleon separation energies.

In Fig. 3, the experimental results are compared with the model calculations using the Particle and Heavy-Ion Transport code System (PHITS) 2.82 [9]. Spallation reactions are well described as a two-step process composed of the formation of prefragments via an intra-nuclear cascade process and a de-excitation process of the prefragments by evaporation of light particles. In this work, the Liege Intranuclear Cascade model (INCL 4.6) [10] and the generalized evaporation model (GEM) [11] were employed for these processes. The lines in Fig. 3 show the cross sections calculated by PHITS. The black dashed line and the red solid line correspond to the proton induced and the deuteron induced cross sections, respectively.

The general behavior of the isotopic production cross sections are apparently well reproduced by the PHITS calculations, but the distributions are shifted to heavier isotopes especially in proton-odd isotopes (Nb and Y). The production cross section of ^{92}Y is much overestimated in both the proton- and deuteron-induced case. This can probably be understood by the poor reproduction of the excitation energy of reaction residue after the direct process, as pointed out in Ref. [1]. The models used in PHITS are expected to be improved in the near future after close analysis of the spallation reaction data over a wide range of incident energies.

4. Summary and outlook

The isotopic production cross sections of the proton- and deuteron-induced spallation reactions on ^{93}Zr at 200 MeV/nucleon were measured in inverse kinematics at the RIKEN RI Beam Factory. The overall behavior of the cross section was in good agreement with the PHITS calculations with INCL 4.6 for the intranuclear cascade

process and GEM for the evaporation process. However a small shift of the calculated isotopic distributions to heavier isotopes was seen as in the measurement at 105 MeV/nucleon. More recently, we performed a series of similar measurements at 50 and 30 MeV/nucleon at RIKEN RIBF. In future, the energy dependence of the reactions will be discussed by a comparison with the results of the lower energy measurements.

Acknowledgments

We are grateful to the accelerator staff of the RIKEN Nishina Center for providing a high-quality ^{238}U beam. This work was funded by ImPACT Program of Council for Science, Technology and Innovation (Cabinet Office, Government of Japan).

References

[1] S. Kawase et al., Prog. Theor. Exp. Phys. **2017**, 093D03 (2017).

[2] T. Kubo et al., Prog. Theor. Exp. Phys. **2012**, 03C003 (2012).

[3] N. Fukuda et al., Nucl. Instr. Meth. Phys. Res. B **317**, 323 (2013).

[4] H. Ryuto et al., Nucl. Instrum. Meth. Phys. Res. A **555**, 1 (2005).

[5] T. Kobayashi et al., Nucl. Instrum. Meth. Phys. Res. B **317**, 294 (2013).

[6] T. Nakamura and Y. Kondo, Nucl. Instrum. Meth. Phys. Res. B **376**, 156 (2016).

[7] T. Aumann, the R^{3}B collaboration, R^{3}B technical design report, 2011 (accessed 2018-04-01). http://www.fair-center.eu/fileadmin/fair/publications_exp/NeuLAND-TDR-Web.pdf.

[8] H. Wang et al., Phys. Lett. B **754**, 104 (2016).

[9] T. Sato et al., J. Nucl. Sci. Technol. **50**, 913 (2013).

[10] A. Boudard et al., Phys. Rev. C **87**, 014606 (2013).

[11] S. Furihata, Nucl. Instrum. Meth. Phys. Res. B **171**, 251 (2000).

20 The measurement of the excitation function of alpha induced reaction on ^{nat}Yb to produce ^{177}Lu

Moemi Saito[1], Masayuki Aikawa[1], Tomohiro Murata[2], Naoyuki Ukon[3], Yukiko Komori[4], Hiromitsu Haba[4], Sándor Takács[5]

[1] *Graduate School of Biomedical Science and Engineering, Hokkaido Univ., Sapporo 060-8638, Japan*

[2] *School of Science, Hokkaido Univ., Sapporo 060-0810, Japan*

[3] *Advanced Clinical Research Center, Fukushima Medical Univ., Fukushima 960-1295, Japan*

[4] *Nishina Center for Accelerator-Based Science, RIKEN, Wako 351-0198, Japan*

[5] *Institute for Nuclear Research, Hungarian Academy of Sciences (ATOMKI), 4026 Debrecen, Hungary*

e-mail: moemi@nds.sci.hokudai.ac.jp

Lutetium-177 is a candidate of the theranostic radioisotopes and its possible production routes are worthy of investigation. One of those production routes is the alpha particle induced reactions on ^{nat}Yb, of which only one previous study exists. Therefore, we performed an experiment to determine the cross sections of the ^{nat}Yb(α,x)^{177g}Lu reaction. The preliminary result shows rapid increase of the cross sections with increasing energy and some deviations from the previous data and theoretical calculation.

1. Introduction

Radioisotopes (RI) are used in many application fields, such as engineering, medicine, and so on. In nuclear medicine, RIs are used for therapy and diagnosis. Recently, RIs for theranosis, which is combination of therapy and diagnosis, are investigated. Lutetium-177 ($T_{1/2}$ = 6.6 d) is one of the candidates of the theranostic RI [1]. It emits β-rays (E_{mean} = 134.2 keV) and γ-rays (E_γ = 112.95 keV (I_γ = 6.17%) and 208.37 keV (I_γ = 10.36%) simultaneously. The former is suitable for therapy and the latter for diagnosis.

Well defined energy dependence of the cross section data are required to find the best way to produce ^{177}Lu among several possible reaction routes. In this paper, we focused on the cross sections of the alpha induced reaction on ^{nat}Yb. The cross sections were previously measured up to 40 MeV [2]. Therefore, we performed an experiment to measure the cross sections up to 50 MeV.

2. Method

The experiment was performed at the AVF cyclotron of the RIKEN RI Beam Factory. Cross section data were measured by the stacked-foil activation method using the γ-ray spectrometry. Natural ytterbium (purity: 99%, Goodfellow Co., Ltd., UK) foils and natural titanium (purity: 99.6%, Goodfellow Co., Ltd., UK) monitor foils were stacked together as a target. The ^{nat}Ti monitor foils were used to assess beam parameters. The stacked target was irradiated by a 50 MeV alpha beam with an average intensity of 207 particle nA for 2 hours. Nuclear data used in the data evaluation are shown in Table 1.

Table 1

Decay data of reaction products [4].

Reaction product	Half-life (d)	Decay mode (%)	Eγ (keV)	Iγ (%)
^{177g}Lu	6.6	β- (100)	55.79	2.77(9)
			112.9498(4)	6.17(7)
			208.3662(4)	10.36
^{51}Cr	27.7	ε (100)	320.0824	9.910(10)

3. Results

^{nat}Ti(α,x)^{51}Cr monitor reaction

The initial beam energy was determined by time of flight measurement before and after the irradiation [5]. The beam energy degradation in the target was calculated by the SRIM code available online [6]. To check the energy degradation, cross sections of the ^{nat}Ti(α,x)^{51}Cr monitor reaction were derived by measuring the activity of the γ-line at E_γ = 320.08 keV (I_γ = 9.91%). The result is compared with the recommended values [7] as shown in Fig. 1.

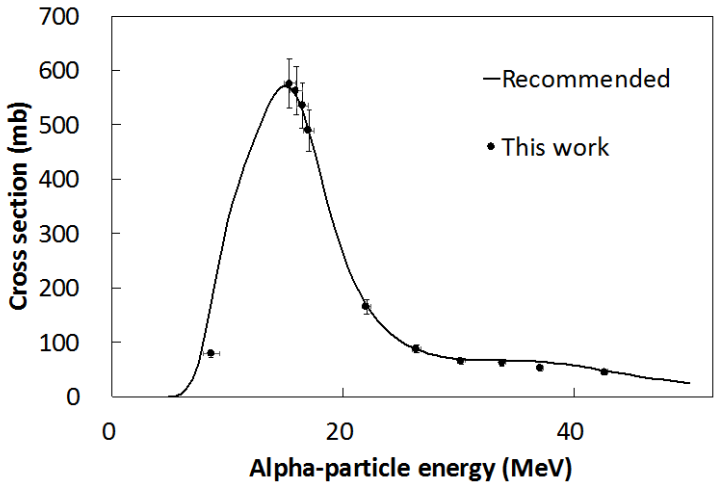

Fig. 1 Comparison of the experimental and recommended cross sections for the ^{nat}Ti(α,x)^{51}Cr monitor reaction.

As good agreement was found among the measured and recommended values no adjustment was applied for the beam parameters.

^{nat}Yb(α,x)^{177g}Lu reaction

Cross sections of the ^{nat}Yb(α,x)^{177g}Lu reaction were derived by measuring the activity of the irradiated target foils using the γ-line at E_γ = 208.37 keV (I_γ = 10.36%). The preliminary result is shown in Fig.2 in comparison with the previous data [2] and TENDL-2015 data [3]. Our result determines a smooth curve, however disagrees with the previous data. It may require a more detailed analysis to confirm this deviation.

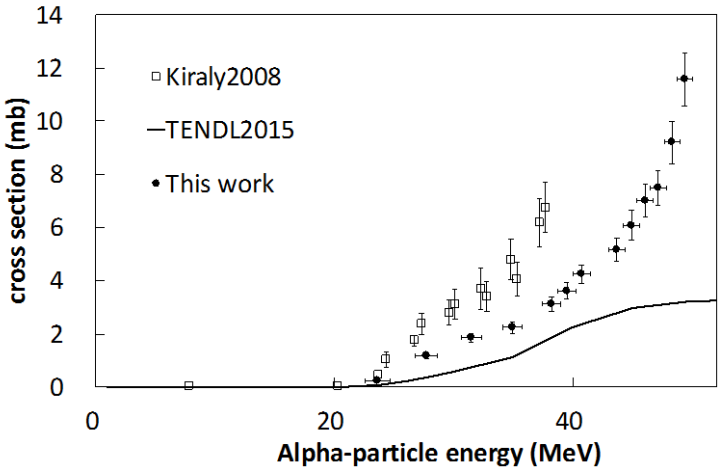

Fig. 2 Cross sections of the ^{nat}Yb(α,x)^{177g}Lu reaction in comparison with the previous data [2] and TENDL-2015 data [3].

4. Conclusion

Theranosis is one of hot topics in nuclear medicine. One of candidates of the theranostic RI is ^{177g}Lu, which emits β- suitable for therapy and low energy low intensity γ-rays suitable for diagnostics simultaneously. The production route of ^{177g}Lu has not been established yet. The ^{nat}Yb(α,x)^{177g}Lu process as a possible production reaction route was focused and investigated by performing an experiment up to 50 MeV at the AVF cyclotron of the RIKEN RI Beam Factory by using the standard stacked-foil method and the γ-ray spectrometry. A 50 MeV alpha beam with an average intensity of 207 particle nA was irradiated on the stacked ^{nat}Yb target for 2 hours.

The obtained data show a monotonically increasing with energy up to 50 MeV. The amplitude

is deferent from the previous data and TENDL-2015 data. The data will be analyzed in more detail and finalized soon.

Acknowledgements

This work was carried out at RI Beam Factory operated by RIKEN Nishina Center and CNS, University of Tokyo, Japan. This work was supported by Hokkaido University Nitobe School Advanced Program Research Grant and JSPS KAKENHI Grant Number 17K07004.

References

[1] Rahbar K, Ahmadzadehfar H, Kratochwil C, Haberkorn U, Schäfers M, Essler M, Baum RP, Kulkarni HR, Schmidt M, Drzezga A, Bartenstein P, Pfestroff A, Luster M, Lützen U, Marx M, Prasad V, Brenner W, Heinzel A, M. Mottaghy F, Ruf J, Meyer PT, Heuschkel M, Eveslage M, Bögemann M, Fendler WP, Krause BJ. German Multicenter Study Investigating 177Lu-PSMA-617 Radioligand Therapy in Advanced Prostate Cancer Patients. J. Nucl. Med. 2017; 58: 85-90.

[2] Király B, Tárkányi F, Takács S, Hermanne A, Kovalev SF, Ignatyuk AV. Excitation functions of alpha-particle induced nuclear reactions on natural ytterbium. Nucl. Instrum. Methods Phys. Res. B. 2008; 266: 3919-3926.

[3] Koning AJ and D. Rochman. Modern nuclear data evaluation with the TALYS code system. Nucl. Data Sheets 2018; 113: 2841-2934.

[4] NuDat 2.6, 2011. National Nuclear Data Center database, Data available online ⟨http://www.nndc.bnl.gov/nudat2/⟩ (accessed 2018-04-01).

[5] Watanabe T, Fujimaki M, Fukunishi N, Imao H, Kamigaito O, Kase M, Komiyama M, Sakamoto N, Suda K, Wakasugi M, Yamada K. Beam energy and longitudinal beam profile measurement system at RIBF. Proc. 5th International Part. Accel. Conference (IPAC2014); 2014 Jun 15-20; Dresden (Germany).

[6] SRIM: the Stopping and Range of Ions in Matter, available online ⟨http://www.srim.org⟩ (accessed 2018-04-01).

[7] Tárkányi F, Takács S, Gul K, Hermanne A, Mustafa MG, Nortier M, Oblozinsky P, Qaim SM, Scholten B, Shubin YN, Youxiang Z, 2007. Charged particle crosssection database for medical radioisotope production: diagnostic radioisotopes and monitor reactions, IAEA-TECDOC 1211. Updated web-version at ⟨http://www-nds.iaea.org/medical/⟩ (accessed 2018-04-01).

21 Survival Probability and Evaporation Residue Cross Section for Synthesizing Superheavy Nucleus

Nur Liyana Mohd Anuar, Yoshihiro Aritomo, Shoya Tanaka, Baku Yanagi
Faculty of Science and Engineering, Kindai University
3-4-1 Kowakae, Higashiosaka City, Osaka 577-8502, Japan
yaya940817@gmail.com

The evaporation residue cross section of synthesizing superheavy elements requires touching probability, formation probability and survival probability. Survival probability and evaporation residue cross section appear in the last stage of synthesizing superheavy element. There are many uncertain parameters in each probability, here we focused on uncertain parameter in the survival probability that has also affect the evaporation residue cross section. As the parameters change, the calculation results also change. To adjust these parameters to fit with experiment value, we adopt the covariance method to arrange it more mathematically. There are also many possible systems for the same element especially the element that has not been discovered yet.

1. Introduction

On 28 November 2016, IUPAC announced the new superheavy elements: 113 Nihonium (Nh), 115 Moscovium (Mc), 117 Tennessine(Ts) and 118 Oganesson (Og). This was the big discovery in the periodic table. There are still many elements that has not be discovered yet and the periodic table will be continued to the 8^{th} period. Now, we are aiming the element 119 and above.

There are also many theoretical studies about island of stability. Island of stability is the region with the proton number Z=114 and neutron number N=184. Until now, there are still no stable combinations of projectile and target nucleus. We believe that the island of stability is there.

Accurate prediction is important to synthesize new nuclei and superheavy elements. Here, we focused on the last stage of synthesis of superheavy element which includes survival probability and evaporation residue cross section. Since there are uncertainties of some parameters, we discuss the parameters and look how these uncertainties affect the calculation results. We calculated the superheavy element from element 104 Rutherfordium till superheavy element 124 and more focusing on atomic number 119 and above which are the elements that had not been discovered yet.

2. Synthesis of superheavy element

The synthesis of superheavy element are divided into 3 stages by different of reaction time. The first stage is touching stage, where the projectile and target nucleus are approaching. From this stage, we calculate the touching probability T_l by coupled-channel model [1,2]. The second stage is formation or fusion stage where the fusion and quasi-fission processes are competing. Here, 90-99% of the process in the second stage will undergo quasi-fission reaction. The percentage to form the compound nucleus is very small about 1-10% only. In this stage, fusion probability (formation of compound nucleus) P_{fus} can be calculated using Langevin equation, which is a dynamical model [3,4].

$$P_{fus}(E,l) = \int_0^1 d(cos\,\theta)\, T_l(E;\theta) P_{CN}(E,l,\theta) \quad (1)$$

The third stage is a decay process which in this stage the evaporation residue and fusion-fission process will be occur. In this stage, it is important to know the survival probability P_{sur} and it can be calculated by statistical model [5]. From all the probabilities in these 3 stages, we calculated the evaporation residue cross sections σ_{ER}

$$P_{sur} = \prod_{i=1}^{N} \frac{\Gamma_n^{(i)}}{\Gamma_n^{(i)}+\Gamma_f^{(i)}} \quad (2)$$

$$\sigma_{ER} = \frac{\pi h}{2\mu_0 \mathrm{E_{c.m}}} \sum_{l=0}^{\infty} (2l+1)\, \mathrm{T_l(E_{c.m}, l)} P_{fus}(\mathrm{E}^*, l) P_{suv}(\mathrm{E}^*, l) \quad (3).$$

$\mathrm{E_{c.m}}$ and E^* denote to the incident energy and excitation energy while μ_0 and l are reduced mass in the entrance channel and angular momentum respectively. There are some uncertain parameters in each stage. For example, in the first stage the potential parameters like potential depth, diffuseness, etc., are not clear especially for the unknown nuclei. For the second stage, in the Langevin equation, there are potential energy parameters for liquid drop model and shell correction energy. There are also nuclear shape parameter and transport coefficients parameter.

In the third stage from equation (2) of survival probability [6], the uncertain parameters include fission barrier height parameter δB_f, friction parameter γ and level density parameter

a_f/a_n (4). In the superheavy element region, it is no determined which values to be used [7,8]. The survival probability can be expresses as

$$\frac{\Gamma_n}{\Gamma_f} = \frac{k_{coll}(gr.st.)}{k_{coll}(saddle) \cdot k_{\mathrm{kramers}}} A_0 exp\left[2\sqrt{a_n E_n^*} - 2\sqrt{a_f E_f^*}\right]$$

$$\mathrm{E_n^* = E_{int} - B_n} \quad , \quad \mathrm{E_f^* = E_{int} - B_f}$$

$$\mathrm{k_{kramers} = \frac{\hbar\omega_1}{\sqrt{E_{int}}}\left(\sqrt{1 + x^2} - x\right)}$$

$$\mathrm{x \equiv \gamma / 2\,\omega_1}$$

(4).

Γ_n and Γ_f are neutron evaporation width and fission decay width respectively while $\mathrm{B_n}$ is neutron separation energy. We need to know the parameter dependence of the survival probability and to see how these uncertainties influence the survival probability and evaporation residue cross section. The uncertainty parameters that we change this time is fission barrier height parameter $\delta \mathrm{B_f}$, friction parameter γ and level density parameter a_f/a_n.

3. Results

In this calculation, we can see the relation between formation cross section, survival probability and evaporation residue cross section. We change these three parameters, fission barrier height parameter $\delta \mathrm{B_f}$, friction parameter γ and level density parameter a_f/a_n, and see the differences in each parameter.

Then, we look how the uncertainty parameters affect the calculation results of survival probability. It seems that the survival probability changes as $\delta \mathrm{B_f}$ change. We also check the dependence on the friction parameter γ for the survival probability. As the uncertainty parameters affect the survival probability's calculation result, the evaporation residue cross section's result change. We took $^{48}\mathrm{Ca}+^{244}\mathrm{Pu}\rightarrow{}^{292}\mathrm{Fl}$ system as an example. (Figure 1)

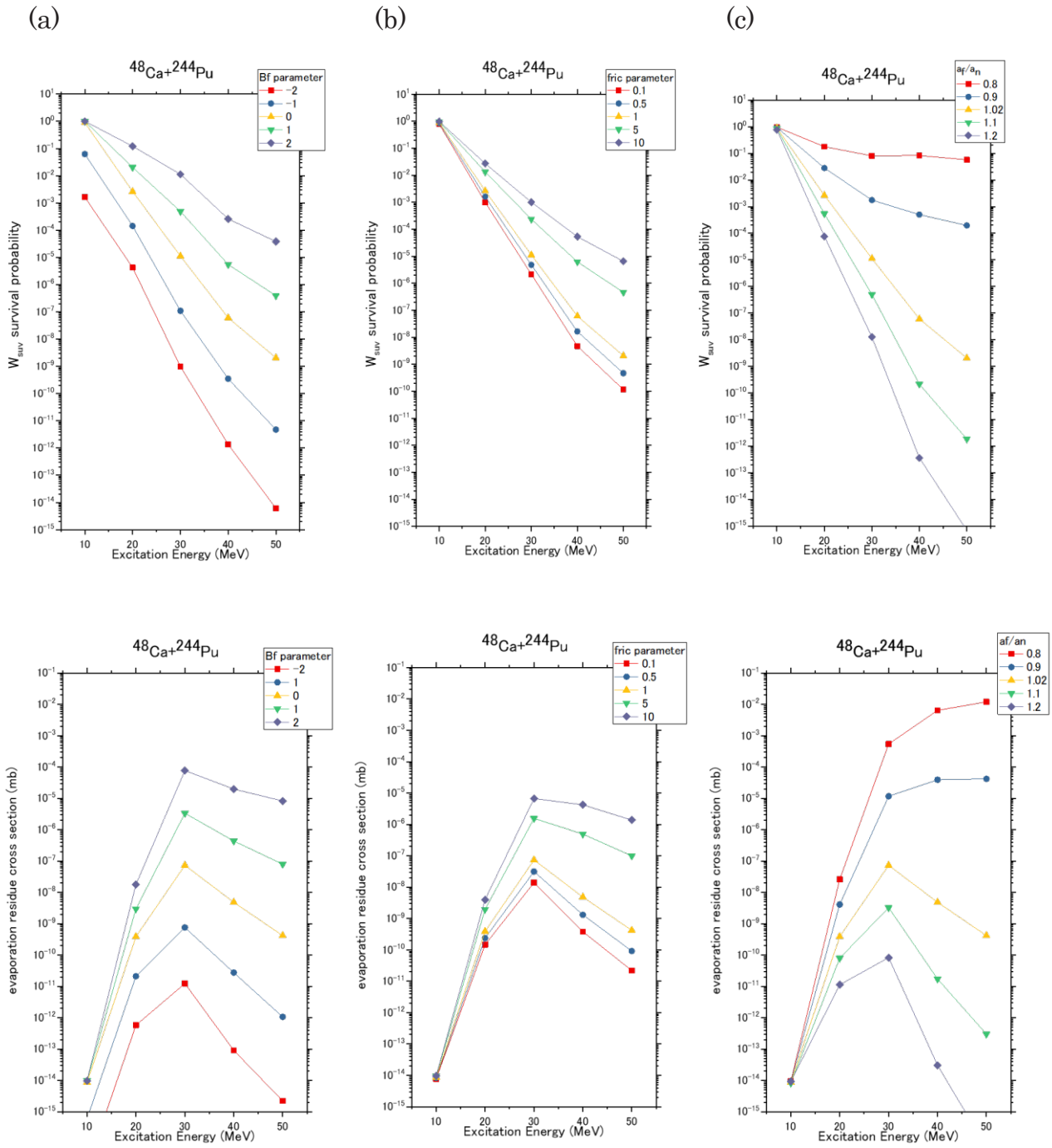

Figure1. The calculation results of survival probability (above) and evaporation residue cross section (below) for $^{48}Ca+^{244}Pu \rightarrow ^{292}Fl$ based on different uncertainty parameters (a) fission barrier height parameter (δB_f = -2,-1,0,1,2 [MeV]) (b) friction parameter (γ= 0.1,0.5,1,5,10 x10^{21} s^{-1}) (c) level density parameter (a_f/a_n= 0.8,0.9,1.02,1.1,1.2).

4. Discussion

The patterns of the changes in each element are uniform. From the calculation results of evaporation residue cross section, we took the maximum point of ER and summarize the results as below. (Figure 2)

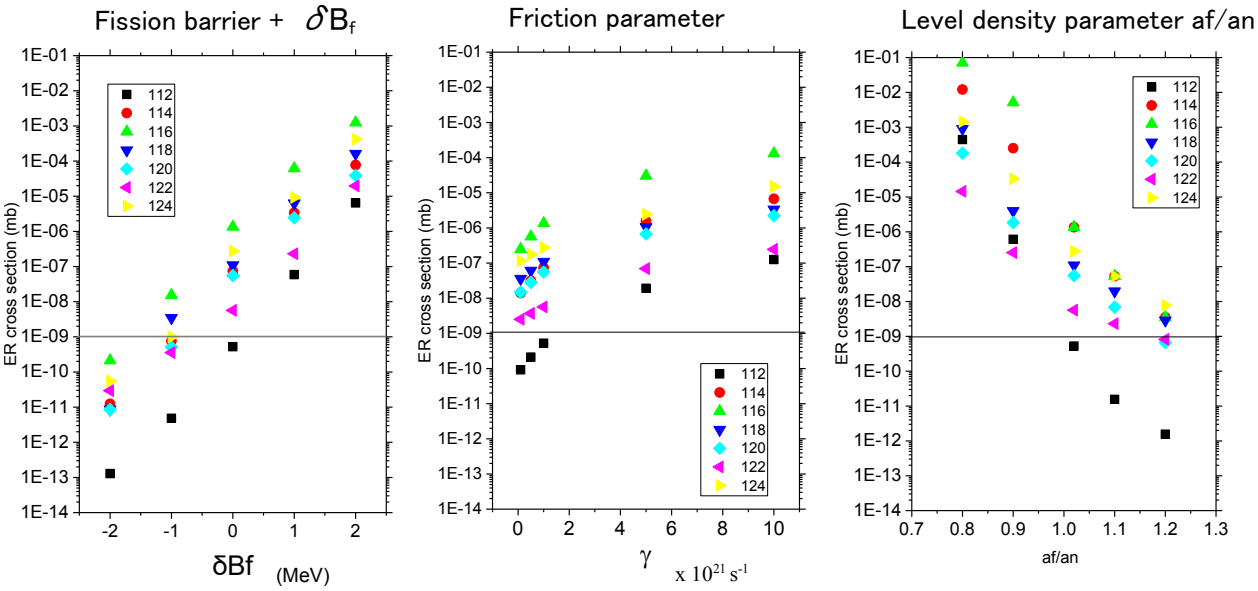

Figure 2. The summary of calculation results from Z number 112-124 based on different parameter. These are the maximum value of evaporation residue cross section based on different uncertainty parameters. We used ^{70}Zn+^{208}Pb→^{278}Cn cold fusion system for Z number ≦113 and ^{48}Ca+^{244}Pu→^{292}Fl, ^{48}Ca+^{248}Cm→^{296}Lv, ^{48}Ca+^{249}Cf→^{297}Og [9] hot fusion system for Z number ≧114. For element that had not been discovered yet, we used ^{54}Cr+^{248}Cm→^{302}120, ^{54}Cr+^{249}Cf→^{303}122 and ^{56}Fe+^{249}Cf→^{305}124 systems.

As the fission barrier height parameter δB_f increases, the fission process becomes hard and the fusion process will become easier. The survival probability will increase thus cause the increase of the evaporation residue cross section. For friction γ parameter, as friction parameter γ increases, fission process becomes harder and the fusion process will become easier thus the increase of the survival probability also causes the increase of the evaporation residue cross section. Meanwhile as the value of level density parameter a_f/a_n increases, the survival probability decreases thus cause the evaporation residue cross section decrease.

To fit the calculation results to experiment data, we try to find the reasonable parameter value. Since these changes were made one by one (when one parameter change, other parameters are constant), it is hard to find the reasonable value to fit with experiment data. Therefore, it is important to arrange it mathematically for example analysis using covariance method. Furthermore, based on equation E* = $E_{c.m}$ - Q-value (E*: excitation energy, $E_{c.m}$:

incident energy), Q-value also had been influenced in this calculation. We plan to change the value of reaction Q-value parameter for the next future work calculation. There are also many possible systems for Z number ≧ 119, the element that has not been discovered yet. As the systems change, the calculation results change. From this calculation, we can predict the uncertainty parameters for the next new superheavy element.

5. Conclusion

Survival probability and evaporation residue are some of the important parts in synthesizing superheavy element. However, there are some uncertain parameters in survival probability. As the parameters change, the calculation results also change. To adjust these parameters to fit with experiment value, it is important to arrange it mathematically for example analysis using covariance method. By this calculation, it will give the experiment team a guide to discover the new elements.

Acknowledgements

The authors want to make some appreciation to Prof. T. Wada for the original Langevin code. Prof. M. Ohta for his guide and clear explanation about the theories. The members of Nuclear Reaction Energy Laboratory for helping to do some of the calculations.

References

[1] K. Hagino and N. Rowley, Phys. Rev. C 69, 054610 (2004).
[2] K. Hagino, N. Rowley and A. T. Kruppa, Comput. Phys. Commun. 123,143 (1999).
[3] Y. Aritomo, K. Hagino, K. Nishio, S. Chiba, Phys. Rev. C 85, 044614 (2012).
[4] Y. Abe, K. Okazaki, Y. Aritomo, T.Wada and M. Ohta, “Dynamical theory for synthesis of superheavy elements”, Int. Workshop on Nuclear Reactions and Beyond, Lanzhou, China, 24-27 Aug, 1999.
[5] M. Ohta, in: Proceeding of Fusion Dynamics at the Extremes, Dubna, 25-27 May 2000, World Scientific, Singapore, 2001, p. 110.
[6] Yasuhisa Abe, Takahiro Wada, “Theory of Synthesis of Superheavy Elements” JAERI-Conf 99-015 p. 76-79.
[7] Y. Aritomo, T. Wada, M. Ohta and Y. Abe, Phys. Rev. C VOLUME 59, NUMBER 2 February 1999.
[8] Masahisa Ohta, Yoshihiro Aritomo, “Systematic on Superheavy Element Formation” Journal of NUCLEAR SCIENCE and TECHNOLOGY, Supplement 2, p.586-591 (August 2002).
[9] Yu.Ts. Oganessian et.al., NPA994,62. 2015.

22 Measurement of the Neutron Capture Cross Section of ^{237}Np using ANNRI at MLF/J-PARC

Gerard Rovira[1*], T. Katabuchi[1], K. Tosaka[1], A. Kimura[2], S. Nakamura[2]

1) Laboratory for Advanced Nuclear Energy, Tokyo Institute of Technology
2-12-1 Ookayama, Meguro-ku, Tokyo 152-8550, Japan
2) Nuclear Science and Engineering Directorate, Japan Atomic Energy Agency
2-4 Shirakata Shirane, Tokai, Naka, Ibaraki, 319-1195, Japan

author: rovira.g.aa@m.titech.ac.jp

Abstract

Neutron capture cross section measurements for ^{237}Np have been conducted with the Accurate Neutron Nucleus Reaction Measurement Instrument (ANNRI) at the Materials and Life Science Facility (MLF) of the Japan Proton Accelerator Research Complex (J-PARC) using neutrons with energy ranging from thermal energy to several hundred keV. A Time of Flight (TOF) method using a NaI(Tl) detector was employed for this measurement and the data were analyzed based on a pulse-height weighting technique in order to derive a neutron capture cross section. Instead of pulse-height measurement in a traditional acquisition method, the pulse width of the detector signal was measured with a fast time digitizer for fast data acquisition. Then, the pulse width was converted into pulse height offline. Two ^{237}Np samples of 1 MBq and 5 MBq were measured. The incident neutron spectrum was calculated using both ^{197}Au(n, γ)^{198}Au events and ^{10}B(n, α)^{7}Li events.

I. Introduction

Precise nuclear data for neutron capture cross sections on minor actinides (MAs) are of the essence for fundamental studies and applications in nuclear science and engineering. Numerous types of MA are produced in nuclear reactors and are present in high level radioactive waste (HLW). Accurate nuclear data are necessary in order to examine their production and long term burn-up characteristics. Data for MA are also crucial for studying the transmutation methods in the nuclear waste management.

Neptunium-237 is one of the most abundant MAs in spent nuclear fuels. It possesses a long half-life of 2.144 x 10^6 years and it produces an intense α-emitter of ^{238}Pu by neutron capture and a subsequent β decay. Hence, it is essential to determine the thermal neutron capture cross section (σ_0), the resonance parameters and the neutron cross section in the high energy accurately for examining the nuclear transmutation of ^{237}Np.

An extensive set of experimental data has been reported on the ^{237}Np (n, γ) reaction using both activation and time-of-flight (TOF) methods [1–16]. Up until now, it has not been possible to obtain a steady value for the thermal cross section (σ_0) as the differences between experiments vary from 7.5% up to 15%. At the high-energy range, the available experimental data is scarce and the differences between measurements are up to 200%

In this paper, preliminary results of the neutron capture cross section for ^{237}Np are presented for incident neutron energy ranging from thermal energy to several hundred keV using the TOF method with special emphasis in the high energy region. Details of the experimental setup and the data analysis are also provided.

II. Experimental Procedure

1. *Experimental Setup*

The experiments were performed using the Accurate Neutron Nucleus Reaction Measurement Instrument (ANNRI) at the Materials and Life Science Facility (MLF) of the Japan Proton Accelerator

Research Complex (J-PARC). Intense pulsed neutrons were produced by the Japanese Spallation Neutron Source (JSNS) in the MLF using the 3 GeV proton beam of the J-PARC facility. The proton pulses were shot at the spallation target every 40 ms and a beam power of 400 kW.

A TOF method was employed in the present experiment with a flight path of 27.9 m up to the sample position. Emitted γ-rays from the sample were detected by a NaI(Tl) detector surrounded by annular plastic scintillation detectors to suppress cosmic-ray background by anti-coincidence detection. Detected capture events were stored sequentially in a computer as a list format data.

2. *Samples*

Two capture samples of ^{237}Np were used for the measurements. The first sample consisted of 227 mg of neptunium dioxide (NpO_2) powder together with 624.5 mg of Al powder and it possessed an activity of 5 MBq. The second sample was formed by 43.13 mg of neptunium dioxide (NpO_2) powder mixed with 686 mg of Al powder with an activity of 1 MBq. The isotopic purity of ^{237}Np for both samples was 99.99%. The powders were packed into Al pellets with a 20 mm diameter and 0.4 mm thick walls. A dummy container was also used for a background measurement.

An neutron spectrum was obtained in this experiments using γ-rays from the ^{197}Au(n, γ) reaction with a 20 mm in diameter and 1 mm in thickness gold sample and, also, using the 478 keV γ-rays from the ^{10}B(n, α)^{7}Li reaction with a boron sample containing enriched ^{10}B up to 90% and having a diameter of 10 mm and a thickness of 0.5 mm.

Background events due to scattered neutrons were derived using a ^{nat}C sample with a 10 mm diameter and 0.5 mm thickness.

3. *Data Acquisition*

A multi-event time digitizer FAST ComTec MPA4T was used for fast data acquisition purposes [18]. This module digitizes the time between a starting trigger event and successive multiple stop events. The signal coming from the JSNS proton beam monitor was used as a trigger signal for the MPA4T module. Signals coming from the anode of the NaI(Tl) detector were fed into the MPA4T as a stop signal. Time differences between the trigger signal and the NaI(Tl) anode signal was used for the TOF measurement of the incident neutrons. Simultaneously, signals from the dynode of the NaI(Tl) detector were amplified and shaped, and then fed into an analog-to-digital converter (ADC) for pulse height measurement. However, traditional pulse analysis technique using the ADC does not work well in the energy region higher than 1 keV. Strong γ-ray burst, called gamma flash, from the neutron source after the spallation reaction induce baseline distortion into the analog modules, making pulse height measurement impossible in the fast TOF region. Faster data acquisition was needed in the high energy region. Thus, along with the pulse height measurement, the pulse width calculated from the time difference between the rising and the falling edges of the anode signal was recorded. The pulse width was converted into pulse height in offline analysis.

III. Data Analysis

1. *Pulse Width to Pulse Height Conversion*

In order to derive the pulse height value of the γ-ray in the fast TOF region from its pulse width, a coversion relation was obtained between the pulse height and the pulse width. The relation was derived by poltting the pulse height value along with the pulse width value of each detected γ-ray. More information about the pulse width analysis is described by Katabuchi et al [19].

2. *Background Removal*

In order to derive the cross section accurately, several background events have to be removed and other corrections have to be applied.

A dead time correction is applied to all measurements in order to estimate the count loss in the experiment [19]. The main cause for this count loss is the pile-up of two consecutive signals.

Frame overlaping from previous neutron bursts have to be substacted. Every proton event induces neutron events with a frame length of 40 ms, as the proton beam repetition is 25 Hz. Slow neutrons (TOF 40 ms) from earlier frames overlap subsequent frames. Overlaping background was estimated using J-PARC's unique operation pattern. A small part of the proton beam pulses from the 3-GeV synchrotron are injected into the 50-GeV synchrotron ring instead of JSNS. As no proton is shot into the JSNS, the measured TOF of the previous proton pulse is extended up to 80 ms, doubling the normal frame length. Hence, the overlap background is estimated from the recorded events from 40 ms to 80 ms . The overlap background is then removed by fitting a curve in the frame spectra from 40 ms to 80 ms and normalizing by referring it to the total number of proton bursts. A detailed explanation is provided by Hirose et al [16].

Blank background is subtracted using the data retrieved from a measurement with no sample. Likewise, the background events induced due to scattered neutrons at the sample and the events induced by the sample case are removed using the ^{nat}C and the TOF spectra obtained from the aluminum case respectively.

3. *Pulse Height Weighting Technique*

The Pulse Height weighting technique (PHWT) enables the calculation of the neutron capture yields from the pulse height spectrum [20]. The first step to apply the PHWT is to calculate a detector response function using the experimental configuration. This response function ***R(I, E)*** was defined as the probability that a γ-ray with an energy of E was counted in the I channel of the detecting system. This response function was used in order to derive a weighting function ***W(I)***. The weighting function is essential in order to apply the PHWT and it is defined as follows:

$$\sum_I W(I)R(I,E) = E. \tag{1}$$

On the condition that the detection efficiency for γ-rays is so small that only one γ-ray per capture event can be detected, the real capture γ-ray pulse height spectrum ***S(I)*** should be expressed as:

$$S(I) = \sum_i m_i \sum_j R(I, E_{ij}) \tag{2}$$

where E_{ij} is the energy of the j-th γ-ray emitted in the i-th mode and m_i the number of capture events which disintegrated through the i-th mode. At the same time, since the sum energy of the γ-ray cascades emitted per capture event is equal to:

$$\sum_j E_{ij} = B_n + E_n^{'} \tag{3}$$

being B_n the binding energy of the target nucleus and $E_n^{'}$ the incident neutron energy in the center-of-mass system. Finally, as the sum of m_i with respect to i is equal to the capture yield, the neutron capture yield can be expressed as follows:

$$Y = \frac{\sum_i W(I)S(I)}{B_n + E_n^{'}} \tag{4}$$

4. *Neutron Spectrum*

The neutron spectrum was estimated using the gold and boron samples. The obtained TOF spectrum for both runs was divided by the reaction rate simulated using the PHITS program [21]. Figure 1 shows a good agreement of the incident neutron distribution between the two samples except for the resolved resonance region of gold.

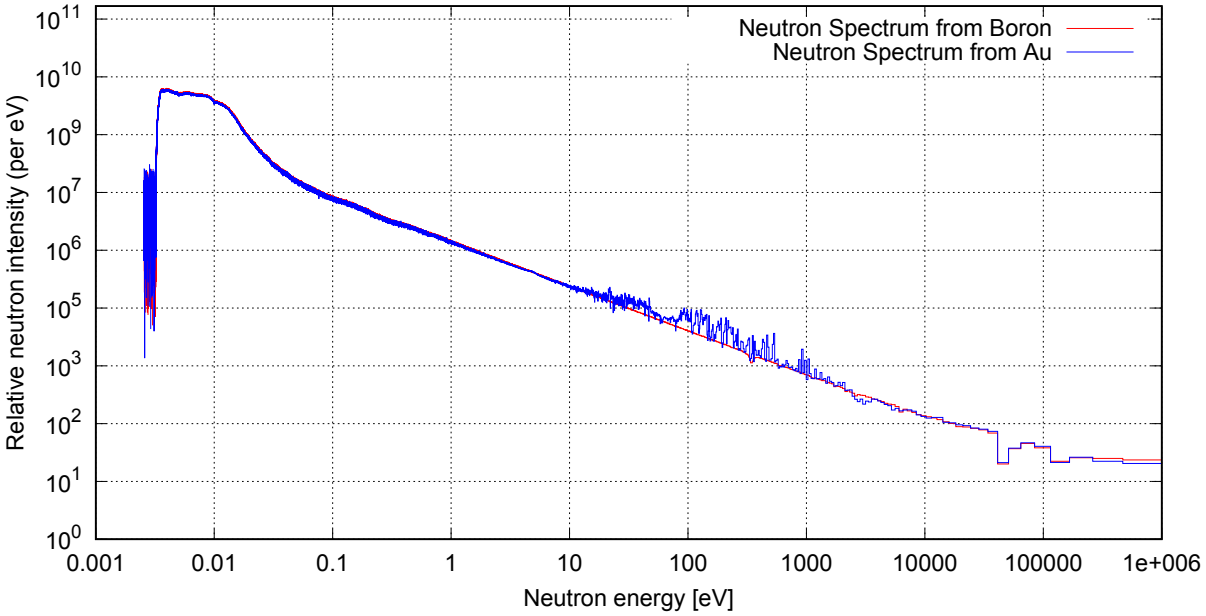

Figure 1: *Incident Neutron Spectrum*

IV. Results and Discussion

The neutron capture cross section was derived from the neutron capture yields and the incident neutron spectrum finally using only the large ^{237}Np sample for better statistics. For comparison, the measured ^{237}Np capture cross section using the neutron spectrum with the boron sample is plotted along with evaluated data from JENDL-4.0 (Fig. 2). The capture cross section was measured from thermal energy up to 500 keV. The data was normalized at the JENDL 4.0 thermal value of the cross section. There is a good agreement from thermal region up to 30 keV. Over that energy, the JENDL-4.0 provides a slightly higher value than the present value. There are two main sets of data available that were measured using the TOF method in the high energy region. Experimental data from Weston [9] include total uncertainties up to 15% and Esch [13] data include a steady value for the total uncertainty of 5% in the high energy region. The present experimental data has similar values to those experimental data but, over 30 keV, the present data presents lower values (Fig. 3). As the present measured data is preliminary, only the statistical error is included. Uncertainties amount to 5% over the resolved resonance region, higher than 0.5 keV. Further measurements ought to be performed with increased measuring time and beam power. Should the beam power increase to 1 MW, which is the operational goal for J-PARC, with doubling the measuring time, the statistical uncertainties can be reduced below 2.5%.

In the present analysis, the data was normalized to the thermal value of the JENDL-4.0 cross section. It is possible to determine the absolute value of the cross secton using the saturated resonance method without evaluated cross section data. For that method, further measurements will be performed using a new thicker sample in order to saturate the first resonance. Nonetheless, the resonance region is well characterized enough for a resonance analysis.

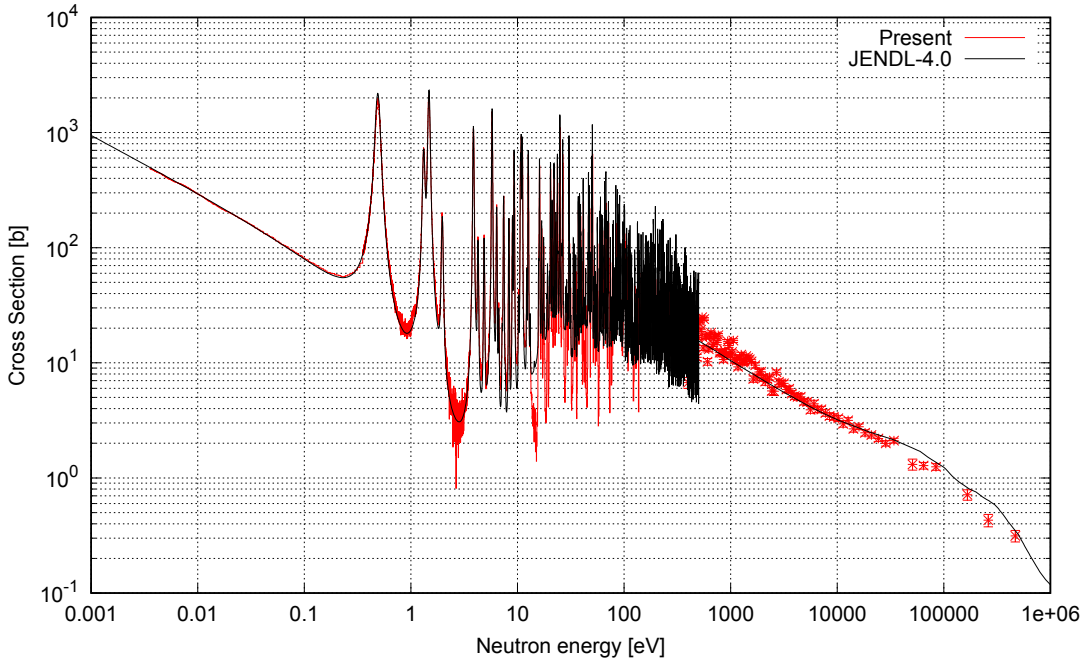

Figure 2: ^{237}*Np neutron capture cross section*

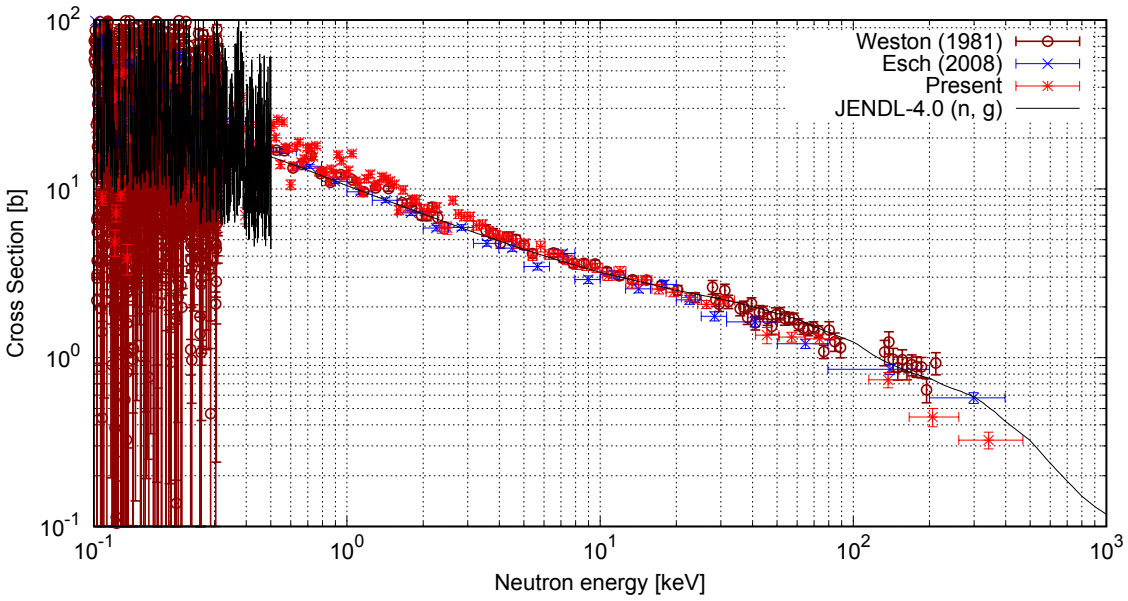

Figure 3: ^{237}*Np neutron capture cross section - High energy region*

V. Conclusions

The ^{237}Np neutron capture cross section was measured using the pulsed neutron beam generated by the Japanese Spallation Neutron Source in the Materials and Life science Facility at the Japan Proton Accelerator Research Complex. Using pulse width analysis along with pulse-height weighting technique, the neutron capture cross was succesfully dertermined from thermal energy region up to 500 keV. However, analysis shows that the neutron capture yield in the high energy region should be increased in order to reduce the statistical uncertainties. Measurements aiming to deduce the absolute cross section value accurately are planned using a new thicker sample along with increased beam power and measuring time. A resonance analysis is also underway in order to derive the resonance parameters.

References

[1] K. Kobayashi et al., J. Nucl. Sci. Technol. 1994; 31:12349-1247.
[2] T. Katoh et al., J. Nucl. Sci. Technol. 2003; 40:559-568.
[3] H. Harada et al., J. Nucl. Sci. Technol. 2006; 43:1289-1297.
[4] N. N. Buleeva et al., AE, 65(6), 1988.
[5] A. Letourneau et al., Appl. Radiat. Isot. 2010; 68:432-438.
[6] Ju. N. Trofimov et al., Conf: 6.All-Union Conf.on Neutron Physics,Kiev,2-6 Oct.1983, Vol.2, p.142 (1983), USSR.
[7] M. Lindner et al., J. Nucl. Sci. Eng. Vol.59, p.381 (1976), USA.
[8] D. C. Stupegia et al., J. Nucl. Sci. Eng. Vol.29, p.218 (1967), USA.
[9] L.W. Weston et al., Nucl. Sci. Eng. 1981; 79:184-196.
[10] K. Kobayashi et al., J. Nucl. Sci. Technol. 2002; 39:111-119.
[11] O. Shcherbakov et al., J. Nucl. Sci. Technol. 2005; 42:135-144.
[12] M. Mizumoto et al., http://doi.org/10.1051/ndata:07463 (accessed 2018-04-01).
[13] E-I. Esch et al., Phys. Rev. 2008; C77:034309.
[14] C. Guerrero (n-TOF Collaboration), Phys. Rev. 2012; C85:044616.
[15] M.D. Semon et al., BAP 21, 655 (JE3), 1976.
[16] K. Hirose et al., J. Nucl. Sci. Technol. 2013; 50:188-200.
[17] T. Katabuchi et al., IAEA-TECDOC–1743 332-340, 2014. International Atomic Energy Agency (IAEA).
[18] FAST ComTec MPA4T `https://www.fastcomtec.com/products/mpa/mpa4t0/` (accessed 2018-04-01).
[19] T. Katabuchi et al., Nucl. Ins. and Meth. in Phy. Res. A, 764 (2014) 369-377., Nucl. Ins. and Meth in Phy. Res. A 626-627(2011)58-66.
[20] R. L. Macklin et al., Nuc. Ins. and Meth. in Phy. Res. 91 (1971) 565.
[21] `https://phits.jaea.go.jp/lec/phits-introduction-en.pdf` (accessed 2018-04-01).

23 Systematic measurement of double-differential (d,xn) cross sections at an incident energy of 200 MeV

Hiroki SADAMATSU[1], Shouhei ARAKI[1,2], Yukinobu WATANABE[1], Keita NAKANO[1], Shoichiro KAWASE[1], Tadahiro KIN[1], Yosuke IWAMOTO[2], Daiki SATOH[2], Masayuki HAGIWARA[3], Hiroshi YASHIMA[4] and Tatsushi SHIMA[5]

[1]*Department of Advanced Energy Engineering Science, Kyushu University 6-1 Kasuga, Fukuoka 816-8580, Japan*

[2]*Japan Atomic Energy Agency (JAEA), 2-4 Shirakata, Tokai, Naka, Ibaraki 319-1195, Japan*

[3] *High Energy Accelerator Research Organization (KEK), 1-1 Oho, Tsukuba, Ibaraki 305-0801, Japan*

[4]*Research Reactor Institute, Kyoto University, 2-1010 Asashiro-nishi, Kumatori, Sennan, Osaka 590-0494, Japan*

[5]*Research Center for Nuclear Physics (RCNP), Osaka University, 10-1 Mihogaoka, Ibaraki, Osaka 567-0047, Japan*

E-mail: watanabe@aees.kyushu-u.ac.jp

Double-differential neutron production cross sections (DDXs) for deuteron-induced reactions on Li, Be, C, Al, Cu, Nb, In, Ta, and Au at 200 MeV were measured at forward angles ≤ 25° by means of a time of flight (TOF) method with EJ301 liquid organic scintillators at the Research Center of Nuclear Physics (RCNP), Osaka University. The measured DDXs at 0° were compared with theoretical model calculations by the DEURACS and PHITS codes. The DEURACS calculation showed better agreement with the measured DDXs than the PHITS calculation.

This work was funded by ImPACT Program of Council for Science, Technology and Innovation (Cabinet Office, Government of Japan).

Keyword : ImPACT, deuteron-induced neutron production, 200 MeV, measurement, time of flight method, double-differential cross section

1. Introduction

Accelerator-based neutron sources with deuteron beam are attractive for various applications such as nuclear transmutation of radioactive waste, estimation of radiation damage for fusion reactor materials, production of medical radioisotopes, and so on. Experimental neutron production data from various materials are required for optimized design of the neutron source. However, the experimental data, particularly double-differential neutron production cross sections (DDXs), are not sufficient over a wide range of incident energy.

In the present work, therefore, we have conducted a series of DDX measurements for nine target nuclei over a wide range of atomic numbers (Li, Be, C, Al, Cu, Nb, In, Ta, and Au) at an incident energy of 200 MeV in the Research Center for Nuclear Physics (RCNP), Osaka University. This work is an extension of our previous measurement at 102 MeV [1].

2. Experiments

The experimental setup was basically the same as that used in the 102-MeV (d,xn) measurement [1]. The experiment was carried out at the N0 course of RCNP. A deuteron beam accelerated to 200 MeV was transported to the neutron experimental hall and focused on a thin target foil placed in the beam swinger magnet. The beam current was changed from 3 to 110 nA, depending on targets and measurement angles.

The characteristics of the target samples used in this experiment are summarized in Table 1. Each sample is a thin plate with dimensions of 20 mm × 25 mm with its thickness given in Table 1.

Table 1. Characteristics of target samples

Target	Thickness [mg/cm^2]	Purity [%]
Li	53	99.9
Be	34.3	99
C	14.6	99
Al	26.2	99.999
Cu	8.72	99.9
Nb	11.1	99.9
In	12.6	99.99
Ta	16.0	99.95
Au	19.9	99.95

Neutrons emitted from the targets were detected by two different-size EJ301 liquid organic scintillators (2” in dia.×2” thick and 5” in dia. ×5” thick) located at two different distances of 7 m and 20 m, respectively. The neutron DDXs were measured at angles of 0°, 5°, 10°, 15°, 20° and 25° for Li, Be, C, Al, Cu, Nb, Au (0°, 5°, 10°, 20° and 25° for In, Ta) by moving the target along the beam trajectory in the swinger magnet. The two-gate integration method was adopted to eliminate gamma-ray background. The neutron energy was determined by the time-of-flight (TOF) method. To obtain the absolute neutron flight time, the prompt gamma peak observed in the measured TOF spectrum was used as a reference point. The neutron energy was calculated from the flight time by the following equation:

$$E_n = \frac{mc^2}{\sqrt{1-\left(\frac{L}{L+c\Delta t}\right)^2}} - mc^2 , \tag{1}$$

where E_n is the neutron energy, m is the rest mass of neutron, c is the velocity of light, L is the flight path, and Δt is the time difference between the prompt gamma and neutron. Thus, the TOF spectrum was converted to the energy spectrum, $N_n(E_{n,}\theta)$. Next, the DDXs were derived from the energy spectrum by considering the target thickness, the solid angle subtended by the detector, the deuteron beam current, the neutron detection efficiency, and the attenuation correction of neutron fluxes as follows:

$$\frac{d^2\sigma}{dE_n d\Omega}(E_n,\theta) = \frac{1}{N_d D}\frac{N_n(E_n,\theta)}{\Delta\Omega\Delta E_n}\frac{1}{\varepsilon(E_n)}\frac{1}{A(E_n)}, \tag{2}$$

where $d^2\sigma/(dE_n d\Omega)$ is the DDXs, N_d is the number of incident deuterons, D is the areal density, $\Delta\Omega$ is the

solid angle subtended by the detector, ΔE_n is the energy bin, ε is the neutron detection efficiency, and A is the attenuation correction of neutron fluxes. The neutron detection efficiency calculated by the SCINFUL-QMD code [2] is shown for the 5" detector in Fig. 1. The attenuation of neutron fluxes in air at 7 m and 20 m was estimated by the PHITS code [3] with JENDL/HE-2007 [4] as in Ref. [1]. Fig. 2 presents the estimated attenuation fraction of neutron fluxes at 20 m as a function of neutron energy.

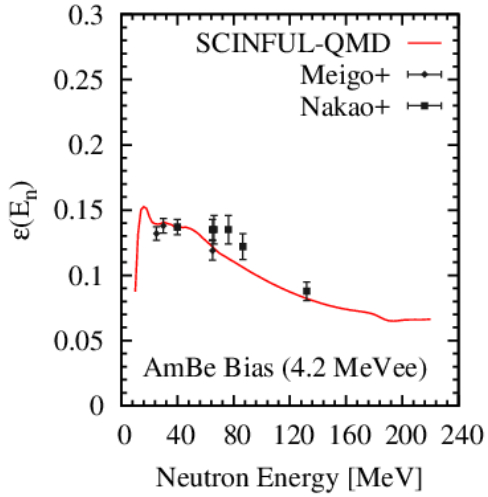

Fig. 1. Neutron detection efficiency calculated with SCINFUL-QMD and measured by Meigo and Nakao [5,6]

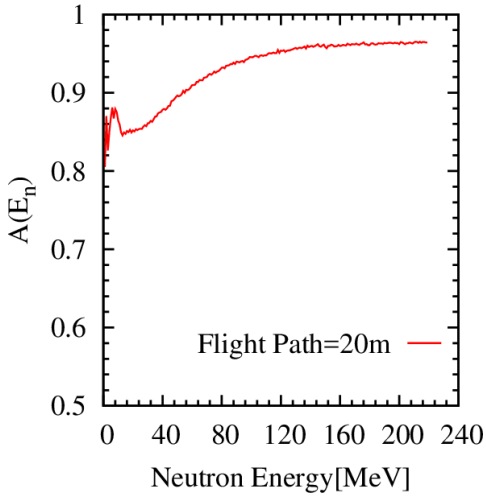

Fig. 2. Estimated attenuation fraction of neutron fluxes in air at the positions of 20 m

3. Results and discussion

3.1. Experimental results

In Fig. 3, the measured DDXs for Li, Be, C, Al, Cu, Nb, In, Ta, and Au at 0° are shown in comparison with theoretical model calculations by DEURACS [7] and PHITS [3]. It should be noted that these data were obtained by the data analysis of the 5" detector located at 20 m. Since the data analysis of the 2" detector located at 7 m has not yet been completed, the data below 12 MeV are not given. A broad peak around half of the incident energy (i.e., 100 MeV) is observed for each target. This characteristic peak is known to originate from elastic and non-elastic deuteron breakup reactions. The measured DDXs show monotonic increase with increasing target atomic mass. This tendency is also the same as in the previous data of 102 MeV [1].

3.2. Comparison with DEURACS calculations

The DEURACS calculation results are shown by the solid lines in Fig. 3. In DEURACS, elastic and non-elastic breakup reactions are described by the Continuum Discretized Coupled Channel (CDCC) [8] theory and the Glauber model [9,10], respectively. In addition, the Distorted Wave Born Approximation (DWBA) is employed for single-proton transfer reactions to bound states in the residual nuclei. Finally, the statistical decay process is calculated using the Hauser-Feshbach and exciton models implemented in the CCONE code [11,12]. Note that the above-mentioned DWBA component is not included in the DEURACS calculation shown in Fig.3. The DEURACS calculation is in excellent agreement with the experimental data, particularly in the broad peak region. However, some discrepancies between the DEURACS calculation and the experimental data are seen in the low emission

energy region below 50 MeV.

3.3. Comparison with PHITS calculations

The PHITS calculation results are shown by the dashed lines in Fig. 3. The PHITS code is based on a combination of different models to describe the total reaction cross section, the dynamical process, and the subsequent evaporation process. In the calculation, the dynamical and subsequent evaporation processes are described with the intra-nuclear cascade of Liège (INCL) model [13] and the generalized evaporation model (GEM) [14], respectively. In the present work, the MWO formula [15] is chosen for calculation of total reaction cross sections. Although the INCL component gives the board peak seen around 100 MeV for whole targets, the shape is slightly boarder than that seen in the experimental data. Also, it is found that the calculated cross sections around the peak underestimate the experimental ones considerably for C, Ta, and Au.

3.4. Angle-differential cross section at 0°

We obtained the angle-differential cross sections (ADXs) at 0° by integrating the DDXs over the emission energy range above 12 MeV. The results are shown as a function of target atomic number in Fig. 4. The DEURACS calculation is in better agreement with the experimental data than the PHITS calculation.

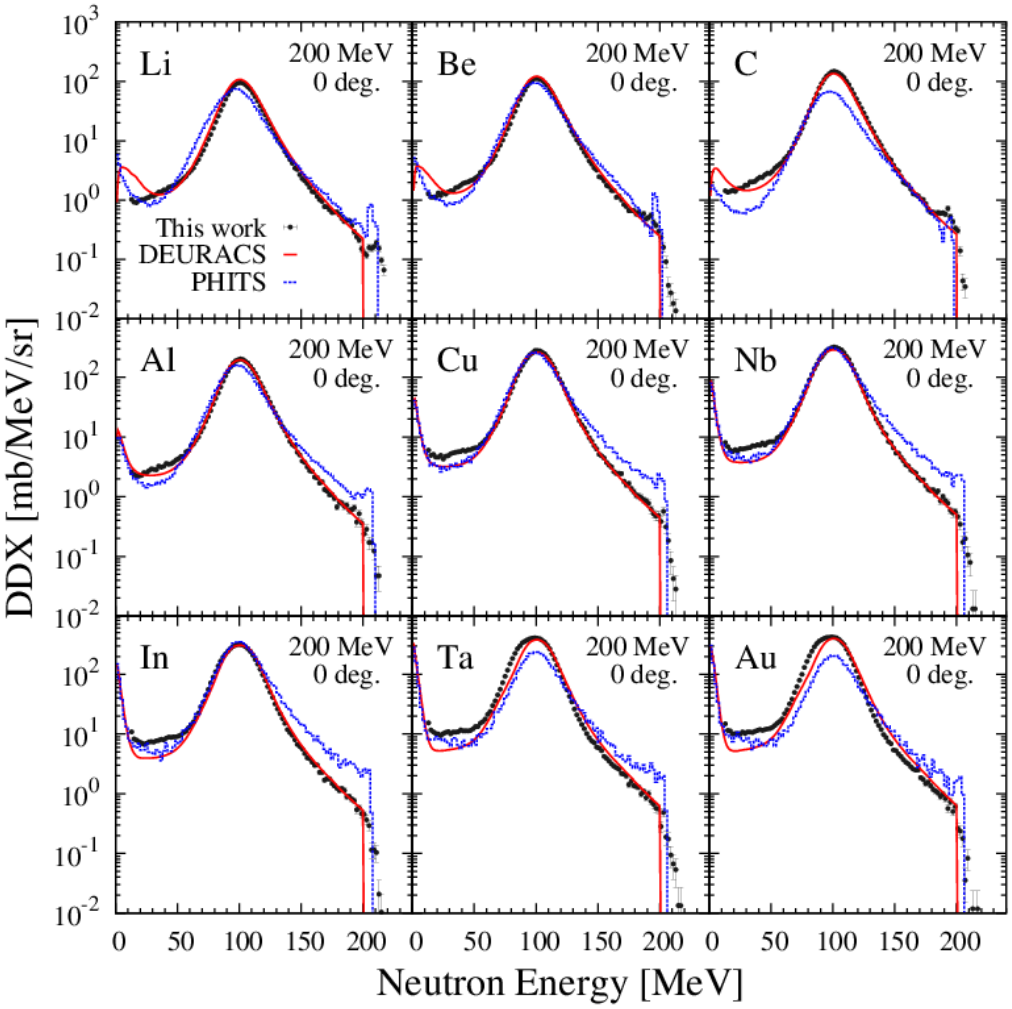

Fig. 3. Comparison of measured double-differential cross sections (DDXs) of 200 MeV (d,xn) reaction on Li, Be, C, Al, Cu, Nb, In, Ta, and Au at 0° with DEURACS and PHITS calculations.

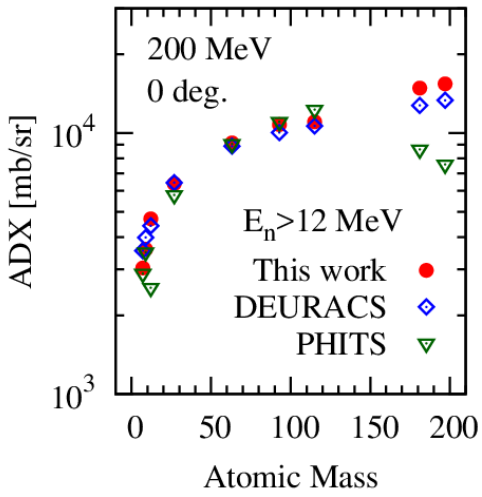

Fig. 4. Comparison of measured angle-differential (d,xn) cross section at 0° with DEURACS and PHITS calculations

4. Summary and outlook

The double-differential cross sections (DDXs) for 200-MeV (d,xn) reactions on Li, Be, C, Al, Cu, Nb, In, Ta, and Au were measured by the TOF method. The measured DDXs at 0° were compared with the DEURACS and PHITS calculations. The PHITS calculation reproduced the measured DDXs generally well, however the calculated broad peak around 100 MeV was found to be wider than the measured one. On the other hand, the DEURACS calculation showed excellent agreement with the measured DDXs, except in the low emission energy region below 50 MeV where the evaporation and pre-equilibrium processes are dominant.

In the future, we will derive the experimental DDXs in the low emission energy range below 12 MeV from the data taken by the 2" EJ301 detector, and then validate both the DEURACS and PHITS codes over whole ranges of emission energy and angle.

Acknowledgement

The authors wish to thank the staff of the RCNP for providing high-quality deuteron beams and for their assistance during the E474 experiment.

References

[1] S. Araki, et al., Nucl. Instr. Meth. A 841, 62-70 (2017).

[2] D. Satoh, et al., JAEA-Data/Code 2006-023 (2006).

[3] T. Sato, et al., J. Nucl. Sci. Tech. 50, 913 (2013).

[4] Y. Watanabe et al., Journal of the Korean Phys. Society, 59(2), 1040-1045 (2011).

[5] S. Meigo. Nucl. Inst. and Meth. in Phys. Res. A 401, 365 (1997).

[6] N. Nakao, Nucl. Inst. and Meth. in Phys. Res. A 463, 275 (2001).

[7] S. Nakayama et al., Phys. Rev. C 94, 014618 (2016).

[8] M. Yahiro et al., Prog. Theor. Exp. Phys. 2012, 01A206 (2012), and references therein.

[9] T. Ye, et al., Phys. Rev. C 80, 014604 (2009).
[10] T. Ye, et al., Phys. Rev. C 84, 054606 (2011).
[11] O. Iwamoto, J. Nucl. Sci. Technol. 44, 687 (2007).
[12] O. Iwamoto, et al., Nucl. Data Sheets 131, 259 (2016).
[13] A. Boudard, et al., Phys. Rev. C 87, 014606 (2013).
[14] S. Furihata, Nucl. Instr. Meth. B 171, 251 (2000).
[15] K. Minomo, et al., J. Nucl. Sci. Technol. 54 (1), 127-130 (2017).

24 Neutron Energy Spectra from Heavy Ion Reaction Using Efficiency by PHITS

Chihaya Tokumoto[1], Eunji Lee[1], Nobuhiro Shigyo[1], Tsuyoshi Kajimoto[2],
Naruhiro Matsufuji[3], Chalmin Ham[4], Tae-Sun Park[4],
Seung-Woo Hong[4], Koan Sik Joo[5]
[1] Kyushu University, [2] Hiroshima University,
[3] National Institute of Radiogical Sciences,
[4] Sungkyuankwan University, [5]Myongji University

Neutron production double-differential cross-section (DDX) and thick target yields (TTY) for carbon bombarded with 800 MeV/u silicon beam were measured by the time-of-flight method with NE213 liquid organic scintillators at six directions of 15, 30, 45, 60, 75, 90°. The detector response and detection efficiency of the scintillator to neutron were calculated by PHITS and SCINFUL-QMD, SCINFUL-QMD2. DDX and TTY were derived using the efficiencies and compared with simulation by PHITS and Geant4.

1. Introduction

Heavy ion accelerator facilities have been used for wide field including nuclear physics and material science, industrial and medical applications. In Korea, new heavy ion accelerator facility "RAON" construction is planned. Various kinds of secondary particles are emitted from a target irradiated by heavy ion beam. On the occasion of constructing heavy ion accelerator facilities, the shielding design for those secondary particles is important. In particular, neutron and γ-ray have a large effect for the human body due to their long mean free path.

Monte Carlo particle transport codes are useful tools to estimate radiation dose in accelerator facilities. However, experimental data of heavy ion incident neutron production as the source term are desired to validate the codes.

We measured neutron production double-differential cross-section (DDX) and thick target yield (TTY) on a graphite target bombarded with 800 MeV/u silicon beam by time-of-flight (TOF) method with NE213 liquid organic scintillators. The combination of beam and target is close to candidates in RAON. The experimental da-ta were compared with calculated results by Monte Carlo particle transport codes, PHITS [1] and Geant4 [2].

Neutron detection efficiency of the scintillator is one of essential information to obtain neutron energy spectra. Efficiencies by the SCINFUL-QMD [3] and SCINFUL-QMD2 codes [4] have been adopted. The SCINFUL-QMD agrees experimental data of detection efficiency in wide neutron energy range except for a gap at 150 MeV. The gap mainly comes from difference reaction rates between SCINFUL original database [5] and JQMD model. In this study, PHITS is applied to calculate detection efficiency from 1 to several hundred MeV in order to clear the gap problem.

2. Experiment

The experiment was performed at PH2 beam line of HIMAC facility in National Institute of Radiological Sciences. The experimental set-up is illustrated in Fig. 1.

A 5 cm × 5 cm × 2 cm (thin target) and a 5 cm × 5 cm × 24 cm (thick target) graphite targets for neutron production DDX and TTY measurements were irradiated with 800 MeV/u silicon beam. The thin target was placed on beam axis being rotated with 45° according to the axis, because the thin target thickness should have been kept almost same to all measurement directions. The effective thickness on the beam axis was 2.83 cm. The incident silicon ions lost 7 % of the energy in the target. The thickness of the thick target was larger than the range of the silicon beam.

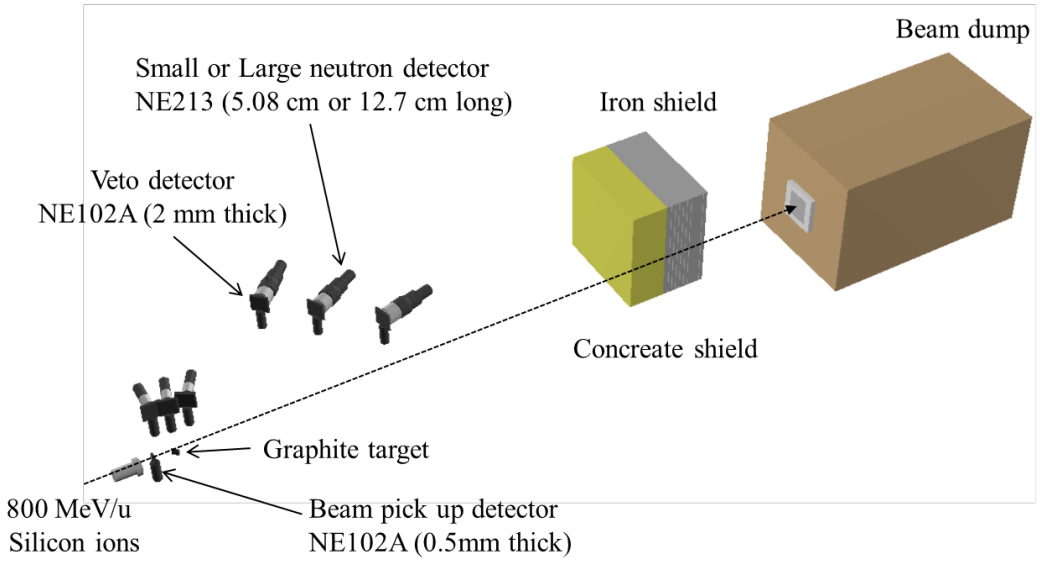

Fig. 1: Experimental set-up at PH2 beam line of HIMAC facility in NIRS.

The 0.5 mm thick NE102A plastic scintillators (beam pick up detector) were placed in front of the target to measure beam intensity and make timing signal for TOF experiment. The silicon ions were passed though the beam pick up detectors and were irradiated to the graphite target. Neutrons produced in the graphite target were measured with two sizes of NE213 liquid organic scintillators placed at six directions of 15, 30, 45, 60, 75 and 90°. The diameter and thickness of the large detector were 12.7 cm. These detectors were used to measure neutron above 5 MeV. On the other hand, the small detector was 5.08 cm long and in diameter, and used for neutrons below 10 MeV. The distance between the target and each neutron detector, i.e. flight path length, are tabulated in Table 1. To determine signal bias level, light outputs of neutron detectors were calibrated with γ-ray sources as ^{241}Am, ^{133}Ba, ^{137}Cs, ^{60}Co, and ^{241}Am-Be. A 2 mm thick NE102A scintillator was placed in front of each neutron detector as a veto counter. The light output data of veto detector were used to extract non-charged particle events. The concrete and iron shields were placed as drawn in Fig. 1 to reduce neutron background events from the beam dump. The thickness of concreate and iron were 50 and 63 cm, respectively.

Table 1: Flight path lengths.

Angle (deg.)	Flight path length (m) Large	Small
15	3.597	2.612
30	3.605	2.635
45	3.177	2.490
60	1.718	1.349
75	1.710	1.098
90	1.518	1.060

Neutron indirectly came from the target to the NE213 detectors should have been eliminated as background events, and those events were measured using iron shadow bars placed between the target and the neutron detectors. The lengths of shadow bars were 60 and 110 cm for small and large detectors, respectively.

NIM and CAMAC modules were used to process signal from all detectors. Data about amount of light output of all detectors were obtained with analog-to-digital converters (ADCs). The time difference between a signal of the NE213 detector and a signal of the beam pick up detector was obtained with a time-to-digital converter (TDC).

3. Analysis

In order to obtain energy spectra of neutron, experimental data were analyzed with main two processes. The first process was discrimination of neutron events. The second process was determination energy of neutron by time of flight data.

Non-charged particle events were extracted using light output data of the veto detector. The light output data of the detector is shown in Fig. 2. Events below 150 ch were extracted as non-charged particle events.

Neutron events were separated by using a 2D plot of light output for the neutron detector as shown in Fig. 3. The horizontal axis of the plot is integrated value of whole signal pulse (ADC total) and the vertical axis is integrated value of decay part of the signal pulse (ADC delayed). The widths of ADC total gate and ADC delayed gate were 200 and 150 ns. Events surrounded by red line in Fig. 3 were extracted as neutron events.

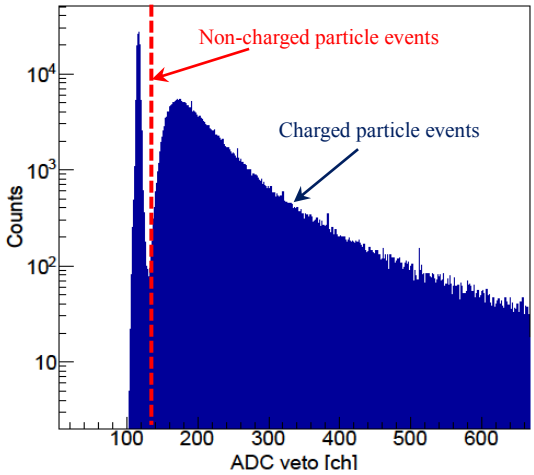

Fig. 2: Light output spectrum for the veto detector at 15°.

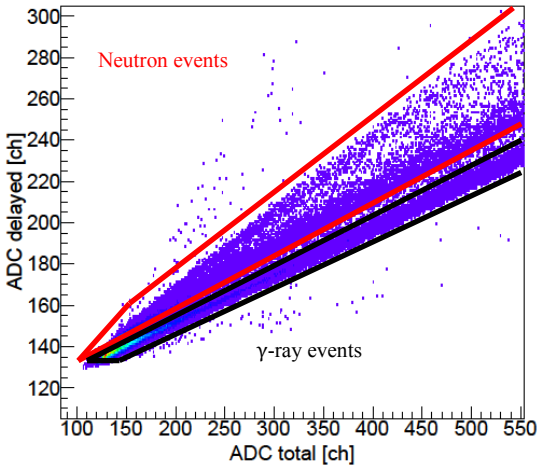

Fig. 3: Two-dimensional histogram of the light output for the neutron detector at 15°.

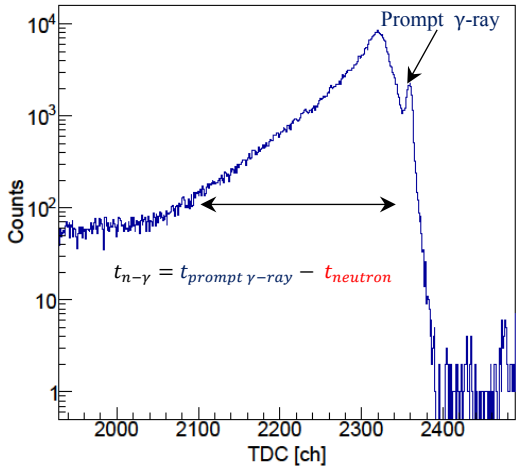

Fig. 4: Inverse TOF spectrum for the large neutron detector at 15°.

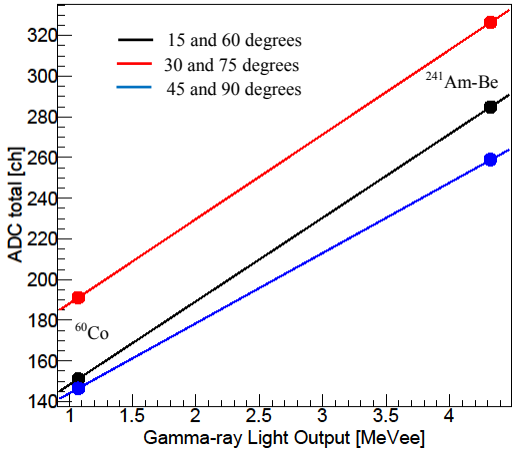

Fig. 5: Light output calibration line for large neutron detectors.

Figure 4 exhibits TOF spectrum for the large neutron detector at 15°. The horizontal axis is time difference between start signal of the neutron detector and stop signal of the beam pick up detector. The peak corresponding to prompt γ-ray events appeared at 2380 ch. Neutron kinetic energy E_n was determined by using the following formula (1):

$$E_n = \frac{m_n c^2}{\sqrt{1-\left(\frac{L}{ct_{n-\gamma}+L}\right)^2}} - m_n c^2 \qquad (1).$$

where m_n is rest mass of neutron, L is distance from the target to the neutron detector, c is velocity of light and $t_{n-\gamma}$ is difference of flight time between the prompt γ-ray and neutron. In this analysis, the bias level for the small detector was set to 0.073 MeVee and that for the large detector was set to 1.041 MeVee. The light outputs of detectors were calibrated by fitting data points obtained with the Compton edges of γ-ray sourece. The example of calibration curve is shown in Fig. 5.

Finally, neutron energy spectra were converted to DDX and TTY by the following equations (2) and (3):

$$DDX = \frac{N_n(E_n)}{N_{ion}\varepsilon\rho\Delta\Omega\Delta E} \qquad (2). \qquad TTY = \frac{N_n(E_n)}{N_{ion}\varepsilon\Delta\Omega\Delta E} \qquad (3).$$

where ε is neutron detection efficiency, N_n is the number of detected neutron, N_{ion} is the number of incident heavy ions, $\Delta\Omega$ is detector solid angle and ΔE is width of energy bin and ρ is density per unit of area. These parameters except for neutron detection efficiency were able to obtain from measurement data. Determination of neutron detection efficiency was described in the next chapter.

4. Detector response and detection efficiency

Neutron detection efficiencies by the SCINFUL-QMD and SCINFUL-QMD2 codes have been adopted. But a gap remains at 150 MeV. Therefore neutron detection efficiency was calculated with PHITS and JQMD-2.0 [6] was used as the nuclear reaction model in PHITS in order to clear gap problem. Neutrons were detected as light output of the scintillator converted from energy loss of secondary particles in the NE213 scintillator. The first step determination of detection efficiency was to calculate the deposition energies of the secondary particles. Then the deposition energies were converted into light output and light yield distribution (response function) was constructed. Deposited energy by secondary particles was converted by using the following equation (4) [7]:

$$L = a_1 E - a_2\{1 - exp(-a_3 E)\} \qquad (4).$$

where L (MeVee) is light output, E is deposition energy of the charged particle. The parameters of a_1, a_2 and a_3 were evaluated from the present experimental data by fitting to Eq. (4) with the least-square method. The values of the parameters are listed in Table. 2. The light-output curves given by the equation are indicated in Fig. 6.

Table 2: Parameters of Eq. (4).

Particle	Parameters		
	a_1	a_2	a_3
p	0.81	2.43	0.29
d	0.74	3.45	0.20
t	0.72	7.19	0.07
^{3}He	0.54	3.97	0.20
α	0.51	6.42	0.08

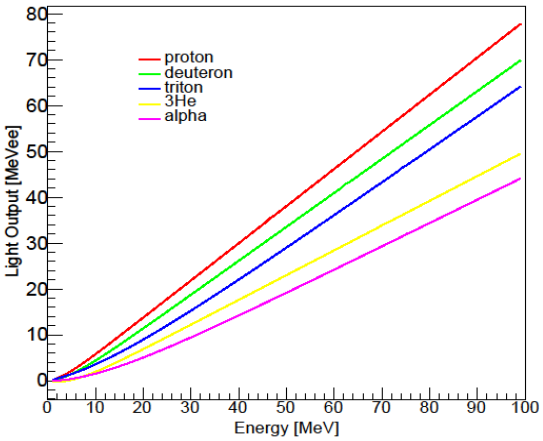

Fig. 6: Light output of charged particles.

Figure 7 shows the response functions from 120 to 200 MeV neutrons calculated by PHITS, SCINFUL-QMD and SCINFUL-QMD2. Furthermore, experimental data [4] are also indicated. For 170 and 200 MeV neutrons, PHITS express better agreement with experimental data in high light output region.

Finally, detection efficiency was derived by integrating a response function above the threshold level by using the following equation (5):

$$\varepsilon(E_n) = \int_{E_{min}}^{\infty} R(E_n, E_e) dE_e \qquad (5).$$

where $\varepsilon(E_n)$ is the detection efficiency for E_n (MeV) neutrons, E_{min} is the lower limit of light output (threshold level), $R(E_n, E_e)$ is the response function for E_n (MeV) neutrons. In Fig. 8, the detection efficiency for 5 MeVee threshold level calculated by PHITS was compared with the SCINFUL-QMD, SCINFUL-QMD2, and experimental data [4]. In case of detection efficiency calculated by PHITS, the gap at 150 MeV disappears. The calculated detection efficiencies by PHITS are in good agreement with experimental data below 200 MeV.

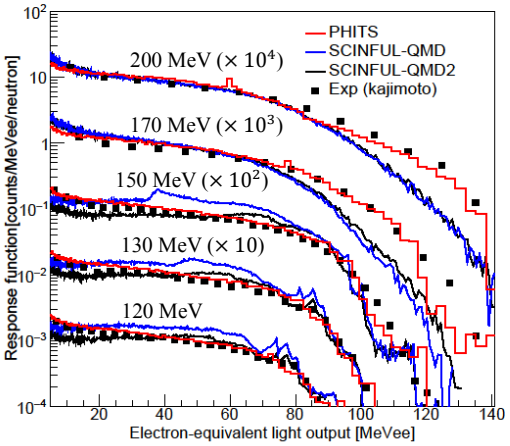

Fig. 7: Response function for 120 ~ 200 MeV neutrons.

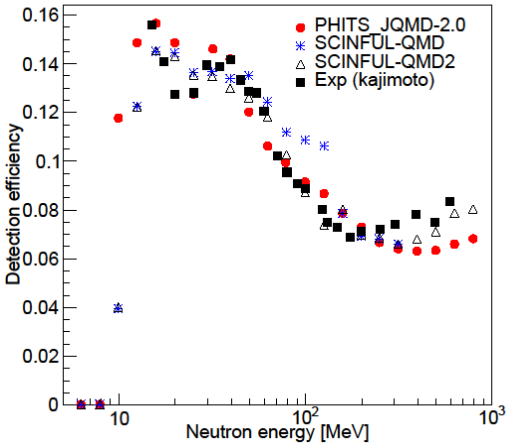

Fig. 8: Neutron detection efficiency for 5 MeVee threshold level.

5. Results

The experimental DDX and TTY were obtained by large size scintillators above 10 MeV as shown in the following figures. The neutron production simulations using PHITS and Geant4 were also performed. JQMD-2.0 (Quantum Molecular Dynamics) and GEM (Generalized Evaporation Model) were used for simulation of hadronic interaction caused by heavy ion in PHITS. And G4QMD and GEM models were applied in Geant4.

Figure 9 shows neutron production DDX for a graphite target bombarded with 800 MeV/u silicon ions at six directions. PHITS generally reproduced the experimental data. Geant4 largely underestimated the experimental data at 15, 30 and 45°.

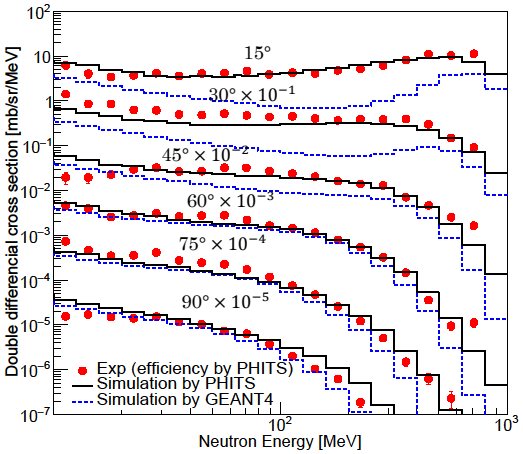

Fig. 9: Neutron production DDX at 15, 30, 45, 60, 75, and 90°.

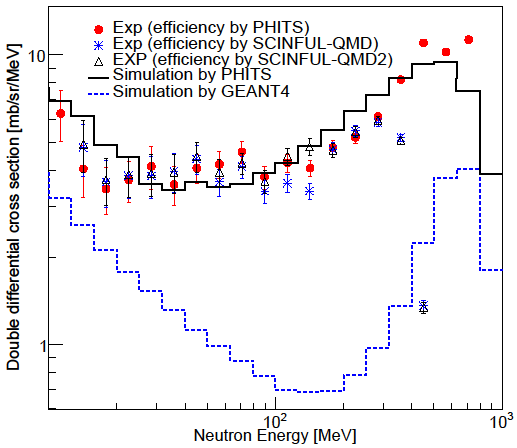

Fig. 10: Neutron production DDX at 15°.

In Fig. 10, DDXs at 15° derived using neutron detection efficiency calculated by PHITS, SCINFUL-QMD, SCINFUL-QMD2 were compared with calculated results by PHITS and Geant4 to see change of the energy spectrum among 3 detection efficiency calculations. The experimental DDX with detection efficiency by PHITS had the smallest change around 150 MeV among those DDXs by 3 codes and had large component above 400 MeV than those by other 2 codes. On the other hand, the DDX with detection efficiency by SCINFUL-QMD had a small drop around 150 MeV.

Figure 11 exhibits neutron production TTY for the reaction of 800 MeV/u silicon beam on the graphite target at six directions. PHITS reproduced the experimental data at forward angles better than Geant4. PHITS and Geant4 overestimated the experimental data at 90°.

In Fig. 12, TTY at 15° derived using neutron detection efficiencies calculated by 3 codes were compared with calculated results by PHITS and Geant4. The energy spectrum using detection efficiency by PHITS varied minimally with energy around 150 MeV. The drop around 150 MeV by SCINFUL-QMD was larger than other 2 codes.

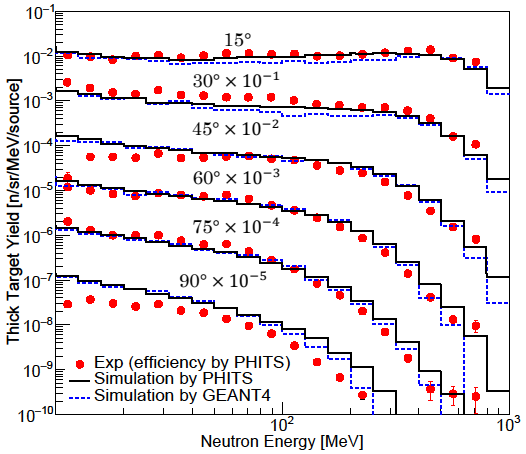

Fig. 11: Neutron production TTY at 15, 30, 45, 60, 75, and 90°.

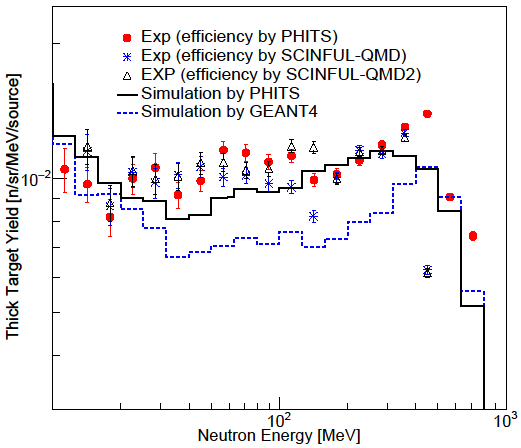

Fig. 12: Neutron production TTY at 15°.

6. Conclusion

Neutron production DDX and TTY for carbon bombarded with 800 MeV/nucleon silicon ions were measured. We examined neutron detection efficiencies for NE213 liquid organic scintillators calculated by PHITS and SCINFUL-QMD, SCINFUL-QMD2. We obtained the DDX and TTY above 10 MeV at six directions from 15 to 90° using calculated detection efficiencies with PHITS. The experimental DDX and TTY were compared with calculated results by Monte Carlo codes. PHITS generally reproduced the experimental data better than Geant4.

Acknowledgements

This work was performed as a Research Project with Heavy Ions at NIRS-HIMAC.

References

[1] T. Sato, et al.: J. Nucl. Sci. Technol., 50 (2013) 913.
[2] J. Allison, et al.: Nucl. Instrum. Meth., A835 (2016) 186.
[3] D. Satoh, et al.: JAEA-Data/Code, 2006-023 (2006).
[4] T. Kajimoto, et al.: Nucl. Instrum. Meth., A665 (2011). 80.
[5] J.K. Dickens: ORNL-6436 (1988).
[6] T. Ogawa, et al.: Phys. Rev., C92 (2015) 024614.
[7] N. Nakao, et al.: Nucl. Instrum. Meth., A362 (1995) 454.

25 Study on Nuclear Fission by Antisymmetrized Molecular Dynamics

Atsuhiko Etori[1], Akira Ono[2], Masaaki Kimura[3], Chikako Ishizuka[1], Shin Okumura[1], and Satoshi Chiba[1]

[1]Tokyo Institute of Technology, 2-12-1 Ookayama, Meguro-ku, Tokyo 152-8550, Japan
[2]Tohoku University, 6-3 Aramaki Aza-Aoba, Aoba-ku, Sendai 980-8578, Japan
[3]Hokkaido University, Kita 10, Nishi 8, Kita-ku, Sapporo 060-0810, Japan
[1]E-mail:etori.a.aa@m.titech.ac.jp

Abstract

We propose a new microscopic and dynamical model of nuclear fission in terms of antisymmetrized molecular dynamics (AMD). In this approach, the ground state of a heavy nucleus is prepared by the frictional cooling, and a boost momentum is given to constituent nucleons to the direction to split the nucleus into two fission fragments. As a first step, we give a simple boost momentum to simulate symmetric scission of ^{236}U at excitation of around 300 MeV, and calculate various quantities characterizing the fission fragments, namely, excitation energy, total kinetic energy (TKE), rotational angular momentum, and direction of emission of the fragments with respect to the initial elongation. It was found that distributions in these quantities were obtained, not as delta functions, due to various stochastic features inherent in AMD model. This is in sharp contrast and advantage of AMD model compared to deterministic theories such as TDHF (or TDDFT), which cannot give "distributions" unless some hypothetical initial distributions are given. It was found two-nucleon collision is essential in giving the distributions to these observables. The distribution of excitation energy as a function of the fragment mass numbers has a trend proportional to the fragment mass numbers, indicating that these fragments are formed after system has reached to a thermal equilibrium. It was also found that TKE values are in very good accord with experimental data at much low excitation energy, indicating a fact that the scission shape is pretty similar in both excitation energies. The average rotational angular momentum was found to be around 7 $\hbar$, which is very close to the extra-spin which fission fragments are believed to posses at scission. Furthermore, it was found that the fission fragments may not be necessarily emitted to the direction to which the initial elongation is oriented.

1. Introduction

About 80 years have passed since the phenomenon of nuclear fission was first discovered in experiments, but it is still difficult to understand nuclear fission processes from microscopical point of view precisely. In particular, the process from a compound nucleus through the saddle point to scission is a dominant process that determines the nature of the subsequent nuclei, but any theory which can give a rational explanation is not established yet. Furthermore, Auman *et al.* [1] showed experimental data that the spin difference between the compound nucleus and fission fragments is about 7$\hbar$. Unfortunately, no theoretical models can completely explain the origin of this extra spin. In recent years, experimental fission fragment mass yield distribution has been reproduced by Langevin model [2]. Such Langevin model is, however, a macroscopic-microscopic model that uses at most 3 to 4 variables to express the shape of the nucleus as dynamical parameters, and is based on adiabatic potential and transport coefficients. Studies based on these models should be continued from the perspective of nuclear data, but it is definitely required to establish a microscopic model to advance the understanding of fission processes as mentioned at the beginning. Therefore, in this study, we investigate the extent to describe the complicated large-amplitude collective decay mode of heavy nucleus, nuclear fission, using microscopic Antisymmetrized Molecular Dynamics (AMD) model. AMD model is known to have a great advantage to reproduce experimental data not only in nuclear structure [3] but also in nuclear reaction [4].

On the same way, research on the nuclear fission by the Time Dependent Density Functional Theory (TDDFT), which is a microscopic, non-adiabatic and also a dynamical model, has been actively conducted in recent years. Two examples of researches, which were recently published, related to nuclear fission by TDDFT are explained below. First, Goddard *et al.* [5] studied boost-induced fission (BIF) in the framework of TDDFT, where they calculate time evolutions from two starting points: the isomeric state and the second peak of the fission barrier. In addition, boosting method is a boost which made Hamiltonian with a quadrupole boost whose kinetic energy is uniquely determined by gauge conversion, and a time dependent excitation external field. All of them reproduced favorably well the peak of mass number distribution on ^{240}Pu, but the width of the mass distribution is out of the scope of these calculations. Secondly, Tanimura *et al.* [6] diversified the initial state deformation in a stochastic way, and calculated time evolutions from each point. This research overcame the disadvantages of the deterministic TDDFT and is a wonderful work to reproduce the distribution of TKE. However, the final distribution depends on the initial distribution, and there seems to be no way to uniquely determine the initial distribution on a reasonable footing.

To overcome the problems in deterministic theories, we developed a model named as the "boost model" in the framework of AMD. Unlike TDDFT, the AMD model can involve stochastic processes because two-nucleon collisions are taken into account. Therefore, distribution in the final results arises even if the calculations are stared from one ground state. Moreover, in this study, the time evolution is calculated from the ground state, rather than calculating from the outside the fission barrier. These are also different points from the TDDFT researches mentioned above. We can calculate the excitation energy and the rotational angular momentum of the fission fragments in addition to TKE, and verify the validity of the AMD model.

2. Boost model in AMD

In the AMD model, single-particle wave functions of nucleons are written in a form of Gaussian whose central position is represented by $\boldsymbol{Z}_i = \{\boldsymbol{r}_i, \boldsymbol{p}_i\}$ as $\boldsymbol{Z}_i = \sqrt{\nu}\boldsymbol{r}_i + \frac{i}{2\hbar\sqrt{\nu}}\boldsymbol{p}_i$, where ν denotes spacial width of the wave packet. Note that $\boldsymbol{r}$ and $\boldsymbol{p}$ do not express physical centers of the position and momenta of i-th nucleon. Total wave function of the system can be calculated by their Slater determinant where antisymmtrization is directly taken into account. More detailed explanation of the AMD model can be found in the previous works in the AMD model [7, 8]. In this study we focus on three stochastic effects included in the AMD model, namely, two-nucleon collisions, momentum fluctuation of emitted particles, and the rotational angle of the nucleus. Two-nucleon collision process evolves as follows: Test particles are randomly sampled regarding exact Wigner distribution of the AMD wave function as a probability distribution [8], then two nucleons are judged whether they can collide with each other by a nearest neighbor model [9]. When the test particle is sampled at the skirts of the Wigner distribution lying outside the fission barrier, the single particle can exceed the potential by this effect, even if it is trapped by the fission barrier. Thus the AMD model can take the tunneling effect of a single particle into account. The momentum fluctuation is also a longstanding problem in molecular dynamics approaches for quantum systems. The earlier AMD models had a problem to describe the time evolution that separately branches a small wave packet such as emission of particles. However, the recent AMD model [10, 11] can deal with even such minor branches. The third effect is the rotational angle of the nucleus. In this study, the position vectors of nucleons which are given as the real parts of $\boldsymbol{Z}$, are rotated by a three-dimensional rotation matrix for each event before the time evolution begins. Contrary to a deterministic framework, the time evolution in the AMD model is calculated from one initial state and some distributions, *e.g.* fission fragment mass distribution are obtained due to these three stochastic processes.

Next, we describe the boost model developed to simulate a nuclear fission process. In the boost model, a simple symmetric boost, to be explained below, is considered: The boost adds a certain amount of momenta based on the sign of $\boldsymbol{r}_z$ component of the position of each nucleon state, to the ground state of the initial compound nucleus for ^{236}U in this study. Under this prescription, we added the excitation energy to an initial state as a form of the kinetic energy to the extension direction. The calculation of the boost model in this study follows three steps. First, the initial rotational angle relative to fixed system of coordinates is randomly changed by the three-dimensional matrix. Then, a positive/negative momentum

will be added if r_Z is positive/negative, as follows:

$$\boldsymbol{p} \to \boldsymbol{p} + \left(0, 0, \frac{r_z}{|r_z|} \cdot p_{boost}\right). \tag{1}$$

Finally, we correct total angular momentum to be zero, in order to remove the influence of the angular momentum introduced by the boost. This is achieved in the following way:
We calculate the moment of inertia of the centroids according its definition, and example is given as below:

$$\boldsymbol{I}_{xx} = -m\sum_i (y_i^2 + z_i^2),\ \boldsymbol{I}_{xy} = -m\sum_i x_i y_i \tag{2}$$

then, we calculate other components by cyclically changing (x, y, z). The angular velocity vector of the system is given as a rigid rotor to be

$$\boldsymbol{\omega} = \boldsymbol{I}^{-1}\boldsymbol{L} \tag{3}$$

and the velocity of each particles (or states) associated with this rotation and total rotational angular momentum are given as

$$\boldsymbol{v}_i = \boldsymbol{\omega} \times \boldsymbol{r}_i, \tag{4}$$

$$\boldsymbol{L} = m\sum_i \boldsymbol{r}_i \times (\boldsymbol{\omega}_i \times \boldsymbol{r}_i). \tag{5}$$

Therefore, we subtract this velocity from each particle state:

$$\boldsymbol{p}_i^{'} = \boldsymbol{p}_i - m\boldsymbol{\omega} \times \boldsymbol{r}_i \tag{6}$$

With this corrected momenta, the rotational angular momentum of the whole system can be set to zero, as shown below,

$$\boldsymbol{L}^{'} = \sum_i \boldsymbol{r}_i \times \boldsymbol{p}_i^{'} \tag{7}$$

$$= \sum_i \boldsymbol{r}_i \times \boldsymbol{p}_i - m\sum_i \boldsymbol{r}_i \times (\boldsymbol{\omega} \times \boldsymbol{r}_i)$$

$$= \boldsymbol{L} - \boldsymbol{L} = 0 \tag{8}$$

In this way, we can inhibit rotation of the initial system due to introduction of the boost momentum.

In present calculations, we employ the Skyrme SLy4 force [12] as the effective interaction except for spin-orbit terms. The corresponding nuclear-matter incompressibility is $K = 230$ MeV at saturation density $\rho_0 = 0.160$ fm^{-3}. Also, the given boost, *i.e.* the applied momentum, p_{boost}, is 55 MeV/c. The time evolution of the system was calculated up to 10000 fm/c which is the range where actual fission can occur.

3. Results

In this study, the cases if one of the fragments has 50-80 % of the compound nucleus mass are regarded as nuclear fission event. We also observed many events that the nucleus released some neutrons before the statistical decay and that nuclear fission does not occur even if the excitation energy of the system is 310.09 MeV on average by boost. It is far from the excitation energy of several MeV on neutron-induced fission $n_{th} + {}^{235}\mathrm{U} \to {}^{236}\mathrm{U}$ which can occur in the nuclear reactors. However, the excitation energy is on the order of 200 MeV in the TDDFT calculations performed by Goddard *et al.* [5], where the time evolution starts from two initial states: isomeric state of the fission barrier and the second peak of fission barrier. In this paper, we discuss the possibility on such high excitation energy fission and we intend to improve this excitation energy problem in the future.

First, we will describe the ground state of ^{236}U which is the subject of this work. We solved the friction cooling equation and found the ground state. Figure 1 compares binding energies of uranium isotopes by the AMD calculations with corresponding experimental values. As can be seen from Figure 1, the binding energy of the ground state can be reproduced within a difference of several 10 keV. The enhancement can be reduced by changing the value of ν which is the width of the wave packet, although in this calculation we fixed it as $\nu = 0.16$ fm^{-2}. Next, we present the time evolution of nuclear fission calculated by boost model with snapshots.

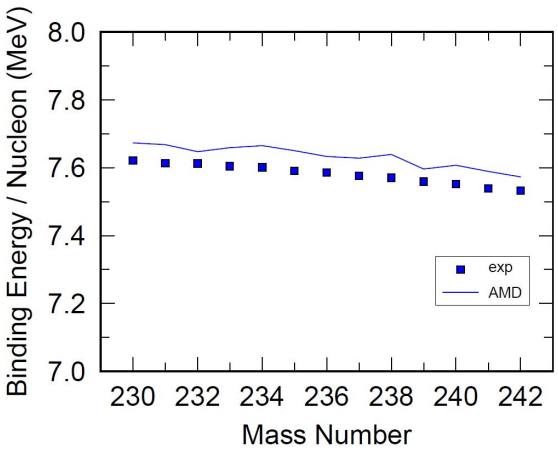

Figure 1: Comparison of experimental and calculated binding energy per nucleon for uranium isotopes.

In Figure 2, we picked four snapshots from the time-evolution of a fission configuration based on the boost model. In the first panel, the two-dimensional density distribution of the ground state at 0 fm/c is shown. In the second panel, one can see that the boost elongates the nucleus in the direction of the boost. It shows that the aspect of a super deformation between the first peak and the second peak of the fission barrier. In the third panel, super-deformed nucleus begins to rotate, but nucleus is still deforming even if the time evolution has reached 4500 fm/c. Also, we can see that the neck is developing. At the last panel, one can see that the compound nucleus finally split into two fragments. We were surprised that it took about 5000 fm/c to the scission point. Initially, the compound

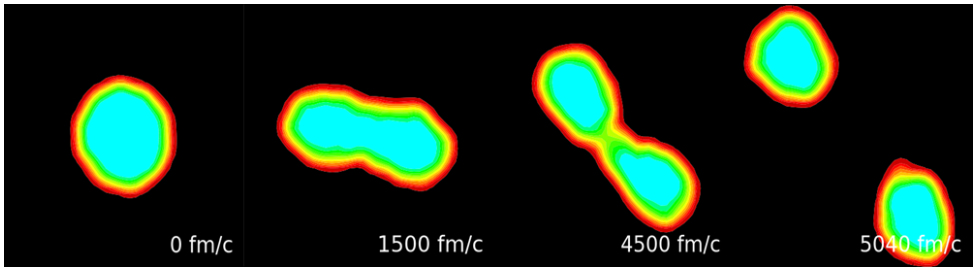

Figure 2: Density distribution of boosted ^{236}U. The size of the plot area in each time step is rectangular with 40 fm $\times$ 40 fm.

nucleus was excited by around 300 MeV due to the given 55 MeV/c momentum. We imagined that the nucleus would be torn immediately by boost. However, far exceeding our imagination, in many events nuclei have been deformed, the neck was developed, and scission occurred as a result. We analyzed that this is because thermal nuclear reactions occurred over a long period of time, i.e., because the thermal equilibrium was established. Therefore we believe that the two nuclei populated by the boost model can be regarded as the fragments made by nuclear fission. In Figure 3, the excitation energies of the fission fragments are plotted as a function of the mass number of fragments. Each point corresponds to the nucleus that appeared at each event. The excitation energy is obtained by subtracting the experimental binding energy of the corresponding nucleus from the calculated energy of each fragment. We refer to AME 12 [15] as experimental values. First, it should be noted that excitation energies of individual fission fragments, which are not discussed in other models, can be calculated by AMD. As can be seen from Figure 3, the excitation energy of the fission fragments calculated in each event is proportional to the mass number. From this result, the excitation energy of the fission fragment obtained by boost model obeys law of equipartition of energy. That means the compound nucleus became a thermal-equilibrium system before scission. Although there is a difference from the case of low excitation energy, the boost model has been able to describe the subsequent time evolution from the thermal-equilibrium state, regardless of which state was generated from the initial state by the boost.

In Figure 4, the total kinetic energy (TKE) calculated by the boost model is compared with experi-

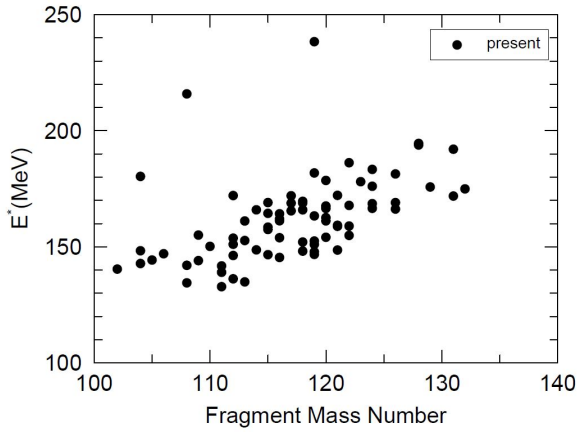

Figure 3: Excitation energy of fission fragments.

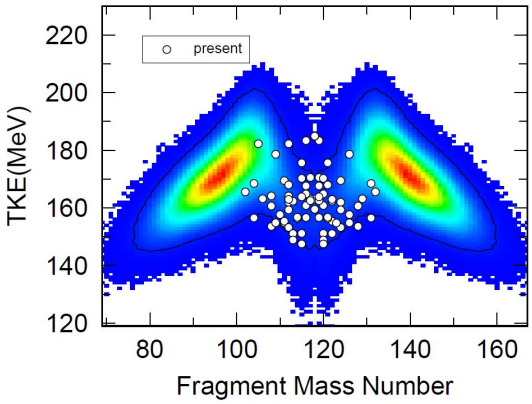

Figure 4: Total kinetic energy of fission fragments.

mental results [13] shown by the contour map. White circles are the calculated TKE. We can not treat asymmetric fission modes properly, because we introduced the symmetrical boost in the present model. Therefore, we mainly discuss symmetric fission mode by the boost model. In spite of the significant difference of the excitation energies, our calculation reproduces the TKE in the symmetric region , which will be supported from the experimental fact that the average TKE stays nearly constant value of 170 MeV [14].

Based on this experimental result, we can say that it is a great advantage to be able to reproduce such physical quantities with a microscopic model. It indicates that the TKE of fission fragments from thermally-equilibrated system has a kind of self-organized mechanisms.

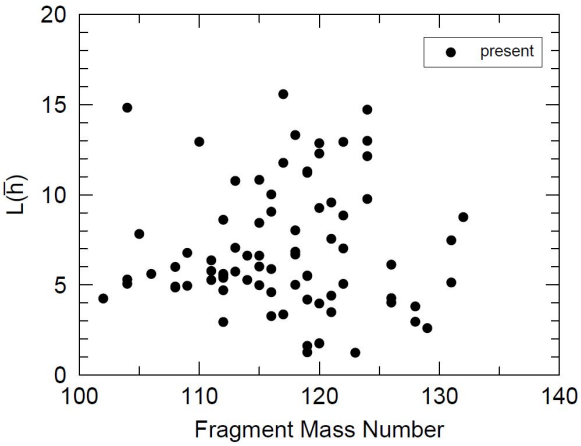

Figure 5: Rotational angular momentum of fission fragments.

Figure 5 shows the distribution of the rotational angular momentum of the fission fragments by the boost model. The calculated rotational angular momenta have values up to 15 $\hbar$, on average it is 7.12 $\hbar$. This result coincides with the result of experiment where the spin difference of the compound nucleus and fission fragment was found to be around 7$\hbar$ as mentioned before. Although further investigations and improvements of the model are still needed, we may say that this coincidence presents the possibility to explain the origin of spin brought by the nuclear fission.

Figure 6 shows that a ratio of angular momentum of the fission fragments $l_{\mathrm{H}}/l_{\mathrm{L}}$. This figure explains why the system starts to rotate in the middle of the reaction as shown in Figure 2. If the ratio of the angular momentum of the fission fragment is one, the two fragments cancel the rotation each other and the system will not rotate as a whole. Otherwise, the system starts rotating to conserve the angular momentum to be zero due to corrected angular momentum before time evolution in this work. This

result shows that the ratios of angular momentum of most of fission events are not one; it confirms that the system rotated so as to preserve angular momentum conservation.

In Figure 7, direction of emission of fission fragments are plotted as a function of angle θ relative to the boost direction. As already shown in the third panel of Figure 6, the system may start rotating before the scission. It weakens the attractive effect of the nuclear force in the neck region where the density of the neck becomes lower after a certain elongation of the neck region. Then, the nucleon flow tends not to move thorough the neck toward the other fragment but to stay in each fragment because the densities of the fragments are higher than that of the neck. Due to this effect, the collective rotation starts in spite of the existence of the neck. As the result, it is expected that the fission fragment can be emitted to the different direction from the initial boost one. As you can see from this figure, most of the fission events occurred in the same line of elongation (0 and 180 degree binary pairs). Additionally we also obtain the events where the fragments are released into the different direction from the one of elongation (10-170 degree binary pairs). By the summation of these counts, we find that total numbers of fission with/without rotation seem to be comparable.

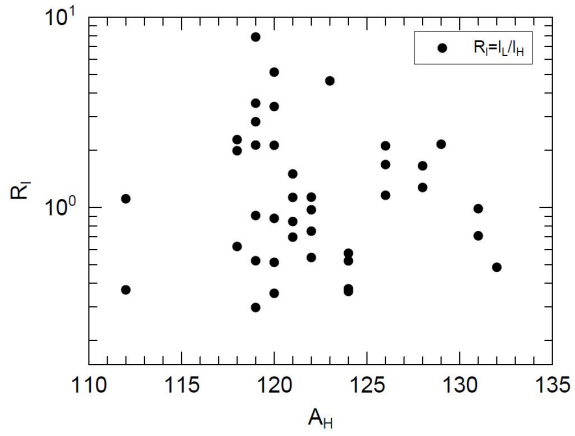

Figure 6: Ratio of angular momentum of fission fragments.

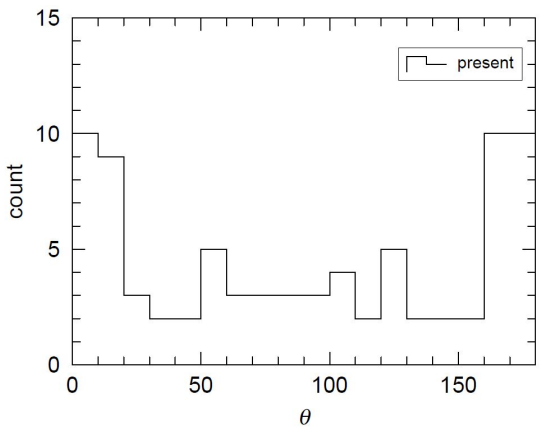

Figure 7: Direction of emission of fission fragments.

4. Conclusion

We developed the boost model to simulate nuclear fission by the AMD model. We found that the excitation energy of the fission fragments calculated in each event is proportional to the mass number and the boost model has been able to describe the subsequent time evolution from the thermal-equilibrium state. For TKE, we discussed only symmetric fission mode of mass distribution because of the boost model employed in this work. The calculated value is consistent with the expectation from experiments at low excitation energies, clearly shows a possibility that we may be able to extract information of the low-energy nuclear fission from such simulation study.

It was also found that the angular momentum of each fission fragment is around $7\hbar$. In addition, we also may present the probability to identify the origin of difference of spin between compound nucleus and fission fragments. The rotation before scission yields the fission fragments emitted to the different angle compared with the boost direction.

References

[1] D.C. Auman *et al.*: Phys. Rev.C **16**, 254 (1977).

[2] M.D. Usang *et al.*: Phys. Rev.C **94**, 004602 (2016).

[3] A. Ono *et al.*: Prog. Theor. Phys. **87**, 5 (1992).

[4] Y. Kanada-En'yo *et al.*: C.R.Physique 497 (2003).

[5] P. Goddard *et al.*: Phy. Rev. C **93**, 014620 (2016).

[6] Y. Tanimura *et al.*: Phys. Rev. Lett. **118**, 152501 (2017).

[7] A. Ono: J. Phys.: Conf. Ser. **420**, 012103 (2013).

[8] N. Ikeno *et al.*: Phys. Rev. C **93**, 044612 (2016).

[9] G. F. Bertsch *et al.*: Phys. Rep. **160**, 189 (1988).

[10] A. Ono: Euro. Phys. J. Web of Conferences **122**, 11001 (2016).

[11] A. Ono and H. Horiuchi: Phys. Rev. C **53**, 865 (1996).

[12] E. Chabanet *et al.*: Nucl. Phys. A **635**, 231 (1998).

[13] B. Becker *et al.*: Phys. Rev. C **87**, 014617 (2013).

[14] D.L. Duke, Ph.D. thesis, Colorado School of Mines, 2015 (unpublished).

[15] AME12: http://amdc.in2p3.fr/web/masseval.html (January 18 2018).

This is a blank page.

26 Microscopic Friction Coefficient and Potential for Fission Analysis

Takashi Nishikawa[1], Yoritaka Iwata[1], and Satoshi Chiba[1]
[1]Tokyo Institute of Technology
Email:nishikawa.t.ah@m.titech.ac.jp

We propose a new method to calculate friction coefficients, which affect dynamics of both the fusion and fission reactions, in a microscopic and dynamical way based on the time dependent density functional theory. It was found that calculated friction coefficients decrease as a function of collision energy due primarily to the spin-orbit interaction in the effective nucleon-nucleon force. Our friction coefficients are fairly close to the values calculated by a semi-classical wall-and-window method which is frequently used in Langevin calculation of nuclear fission.

1. Introduction

Energy dissipation and potential are important ingredients in understanding nuclear dynamics. Energy dissipation treated as friction coefficients in e.g. Langevin model, influences the phenomena like extra-push in fusion reactions, and timescale and pre-scission neutron emission in fission, etc. In most of previous studies on nuclear fission, friction coefficients are calculated by static frameworks, for example, the wall-and-window formula and the liner response theory. The wall-and-window formula gives the nuclear friction in a semi-classical way without any information on single particle structure nor the temperature dependence of nuclei [1]. On the contrary, the liner response theory gives nuclear frictions based on the single-particle structure calculated by macro-micro treatment in an adiabatic way [1]. If it is used in conjunction with BCS model, the nuclear friction increases as a function of temperature due to the breakage of Cooper pair as excitation energy gets larger [1], and tend to saturate at the value given by the wall-and-window formula as the high-temperature limit. This feature affects the fission mechanisms as a function of excitation energy. The nucleus-nucleus potential is also an important ingredient since it gives the driving force for both the fusion and fission reactions. Here, however, we focus on proposing a new method to calculate the friction coefficient as a first step from a microscopic and dynamical framework: Time-Dependent Density Functional Theory (TDDFT).

2. Methods

2.1 Time-Dependent Density Functional Theory(TDDFT) using Skyrme Force

TDDFT gives the single-particle wave functions in a self-consistent way based on nucleon-nucleon interaction, and the interaction used in this study includes spin-orbit force (LS force) which is important for giving shell effects for medium to heavy nuclei. Describing fission in terms of nucleon degree of freedom is an important subject in both nuclear physics and nuclear engineering (nuclear data) fields. There are some works describing fission by TDDFT [2,3] directly, but they are not sufficient yet since most of the calculations have to be started outside the barrier [3]. Instead of treating the fission explicitly by the TDDHF, we calculate here the friction coefficients in a microscopic and dynamical manner, which may then be used in the Langevin-type calculations.

We simulate nuclear collision reaction by TDDFT using Skyrme force [4]. In order to simulate nuclear reaction, we have to prepare good initial state reproducing nuclear property by DFT calculation. Skyrme interaction has a number of parameters. There are many parameter set, and by choosing appropriate parameter set, we can reproduce nuclear property. In this work, we use SV-bas [5] as the parameter set. SV-bas reproduces nuclear bulk property of magic and semi-magic nuclei. In TDDFT framework, nuclear reaction is calculated in a self-consistent manner. TDDFT does not include the effect of nucleon-nucleon collision in nuclei and the effect of tunneling is not treated sufficiently. The probability of nucleon-nucleon collisions increases as the collision energy increases. The approximated collision energy range without nucleon-nucleon collision is believed to be below 10 MeV per nucleon. Therefore, we limit the collision energy per nucleon from 1 MeV to 10 MeV in this study.

2.2 Friction Coefficient

A method to calculate friction coefficients in terms of the TDDFT has been proposed in a previous study [9]. In their study, the authors simulate head-on collisions of two nuclei at collision energy E, and calculate a time-dependence of distance $R(t)$ between centers of mass of the two nuclei based on the wave function $\Psi(\boldsymbol{r}, t)$. By fitting this TDDFT trajectory $R(t)$ with the following Newtonian equation of motion, the friction coefficients are derived:

$$\mu\ddot{R}(t) + \frac{dV}{dR} + \gamma\dot{R}(t) = 0 \ldots (1)$$

where coefficients μ, V, γ are reduced mass, potential and friction coefficient, respectively. In previous study [6], they used the same equation as Eq.(1) for slight different collision energy E+ΔE to calculate two coefficient γ, dV/dR simultaneously. However, this method has the risk that two coefficients diverge. Therefore, the method has difficulty for a systematical calculation and

In this study, we propose a new method to calculate γ by using a single $R(t)$ at specific collision energies as the average friction coefficient, where "average" denotes averaged over time during two nuclei overlap. Multiplying $\dot{R}(t)$ to both sides of Eq.(1), and integrating Eq. (1) by time t, we can obtain the following average friction coefficient γ:

$$\int_i^f \mu \ddot{R}\dot{R}dt + \gamma \int_i^f \dot{R}\dot{R}dt + \int_i^f \frac{dV}{dR}\dot{R}dt = 0$$

$$\Leftrightarrow \gamma = \left\{\left(\frac{1}{2}\mu\dot{R}_f^2 - V_f\right) - \left(\frac{1}{2}\mu\dot{R}_i^2 - V_i\right)\right\} \Big/ \int_i^f \dot{R}\dot{R}dt \ldots (2)$$

where the subscripts i and f represent the time just before fusion and after separation of the two nuclei, respectively. The numerator in Eq.(2) is the total energy loss of the two nuclei during they are in touch with each other. This calculation method enables us to derive γ systematically for definite collision energy and to analysis energy dependence of it explicitly.

3. Results and Discussion

Figure 1 shows collision-energy dependencies of friction coefficients for 4 combinations of collision partners, namely, ^{16}O+^{16}O, ^{40}Ca+^{40}Ca, ^{56}Ni+^{56}Ni and ^{100}Sn+^{100}Sn. We notice that the friction coefficients get larger for collisions of nuclei having larger mass numbers. This is probably due to the fact that the friction must get stronger to decelerate heavier nuclei. However, the values are almost similar when we divide the friction coefficient by the total mass number (see the value denoted in each panel of Fig.1, which is $\gamma/(2A)$ at 7 MeV/A). Those findings suggest that the friction coefficients are almost proportional to the mass number. We also notice that the calculated friction coefficients for different systems have a common tendency to decrease as functions of collision energy. This may be again due to the fact that the duration time is shorter for higher incident energy. However, this conclusion may be significantly altered when the pairing interaction is included especially at low collision energy, as was obtained by the linear response theory [1] mentioned above.

Figure 2 compares friction coefficients with full nuclear force (mesh bar) and when LS force is discarded (filled bar) for collisions between two ^{16}O nuclei. We notice that the friction coefficients are almost constant in the calculation without LS force. It means that the collision energy dependence of friction coefficient is brought almost thoroughly by the LS force.

Figure 3 shows a comparison of the friction coefficient calculated by the present method (TDDFT) at 3 to 10 (MeV/A) with that calculated by wall-and-window formula, which is used in Langevin calculation [1]. Note that the friction coefficient in this study does not have R dependence because it is averaged over time t. This graph shows that the magnitude of the friction coefficient obtained by the present approach is in the range of that calculated by the semi-classical wall-and-window formula.

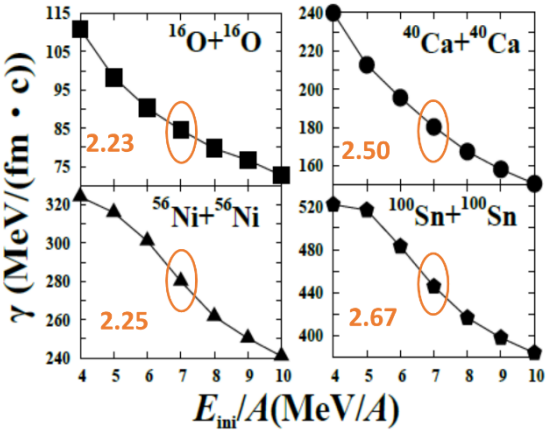

Fig 1. Time-averaged friction coefficients for different combinations of colliding nuclei

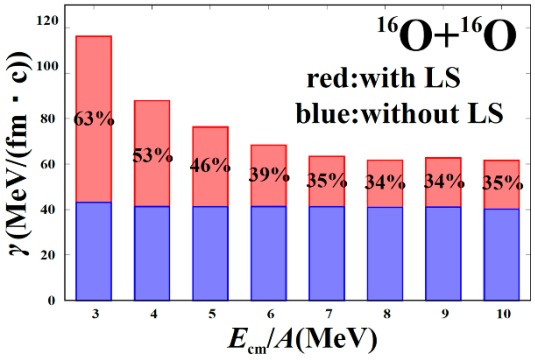

Fig 2. Friction coefficients with and without LS force

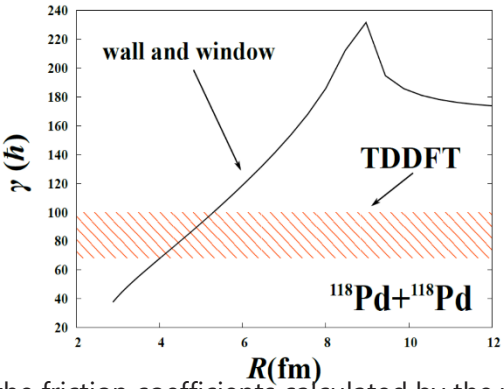

Fig 3. Comparison of the friction coefficients calculated by the wall-and-window formula (solid line) and present method (shaded area) for ^{118}Pd+^{118}Pd reaction leading to ^{236}U compound nucleus at 7 (MeV/A)

4. Summary

We propose a new method to calculate friction coefficients of nuclear collision from microscopic dynamical framework, TDDFT. We found that the friction coefficient divided by the total mass number does not differ much from system to system, and that the friction coefficients decrease as functions of the collision energy. This decrease was found to be brought almost thoroughly by the spin-orbit force in the nuclear force.

References

[1]M.D.Usang, et al., Phys. Rev. C 94 (2016) 044602.

[2]J. W. Negele, et al., Phys. Rev. C 17 (1978)1098-1115.

[3]Aurel Bulgac, et al., Rhys . Rev. Lett. 116 (2016) 122504.

[4]D. Vautherin and D. M. Brink, Phys. Rev. C 5 (1972)626.

[5]P. Klupfel, et al., Phys. Rev. C 79 (2009) 034310.

[6]K. Washiyama and D.Lacroix, Phys. Rev. C 78 (2008) 024610.

This is a blank page.

27 Independent Yields Derived from Nuclear Shell Correction and Boltzmann Weight

Kohsuke TSUBAKIHARA, Shin OKUMURA, Chikako ISHIZUKA, Tadashi YOSHIDA
and Satoshi CHIBA
Laboratory for Advanced Nuclear Energy, Tokyo Institute of Technology.
e-mail: tsubakihara.k.aa@m.titech.ac.jp

The fission product yields play a crucial role to determine the property of the decay heat (DH) and the delayed neutron (DN) and they strongly affect to the calculated results about the post-irradiation examination of nuclear reactors. In this work, we estimate how the isobaric independent yields increase or decrease from systematic Gaussian distribution depending on the *Z* and *N* number of produced nucleus, which is regarded as odd-even effects. We propose a new formula for fission product yield evaluation as a form of Boltzmann factor calculated with shell correction energies ΔE_{sh} estimated by a theoretical mass formula and paring energies. Based on this formula, independent yields of $^{235}\mathrm{U}+\mathrm{n_{th}}$, $^{235}\mathrm{U}+\mathrm{n_f}$ and $^{239}\mathrm{Pu}+\mathrm{n_{th}}$ are calculated, where the model parameters are fixed to reproduce odd-even staggering from Gaussian distribution. Derived independent yields are validated from DH and DN in burst fission. We find the present formula has enough reproduction power and an isomer ratio has a decisive role to DN and tend to enhance it.

1. Introduction

Evaluation of fission product yield (FPY) of long-lived fission products (LLFP) is highly important when we consider the burn-up calculation and the transmutation of LLFP in fast reactors [1] and aim to make them precise. In addition, FPY plays a crucial role to determine the property of the decay heat (DH) and the delayed neutron (DN). They also affect to the calculated results about the post-irradiation examination of nuclear reactors. There are, however, less available data of fast-neutron-induced fission reactions. Thus, it is strongly needed to establish the method which is applicable in wide ranges of mass numbers and excitation energies.

These isobaric independent yields tend to increase or decrease from systematic Gaussian distribution depending on the Z and N numbers of produced nucleus, which is regarded as odd-even effects. The pairing effects between nucleons are known as one of candidates to make an even-even nucleus more energetically stable than an odd-odd nucleus. In previous works by Wahl [2], the odd-even effects are treated phenomenologically and parameters concerning about them are determined so as to reproduce

experimental independent yields. This model has been quite successful but it is less predictive: it cannot be applied to the system where there are not enough experimental data. The stability coming from the odd-even effects determines how much each nucleus is produced as independent fission products, and it should be taken into account if we aim to establish a theoretical framework to evaluate FPY based on the knowledge of nuclear theory.

In this work, a new formula for FPY evaluation as a form of Boltzmann factor calculated with a shell correction energy ΔE_{sh} which are calculated by theoretical mass formula [3]. Based on this formula, independent yields of ^{235}U+n_{th}, ^{235}U+n_f and ^{239}Pu+n_{th} reactions are calculated, where the model parameters are fixed so as to reproduce odd-even staggering from Gaussian distribution. Derived independent yields are validated by calculating DH and DN in a burst fission.

2. Evaluation Method

According to the scission point model by Fong [4] and Wilkins[5], the independent yields $Y_I(Z,A)$ can be calculated based on the Boltzmann factor of the potential at the scission point as,

$$Y_I(Z,A) \propto \exp\left[-\frac{E_{\mathrm{LD}}(Z,A)+\Phi(E^*)\Delta E_{\mathrm{sh}}(Z,A)}{T(Z,A)}\right] .$$

In this work, we assume this Boltzmann factor can be divided into two parts: normalized Gaussian distribution on each isobar and the damping factor estimated by the shell correction energy. Then, $Y_I(Z,A)$ can be calculated as the product of them as follows,

$$Y_I(Z,A) = Y(A) \times F_{\mathrm{oe}} \times \frac{1}{\sqrt{2\pi}\sigma(A)} \int_{-0.5}^{0.5} \exp\left[-\frac{\left(Z - Z_p(A) + t\right)^2}{2\sigma(A)^2}\right] dt$$

$$F_{\mathrm{oe}} = \exp\left[-\frac{\Delta E_{\mathrm{sh}}(Z,A)}{E\ (A)}\right]$$

where we employ the Boltzmann-factor-type weight F_{oe} to represent a fine structure from odd-even effect, which schematic view is shown in Figure 1; FPYs of even-even (odd-odd) nuclei tend to be larger (smaller)

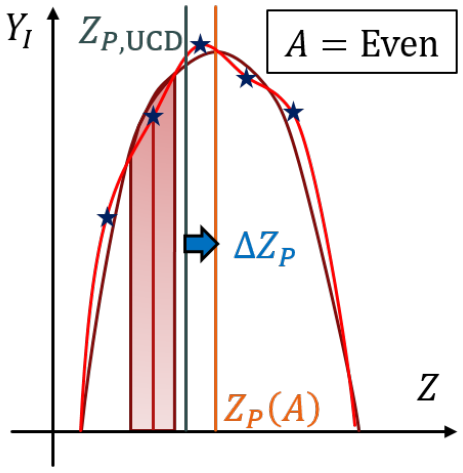

Figure 1: Schematic view of $Y_I(Z,A)$ on isobars

than expected Gaussian distribution. KTUY mass formula [3] is applied to estimate the shell correction energy $\Delta E_{\mathrm{sh}}(Z,A)$. Paring energies are included in $\Delta E_{\mathrm{sh}}(Z,A)$ with a simple form as,

$$E_{\mathrm{pair}} = {}^{12}/_{\sqrt{A}} \text{ MeV(odd-odd nucleus)}, \ -{}^{12}/_{\sqrt{A}} \text{ MeV(even-even nucleus)}, 0 \text{ (the others)},$$

respectively. By comparing experimental data taken from EXFOR database [6] and evaluation data, JENDL/FPY-2011 and JEFF-3.1, the parameters in the formula, $\sigma(A)$, $Z_{\mathrm{p}}(A)$ and $E_{\mathrm{d}}(A)$ are determined on each mass number, A. Hereafter, we rewrite the parameter $Z_{\mathrm{p}}(A)$ by using a deviation $\Delta Z_{\mathrm{p}}(A)$ from UCD (Unchanged Charge Density) ansatz where the ratio between Z and A numbers is "unchanged" after the scission compared to the one of compound nucleus. Based on this anstaz, $Z_{\mathrm{p}}(A)$ is represented as,

$$Z_{\mathrm{P,UCD}}(A) = \left({}^{Z_{\mathrm{comp}}}/_{A_{\mathrm{comp}}}\right) \times A, Z_{\mathrm{p}}(A) = Z_{\mathrm{P,UCD}}(A) + \Delta Z_{\mathrm{p}}(A),$$

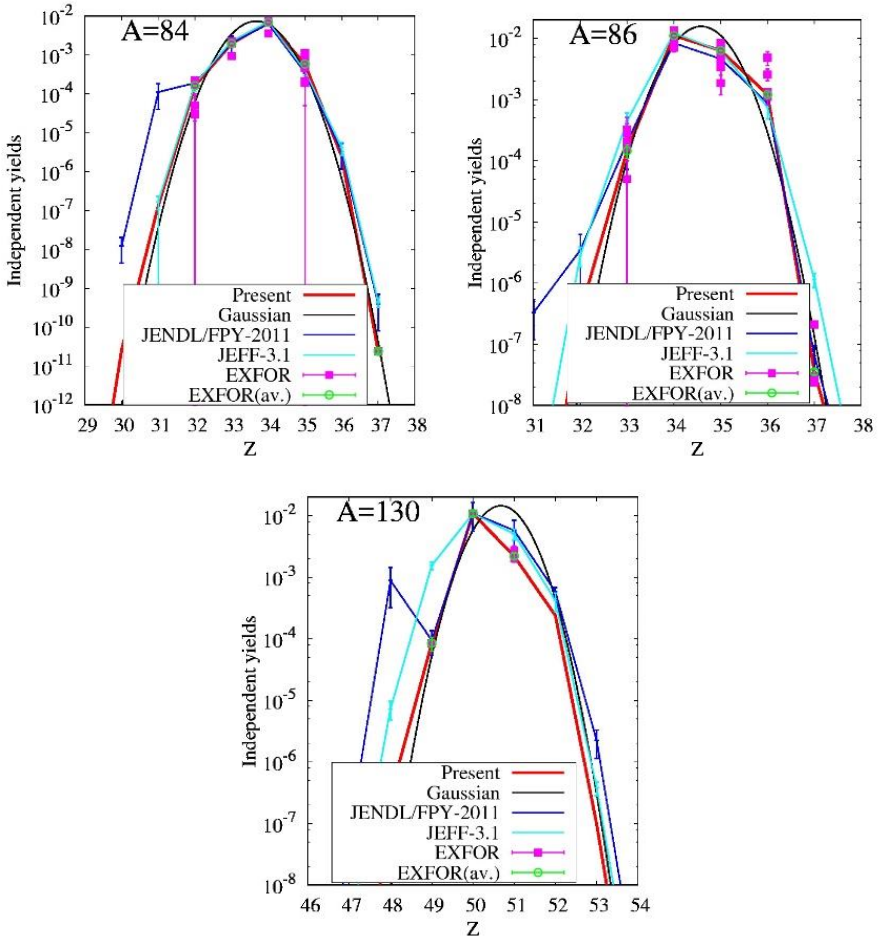

Figure 2: The charge number distributions of $Y_I(Z,A)$ at A=84 (left panel), A=86 (middle panel), and A=130 (right panel). Red lines show the results of the present formula. Black lines present the results of pure Gaussian distributions without odd-even effects. Blue and cyan lines correspond to the result of evaluation database, JENDL/FPY-2011 and JEFF-3.1, respectively. Magenta and green points are experimental independent yields taken from EXFOR and their averages, respectively.

where Z_{comp} and A_{comp} are the charge and mass number of the compound nucleus. Calculated FPY should be validated by estimating the decay heats and the delayed neutrons in burst fission and we compute them by applying Oyak-code[7].

3. Results

First, we present how well odd-even staggering is explained by the present formula. In Fig. 2, calculated FPYs at A=84 (left panel), A=86 (middle panel), and A=130 (right panel) are plotted as a function of charge number Z and compared with evaluated database, JENDL/FPY-2011 and JEFF-3.1, and experimental data taken from EXFOR. With the present formula, the distributions which are distorted from pure Gaussian distribution shown by black lines can be well reproduced at both light and heavy mass distributions as shown in Fig. 2.

In Fig. 3, $Y_I(Z, A)$ of the isotopes of LLFP are shown as a function of mass number A. As shown in this figure, LLFPs locate at the skirt of $Y_I(Z, A)$ distribution except for ^{126}Sn. Thus, that implies cumulative

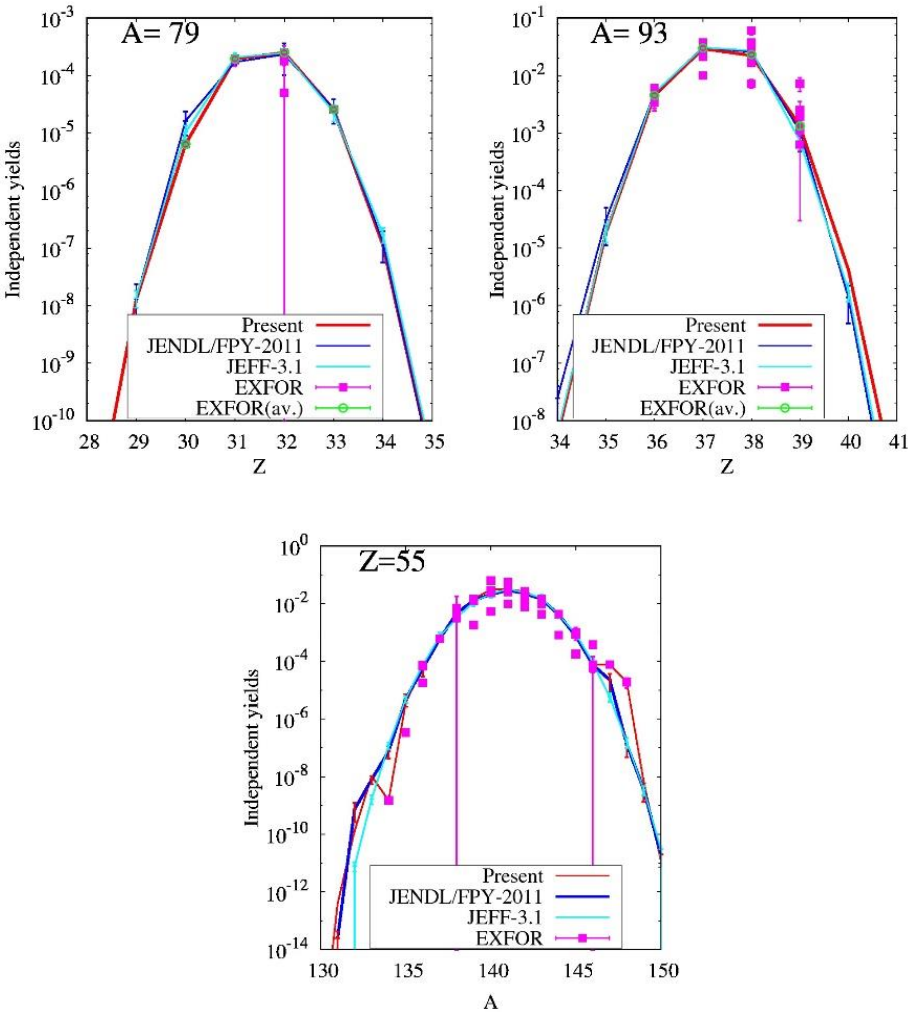

Figure 3: Independent yields in the region where LLFP are included. All legends are same as Fig. 2.

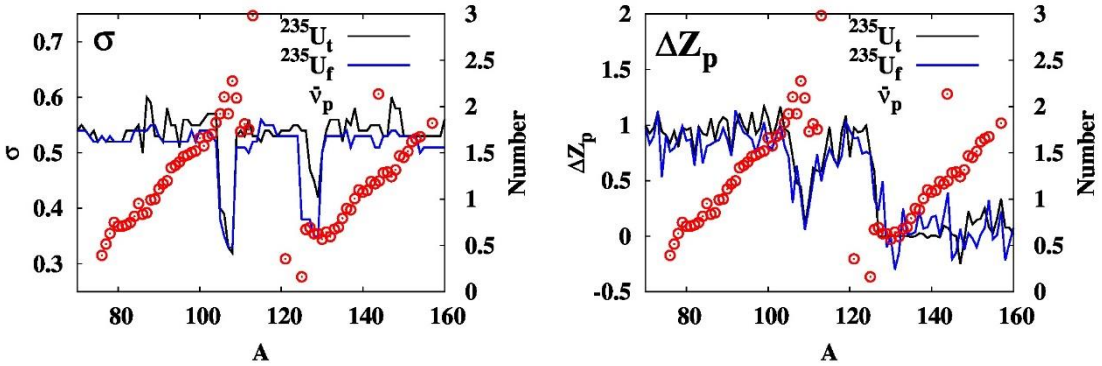

Figure 4: Deduced parameters for ^{235}U+n$_{th}$ and ^{235}U+n$_f$ fissions. Black and blue lines correspond to ^{235}U+n$_{th}$ and ^{235}U+n$_f$ fissions in left ($\sigma(A)$) and right ($\Delta Z_p(A)$) panels, respectively. Using right-y axis, experimental neutron multiplicities $\bar{\nu}(A)$ of ^{235}U+n$_{th}$ are also plotted by red points in both panels.

yields are important in these LLFP region. We will derive them based on statistical decay based on newly-calculated independent yields and we will examine their properties around LLFP regions.

Deduced parameters $\sigma(A)$ and $\Delta Z_p(A)$ so as to reproduce the experimental and evaluated FPY of ^{235}U+n$_{th}$ and ^{235}U+n$_f$ are plotted in left and right panel of Fig. 4, respectively. Both two parameters have characteristic behavior around $A \cong 130$ region which lies at around the minimum of neutron multiplicities $\bar{\nu}(A)$ shown by red points and right-y axis. We also find same behavior around $A \cong 105$ region as a pair of $A \cong 130$ fission products. From this result, the position of these dips seems to have some connections with $\bar{\nu}(A)$. Recently, Ishizuka *et al.*[8] proposed a four-dimensional (4D) Langevin model, which enables

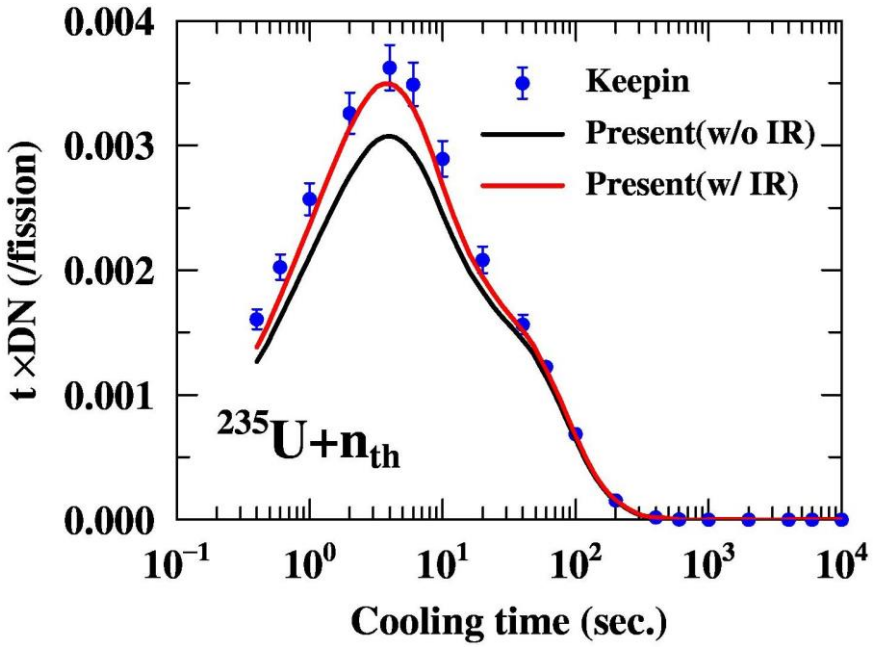

Figure 5: Calculated delayed neutrons (DN) on ^{235}U+n$_{th}$ as a function of cooling time. Black and red lines correspond to the results with or without isomer ratio contribution, respectively. Experimental DNs estimated by Keepin are also plotted by blue points.

to deal with the deformation of each fragment independently. With this model, they found the deformation of fission fragments shows a sawtooth structure as a function of mass number A, corresponding to similar structure of $\bar{\upsilon}(A)$. Thus, we may predict the position of the dips if $\bar{\upsilon}(A)$ or other quantities connecting to $\bar{\upsilon}_{\mathrm{P}}(A)$ are estimated reliably based on such theoretical model in future.

Finally, calculated DNs with the present formula are revealed in Fig. 5. Experimental data are also presented with the legend "Keepin." In this calculation, we employ same isomeric ratio (IR) as the one applied to JENDL/FPY-2011. From these results, DN should be enhanced if IR is introduced to FPY and by including IR, DN of ^{235}U+n_{th}as shown by red line in Fig. 5. Meanwhile, DHs have also been calculated and they are in good agreement with the experimental results regardless of whether IR is applied to FPY.

4. Conclusion

For the transmutation of LLFP in fast reactors, we present a new type of evaluation formula including nuclear shell effects as a Boltzmann factor form. As the result, this formula can reproduce experimental and evaluated independent yields of ^{235}U+n_{th}, ^{235}U+n_f, and ^{239}Pu+n_{th}. With this factor, especially the odd-even staggering on the Z-distribution of FPY are reasonably represented. With calculated FPY, the data of DN and DH are also well explained by including isomeric ratio compiled in JENDL.

Acknowledgements

This study comprises the results of "Research and development of an innovative transmutation system of LLFP by fast reactors", entrusted to the Tokyo Institute of Technology by the Ministry of Education, Culture, Sports, Science and Technology of Japan (MEXT).

References

[1] S. Chiba*etal.*: Scientific Reports **7**, 13961 (2017).
[2] A.C. Wahl: LA-13928 (2002).
[3] H. Koura, T. Tachibana, M. Uno and M. Yamada: Prog. Theor. Phys. **113**, 305 (2005).
[4] P. Fong: Phys. Rev. **102**, 434 (1956).
[5] B.D. Wilkins, E.P. Steingerg and R.R. Chasman: Phys. Rev. C **14**, 1832 (1976).
[6] EXFOR: https://www-nds.iaea.org/exfor/exfor.htm (accessed 2018-04-01).
[7] K. Oyamatsu: Proc. 1998 Sympo. on Nucl. Data, JAERI-Conf. 1999.
[8] C. Ishizuka, M.D. Usang, F.A. Ivanyuk, J.A. Maruhn, K. Nishio, and S. Chiba: Phys. Rev. C **96**, 064616 (2007).

28 Analyses of Kinetic Parameters Based on JENDL-4.0 for Reactor Period Measurement

Yasushi Nauchi
Nuclear Technology Research Laboratory, Central Research Institute of Electric Power Industry
2-6-1, Nagasaka, Yokosuka-Shi, Kanagawa, 240-0196 JAPAN
nauchi@criepi.denken.or.jp

Effective delayed neutron fraction repartition per fission nuclide and precursor families is calculated for cores with library based on JENDL-4.0. With reported reactor period T and the fraction, the reactivity is estimated according to the inhour equation. The reactivity is compared to that by eigenvalue calculations for the critical and the reactivity inserted conditions.

1. Introduction

When positive / negative reactivity ρ is inserted into a critical core, power of the core increases / decreases. The time rate change of the power asymptotes to an exponential function which is characterized by the reactor period T. The delayed neutron fraction repartition per fission nuclide i and precursor family j, $\beta_{eff,ij}$, and the neutron generation time Λ can relate T to ρ in accordance with the inhour equation.

$$\rho_{in} = \frac{\Lambda}{T} + \sum_{ij} \frac{\beta_{eff,ij}}{1+\lambda_{ij}T} \quad (1)$$

The accuracy of reactivity ρ_{in} is determined by 1) the measurement of T and 2) the estimation of the kinetic parameters such as $\beta_{eff,ij}$ and Λ. The error in the estimation is originated in 2-1) the calculation input, 2-2) the calculation method, and 2-3) the nuclear data library used for the calculation. Whereas, the reactivity can be deduced by two calculations of the effective multiplication factor k_{eff} for critical / perturbed system.

$$\rho_{static} = \frac{1}{k_{eff,cri}} - \frac{1}{k_{eff,pert}} \quad (2)$$

Accordingly, the estimation scheme of the reactivity would be comprehensively validated by agreement of ρ_{in} and ρ_{static}.

The author had developed approximation methods of $\beta_{eff,ij}$ and Λ and compared ρ_{in} to ρ_{static} for cores of STACY [1], TCA [2,3], CROCUS [4], and SAXTON [5] with libraries based on ENDF-B/VI.6, ENDF/B-VII.0, JEFF-3.1, and JENDL-3.3 [6, 7]. Then he had proposed exact calculation methods of β_{eff} and Λ [8] and enhanced them to calculate $\beta_{eff,ij}$ [9]. The methods were implemented into MCNP-5.1.30 [10] and the code was tested against the STACY core with a library based on JENDL-4.0 [9]. The enhanced MCNP-5 was verified by code to code comparisons to the TRIPOLI-4 code developed by CEA and

validated against the CROCUS core with libraries based on ENDF/B-VII.0, JEFF-3.1.1, and JENDL-4.0 [11].

In the present work, those comparisons of the reactivities are performed for the TCA and SAXTON cores with the JENDL-4.0 library and the trend of the ratio ρ_{in} / ρ_{static} are discussed together with the previous results.

2. Calculation

2.1 Definition of Kinetic Parameters

Kinetic parameters in the perturbed system are defined with the asymptotic angular neutron flux satisfying the natural mode equation [12] and with the adjoint angular flux satisfying the adjoint static equation of which eigenvalue is $k_{eff,pert}$. However, it is assumed that the kinetic parameters are perturbed little by the reactivity insertions for the cores [1-5] in the previous [6,7,9,11] and the present works. Then they are expressed as

$$\beta_{eff,ij} = \frac{\int d\Omega dE dr^3 \int d\Omega' dE' \phi^\dagger \chi_{d,ij} \nu_{d,ij} N_i \sigma_{f,i} \phi}{\sum_i \int d\Omega dE dr^3 \int d\Omega' dE' \phi^\dagger \chi_{t,i} \nu_{t,i} N_i \sigma_{f,i} \phi} \quad , \tag{3}$$

$$\Lambda = \frac{4\pi \int d\Omega dE dr^3 \phi^\dagger \frac{1}{V} \phi}{\sum_i \int d\Omega dE dr^3 \int d\Omega' dE' \phi^\dagger \chi_{t,i} \nu_{t,i} N_i \sigma_{f,i} \phi} \quad . \tag{4}$$

Here, r, E, Ω and V mean the position, the energy, the flying direction, and the speed of a neutron, respectively. E' and Ω'mean those of neutrons which induce the fission. ϕ and $\phi^\dagger$ are the angular neutron flux and its adjoint, respectively. χ, ν, N, σ_f are the neutron emission spectrum, the number of neutron emission per fission, the number density of fission nuclide, and the microscopic fission cross section, respectively. Subscript d / t means that of delayed / total neutrons.

$\beta_{eff,ij}$ and Λ were calculated by the iterated fission probability method in which the adjoint flux is interpreted as the expected number of fission neutrons after a certain generations [8].

2-2 Critical and Perturbed Cores

Kinetic parameters and reactivities have been estimated for 5 cores where critical / perturbed geometries and the measured T were reported. They were listed in Table 1. STACY is a critical tank of uranyl nitrate solution of 9.7 wt%-^{235}U enrichment (9.7% EU). [1]. CROCUS is a light water moderated critical lattice which consists of UO_2 rods of 1.81% EU and uranium metal rods of 0.97% EU. TCA is also a light water moderated critical lattice in which UO_2 rods of 2.6% EU are loaded. SAXTON is also a light water moderated critical lattice but uranium and plutonium mixed oxide (MOX) rods are loaded as well as UO_2 rods of 5.7% EU. The isotopic composition of the plutonium is so-called weapon grade. There are two types of lattice in the SAXTON, the one is fully filled with the MOX fuel rods and the other is partially filled with the MOX fuel rods surrounded by the UO_2 rods. The schematic view of the lattices of TCA and SAXTON are shown in **Fig. 1**. Their criticality is attained by adjusting the height of the moderator level. The positive reactivity was inserted by raising the moderator level from the critical height.

$\beta_{eff,ij}$, Λ, ρ_{in}, and ρ_{static} had already been estimated for STACY and CROCUS cores [9, 11]. Calculations of those were performed additionally for TCA and SAXTON cores in this work. For the calculation of k_{eff}s to estimate ρ_{static}, the original version of MCNP-5.1.30 was employed together with the library AcelibJ40 [13]. Nominally 1000,000 neutrons were transported per cycle and 10,800 cycles of iteration calculations were performed. There might be modeling errors of geometry inputs to calculate k_{eff}s so that the $k_{eff,\ cri}$s are 1.001789, 1.006372, and 1.006998 for the cores of TCA, SAXTON-partial MOX, and SAXTON-full MOX, respectively. However, the difference between the critical and perturbed cores are only the level of the moderator both in the calculation models and the experimental geometries so that the biases in the geometrical model might be canceled by taking the difference of the reciprocal of the k_{eff}s, to some extent.

Using the same calculation input for the critical cores with the same library, $\beta_{eff,ij}$ and Λ were calculated with the enhanced MCNP-5.1.30 code. For the calculation, 2,000,000 neutrons were transported per cycle. The latent cycles[1] of 25 were taken for the adjoint flux calculation. The delayed neutron source and the flight time were calculated for 50 cycles. Even more, 16 independent calculations were performed for each core by changing the initial seed of the random number series. With the reported reactor period T and calculated $\beta_{eff,ij}$ and Λ, the reactivity ρ_{in} was deduced in accordance with the inhour equation.

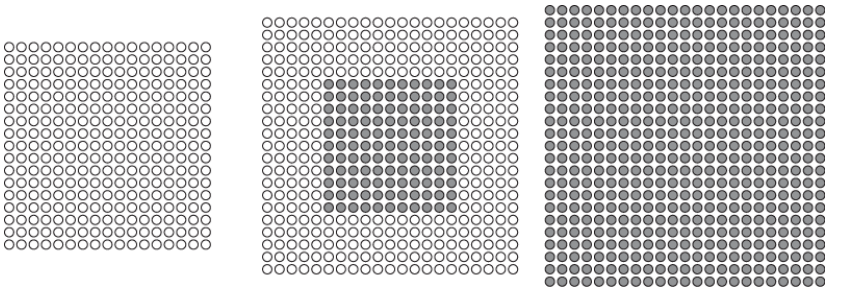

Fig. 1. Horizontal view of TCA and CROCUS cores.

3. Results and Discussion

In Table 1, the calculated reactivities are shown. Errors in the reactivities are evaluated based on the statistical one in the Monte Carlo calculations and the measurement one of the period T. For the newly calculated cases, the convergence of ρ_{static} during the 10,800 cycles were checked and the statistical fluctuations are confirmed within the error in Table 1. Except for the SAXTON full MOX case, ρ_{in} agrees with ρ_{static} within $\pm$ 4.5%.

In order to capture the trend of ρ_{in} / ρ_{static}, ρ_{in} repartition per i and j is focused on. The reactivity component per j is calculated for the TCA core in relation to the inserted reactivity as shown in In **Fig. 2**.

[1] When delayed neutrons are put in a core, their descendants make source of the fundamental mode after a certain number of cycles. “25” is determined so as to exceed the number.

The period T is also plotted in the figure. Practically, a positive reactivity measurements with period less than 15 second is difficult. Accordingly, the most significant component is of the 2nd family for the reactivity measurement. Contrarily, the significance of the components of the 3rd to the 6th families and the generation time (ρ_Λ) are enhanced when the larger reactivity is inserted, such as in the case of criticality accident.

Table 1: Comparison of reactivity by inhour equation with estimated kinetic parameters to that by static eigenvalue calculations

Core	Fuel	ρ_{in} (pcm)	error (pcm)	ρ_{static} (pcm)	error (pcm)	ρ_{in}/ρ_{static}	error
STACY	U-nitrate [9]	115.6	0.9	110.8	2.1	1.044	0.021
CROCUS	Umetal+UO_2 [11]	87.5	0.2	90.1	2.2	0.971	0.025
TCA	UO_2	69.7	0.1	70.1	1.0	0.994	0.014
SAXTON	MOX+UO_2	92.4	0.2	95.7	1.1	0.966	0.012
SAXTON	MOX	82.9	0.2	72.5	1.1	1.143	0.016

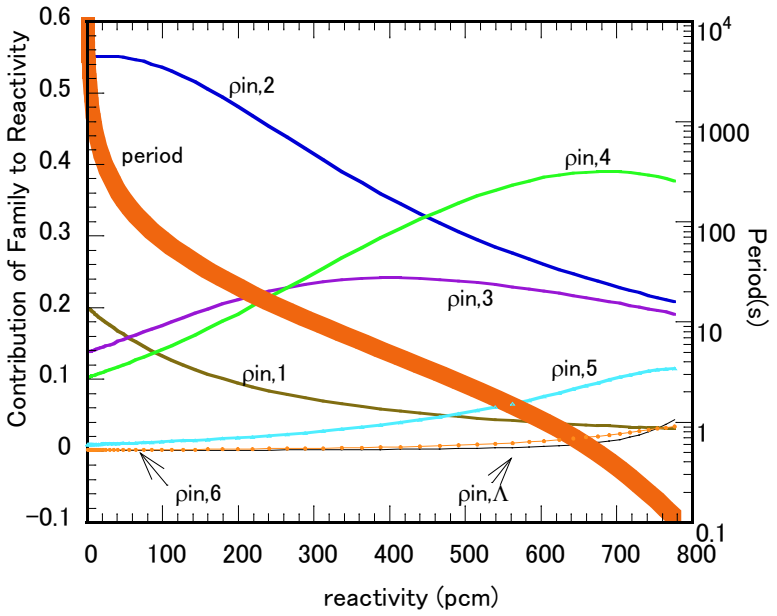

Fig. 2 Reactivity repartition per precursor family and positive reactor period.

Reactivity repartitions per fission nuclide, $\rho_{in,235U}$, $\rho_{in,238U}$, $\rho_{in,239Pu}$, $\rho_{in,241Pu}$ were calculated as shown in **Fig. 3**. In STACY, ρ_{in} is almost determined by $\rho_{in,235U}$. Whereas, $\rho_{in,238U}$ is found both in the CROCUS and TCA cores. In the SAXTON cores, $\rho_{in,241Pu}$ is not found since the weapon grade Pu is used in the MOX fuel. In the SAXTON partial MOX core, the major component of the reactivity is still $\rho_{in,235U}$ followed by $\rho_{in,239Pu}$ and $\rho_{in,238U}$. In the SAXTON full MOX core, $\rho_{in,239Pu}$ becomes the major component

followed by $\rho_{in,238U}$ and $\rho_{in,235U}$.

Comparing the Fig. 3 and Table 1, the reactivity component of $\rho_{in,239Pu}$ is considered to be overestimated since ρ_{in} / ρ_{static} increases as the loading ratio of MOX fuel rods increases. By comparing the results for the STACY, CROCUS, and TCA cores, there is the tendency that ρ_{in} / ρ_{static} increases as the average EU increases. Accordingly, either $\rho_{in,235U}$ might be overestimated or $\rho_{in,238U}$ might be underestimated. In the SAXTON partial MOX core, the ratio of the component of $\rho_{in,238U}$ / $\rho_{in,235U}$ is larger than those in TCA and CROCUS so $\rho_{in,235U}$ + $\rho_{in,238U}$ might be underestimated. Oppositely, $\rho_{in,239Pu}$ is overestimated. ρ_{in} / ρ_{static} < 1 would be due to the balance of the over / underestimations. Since the calculated $k_{eff,cri}$ agrees with unity within ±0.7% Δk/k, the over / underestimation of ρ_{in} component might not be due to $\sigma_{f,i}$, $\nu_{t,i}$, and $\chi_{t,i}$ but be due to $\nu_{d,ij}$, $\chi_{d,ij}$, and λ_{ij}.

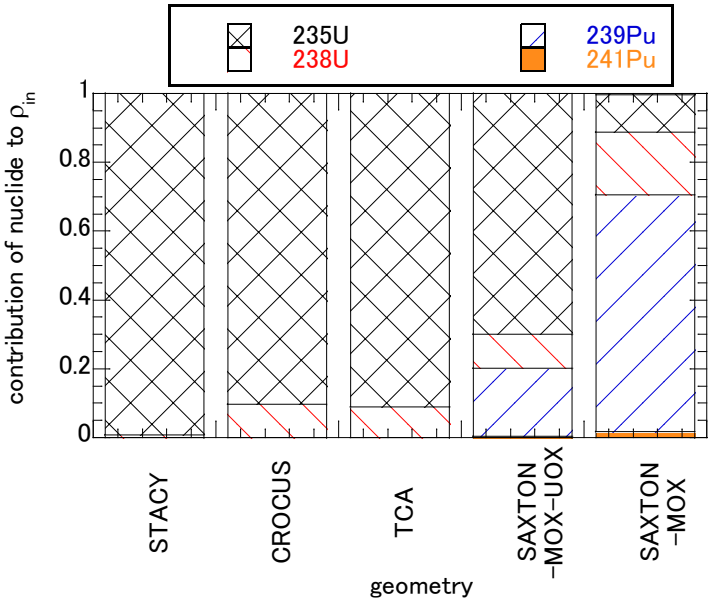

Fig. 3 reactivity repartition per fission nuclide.

4. Summary

Kinetic parameters are calculated for TCA and SAXTON cores with library based on JENDL-4.0. With the calculated parameters and the reported reactor period Ts, reactivities ρ_{in}s are estimated according to the inhour equation. Then ρ_{in} is compared to the reactivity ρ_{static} which is given by k_{eff} calculations for the critical / perturbed conditions. The previous works for STACY and CROCUS are also reviewed. As the results, significances of reactivity components concerning $\nu_{d,jj}$, $\chi_{d,ij}$, and λ_{ij} of j=2 are clarified for conventional reactivity measurements. Moreover, an overestimation of reactivity component of ^{239}Pu is indicated.

To improve the accuracy of ρ_{in}, the parameters used for kinetic parameter, such as $\nu_{d,ij}$ and $\chi_{d,ij}$, together with λ_{ij}, should be reviewed again referring the integral experiments comparing ρ_{in} to ρ_{static}. For the purpose, comprehensive experimental data sets of reactivity measurements varying the fission nuclide

compositions and the amount of reactivity insertion should be prepared.

References

[1] Onodera S, Sono H, Hirose H, Tanino S, Nagasawa M, Murakami K, Sakuraba K, Miyauchi M, Kikuchi T, Ohno A. Annual report of STACY Operation in F.Y. 1998 (1) - 280mm Thickness Slab Core-10% Enriched Uranyl Nitrate Solution-. Tokai: Japan Atomic Energy Research Institute; 1999. (JAERI-Tech 99-084)

[2] Suzaki T, Sakurai K, Nakajima K, and Horiki O. Precise Determination of β_{eff} for Water-Moderated U and U-Pu Cores by a Method Using Buckling Coefficient of Reactivity. In: Proceedings of ICNC'99; 1999 September 20-24; Versailles, p. 386.

[3] Suzaki T. private communication.

[4] Paratte JM, Fruh R, Kasemeyer U, Kalugin MA, Timm W, Chawla R. A benchmark on the calculation of kinetic parameters based on reactivity effect experiments in the CROCUS reactor, Annals of Nuclear Energy 2006;33:739-748.

[5] Taylor E.G. SAXTON plutonium program: Westinghouse Electric Corporation; 1965. (EURAEC-1493, WCAP-3385-54)

[6] Y. Nauchi and T. Kameyama. Estimation of 6 Groups of Effective Delayed Neutron Fraction Based on Continuous Energy Monte Carlo Method. In: Proceedings of PHYSOR-2006; 2006 September 10-14; Vancouver.

[7] Y. Nauchi Y and Kameyama T. Comparison of kinetic parameters based on continuous energy Monte Carlo method and evaluated nuclear data libraries for reactivity of MOX fuel cores. In: Proceedings of PHYSOR'08; 2008 September 14-19; Interlaken.

[8] Nauchi Y, Kameyama T. Development of Calculation Technique for Iterated Fission Probability and Reactor Kinetic Parameters Using Continuous-Energy Monte Carlo Method. J Nucl Sci Technol. 2010 Nov; 47: 977–990.

[9] Nauchi Y. Delayed neutron fraction repartition per precursor group weighted by Iterated Fission Probability. In: Preprints of the 2016 annual meeting of Atomic Energy Society of Japan; 2016 March; Hiratsuka. 1O12 [in Japanese].

[10] X-5 Monte Carlo Team. MCNPTM – A General Monte Carlo N - Particle Transport Code, Version 5. Los Alamos: Los Alamos National Laboratory; 2003. (LA-UR-03-1987)

[11] Zoia A, Nauchi Y, Brun E, and Jouanne C, Monte Carlo analysis of the CROCUS benchmark on kinetics parameters calculation, Annals of Nuclear Energy. 2016; 96: 377-388.

[12] Stacey YM Jr. Nuclear Science and Technology: Vol. 5 Space-Time Nuclear Reactor Kinetics. Academic press; 1969.

[13] Hagura H, Okumura K, Iwamoto Y, Nagase F. Development of neutron, photon and electron transport libraries based on JENDL-4.0 for PHITS code, In: Preprints of 2012 Fall Meeting of Atomic Energy Society of Japan; 2012 September 19-21; Hiroshima [in Japanese].

29 Fission Barrier Heights of Actinide Nuclei Obtained in Multi-Nucleon Transfer Reactions of $^{18}O + ^{237}Np$

Kun Ratha Kean[1], Katsuhisa Nishio[2], Kentaro Hirose[2], Mark Vermeulen[2], Hiroyuki Makii[2], Riccardo Orlandi[2], Kazuaki Tsukada[2], Yoritaka Iwata[1], A.N. Andreyev[2,3], I. Tsekhanovich[4] and Satoshi Chiba[1]

[1]*Laboratory for Advanced Nuclear Energy, Institute for Innovative Research, Department of Transdisciplinary Science and Engineering, School of Environment and Society,Tokyo Institute of Technology, 2-12-1-N1-19, Ookayama, Meguro-ku, Tokyo 152-8550, Japan*

[2]*Advanced Science Research Center, Japan Atomic Energy Agency(JAEA), Tokai, Ibaraki 319-1195, Japan*

[3]*Department of Physics, University of York, York YO10, United Kingdom*

[4]*University of Bordeaux, 351 Cours de la Libration, 33405 Talence Cedex, France*

Abstract

The validity of multi-nucleon transfer reaction approach for the measurements of fission barrier heights, using heavy ion beam ^{18}O with ^{237}Np target, was investigated in JAEA tandem accelerator facility. In this study, fission barrier heights were obtained for $^{237-239}Np$ and $^{239,240}Pu$ isotopes, and these results are compared with the RIPL2 [1] experimental data and with theoretical predictions of the recent FRLDM [2], Hartree-Fock-BCS [3] and GEF [6] . The systematic fission barrier heights will be the subject of future study.

Keywords: multi-nucleon transfer reaction, fission barrier height.

1. Introduction

Fission barrier height is very essential to evaluate fission cross sections, and also critical to assign fissile or fissionable nucleus. Experimental determination of barrier height for a number of short-lived actinide nuclei by neutron-induced method is often difficult or even impossible due to the lack of available target materials. Neutron-induced fission can give fission barrier data only for fissionable nucleus, and thus available data are extremely limited. Instead, a multi-nucleon transfer reaction technique can generate fission barrier data for a wide range of nuclei. In this approach, the nucleus of interest is created in collisions of a beam with target nuclei, via the exchange of nucleons between them. The compound nucleus of interest is formed in an excited state and may therefore de-excite via fission, emission of gamma-rays, neutrons, etc. Schematic representation of multi-nucleon transfer reaction technique is given in Fig.1. The basics of this technique are explained in [7].

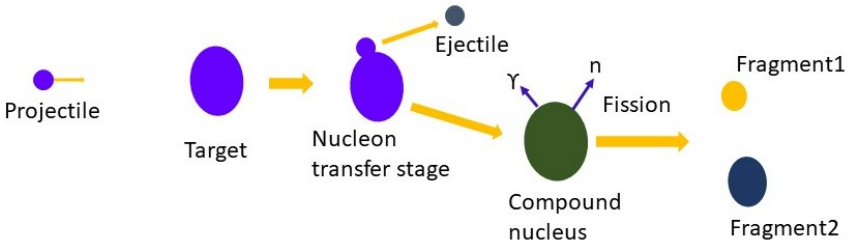

Figure 1: Schematic representation of multi-nucleon-transferred method. Three possible decay modes (fission, gamma and neutron emission) are indicated.

Some data obtained so far with multi-nucleon transfer reactions' method stem from the transfer of just a few nucleons, based on light ion beams, such as ^{2,3}H and ^{3,4}He beams. However, JAEA makes use of the heavier projectile, ^{18}O, which allows one to increase the number of transferred nucleons and thus to obtain, and to study fission properties of a wider range of compound nuclei [8, 9].

In this work, we report on the measurement of the barrier heights of $^{237-239}$Np and ^{239,240}Pu isotopes at the JAEA tandem facility. The obtained data are compared with the literature data and theoretical models.

2. Experiments and Methods

In order to determine fission barrier heights of several isotopes by the multi-nucleon transfer approach, we need, first of all, to produce the fissioning systems by bombarding the ^{237}Np target with the ^{18}O beam. The beam (162.0 MeV, ∼0.5 pnA) was supplied by the JAEA tandem accelerator in Tokai, Japan. The target was made by electorically depositing the ^{237}Np material with the thickness 76.3 μg/cm^2 on a nickel backing (300 μg/cm^2). The detection system composes of a ΔE-E silicon telescope to detect ejectile nucleus and four Multi-Wire Proportional Counters (MWPCs) detectors to detect fission fragments. The detailed description of experimental set-up is shown in [8].

The ΔE-E silicon telescope, developed by JAEA, enables us not only to measure the energies of the ejectiles but also to identify nuclides, which allows us to assign the corresponding compound nucleus. The energy of an ejectile, E_{total}, was measured as a sum of energy loss, ΔE, generated by passing through one of twelve ΔE detectors (75 μm thick) and the remaining energy (residual energy), E_{res}, deposited in one of the 16 annular strips of the E detector of 300 μm in thickness ($E_{total} = \Delta E + E_{res}$). Knowing ΔE and E_{res} for all ejectiles, we are able to make a PID plot as shown in Fig. 2. Consequently, the ejectiles associated with different (A, Z) lines are clearly distinguished by this plot. On each plots, we made gates, using a functional for charge and mass identification in Δ E-E telescope as reported in [10], to fit these lines so that we are able to extract the energies of nucleus of interest and its kinetic energy. Moreover, applying momentum conservation, the excitation energies of the compound nucleus, E^*, can be calculated according to (see also Fig. 3).

$$E^* = Q + E_{pro} - E_{eject} - E_{CN} \tag{1}$$

where E_{pro}, E_{eject} and E_{CN} are the kinetic energy of the projectile, the ejectile and the compound nucleus, respectively, and the reaction Q value is calculated by

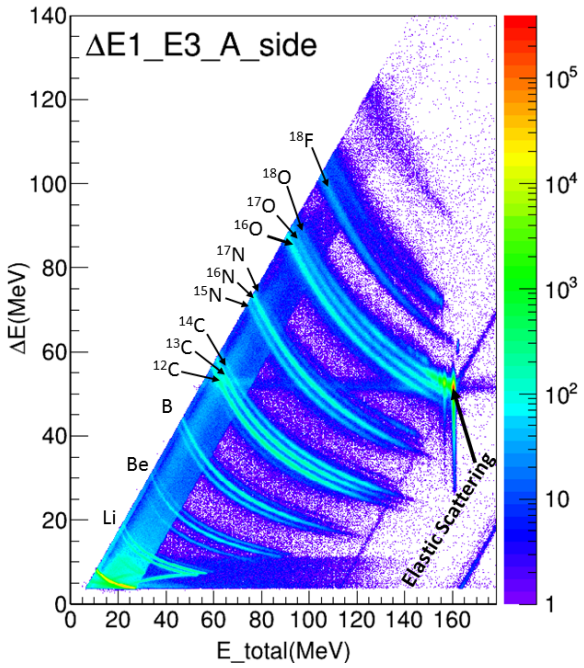

Figure 2: Energy loss versus total energy obtained from ΔE and E detector. The ejectile nuclei are clearly separated.

$$Q = (m_{pro} + m_{target}) - (m_{eject} + m_{CN}) \tag{2}$$

where m_{pro}, m_{target}, m_{eject}, m_{CN} are masses for the projectile, target, ejectile and compound nucleus, respectively. For the interpretation of the experimental data, hereafter we assume that the excitation energy of the exit channel is given to the recoiled nucleus.

The excitation energy distribution of the compound nucleus, ^{240}Pu, called a single spectrum, is plotted in Fig.4 (a), obtained by the transfer channel of ^{237}Np(^{18}O,^{15}N)^{240}Pu.

In the next step, fission event coincided with registered ejectile event is searched within the time window of 400 ns. Coincidence of both fission fragments are imposed for the selection of fission event. The spectrum of coincided events between fission fragments and ejectile is plotted in Fig.4 (b).

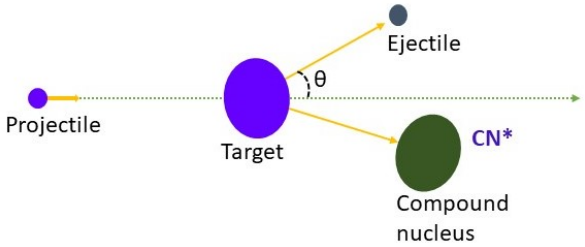

Figure 3: The kinematic representation of the interaction between projectile and target nuclei.

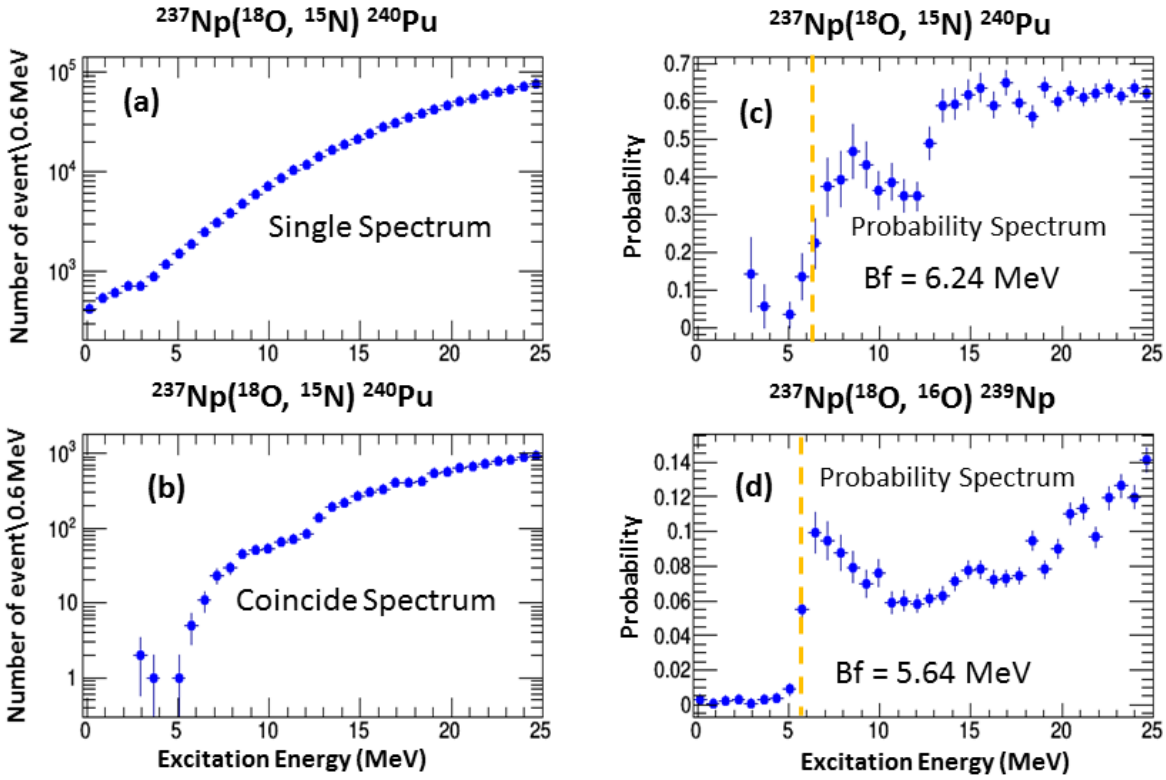

Figure 4: The spectrum (a) represents the number of events of ^{15}N ejectile as a function of the excitation energy. The spectrum (b) is the coincidence between ^{15}N and two fission fragments. The spectra (c) and (d) are the fission probability for ^{240}Pu and ^{237}Np, respectively (preliminary).

Eventually, barrier heights can be deduced as shown in Fig. 4 (c) and (d), obtained by dividing the coincident spectrum (b) by the single spectrum (a) after correcting for the geometry efficiency to detect fission fragments ε(E*) ($\sim$ 10%) [7].

$$P_{fis} = \frac{N_{ejec}^{coin}(E*)}{N_{ejec}^{singles}(E*)\varepsilon(E*)} \tag{3}$$

3. Results and Discussions

We determined the fission barrier heights for five nuclei ^{237}Np, ^{238}Np, ^{239}Np, ^{239}Pu and ^{240}Pu as 6.10 MeV, 6.29 MeV, 5.64 MeV, 6.25 MeV, 6.24 MeV, respectively. These measured barrier heights are compared with the existing experimental data in RIPL2 based on neutron-induced fission, see the table below. Our data agree with the literature data within 0.1 MeV (^{237}Np), 0.21 MeV (^{238}Np), 0.05 MeV (^{239}Pu) and 0.19 MeV (^{240}Pu). Our barrier values are generally in good agreement with those in RIPL2. Note that data for ^{239}Np is not listed in the RIPL2 compilation. These small deviations show the validity of our measurements and our approach using heavy projectile ^{18}O. According to this validity, our assumption on the calculation of the compound-nucleus excitation

Table 1: Fission barrier heights (Bf) in MeV for 5 isotopes from this experiment, RIPL2 [1] and GEF [6], the recent FRLDM [2] and Skyax-BCS (SkM* [5], SlY4 [4]).

Isotopes	Bf(this work)	Bf (RIPL2)	Bf (GEF)	Bf (FRLDM)	Bf (SLy4)	Bf (SkM*)
^{237}Np	6.10	6.00	5.70	4.94	9.53	7.66
^{238}Np	6.29	6.50	6.19	5.36	10.0	8.16
^{239}Np	5.64		5.60	5.57	6.02	9.50
^{239}Pu	6.25	6.20	6.08	5.74	10.1	8.25
^{240}Pu	6.24	6.05	5.70	5.98	10.6	8.76

energy is also correct. The comparison with GEF [6], FRLDM [2] and Skyax-BCS (SkM* [5], SLy4 [4]) are also shown. Our data agree with the GEF calculation within 7.0%, 1.6%, 0.7%, 2.8% and 9.5% for ^{237}Np, ^{238}Np, ^{239}Np, ^{239}Pu and ^{240}Pu, respectively. We found that the estimations of the recent FRLDM are slightly smaller for ^{239}Np, ^{239}Pu, ^{240}Pu with the amount of 0.07 MeV, 0.51 MeV, 0.26 MeV, respectively, and are much smaller (around 1 MeV) for ^{237}Np and ^{238}Np. If we compare with Skyax-BCS f or both SLy4 and SkM*, we observe that differences are very large.

4. Summary and Perspective

In summary, multi-nucleon transfer technique using heavier projectile in direct kinematics is a good experimental tool to determine barrier heights for a wide range of nuclei. We preliminarily obtained the barrier heights of ^{237}Np, ^{238}Np, ^{239}Pu and ^{240}Pu which, in general, agree very well with those from RIPL2. This evidence shows the validity of our measurements and the technique. The experimental results are also compared with some theoretical calculations, namely GEF code, FRLDM and Skyax-BCS method (SLy4 and SkM*). The FRLDM model shows smaller fission barriers than our data. The SkM* and SLy4 calculations generate significantly larger values.

Acknowledgements

The work is partially supported by the "Comprehensive study of delayed-neutron yields for accurate evaluation of kinetics of high burn-up reactors", by the Ministry of Education, Culture, Sports, Science and Technology of Japan (MEXT), and MEXT scholarship program for Cambodian students. We express our gratitude to Dr. F. Minato in JAEA for Skyax code. We thank the tandem accelerator operators who provided the beam with very good conditions.

References

[1] T. Belgya et al., Handbook for calculations of nuclear reaction data, RIPL-2. IAEA-TECDOC -1506 (IAEA, Vienna, 2006).

[2] P. Möller et al., Phys. Rev. C 91, 024310 (2015).

[3] P.-G. Reinhard et al., Phys. Rev. C 60, 014316 (1999).

[4] E. Chabanat et al., Nucl. Phys. A635, 231 (1998); A643, 441(E) (1998).

[5] J. Bartel et al., Nucl. Phys. A386, 79 (1982).

[6] K.-H. Schmidt et al., Nuclear Data Sheets 131, 107-221 (2016).

[7] Q. Ducasse et al., Phys. Rev. C 94, 024614 (2016).

[8] R. Léguillon et al., Phys. Lett. 761, 125-130 (2016).

[9] K. Hirose et al., Phys. Rev. Lett. 119, 222501 (2017).

[10] L. Tassan-Got, Nucl. Instr. Meth. Phys. Res. B 194, 503-512 (2002).

30 Uncertainty Analysis of Neutron Multiplication Factors of Fast Critical Assemblies BFS-61 Simulating Lead-Cooled Fast Reactors

Go CHIBA
Faculty of Engineering, Hokkaido University
Kita-13 Nishi-8, Kita-ku, Sapporo, Hokkaido, 060-8628 Japan
e-mail: go chiba@eng.hokudai.ac.jp

In order to reduce nuclear data-induced uncertainties of neutronics parameters of a commercial-grade accelerator-driven system (ADS), usefulness of integral data obtained during the BFS-61 experiment is assessed. Sensitivities of neutron multiplication factors of three cores in this experiment are calculated by a reactor physics code system CBZ, and nuclear data-induced uncertainties of neutron multiplication factors are quantified with these sensitivities and covariance data of the JENDL-4.0 library. Results show that lead-208 elastic scattering cross section and its angular distribution are dominant contributors to total uncertainties, and that these integral data do not have large sensitivities to inelastic scattering cross section of lead isotopes, which is one of dominant uncertainty sources in neutronics parameters of a commercial-grade ADS.

1. Introduction

The accelerator-driven system (ADS) is one of future promising nuclear systems, and great attentions have been paid in the field of nuclear engineering in recent years. While there are several technical issues which should be overcome to realize ADS, accuracy and reliability of nuclear data have been concerned since neutronics calculations of ADS require nuclear data of specific nuclides such as minor actinoids, lead and bismuth, which have not been generally used in neutronics calculations of conventional (or present) nuclear systems.

Prediction accuracy of neutronics parameters for ADS can be quantified by using covariance data of nuclear data. In a previous work, the authors have quantified nuclear data-induced uncertainties of some neutronics parameters of a commercial-grade ADS designed by Japan Atomic Energy Agency (JAEA) with what is called adjoint-based uncertainty propagation procedure with covariance data given in an evaluated nuclear data library JENDL-4.0[1]. This work has identi-fied some nuclear data whose uncertainties significantly contribute to uncertainties of neutronics parameters of ADS, and has suggested that nuclear data of lead and bismuth, especially inelastic scattering cross section, are important for accurate prediction of coolant void reactivity, which is quite an important neutronics parameter in ADS safety analyses.

In order to reduce prediction uncertainties of ADS neutronics parameters, the authors have utilized some available integral data, which are experimental data of neutronics parameters obtained at several facilities, for nuclear data adjustment calculations[2]. In this work, some integral data related to the lead nuclear data have been used: HMF027, PMF035, HMF064-1, -2 and -3, which are identifications used in the ICSBEP handbook. The nuclear data adjustment calculation with these integral data, however, has shown no significant improvement in prediction accuracy of coolant void reactivity of a commercial-grade ADS since these integral data are rather sensitive to nuclear data related to neutron leakage, such as elastic scattering cross section and its angular distribution. This conclusion has suggested importance of further effort to add other integral data which are considered beneficial to reduce uncertainties of ADS neutronics parameters.

On lead- or lead-bismuth-cooled fast reactors technology, nuclear engineering community in

Russia have significant experiences. They have conducted several critical experiments to simulate lead- or lead-bismuth-cooled fast reactors at the BFS facility[3]. Fortunately one of the experiments, the BFS-61 experiment, has been recently added to the ICSBEP handbook as MIX-MET-FAST-006 and we can now freely access detailed information on this experimental data. In the present study, we construct simplified core model of the BFS-61 experiment, and quantify nuclear data-induced uncertainty of neutron multiplication factors of this data. Through this work, we can get a conclusion whether the BFS-61 data are beneficial for our ADS development or not.

2. Brief description of BFS-61 experimental data

The BFS-61 experiment was carried out in 1990-91 to obtain experimental data of neutronics parameters of a small fast reactor with mixed plutonium-uranium nitride fuel and lead coolant. Three critical configurations were established. In the BFS facility, axial cylindrical tubes made of stainless steel or aluminium, whose inner diameter is around 4.8 cm and thickness is around 0.2 cm, are distributed radially in a hexagonal array, and various types of thin cylindrical material pellets, some of which are covered by canning materials, are stacked inside these tubes. In core regions of BFS-61, material plates made of plutonium, depleted uranium, lead or carbon were loaded. Lead was used to simulate coolant materials, and graphite was used to simulate nitride fuel softening neutron flux energy spectra in comparison with oxide fuel. In all these configurations, a core region is surrounded by a lateral reflector, but compositions of this reflector are different among three configurations. The reflector of the first configuration BFS-61-0 was comprised of lead, steel and depleted-uranium dioxide, that of the second one BFS-61-1 was of lead and depleted-uranium dioxide, and that of the third one BFS-61-2 was of depleted-uranium dioxide. Simplified specification of these cores in the cylindrical coordinate is shown in **Fig. 1**. There are two types of lead region: lead-1 and lead-2. Difference between them is existence of steel can which covers lead plates; lead-1 uses canned lead plates. This difference is not important.

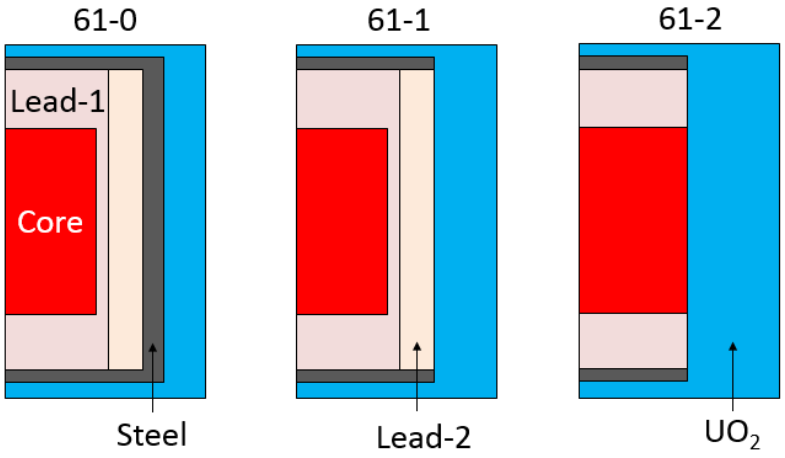

Fig. 1: Simplified specification of the BFS-61 cores

Volume and equivalent radius of core region of these three configurations are shown in **Table 1**. Height of the core region is 86.64 cm. Core region volume of the JAEA-designed ADS is also shown here[4]. It is clearly shown that volume of the BFS-61 cores is much smaller than that of ADS.

Table 1: Core region volume and equivalent radius

Core	Volume [liter]	Equivalent radius [cm]
BFS-61-0	540.6	44.57
BFS-61-1	564.0	45.52
BFS-61-2	675.2	49.81
JAEA-designed ADS	3941.4	

3. Numerical modeling and calculation by CBZ

All the calculations are carried out with a reactor physics code system CBZ, which is under development at Hokkaido University.

Unit cell heterogeneity is ignored in the present study since not neutronics parameters themselves but uncertainties of them are concerned. Nuclide number densities obtained with volume homogenization for each region which includes tube materials containing material pellets (plates) are calculated. Nuclide number densities of homogenized regions are summarized in the appendix. Those might be helpful to construct simplified core model of BFS-61 based on the data provided in the ICSBEP handbook.

A set of 70-group self-shielded cross sections is calculated with infinite homogeneous medium assumption from a JENDL-4.0-based multi-group library, and this set is used in subsequent neutron diffusion calculations by a DHEX solver based on the finite-volume spatial discretization method. A reactor core is modeled in not the cylindrical coordinate but the hexagonal-Z coordinate, and one mesh is assigned to one hexagonal region on horizontal plane. Pitch of the hexagonal array is 5.1 cm. The DHEX code calculates forward and adjoint neutron fluxes, and those are used to calculate sensitivities of neutron multiplication factors with respect to nuclear data.

Uncertainties of neutron multiplication factors are quantified from sensitivities calculated above and covariance data of nuclear data. 70-group covariance data which is obtained by NJOY-99 from JENDL-4.0 are used. Covariance data of the following nuclides are considered: Am-241, Pb-204, -206, -207, -208, Pu-239, -240, -241, U-235, -238, Fe-56 and Cr-52.

4. Results

First, neutron multiplication factors are calculated and compared with those reported by Russian research group[3]. Results are shown in **Table 2**. Results obtained with Russian group are calculated with cell-homogenized model which is consistent with ours. It is interesting to point out that heterogeneous correction, which is also taken from Ref. [3], is significantly large in these cores.

Table 2: k_{eff} in cell-homogeneous model

	61-0	61-1	61-2
Present	0.96511	0.96787	0.97371
Ref. [3]	0.9624	0.9653	0.9677
(Heterogeneous correction)	+0.0254	+0.0236	+0.0226

Next nuclide-wise uncertainties are shown in **Fig. 2**. Two actinoids, plutonium-239 and uranium-238, mainly contribute to total uncertainties in all the cores, and lead-208 also shows large contributions especially in BFS-61-0 and -1, in which radial lead reflectors were employed.

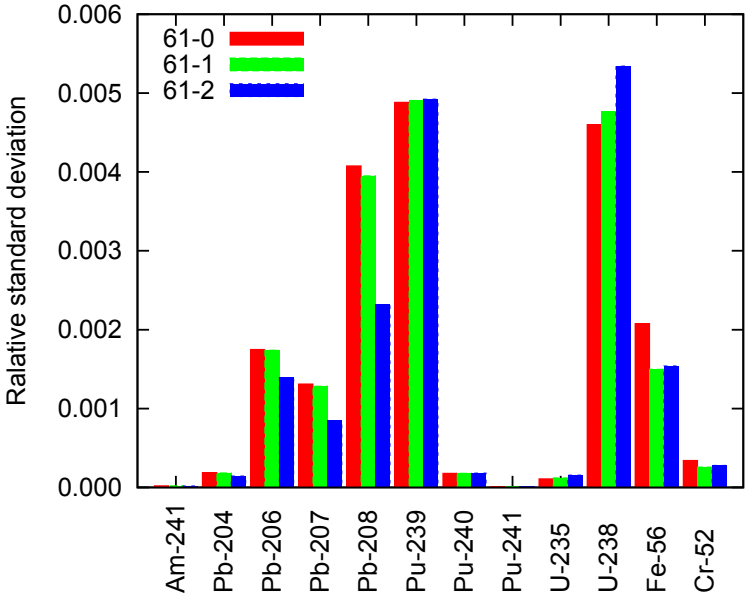

Fig. 2: Nuclide-wise uncertainties of k_{eff} of the BFS-61 cores

Figure 3 shows nuclear data-wise uncertainties. On lead-208-induced uncertainties, elastic scattering cross section and its angular distribution, $\bar{\mu}$, are dominant. Those nuclear data are related to neutron leakage from a system, and those uncertainty contribution of BFS-61 is quite similar with other integral data which was used in our previous study[2]. **Figure 4** shows nuclear data-wise uncertainties of neutron multiplication factor and coolant void reactivity at the beginning of initial cycle of the JAEA-designed ADS[1]. This figure shows significant contribution of inelastic scattering cross section of lead isotopes, but unfortunately those nuclear data do not contribute to total uncertainties in the BFS-61 data.

5. Conclusion

In order to reduce nuclear data-induced uncertainties of neutronics parameters of a commercial-grade ADS, usefulness of integral data obtained in the BFS-61 experiment has been assessed. This experiment was conducted at the BFS facility in Russia to obtain experimental data on neutronics parameters of lead-cooled fast reactors. Sensitivities of neutron multiplication factors of three cores in this experiment have been calculated by a reactor physics code system CBZ, and nuclear data-induced uncertainties of neutron multiplication factors have been quantified with these sensitivities and covariance data of the JENDL-4.0 library. Results have shown that lead-208 elastic scattering cross section and its angular distribution are dominant contributors to total uncertainties, and that these integral data do not have large sensitivities to inelastic scattering cross section of lead isotopes, which is one of dominant uncertainty sources in neutronics parameters of a commercial-grade ADS. This work concludes that the BFS-61 data are not beneficial for our ADS development.

Acknowledgment

This work is supported under the project *Basic Research for Nuclear Transmutation Techniques by Accelerator-Driven System,* a Special Research Program funded by Chubu Electric Power Co., Inc.

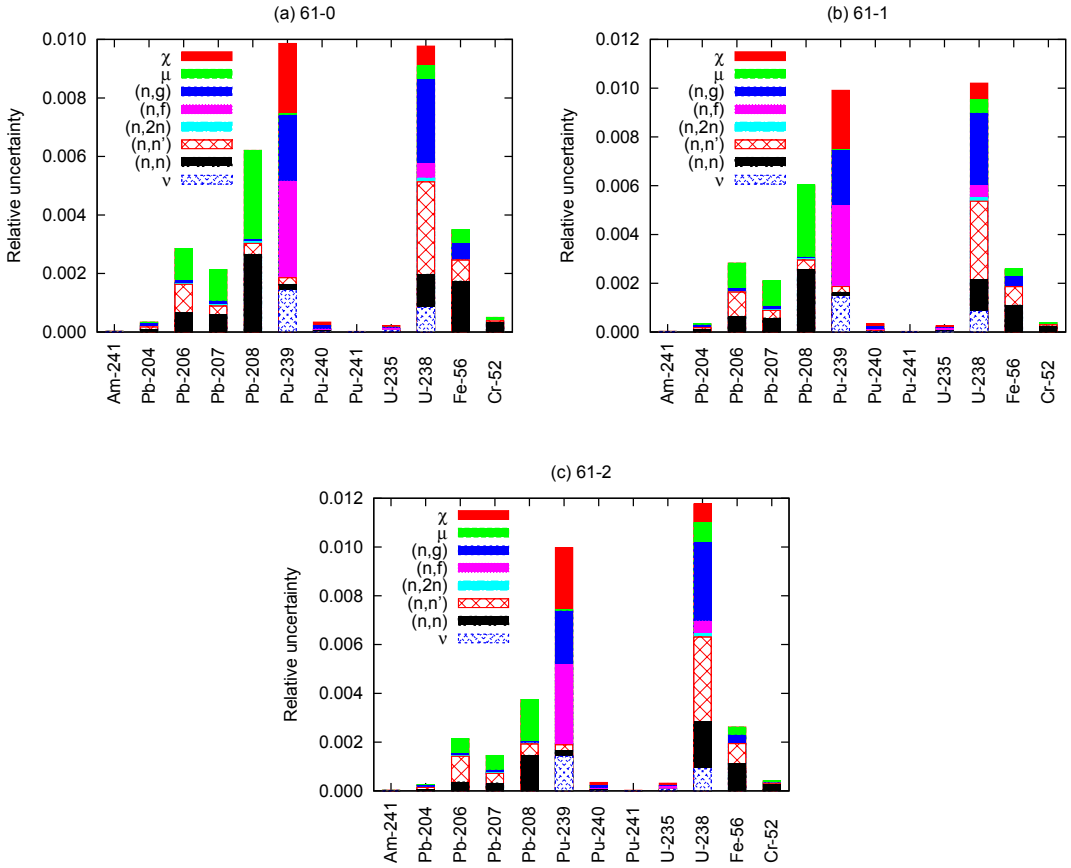

Fig. 3: Nuclear data-wise uncertainties of k_{eff} of the BFS-61 cores

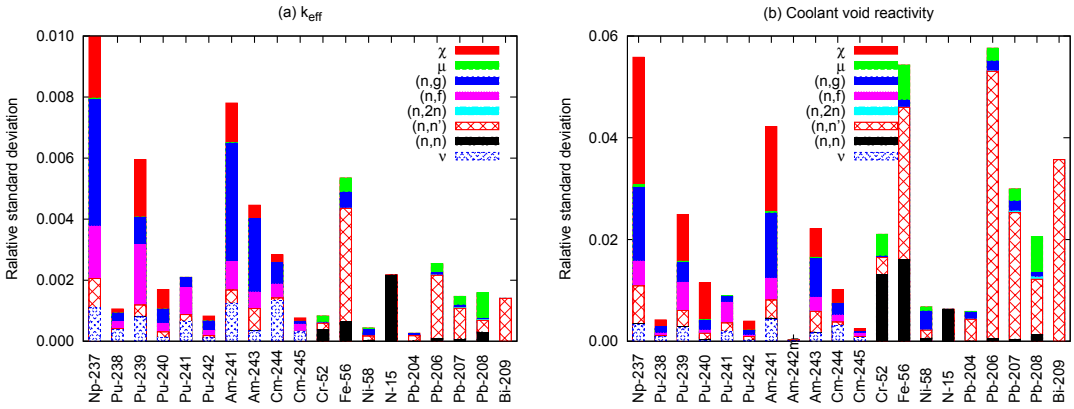

Fig. 4: Nuclear data-wise uncertainties of k_{eff} and coolant void reactivity of JAEA-designed ADS cores

References

[1] G. Chiba, *et al.*: "Nuclear data-induced uncertainty quantification of neutronics parameters of accelerator-driven system," *J. Nucl. Sci. Technol.*, 53, 1653 (2016).

[2] G. Chiba, *et al.*: "On prediction accuracy of neutronics parameters of accelerator-driven

system," *Proc. Int. Conf. on Nuclear Data for Science and Technology, ND2016*, Sep. 11-16, 2016, Brugge, Belgium (2016).

[3] A. Tsiboulia, *et al.*: "Validation of neutron data for Pb and Bi using critical experiments," *J. Nucl. Sci. Technol.*, Supp. 2, 1010 (2002).

[4] K. Tsujimoto, *et al.*: "Neutronics design for lead-bismuth cooled accelerator-driven system for transmutation of minor actinoid," *J. Nucl. Sci. Technol.*, 41, 21 (2004).

A Homogenized nuclide number density data

Table 3: Nuclide number densities in homogenized cell model (unit: [/barn/cm])

	Core unit cell	UO_2 with SS tube	UO_2 with Al tube	Canned Pb with SS tube	Canned Pb with Al tube
H-1		1.1889e-5	1.1889e-5		
C	7.2535e-3	6.9689e-4	6.6902e-4	5.8394e-5	3.0526e-5
O-16		2.8198e-2	2.8198e-2		
Al-27	1.0001e-3	4.4407e-3	8.4899e-3		4.0492e-3
Si	7.1078e-5	5.9590e-5		5.9590e-5	
Ti	8.1149e-5	4.1945e-5		9.6187e-5	5.4242e-5
Cr	1.9598e-3	1.1330e-3		2.1907e-3	1.0577e-3
Mn-55	1.3707e-4	7.3110e-5		1.5653e-4	8.3422e-5
Fe	7.1727e-3	4.2434e-3	2.5452e-4	7.9875e-3	3.8118e-3
Ni	9.8409e-4	5.8172e-4		1.1023e-3	5.2060e-4
Ga	7.7858e-5				
Pb	1.2291e-2			2.1732e-2	2.1732e-2
U-235	3.2881e-5	5.9924e-5	5.9924e-5		
U-238	7.6974e-3	1.4029e-2	1.4029e-2		
Pu-239	1.2882e-3				
Pu-240	6.1735e-5				
Pu-241	1.0655e-6				
Am-241	2.2903e-6				

	SS with SS tube	Mild steel with Al tube	Uncanned Pb with Al tube	Steel unit cell	Mild steel with SS tube
C	3.2436e-4	5.3382e-4		3.5245e-4	5.6168e-4
Al-27		4.0492e-3	4.0492e-3		
Si	1.1373e-3	4.0585e-4		7.1705e-4	4.6544e-4
Ti	5.0308e-4			2.1945e-4	4.1945e-5
Cr	1.3461e-2			1.1402e-2	1.1330e-3
Mn-55	1.0455e-3	3.0474e-4		4.6991e-4	3.7785e-4
Fe	4.8456e-2	6.3171e-2	7.8564e-6	5.4583e-2	6.7347e-2
Ni	6.3461e-3			2.5019e-3	5.8172e-4
Pb			2.5074e-2		

31 Cross Section Measurement to Produce ^{99}Mo by Alpha-Induced Reactions on Natural Zirconium

Tomohiro MURATA[1*], Masayuki AIKAWA[2], Moemi SAITO[2], Naoyuki UKON[3], Yukiko KOMORI[4], Hiromitsu HABA[4], Sándor TAKÁCS[5]

[1] *School of Science, Hokkaido Univ., Sapporo 060-0810, Japan*

[2] *Graduate School of Biomedical Science and Engineering, Hokkaido Univ., Sapporo 060-8638, Japan*

[3] *Advanced Clinical Research Center, Fukushima Medical Univ., Fukushima 960-1295, Japan*

[4] *Nishina Center for Accelerator-Based Science, RIKEN, Wako 351-0198, Japan*

[5] *Institute for Nuclear Research, Hungarian Academy of Sciences (ATOMKI), 4026 Debrecen, Hungary*

*e-mail : murata@nds.sci.hokudai.ac.jp

We measured the cross sections of the ^{96}Zr(α,x)^{99}Mo reaction using the standard stacked-foil activation technique and γ-spectrometry. A 51-MeV α beam was used to irradiate natural zinc foils at the RIKEN AVF cyclotron. The emitted γ-rays from the ^{99}Mo decay were measured with a high resolution HPGe detector. Our result shows some disagreements with the earlier experimental data and the TENDL data.

1. Introduction

Radiopharmaceuticals containing ^{99m}Tc are used for imaging in diagnostic nuclear medicine worldwide. The characteristic properties of ^{99m}Tc enable high quality image processing with low radiation doses to patients and chemical incorporation into various radiopharmaceuticals. Generally, ^{99m}Tc is produced from the decay of ^{99}Mo using a ^{99}Mo-^{99m}Tc generator.

Over 95% of ^{99}Mo is produced by fission of ^{235}U only in a few nuclear reactors [1]. Although those few nuclear reactors can provide enough amounts of global supplies of ^{99}Mo/^{99m}Tc, unplanned shutdown of a reactor due to some technical problems may induces disruptions in the global ^{99}Mo isotope supplies that have severe effects on medical and research plans. In addition, the nuclear waste created by the fission reaction in the nuclear reactors is a concerned problem. For these reasons, alternative production routes of ^{99}Mo are needed.

One of the reactions to create ^{99}Mo is the ^{96}Zr(α,n)^{99}Mo reaction. There are experimental cross section data for this reaction available, however, the earlier published excitation functions [2,3] and the TENDL data [4] for this reaction show discrepancies in their peak positions. It is very important to provide reliable and consistent cross section data for evaluation of the production yields of an isotope. Therefore, we performed an experiment to measure the cross sections for this reaction to improve the quality of the

experimental cross section data.

2. Experimental

The cross sections of the $^{nat}Zr(\alpha,n)^{99}Mo$ reaction were measured using the stacked-foil activation method [5] and off-line high resolution HPGe γ-ray spectrometry. The details of this experiment are given below.

2.1 The stacked-foil activation method

Natural Zr foils (purity: 99.2%, thickness: 20.3 μm, Nilaco Corp., Japan) and natural Ti foils (purity: 99.6 %, thickness: 5.3 μm, Nilaco Corp., Japan) for the $^{nat}Ti(\alpha,x)^{51}Cr$ monitor reaction were stacked together as a target. The stacked target was mounted in a target holder served also as a Faraday cup, and irradiated by a 51 MeV α beam with an average intensity of 203.6 particle nA for 2 hours at the RIKEN AVF cyclotron. The α particle energy in the i-th foil E_i was derived using the stopping power at each foil calculated by the SRIM software [6].

2.2 Gamma-spectrometry

After a cooling time of 12 hours, measurements of the γ-ray spectra on each foil were performed using a high resolution γ-spectrometer with a HPGe detector. The characteristic 739 keV γ-line ($I_\gamma = 12.20\%$) from the decay of ^{99}Mo in the Zr foils and the 320 keV γ-line ($I_\gamma = 9.91\%$) from the decay of ^{51}Cr in the Ti foils were measured to derive the cross sections of the $^{nat}Zr(\alpha,n)^{99}Mo$ and $^{nat}Ti(\alpha,x)^{51}Cr$ reactions, respectively. The distance between the measured foil and the detector was optimized to keep dead time lower than 10 %.

2.3 Cross section determination

To obtain the production cross sections of the assessed radionuclide $\sigma(E_i)$, the well-known activation formula [7] was used:

$$\sigma(E_i) = \frac{\lambda C(E_i)}{n_T I \varepsilon_d \varepsilon_\gamma (1 - e^{-\lambda T_b})(e^{-\lambda T_c})(1 - e^{-\lambda T_m})} \quad (1)$$

where $C(E_i)$ is the net counts of the characteristic γ-line of the assessed radionuclide, λ is the decay constant of the radionuclide, n_T is the areal density of target atoms, I is the intensity of the α beam, ε_d is the efficiency of detection of the given γ-line, ε_γ is the emission probability of the γ-line, T_b is the irradiation time, T_c is the cooling time, and T_m is the measurement time.

The α beam intensity I was considered as constant in the stack to derive the cross sections. The beam energy and intensity as well as the energy loss calculation was confirmed by comparing the derived cross sections of the $^{nat}Ti(\alpha, x)^{51}Cr$ monitor reaction with the IAEA recommended values [8].

3. Results

The measured production cross sections of ^{51}Cr is shown in Fig.1 with the IAEA recommended values. As the deduced cross sections are consistent with the IAEA recommended values, no additional adjustments are necessary to the beam parameters.

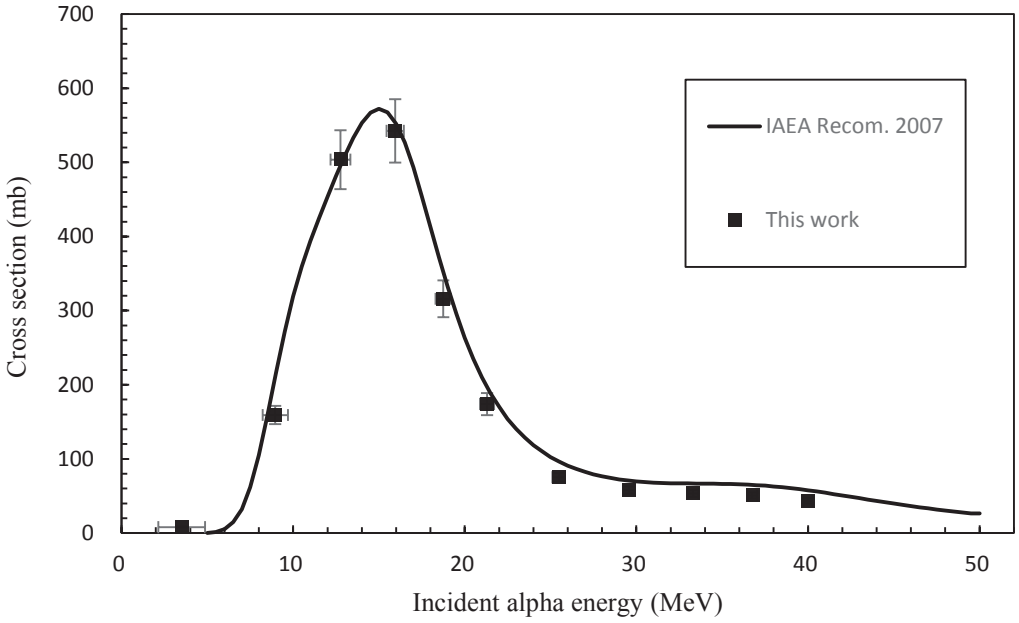

Fig.1 The experimental cross sections of the $^{nat}Ti(\alpha,x)^{51}Cr$ reaction in comparison with the recommended values

The measured production cross sections of ^{99}Mo is shown in Fig.2 with the available previous data [2, 3] and the TENDL data [4]. Our experimental cross section data points determine a smooth curve, which seems to have different peak location and maximum values as the earlier studies. The peak is located around the 14 MeV with a cross section value about 210 mb.

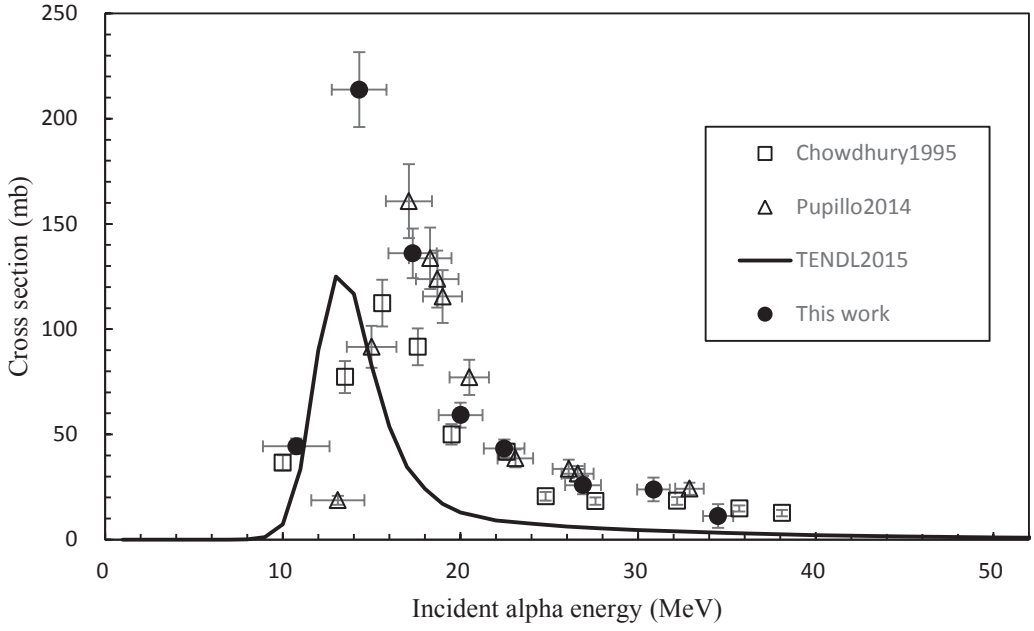

Fig.2 The experimental cross sections of the $^{nat}Zr(\alpha,x)^{99}Mo$ reaction in the comparison with the earlier experimental data and the TENDL data

4. Summary

In this work, the cross sections of the $^{96}Zr(\alpha,n)^{99}Mo$ reaction was measured using the standard stacked target activation technique and high resolution γ-spectrometry. The newly measured cross section data are compared with the earlier experimental data and the TENDL data. The peak of the deduced excitation function is higher than the previous data and located around 14 MeV. To confirm this behavior of the excitation function, we will repeat the experiment in detail in the energy region between 10 and 20 MeV.

Acknowledgements

This work was carried out at the RI Beam Factory operated by RIKEN Nishina Center and CNS, University of Tokyo Japan. This work was partly supported by JSPS KAKENHI Grant Number 17K07004.

References

[1] National Academies of Sciences and Medicine E. Molybdenum-99 for Medical Imaging. Washington, DC: The National Academies Press; 2016. doi:10.17226/23563.

[2] Chowdhury DP, Pal S, Saha SK, Gangadharan S. Determination of cross section of α-induced nuclear reaction on natural Cr and Zr by stacked foil activation for thin layer activation analysis. Nucl Instruments Methods Phys Res Sect B Beam Interact with Mater Atoms. 1995;103(3):261-266.

[3] Pupillo G, Esposito J, Gambaccini M, Haddad F, Michel N. Experimental cross section evaluation for innovative ^{99}Mo production via the (α,n) reaction on ^{96}Zr target. J Radioanal Nucl Chem. 2014;302(2):911-917.

[4] Koning AJ, Rochman D. Modern nuclear data evaluation with the TALYS code system. Nucl Data Sheets. 2012;113:2841-2934.

[5] Khandaker MU, Uddin MS, Kim KS, Lee YS, Kim GN. Measurement of cross-sections for the (p,xn) reactions in natural molybdenum. Nucl Instruments Methods Phys Res Sect B Beam Interact with Mater Atoms. 2007;262(2):171-181.

[6] Ziegler JF, Biersack JP, Ziegler MD. SRIM: the Stopping and Range of Ions in Matter. Available from http://www.srim.org/ (accessed 2018-04-01).

[7] Khandaker MU, Kim K, Lee M, Kim KS, Kim G. Excitation functions of (p,x) reactions on natural nickel up to 40 MeV. Nucl Instruments Methods Phys Res Sect B Beam Interact with Mater Atoms. 2011;269(10):1140-1149.

[8] Tárkányi F, Takács S, Gul K, et al. Beam monitor reactions. In: Charged Particle Cross-Section Database for Medical Radioisotope Production, IAEA-TECDOC-1211. Vienna: IAEA; 2001.

32 Study of α cluster structures in medium-heavy nuclei

M. Nakao[1], H. Umehara[2], S. Ebata[3] and M. Ito[1,4,†]

[1]Department of Pure and Applied Physics, Kansai University, Yamatecho, 3-3-35, Suita 564-8680, Japan
[2]Department of Physics, Osaka University, Machikaneyama-cho, 1-1, Toyonaka 560-0043, Japan
[3]Laboratory for Advanced Nuclear Energy, Institute of Innovative Research, Tokyo Institute of Technology, 2-12-1-N1-16 Ookayama, Meguro-ku 152-8550, Japan
[4]Research Center for Nuclear Physics (RCNP), Osaka University, Mihogaoka 10-1, Suita 567-0047, Japan

[†] itomk@kansai-u.ac.jp

Abstract α potentials are investigated through the analyses of the α elastic scattering on the ^{40}Ca target and the rotational band structures in $^{44}\mathrm{Ti} = \alpha + {}^{40}\mathrm{Ca}$. The α potentials are constructed by the double folding procedure with the combination of the density dependent Michigan 3-range Yukawa (DDM3Y) interaction and the target density approximation (TDA). The DF potential with DDM3Y + TDA is successful in reproducing the differential cross section of the α elastic scattering and the rotational spectra in ^{44}Ti. The application of the DF model to the nuclear waste, such as $^{135}\mathrm{Cs} = \alpha + {}^{131}\mathrm{I}$, is also discussed.

I. INTRODUCTION

An α particle is quite inert and stable because of its spin-isospin saturated property. In atomic nuclear systems, the α particle becomes a building block in constructing the intrinsic structures of nuclei. The nuclear structures described by the α particle is called the α cluster structure. Although ground states of nuclei are nicely described by the shell-model structure, the α cluster structures, in which a nucleus is decomposed into several α particles, appear in the excited states. The α cluster structure have been extensively discussed in the lighter mass region [1–3], up to the mass number of $A \leq 50$. The typical examples of such the α cluster state are $^{8}\mathrm{Be} = 2\alpha$, $^{12}\mathrm{C} = 3\alpha$, $^{16}\mathrm{O} = \alpha + {}^{12}\mathrm{C}$ and $^{20}\mathrm{Ne} = \alpha + {}^{16}\mathrm{O}$ in the lighter mass region, while $^{44}\mathrm{Ti} = \alpha + {}^{40}\mathrm{Ca}$ is a representative system in the region of $A \sim 50$ [4, 5].

The α cluster structures are considered to appear according to the Ikeda's threshold rule [6], which predicts that a possible cluster configuration is realized at the excitation energy near the corresponding threshold. The α particle is tightly bound around the residual nucleus in the ground state but it is weakly coupled at the excitation energy around the respective threshold. In this weak coupling state, the wave function of the $\alpha -$ (residual nucleus) relative motion highly oscillates in the contact region due to the Pauli's exclusion principle, while the main amplitude is prominently extended to the external region of the nuclear potential. Therefore, the feature of the α cluster state, such as the excitation energy and the decay width, is sensitive to the surface behavior of the nuclear interaction. Thus, the α potential is important ingredient in a deep understanding of the α cluster structure.

In usual studies, the α potentials are investigated from the angular distribution of the α elastic scattering. Above the incident energy of $E_\alpha \geq 80$ MeV, the global α potential, which is determined by the phenomenological manner, has already been established, while the double folding (DF) models [7] are applied to the scattering over a wide incident energies. In the double folding model, the real part of the α potential is constructed by folding the effective nucleon-nucleon (NN) interaction with the density of the incident α particle (ρ_α) and the target nucleus (ρ_T). As for the effective NN interaction (v_NN), several g-matrices, which are evaluated inside of the infinite nuclear matter, are proposed [7–10]. The M3Y (Michigan 3-range Yukawa) and DDM3Y (density dependent M3Y) interaction was quite successful in reproducing the elastic scattering of various nucleus – nucleus scattering [7]. In DDM3Y, the factorized density dependence is implemented in the M3Y interaction with the zero-range knock-on exchange, and hence, the nuclear interaction can be easily derived by the double folding procedure [10–12].

DDM3Y was originally tested in the α – nucleus elastic scattering [10], and the stringent application to the nucleus – nucleus scattering was done over a wide systematics [11, 12]. Furthermore, DDM3Y is successful in describing the molecular resonance phenomena in the coupled-channel framework [13]. According to these results, the global reproduction of all the cross section was quite successful but there is a inconsistency about the normalization factor (N_R) in the strength of the DF potential; specifically, $N_R \sim 1.3$ for the α – nucleus systems [10] and $N_R \leq 1.0$ for the heavier nucleus – nucleus systems [11, 12]. $N_R \sim 1.3$ means that the DF potential with DDM3Y generates the shallower potential for the

α scattering, and the potential depth must be artificially increased. One of the reason of the shallow property is considered to originate from the frozen density approximation (FDA), where the total density (ρ) in $v_{\rm NN}(\rho)$ is given by the summation of the folded density, such as $\rho = \rho_\alpha + \rho_{\rm T}$ [10–14]. Recently, the target density approximation (TDA) was proposed, in which the α density is neglected in the density dependence of the effective NN interaction [15]. In Ref. [15], the justification of TDA was discussed on the basis of the multiple scattering theory [15]. In constructing the pragmatic α potential, which is possible to describe the α scattering as well as α cluster structure in a unified manner, we consider that DDM3Y with TDA is one of meaningful approaches.

In the present report, we consider the TDA treatment in the DF potential with DDM3Y, and the DF potential is used for the analyses about the scattering and structure problems in the ^{44}Ti = α + ^{40}Ca system. First, the DF potential is applied to the α scattering, and the optimal normalization factor for the potential strength is searched. Secondly, the normalized DF potential is employed in the calculation of the rotational band in ^{44}Ti = α + ^{40}Ca. From the application to the scattering and structure problems, we discuss the validity of the TDA treatment in the DF potential. The scattering and structure problem in ^{44}Ti = α + ^{40}Ca was analyzed by the several works [4, 5, 10]. Thus, the validity of our results can be checked by comparing with the previous studies.

Furthermore, the TDA potential is applied to the medium-heavy system, such as ^{135}Cs = α + ^{131}I, which is a kind of nuclear waste in nuclear reactors. The reduction of high level radioactive wastes through nuclear transmutation is extensively discussed in the project of ImPACT (Impulsing Paradigm Change through Disruptive Technologies Program) [16]. Studies on the nuclear structure of nuclear waste gives the basic and fundamental informations, which are essential in the nuclear transmutation. The intrinsic structure of the nuclear waste is mainly analyzed on the basis of the mean-field model. However, the threshold energy for the α emission in the medium-heavy systems is reduced in comparison to the lighter systems, for example, about 2.6 MeV in ^{135}Cs. In this situation, there is a possibility that the α cluster structure is developed in the low-lying states of nuclear waste. Therefore, we believe that the application of the α cluster model is still meaningful in considering the properties of the nuclear waste, which needs for the nuclear transmutation of the waste.

The organization of this article is as follows. In Sec. II, the theoretical framework about the double folding model and the structure calculation are explained. The results of the α + ^{40}Ca elastic scattering and the rotational spectra of the compound ^{44}Ti system are shown in Sec. III. In the same section, the preliminarily results about ^{135}Cs = α + ^{131}I are also presented. The final section is devoted to the summary and discussion about future studies.

II. FRAMEWORK

We explain the theoretical framework in ^{44}Ti =α + ^{40}Ca, and the application to ^{135}Cs = α + ^{131}I can be achieved in a straight forward manner. In our analyses, there are two steps in the calculations; first, we solve the scattering problem of the α + ^{40}Ca system by employing the double folding (DF) potential with the target density approximation (TDA), and the strength of the DF potentials are checked. Secondly, the energy spectra of the respective compound systems, ^{44}Ti = α + ^{40}Ca, are calculated by the orthogonality condition model (OCM) [17] with the pseudo potential method [18].

A. Double folding potential

We calculate the differential cross sections of an α particle scattered by ^{40}Ca in the formulation of the microscopic nuclear interaction. The nuclear potential of α and ^{40}Ca is calculated from the double folding (DF) model [7, 13, 14], which is symbolically written as a function of the α − ^{40}Ca relative coordinate $\mathbf{R}$,

$$U_{\rm DF}(\mathbf{R}) = \iint \rho_\alpha(\mathbf{r}_\alpha)\rho_{40}(\mathbf{r}_{40}) \cdot v_{\rm NN}^{\rm DDM3Y}(s,\rho){\rm d}\mathbf{r}_\alpha{\rm d}\mathbf{r}_{40} \tag{1}$$

with $s = |\mathbf{r}_{40} - \mathbf{r}_\alpha - \mathbf{R}|$. Here $\mathbf{r}_\alpha$ ($\mathbf{r}_{40}$) denotes a coordinate measured from the center of mass in α (^{40}Ca). $\rho_\alpha(\mathbf{r}_\alpha)$ is the density of α particle, which reproduce the charge form factor of the electron scattering, while $\rho_{40}(\mathbf{r}_{40})$ represents the density of ^{40}Ca calculated by the mean-filed model [19].

In Eq.(1), $v_{\rm NN}^{\rm DDM3Y}$ represents the effective nucleon-nucleon (NN) interaction which acts between a pair of nucleon contained in the α particle and the ^{40}Ca nucleus. In the present calculation, we adopt

the DDM3Y (density dependent Michigan 3-range Yukawa) interaction [10–12]. The so-called frozen density approximation (FDA), such as $\rho = \rho_\alpha + \rho_{40}$, was mainly employed in DDM3Y [10–12]. FDA approximation is known to give a little shallow potential in the case of the α scattering [10]. Thus, we consider the target density approximation (TDA), in which only the target density of ρ_{40} is taken into account in the density dependence ($\rho = \rho_{40}$), according to the recent prescription [15].

In the realistic calculation of the scattering cross sections, we introduce the absorptive potential ($-iW$) and the Coulomb potential ($V_{\rm C}$) in addition to the nuclear DF potential. The final form of the interaction potential ($U_{\rm int}$) is

$$U_{\rm int} = N_R \cdot U_{\rm DF} + V_{\rm C} - iW. \tag{2}$$

Here we use the Saxon-Woods and its derivative form factor for the absorptive potential. In Eq. (2), we multiply the normalization factor of N_R to the DF potential because there is theoretical ambiguity in the strength of the DF potential. As for the Coulomb potential ($V_{\rm C}$), we assume the uniform charge sphere with a radius of $R_{\rm C} = r_0 \cdot A_{\rm T}^{1/3}$ with $r_0 = 1.21$ fm and $A_{\rm T} = 40$. The six parameters in Saxon-Woods (depth, radius, diffuseness in each form factor) and N_R are tuned so as to reproduce the experimental cross sections as much as possible. This computational condition is same as the setting in the previous analysis by the DF potential [10].

B. Orthogonality condition model

We calculate the energy spectra of the compound system of ^{44}Ti = α + ^{40}Ca from the DF potentials, in which N_R is tuned so as to reproduce the α elastic scattering. In the structure calculation, we apply the orthogonality condition model (OCM). In the strict treatment of OCM, the so-called Pauli allowed states are constructed by solving the eigenvalue problem of the norm kernels [17]. In the present analysis, we simply exclude the Pauli forbidden states by employing the pseudo potential method [18], which was never considered in the previous macroscopic potential model [5].

The OCM equation for the bound state problem in ^{44}Ti = α + ^{40}Ca with the relative orbital spin L and total energy E is symbolically given by

$$\left(T^L + N_R \cdot U_{\rm DF} + V_{\rm C} + V_{\rm PF}^L\right) \Psi^L = E\Psi^L \ . \tag{3}$$

Here T^L denotes the kinetic energy for the relative motion, while $N_R \cdot U_{\rm DF}$ and $V_{\rm C}$ represent the DF potential multiplied by N_R and the Coulomb potential in Eq. (2), respectively. Ψ^L means the relative wave function of α – ^{40}Ca calculated in the Pauli allowed space.

In Eq. (3), $V_{\rm PF}^L$ mean the pseudo potential for the L state, which projects out the forbidden states. In ^{44}Ti = α + ^{40}Ca, the total oscillator quanta in the harmonic oscillator, N, for the α – ^{40}Ca relative motion is restricted to $N \geq 12$ if the internal structure of α and ^{40}Ca are assumed to the lowest shell model configurations, such as the $0s$ and $1s0d$ closed-shells configurations, respectively. Thus, the pseudo potential V_{PF}^L excludes the Pauli forbidden states with $N \leq 10$ from the computational space.

III. RESULTS

A. Analysis of ^{44}Ti = α + ^{40}Ca

The DF potential shown in Eq. (1) is applied to the α elastic scattering by the ^{40}Ca target in the incident energy of $E_\alpha = 29$ and 49.5 MeV, which were also analyzed by previous work [10]. The comparison of the theory with the experiment at $E_\alpha = 29$ MeV is shown in Fig. 1. The search of the optimal parameters in the absorptive potential is done by the computational code of Automatic Local Potential Search (ALPS) [20]. In Fig. 1, we can confirm that the DF potential, which is generated by the prescription of DDM3Y + TDA, can reasonably reproduce the observed cross sections. The χ^2 value, which is a measure of a deviation of the theory and the experiment, is evaluated by setting the experimental error to 5% for all the data points.

In the results at E_α =49.5 MeV, which are not shown in figures, we have also obtained almost the same quality in the reproduction although the reproduction at $E_\alpha = 49.5$ MeV becomes little worse than the reproduction at $E_\alpha = 29$ MeV. The N_R values, which are required to reproduce the experimental data at the individual E_α, are $N_R = 0.79$ at E_α =29 MeV and $N_R = 0.81$ at $E_\alpha = 49.5$ MeV. Thus,

TDA requires about the 20% reduction to reproduce the experimental data. The 20% reduction in the potential strength is also confirmed in the α scattering by the light target, such as $\alpha + {}^{14}\mathrm{C}$ [22].

We have calculated the rotational bands in the compound system, ${}^{44}\mathrm{Ti} = \alpha + {}^{40}\mathrm{Ca}$, by solving OCM equation in Eq. (3) with the ingredient of the DF potential, which is optimized in the scattering calculation. Here we use the DF potential at $E_\alpha = 29$ MeV with $N_R = 0.79$. The normalized DF potential gives the reasonable binding energy of -8.9 MeV with respect to the α threshold, which is close to the experimental observation of -5.1 MeV.

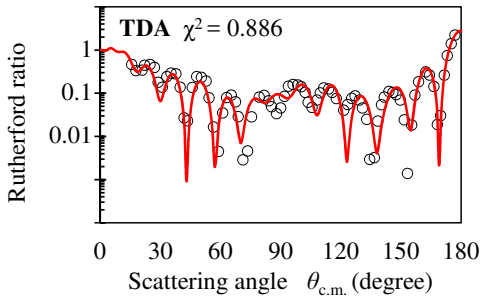

FIG. 1: (Color online) Results of differential cross section of $\alpha + {}^{40}\mathrm{Ca}$ elastic scattering at $E_\alpha = 29$ MeV. The circles represent the experimental data, while the solid curve is the theoretical calculation. The χ^2 value is attached to the figure.

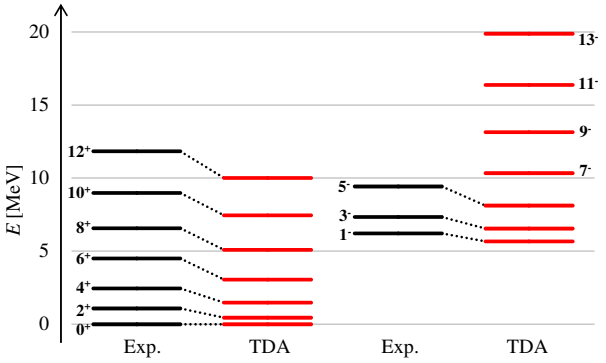

FIG. 2: (Color online) Comparison of the theoretical rotational bands with the experimental bands in ${}^{44}\mathrm{Ti} = \alpha + {}^{40}\mathrm{Ca}$. The left two bands show the ground rotational bands, while the right bands mean the excited negative-parity bands. Exp. and TDA represent the experimental spectra [21] and theoretical ones calculated from the DF potential, respectively.

In order to investigate the moment of inertia for the rotational bands, we have calculated the excited states with the finite spins, which are summarized in Fig. 2. To compare the moment of inertia directly, the energies of the ground 0^+ states are set to zero energy. In the left two sets of the energy spectra, the theoretical spectra (TDA) nicely reproduces the experimental ground band (Exp.) although the level spacing is little compressed in the TDA result. On the contrary, in the excited negative-bands, which are shown in the right two sets of the spectra, the band head energy of the 1^- state and the sequence of the rotational band in theory (TDA) nicely reproduce the feature of the experimental data (Exp.).

In the excited band, the $\alpha + {}^{40}\mathrm{Ca}$ structure is well developed in comparison to the ground band. Therefore, the reproduction of the energy spacing in the negative parity band means that the spatial size of the $\alpha - {}^{40}\mathrm{Ca}$ structure is correctly reproduced. The results of the rotational bands are completely consistent to the previous analyses by RGM with HNY and Volkov No.1 ($m = 0.623$) forces [4] and the coupled-channel calculation with DDM3Y [5].

B. Application to ${}^{135}\mathrm{Cs} = \alpha + {}^{131}\mathrm{I}$

In the previous section, we have confirmed the validity of the DF potential with DDM3Y + TDA in the scattering and structure analyses, and the similar calculation is applied to the ${}^{135}\mathrm{Cs} = \alpha + {}^{131}\mathrm{I}$ system. Since the separation energy of the α particle is about 2.6 MeV, which is much smaller than the nucleon separation energy, there is a possiblity of the developed α cluster structure in ${}^{135}\mathrm{Cs}$ although high Coulomb barrier disturbs the α cluster formation. Here we investigate the α cluster structure in the low-lying states of ${}^{135}\mathrm{Cs}$. In this calculation, we use the Wildermuth condition instead of the pseudo potential method to exclude the Pauli forbidden state. If we assume a simple harmonic oscillator configuration of ${}^{110}\mathrm{Zr} \otimes \pi(2s1d0g)^{13} \otimes \nu(2p1f0h)^8$ for ${}^{131}\mathrm{I}$, the lowest allowed state should have the total oscillator qunanta of $N \geq 18$ and hence, the radial node in the $\alpha - {}^{131}\mathrm{I}$ relative wave function should be larger than $n = 9$ for the $L = 0$ state. The strength of the DF potential is taken to be $N_R \sim 0.8$ so as to reproduce the ground binding energy of -2.6 MeV for the $N = 18$ with $L = 0$ state. This normalization factor is consistent to the case of ${}^{44}\mathrm{Ti}$.

The energy spectra calculated for the $L^\pi = 0^+$ and $L^\pi = 1^-$ states are shown in Fig. 3. The lowest 0^+ and 1^- states correspond to the parity doublet for $\alpha + {}^{131}\mathrm{I}$. The energy splitting in the doublet is about 6.5 MeV, which is close to the energy splitting in the ${}^{20}\mathrm{Ne} = \alpha + {}^{16}\mathrm{O}$ system [1–3]. The doublet states of

0^+ at $E \sim 10$ MeV and 1^- at $E \sim 15$ MeV correspond to the one higher nodal states from the respective yrast states. The energy splitting of the excited doublet states is reduced to be about 4.5 MeV, and this reduction means that the α cluster structure is prominently developed in these excited doublet states.

The wave functions of the ground 0_1^+ and excited 1_2^- states are shown in the left and right panel in Fig. 4, respectively. The wave function plotted by the solid curve shows the results calculated from the cluster model with the DF potential, while the dashed curve represents the harmonic oscillator (HO) wave function with the parameter of $\nu = \mu\omega/2\hbar$ in the Gauss form factor of $e^{-\nu r^2}$ with the reduced mass of μ for $\alpha + {}^{131}$I. In the HO wave function, $\hbar\omega \approx 8$ MeV is calculated from the empirical rule in the mean field picture, such as $\hbar\omega = 41A^{-1/3}$ with the mass number of $A = 135$. Thus, the dashed curve in Fig. 4 corresponds to the shell model limit in the ${}^{135}\mathrm{Cs} = \alpha + {}^{131}\mathrm{I}$ system. In the ground 0_1^+ solution (left panel of Fig. 4), we can clearly understand that the main amplitudes of the shell model wave function are confined inside of about $R = 7$ fm, and it is uniformly distributed. On the contrary, in the cluster model solution, the tail of the wave function is considerably extended by about 1 fm. However, the overall feature of the wave function is almost the same as the shell model limit. Thus, the α cluster structure is not so prominent. The binding energy of the α particle is merely -2.6 MeV but the high Coulomb barrier in $\alpha - {}^{131}$I disturbs the penetration of the α particle to the asymptotic region.

Here we evaluate the nuclear radius of ^{135}Cs by using the following formula about the mean squared radius,

$$135\left\langle r^2\right\rangle_{\mathrm{Cs}} = 4\left\langle r^2\right\rangle_{\alpha} + 131\left\langle r^2\right\rangle_{\mathrm{I}} + \frac{4\times 131}{135}\left\langle R^2\right\rangle \quad , \tag{4}$$

where $\left\langle r^2\right\rangle_i$ represents the mean squared radius for nucleus i, while $\left\langle R^2\right\rangle$ shows the mean squared distance of $\alpha - {}^{131}$I relative wave function. The root mean squared radii in the ground state wave function (left panel in Fig. 4) are $\sqrt{\langle R^2\rangle} = 6.85$ fm and 6.44 fm for the cluster model and shell model limit, respectively. If we use the empirical value of $\sqrt{\langle r^2\rangle_\alpha} = 1.63$ fm for an α particle and $\sqrt{\langle r^2\rangle_{\mathrm{I}}} = 4.79$ fm for ^{131}I, which is calculated from the mean field density, we can get the root mean squared radius of $\sqrt{\langle r^2\rangle_{\mathrm{Cs}}} = 4.87$ fm and 4.85 fm for the cluster model and the shell model limit, respectively. Thus, the enhancement of the nuclear radius induced by the α clustering is so small.

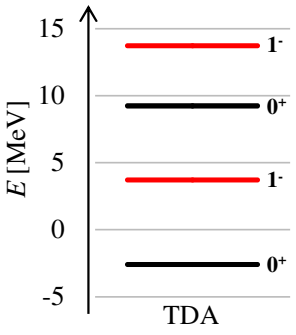

FIG. 3: (Color online) Energy spectra for $L^\pi = 0^+$ and 1^- bands in ${}^{135}\mathrm{Cs} = \alpha + {}^{131}$I calculated from DF potential. The α threshold energy is set to zero energy.

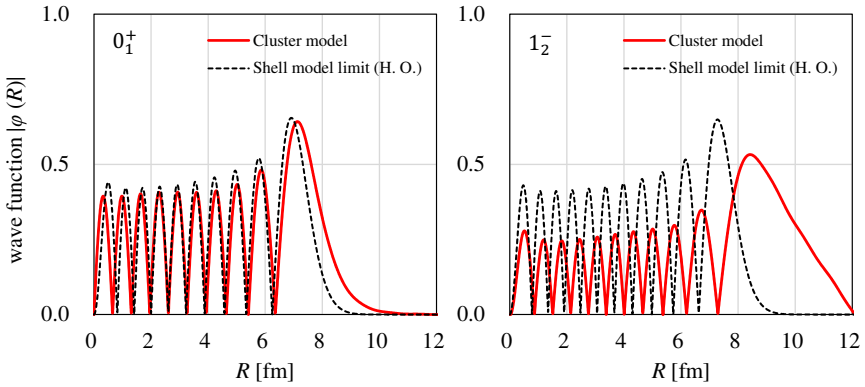

FIG. 4: (Color online) Relative wave functions of ${}^{135}\mathrm{Cs} = \alpha + {}^{131}$I. The dashed curve (Shell model limit) represents the harmonic oscillator wave function, while the solid curve (Cluster model) shows the solution obtained from the $\alpha + {}^{131}$I calculation. The left and right panel shows the results of the groung 0_1^+ and excited 1_2^- states, respectively. See text for details.

We have also investigated the wave function in the 1^- states. In the yrast 1_1^- state, the wave function obtained from the cluster model is almost same as the shell model limit, as discussed in the ground 0_1^+ state (left panel in Fig. 4). However, in the 1_2^- state shown in the right panel of Fig. 4, the wave function calculated by the cluster model (solid curve) prominently extended in comparison to the function of the shell model limit (dashed curve). The 1_2^- state is a resonant state above the Coulomb barrier, and the α emission occurs in this state. Since the dipole transition of $0_1^+ \to 1^-$ is strongly induced by the external Coulomb field, the α emission is possible in the $E1$ transition from 0_1^+ to 1_2^-, which leads to the nuclear transmutation of ${}^{135}\mathrm{Cs} \to {}^{131}$I. Thus, the evaluation of the dissociation cross section by the Coulomb filed is an important and interesting subject.

IV. SUMMARY AND DISCUSSION

In summary, we have performed the scattering and structure analyses for the system of ^{44}Ti = α + ^{40}Ca and investigated the validity of the DF potentials, which are derived from the DDM3Y interaction. We have considered target density approximation (TDA) in handling the density dependence in DDM3Y, which is newly proposed to improve the α elastic scattering [15]. In the scattering calculation, the normalization factor for the DF potential, N_R, is optimized to reproduce the experimental cross sections as much as possible. We have found that about 20% reduction is needed to reproduce the observed differential cross section. This is consistent to the results of the α scattering by a light target [22].

The rotational bands of the compound system of ^{44}Ti = α + ^{40}Ca are also calculated from the DF potential with the renormalized strength in the scattering calculation. The binding energy with respect to the α threshold is reasonably reproduced. Furthermore, the moment of inertia for the ground and excited bands is nicely reproduced. Thus, we can conclude that the DF potential constructed from the DDM3Y with TDA is appropriate to describe the α scattering and the α cluster structure consistently.

One should notice that TDA is not necessarily justified in the strict treatment of the density dependence, which requires the explicit treatment of the Pauli's exclusion principle generated by the anti-symmetrization effect. In Ref. [15], the justification of TDA was discussed by employing the nucleon multiple scattering theory. In this discussion, the Pauli-projection operator for the relative motion of the α – target nucleus is neglected but there is no justification for this approximation. In the previous study on the basis of resonating group method (RGM) [23, 24], the Pauli's exclusion principle or the anti-symmetrization of nucleons between the projectile and the target is essential, especially in the low energy region of $E/A \leq 100$MeV. Since the present analysis is performed at $E_\alpha \leq 60$ MeV, the TDA treatment on the basis of neglecting the anti-symmetrization is not justified in the strict theoretical treatment. However, TDA nicely works in the description of the observables in the scattering and structure phenomena, as demonstrated in the present calculation. Thus, we consider that TDA is useful technique in the pragmatic calculations about the α elastic scattering and the α cluster structure.

The TDA potential is applied to much heavier system, such as ^{135}Cs = α + ^{131}I, which is a kind of nuclear waste. The TDA potential with about 20% reduction, which is consistent to the analysis in ^{44}Ti = α + ^{40}Ca, can reproduce the binding energy of the α particle. The binding energy of the α particle is small, say about -2.6 MeV, but the α cluster structure is not so developed in the ground state. This suppression of the α clustering is due to the high Coulomb barrier in the α + ^{131}I system, and the results of the suppression is valid for the yrast 1^- state. However, in the excited 1^- state, the α – ^{131}I relative wave function is prominently extended in comparison to the simple shell model limit. In this situation, the α particle is easily emitted through the $E1$ transition of $0^+ \to 1^-_2$, which is induced by the external Coulomb field, and photonulcear reaction of (γ,α) may be one of tools to induce the nuclear transmutation, such as ^{135}Cs $\to$ ^{131}I. Of course, (γ,n) reaction is the dominant reaction in photoreaction of the medium nuclei, and there are many studies showing that the photoreaction is too inefficient to give rise to practical transmutation of nuclear wastes. However, the photoreaction is free from the problem of radioactive contamination, which occurs in neutron induced reaction, for example, the (n,$n\alpha$) reaction. Thus, we believe that it is still worth to consider the possibility of the transmutation by the photoreaction. The calculation of dissociation probability of ^{135}Cs into α + ^{131}I by the $E1$ Coulomb filed is now underway.

References

[1] K. Ikeda *et al.*, Prog. Theor. Phys. Suppl. **68**, 1 (1986).
[2] H. Horiuchi *et al.*, Suppl. Prog. Theor. Phys. **192**, 1 (2012), and references therein.
[3] M. Freer, Rep. Prog. Phys. **70**, 2149 (2007).
[4] T. Wada and H. Horiuchi, Phys. Rev. C**38**, 2063 (1988).
[5] S. Ohkubo, Y. Hirabayashi, and T. Sakuda, Phys. Rev. C**57**, 2760 (1998), and references therein.
[6] K. Ikeda *et al.*, Prog. Theor. Phys. Suppl. Extra Number, 464 (1968).
[7] G. R. Satchler and W. G. Love, Phys. Rep. **55** (1979).
[8] N. Yamaguchi, S. Nagata, and J. Michiyama, Prog. Theor. Phys. **76**, 1289 (1986).
[9] K. Amos, P. J. Dortmans, H. V. Von Geramb, S. Karataglidis, and J. Raynal, in Advances in Nuclear Physics, edited by J. W. Negele and E. Vogt (Plenum, New York, 2000), Vol. 25, p. 275.

[10] A. M. Kobos *et al.*, Nucl. Phys. **A384** (1982); A. M. Kobos, B. A. Brown, R. Lindsay and G. R. Satchler, Nucl. Phys. **A425**, 205 (1984).
[11] M. El-Azab Farid and G. R. Satchler, Nucl. Phys. **A438**, 525 (1985).
[12] M. E. Brandan and G. R. Satchler, Nucl. Phys. **A487**, 477 (1988).
[13] M. Ito, Y. Hirabayashi and Y. Sakuragi, Phys. Rev. C **66**, 034307 (2002), and references therein.
[14] S. Ohkubo and Y. Hirabayashi, Phys. Rev. C**70**, 041602(R), (2004).
[15] K. Egashira, K. Minomo, M. Toyokawa, T. Matsumoto, M. Yahiro, Phys. Rev. C **89**,064611 (2014).
[16] R. Fujita *et al.*, Impulsing Paradigm Change through Disruptive Technologies Program (ImPACT), http://www.jst.go.jp/impact/.
[17] S. Saito, Suppl. Prog. Theor. Phys. **62**, 11 (1977).
[18] H. Masui, K. Kato and K. Ikeda, Phys. Rev. C **75**, 034316 (2007).
[19] S. Ebata, T. Nakatsukasa, T. Inakura, K. Yoshida, Y. Hashimoto, and K. Yabana, Phys. Rev. C**82**, 034306 (2010).
[20] Y. Iseri (Private communication).
[21] T. Yamaya, K. Katori, M. Fujiwara, S. Kato and S. Ohkubo, Prog. Theor. Phys. Suppl. **132**, 73 (1998).
[22] M. Nakao, H. Umehara, S. Sonoda, S. Ebata and M. Ito, EPJ Web of Conf. 163, 00040 (2017).
[23] T. Wada and H. Horiuchi, Prog. Theor. Phys. **80**, 488 (1988); *ibid.*, **80**, 502 (1988).
[24] K. Yabana, T. Wada, and H. Horiuchi, Prog. Theor. Phys. **79**, 19 (1988).

This is a blank page.

33 Transmission Measurements for a Neutron Imaging Using a Boron-type Neutron Grid

Kaoru Y. HARA[1)*], Minoru ASAKO[1)], Takashi KAMIYAMA[1)], Hirotaka SATO[1)], Yu UEHARA[1)], Kenichi OIKAWA[2)], and Takenao SHINOHARA[2)]

1) Faculty of Engineering, Hokkaido University, Sapporo 060-8628, Japan
2) J-PARC Center, Japan Atomic Energy Agency, Ibaraki-ken 319-1195, Japan
*e-mail: hara.kaoru@eng.hokudai.ac.jp

Newly designed boron-type neutron grid was tested in NOBORU at J-PARC MLF in order to suppress smearing neutron transmissions caused by scattered neutrons entering into a detector. The results show decrease of 2-3% in transmission rate indicating the positive effects for suppressing scattered neutrons.

1. Introduction

An energy-resolved neutron imaging method is a useful tool to provide information of microstructure including crystalline structures and elemental composition for a bulk sample non-destructively. Since they are obtained from the analysis of neutron transmission spectra, it is important to measure the neutron transmission rate accurately. For this analysis, neutrons scattered by the sample are a background component. A simple countermeasure against the scattered neutrons is to keep a proper distance l_{sd} from the sample to the detector because the solid angle of the scattered neutron entering into the detector decreases with increasing l_{sd} although the image degradation is caused with increasing l_{sd} from the beam divergence. In the previous work [1], an example of the dependence of l_{sd} on Bragg edge transmission spectra of an iron sample were presented by the calculation with the PHITS code [2]. On the other hand, we have tested a grid method for reducing the background due to the scattered neutrons by a gadolinium-type neutron grid using the Hokkaido University neutron source (HUNS) [3].

In this work, we prepared a boron-type neutron grid which is a pair of crossing slits

composed of many layers of boron-evaporated silicon. The dimensions of the slit are 0.4 mm (width), 60 mm × 60 mm (area), and 22 mm (depth). Because the boron has a large neutron-absorption cross section, the neutron grid restricts a solid angle of transmitted neutrons from the sample and suppress the scattered neutrons entering into a detector as shown in Fig. 1. In this paper, the advantage of boron-type neutron grid for measuring neutron transmissions of industrially important materials is reported by comparing those measured without the neutron grid.

2. Experimental

The experiment was performed in the beam-line NOBORU [4] at the Material and Life Science Experimental Facility (MLF) of Japan Proton Accelerator Research Complex (J-PARC). The proton beam power was about 150 kW and the repetition rate of the proton beam pulses was 25 Hz. The schematic view and photograph of the experimental setup are shown in Fig. 2. The two-dimensional transmission images for the sample were measured with the neutron time-of-flight (TOF) technique by a gas electron multiplier (GEM) detector [5]. The neutron grid set on stages of rotary and swivel, was located between a sample and a detector. As shown in Fig. 2(c), the angles of the slits with respect to the incident neutron beam were adjusted with these stages by surveying the maximum counting rate of the GEM detector. The neutron beam was collimated by a removable collimator to 50 mm × 50 mm, which is within the slit area of the neutron grid. The L/D ratio that is related to the angular divergence of neutron beam was approximately 1900, where L was a length between a rotary collimator and sample, and D was the aperture size of rotary collimator.. In addition, the plates of Co, In, Ag, and Cd were used as the neutron black resonance filters in order to estimate other backgrounds except the scattered neutron from the sample. The length of neutron flight path from the moderator to the GEM detector was 15 m. The iron plates with thicknesses of 5 and 10 mm were measured using this setting. Dimensions of the plates are 100 mm × 100 mm in both cases. The neutron transmission for a gold sheet was also measured for the energy calibration through neutron flight time. After the measurement with the neutron grid, the neutron grid was removed from the beam line with keeping the sample and other parameters for comparisons.

3. Results

Figure 3 shows a typical neutron transmission image for the iron plate with 5 mm thickness measured with the neutron grid. The square shadow corresponds to a part of iron plate. The

shape of outer frame corresponds to the neutron shield which was located in front of the neutron grid. The effective field of view is approximately 60 mm × 60 mm while the window area of GEM detector is 100 mm × 100 mm.

Figure 4(a) shows the neutron transmissions of the iron plate with 5 mm thickness measured with and without the neutron grid are shown by the solid and dashed lines, respectively. Several Bragg edges are observed in the neutron transmission spectra. The distance between the iron sample and the GEM detector was fixed at 14 cm. As shown in Fig. 4(a), the neutron transmission measured with the neutron grid is a few percent lower than the one measured without the neutron grid in the neutron wavelength region of λ = 0.2 - 0.5 nm, indicating reduction of entering scattered beam into the detector. The same effect was also observed in the neutron transmissions of the 10-mm thickness iron sample were plotted in Fig. 4(b). Based on the calculation with the PHITS code, the reduction rate will be more effectively enhanced when setting the neutron grid at a shorter l_{sd}.

4. Conclusion

In order to reduce the background neutrons due to the scattered neutrons from the sample, the newly designed boron-type neutron grid was introduced to the neutron transmission measurements in NOBORU at J-PARC MLF. The iron plates with the thicknesses of 5 and 10 mm were measured as the trials. A few percent reductions in the transmission rates of both samples were observed indicating that the neutron grid at l_{sd} = 14 cm was effective for reduction of entering the scattered neutron into the GEM detector for the neutron wavelength region of 0.2 - 0.5 nm. Further optimization of geometry is required for the effective suppression of the scattered beam. The neutron transmission for a sample having a large scattering cross section will be measured using the neutron grid with optimized setting.

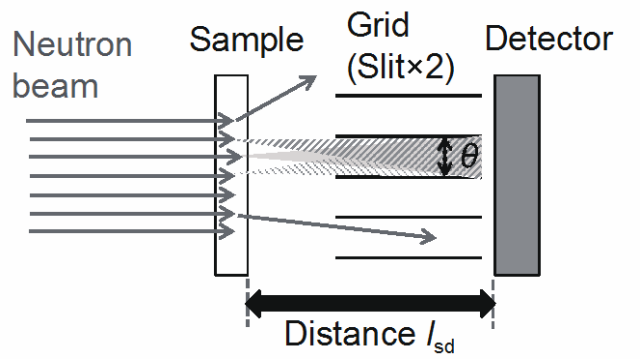

Figure 1: Schematic drawing of neutron grid method

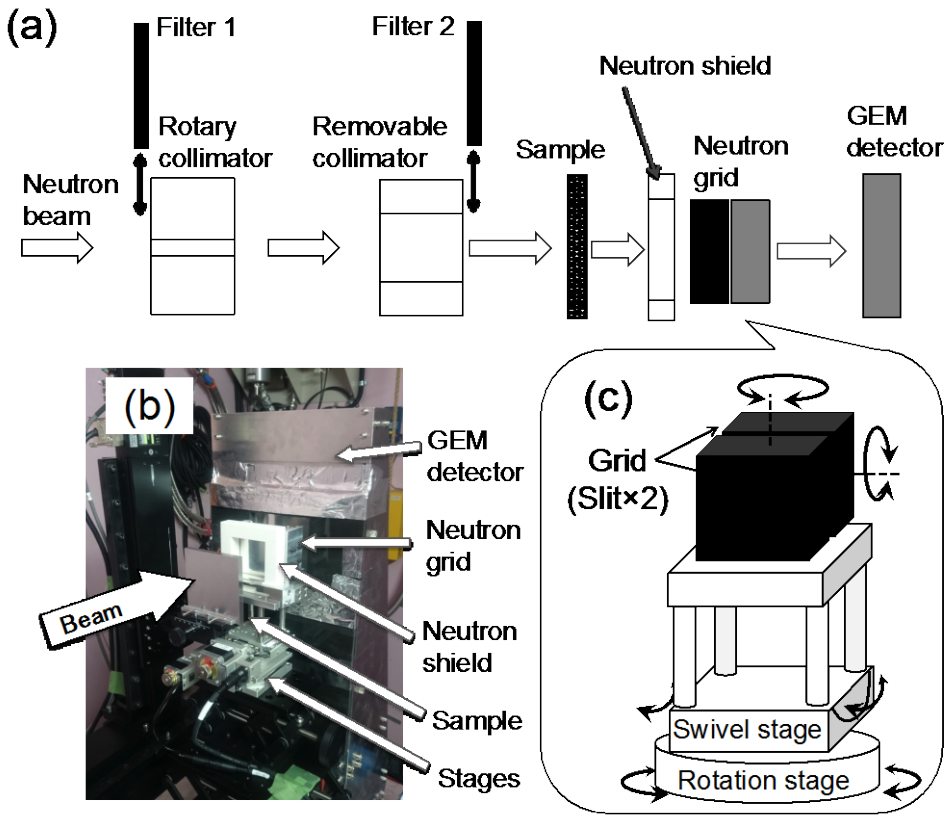

Figure 2: Experimental setup with the neutron grid in NOBORU at J-PARC MLF

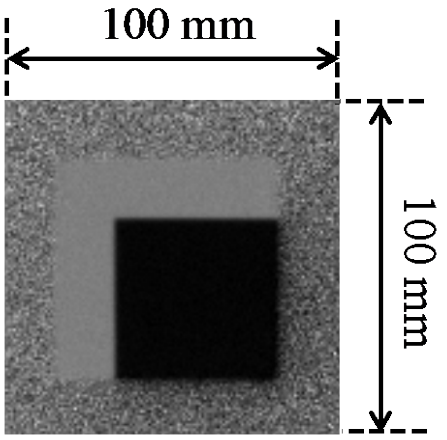

Figure 3: Neutron transmission image for the 5-mm thickness iron sample measured with the neutron grid.

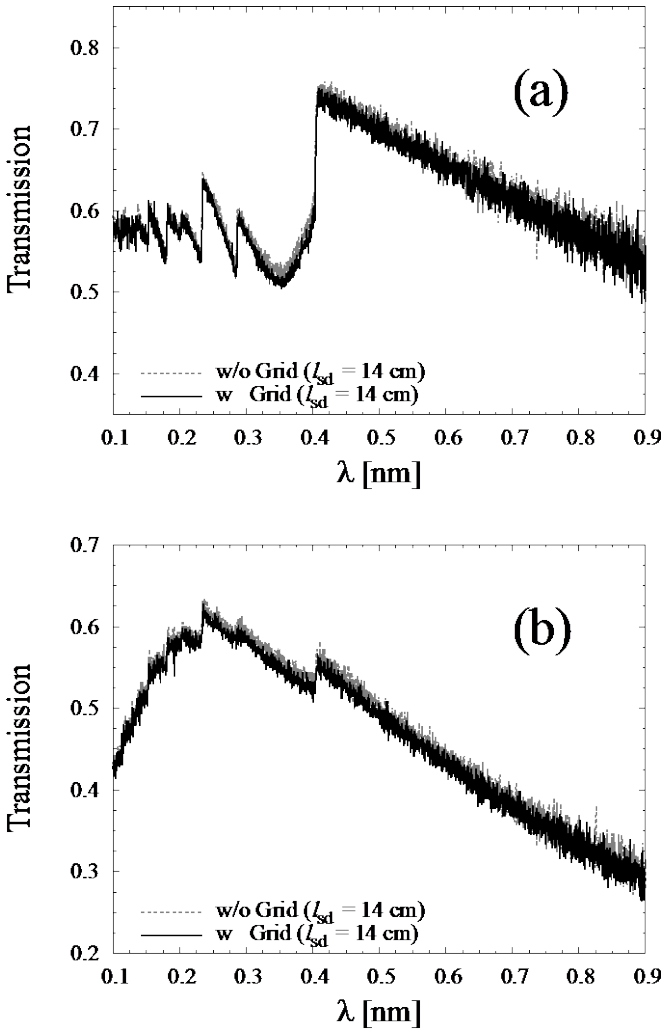

Figure 4: Neutron transmission spectra for the iron samples with the thicknesses of 5 mm (a) and 10 mm (b).

Acknowledgments

This work was supported by the Photon and Quantum Basic Research Coordinated Development Program of the MEXT (Ministry of Education, Culture, Sports, Science, and Technology). This measurement was carried out under the non-proprietary use proposal of the J-PARC MLF entitled “Neutron transmission measurements using a boron-type neutron grid” (Proposal No. 2017A0219).

References

[1] Sato H, Watanabe K, Kiyokawa K, Kiyanagi R, Hara KY, Kamiyama T, Furusaka M, Shinohara T and Kiyanagi Y. Further improvement of the RITS code for pulsed neutron

Bragg-edge transmission imaging. Phys. Proc. 2017;88:322-330.
[2] Sato T, Niita K, Matsuda N, Hashimoto S, Iwamoto Y, Noda S, Ogawa T, Iwase H, Nakashima H, Fukahori T, Okumura K, Kai T, Chiba S, Furuta T and Sihver L. Particle and Heavy Ion Transport Code System PHITS, Version 2.52. J. Nucl. Sci. Technol. 2013;50:913-923.
[3] Hara KY, Sato H, Kamiyama T, Shinohara T. Measurement and simulation for a complementary imaging with the neutron and X-ray beams. EPJ Web Conf. 2017;146: 03032-1-4.
[4] Oikawa K, Maekawa F, Harada M, Kai T, Meigo S, Kasugai Y, Ooi M, Sakai K, Teshigawara M, Hasegawa S, Futakawa M, Ikeda Y, Watanabe N. Design and application of NOBORU−NeutrOn Beam line for Observation and Research Use at J-PARC. Nucl. Instr. Meth. 2008;A589:310-317.
[5] Uno S, Uchida T, Sekimoto M, Murakami T, Miyama K, Shoji M, Nakano E, Koike T, Morita K, Satoh H, Kamiyama T, and Kiyanagi Y. Two-dimensional neutron detector with GEM and its applications. Phys. Proc. 2012;26:142-152.

34 Progress of neutron-capture cross-section measurements
Promoted by ImPACT Project at ANNRI in MLF of J-PARC

Shoji Nakamura[1]*, Atsushi Kimura[1], Brian Yamada Hales[1], Osamu Iwamoto[1],
Yuji Shibahara[2], Akihiro Uehara[2], and Toshiyuki Fujii[3]

1) Japan Atomic Energy Agency, 2-4 Shirakata, Tokai-mura, Naka-gun, Ibaraki 319-1195
2) Institute for Integrated Radiation and Nuclear Science, Kyoto University,2-1010 Asashiro Nishi, Kumatori-cho, Sennan-gun, Osaka 590-0494
3) Osaka University, 2-1 Yamadaoka, Suita, Osaka 565-0871

*e-mail: shoji.nakamura@jaea.go.jp

Study on cross-section measurements has been promoted for ^{135}Cs among long-lived fission products in ImPACT Project. Measurements have been started at ANNRI in MLF of J-PARC using the ^{135}Cs sample prepared in FY 2016. This paper reports research progresses on measurements of neutron-capture cross-section of ^{135}Cs.

This work was funded by ImPACT Program of Council for Science, Technology and Innovation (Cabinet Office, Government of Japan).

Keywords: ImPACT, transmutation, long-lived fission products, Cesium-135, neutron-capture cross-section

1. Introduction

The social acceptability on nuclear power reactors is related to the waste management of long-lived fission products (LLFPs) existing in spent nuclear fuels. The LLFPs are important in the nuclear waste management, because the presence of these nuclides induces long-term radiotoxicity because of their extremely long half-lives. The transmutation is one of the solutions to reduce the radiotoxicity of nuclear wastes [1]. The ImPACT project aims to realize a "large reduction and exploitation of resources in high-level nuclear waste by nuclear transmutation", by using an accelerator to accomplish nuclear transmutation of LLFPs [2]. This project targets the major LLFPs: ^{107}Pd, ^{93}Zr, ^{135}Cs, ^{126}Sn, and ^{79}Se, as well as the medium-lived fission product ^{137}Cs. To perform accelerator-based nuclear transmutation effectively, it is necessary to acquire reaction cross-section data for the radionuclides across a wide spectrum of incident particle energies. As for the current status of reported values of the capture cross-sections of ^{135}Cs, there is only one report of the resonance parameters obtained by the transmission experiment by Anufriev *et al*.[3]. Therefore, our concern was focused to measure the cross-sections of ^{135}Cs because of its long half-life (2.3×10^6 years [4]).

2. Experiments

2.1 Sample preparation of ^{135}Cs

Since a ^{135}Cs sample was not supplied, it was considered to use ^{135}Cs, which would be included as an

impurity in a ^{137}Cs sample. Since Isotope separation is difficult, ^{137}Cs and ^{135}Cs would be present in a ratio of 1:1 from the viewpoint of nuclear fission yield. Cesium-137 has a half-life of 30.08 years [4]. If the samples deteriorated over time, it would be advantageous for the measurement because the ^{135}Cs abundance ratio is larger than unity. We found that Russia's Isotope Research Institute had ^{137}Cs solutions about 30 years old. Therefore, ^{137}Cs solutions of 200 MBq were extracted and pelletized with yttrium oxide (Y_2O_3) as a binder, and then the Cs pellet was fabricated as a sealed source of aluminum disk shape. The radiation source was delivered in March, 2017. **Figure 1** shows the sealed ^{137}Cs source produced in this project. The size of the source is 5 cmϕ, and the active area 1cmϕ. Its radioactivity is nominally 190±9 MBq. To make sure, the source was quantified by a comparison method. **Figure 2** shows the quantitative analysis of the source. A electrically cooled Ge detector was shielded with lead blocks, and the direction of the detection surface was only released. The sealed 200 MBq source was placed at a distance of 2.5 m from the front surface of the Ge detector, and measured for 2 hours. Then, a 1 MBq of ^{137}Cs calibration source was placed at the same position, and measured for 3 days. Since detection efficiencies are same for both sources, the radioactivity of the sealed source can be quantified simply by comparing yields of 662-keV gamma ray obtained with each source. The radioactivity amount of the sealed Cs source was confirmed to be 200.7±2.5 MBq. Although the error of the nominal value was 5%, it was able to be re-calibrated with an accuracy of 1.2%.

Figure 1 The sealed ^{137}Cs source (200 MBq).

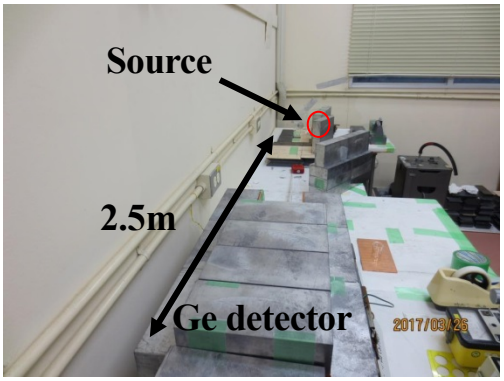

Figure 2 Determination of the activity of the sealed source by a comparison method.

In order to quantify the amount of ^{135}Cs in the sealed ^{137}Cs source, it is necessary to accurately determine the isotope ratio of ^{135}Cs and ^{137}Cs by mass spectrometry. For that reason, we have started to apply mass spectrometry to a very small amount of radioisotope sample, and to confirm its effectiveness. The mass spectrometer TRITON (Thermo Fisher Scientific Inc.) was used for this analysis. Since the sample is radioactive, it is desirable to load very small amount so as not to contaminate the spectrometer. However, the mount of the sample must be increased to obtain high statistical accuracy. High precision experiments were carried out using the ^{137}Cs standard solution and its isotopic ratio of ^{135}Cs and ^{137}Cs was able to be obtained with an accuracy of 0.5% even with very small samples of about 10 Bq.

Figure 3 The ^{137}Cs solution extracted from the same batch as the sealed ^{137}Cs source.

We have obtained the ^{137}Cs stock solution extracted from the same batch as the sealed ^{137}Cs source as shown in **Figure 3**. We plan to perform mass analysis with this solution at Kyoto University.

2.2 Measurements of ^{137}Cs at ANNRI

Experiments were performed by the experimental apparatus called "Accurate Neutron Nucleus Reaction measurement Instrument (ANNRI)" at the Beam Line No.4 (BL04) of the Materials and Life science experimental Facility (MLF) in the J-PARC. The BL04 is shown in **Figure 4**.

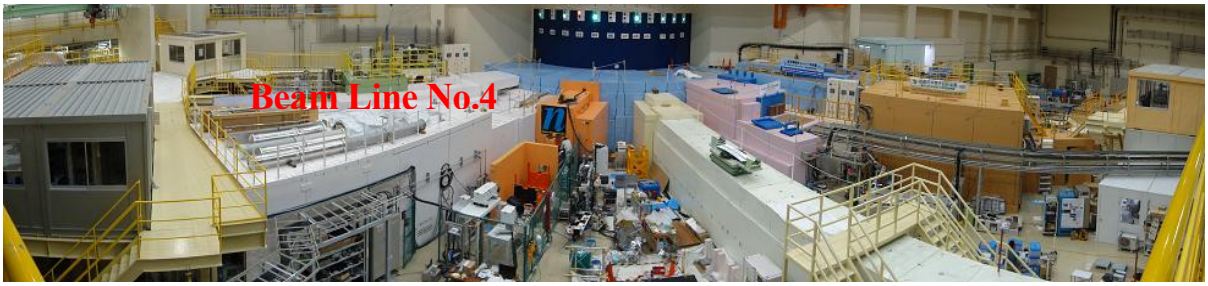

Figure 4 Overview of the experimental apparatus called "Accurate Neutron Nucleus Reaction measurement Instrument (ANNRI)" at BL04 in MLF of J-PARC**.**

The ANNRI aparatus consists of two kinds of detectors and shielding walls for neutron and gamma rays. One of the detectors is a "Ge spectrometer", which consists of two cluster Ge detector, eight coaxial-Ge detectors, and BGO anti-Compton shields as shown in **Figure 5**. Its energy resolutions for 1.33-MeV γ-ray are 5.8 keV in on-beam and 2.4 keV in off-beam conditions. Its peak efficiency for 1.33-MeV γ-ray is 3.64±0.11% as a nominal value [5]. Another one is NaI detectors, which was installed by Tokyo Institute of Technology. The ANNRI has an advantage for the neutron capture cross-section measurements because the MLF facility can provide the highest pulsed neutron intensity in the world when the 1-MW operation would be achieved [6]. In addition to the highest pulsed neutron intensity, ANRRI has also more advantage by introducing High speed data acquisition system based on CAEN digitizers [7].

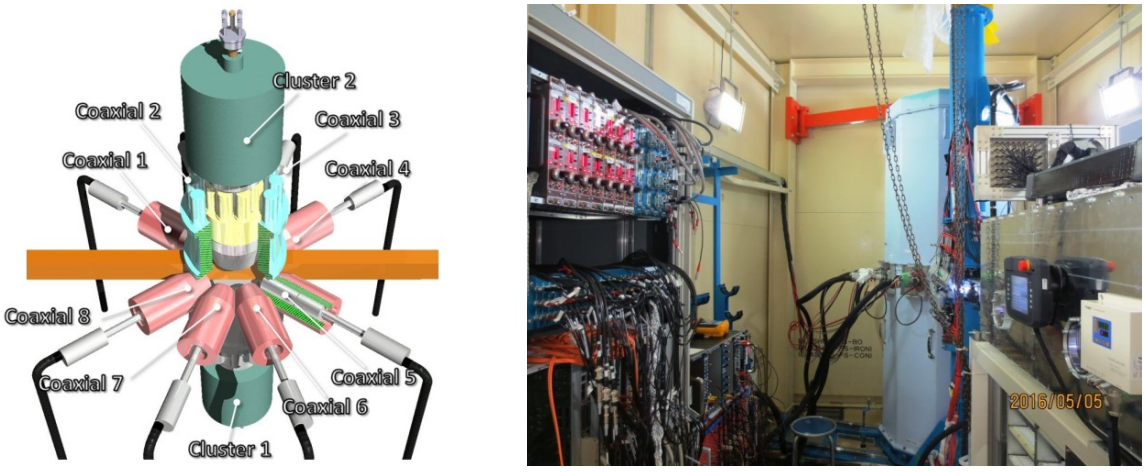

a) **b)**

Figure 5 **a)** the Ge spectrometers installed with ANNRI, **b)** a photo of actual set-up of the Ge spectrometer.

It was necessary to perform Time-Of-Flight (TOF) measurements under the condition that 662-keV gamma rays were emitted from the sealed ^{137}Cs source with radioactivity of 200 MBq, and therefore the beam duct where the source was placed was shielded by lead blocks of 5 cm thickness as shown in **Figure 6 a)**. The cluster-Ge detectors faced so as to sandwich the duct, and lead blocks were laid between the detectors and the duct. Furthermore, in order to strengthen the shielding on the upstream side, lead blocks and LiF filled (40%) polyethylene blocks were installed as shown in **Figure 6 b)**. The neutron beams travel from the left to the right of the beam duct in Fig. 6a).

a)

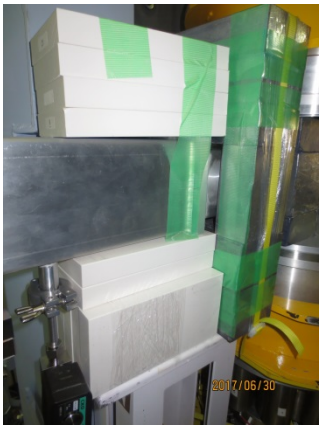

b)

Figure 6 **a)**Lead shielding blocks around the beam duct at a sample position, **b)** lead blocks and polyethylene blocks(40% LiF) at the upper stream of the detectors.

The accelerator of J-PARC was operated in 150-kW power and in single bunch mode. Experimental conditions were as follows: collimator was 7 mmϕ, no Pb filter was used, and X-stage was opened. The sealed ^{137}Cs source was placed in the duct at a position of 21.5 m in flight path. Since the sealed source was used, the inside of the beam duct cannot be evacuated, and therefore the atmosphere in the duct was replaced with He gas.

3. Preliminary result and Discussions

Figure 7 shows an example of TOF spectrum obtained by neutron irradiation of the sealed ^{137}Cs source. Several resonance peaks were observed. The first resonance (6 eV) of ^{133}Cs isotope contained in the ^{137}Cs source was observed. As a result of identification by energy calibration, other weak resonance peaks were attributed to almost ^{133}Cs. Among them, weak resonance peak due to ^{135}Cs was observed at the neutron energy of 42 eV reported by Anufriev *et al*.[3]. It could be said that this is the first observation of the ^{135}Cs resonance in the neutron capture reaction. However, in this experiments, resonance peaks caused by ^{135}Cs other than 42-eV resonance could not be observed.

In Fig.7, broad resonances are observed around 10^5 nsec. This was caused by the neutron capture reaction of Ge, when scattered neutrons entered into the BGO detectors. This indicates that neutron shieldings around the detectors were insufficient. The influence of this neutron scattering makes it difficult to observe resonances in the higher neutron energy region. Thus, in order to search for weak resonances of ^{135}Cs, it is necessary to reduce the background by enhancing neutron shields. Furthermore, since the sample amount was as small as 200 MBq in this experiments, and also the accelerator power was as low as 150-kW, these conditions made the measurements difficult. We have been developing a ^{137}Cs

source of 950 MBq, and plan to improve a signal-to-noise ratio more when the accelerator power will be raised in the future. Of course, in parallel, we will also enhance shielding around the detectors.

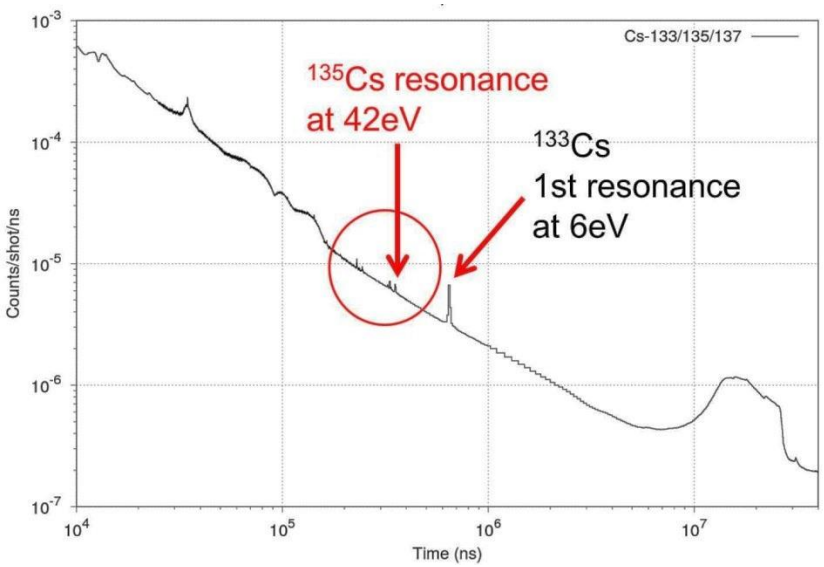

Figure 7 An example of TOF spectrum of the ^{137}Cs sample obtained by neutron irradiations

4. Summary

In the ImPACT project, we have been promoting neutron-capture cross section measurements of ^{135}Cs. Considering the use of ^{135}Cs contained as an impurity in the ^{137}Cs sample, the sealed ^{137}Cs source with 200 MBq in radioactivity had been prepared. We transported the sealed ^{137}Cs source to J-PARC and carried out TOF experiments at ANNRI in MLF. As a preliminary result, we succeeded in observing the 42-eV resonance ascribed to ^{135}Cs for the first time in the neutron capture reaction. Data analysis is in progress. In parallel, we have been strengthening shields around the detectors, and manufacturing another sealed ^{137}Cs source (950 MBq). After the delivery of the sealed ^{137}Cs source, neutron capture cross-section measurements for ^{135}Cs will be carried out again in March, 2018**.**

Acknowledgment

The authors would like to appreciate the staff of J-PARC and Institute for Integrated Radiation and Nuclear Science, Kyoto University for their support.

References

[1] K.Nishihara *et al.*, Proceedings od 21st International Conference & Exhibition: Nuclear Fuel Cycle for a Low-Carbon Future (GLOBAL 2015). 2015: pp.388-395.
[2] http://www.jst.go.jp/impact/index.html (accessed 2018-04-01).
[3]V.A.Anufriev *et al*., Atomnaya Energiya, Vol.63, No.5, pp.346-347 (1987).
[4] R.B. Firestone *et al*., Table of Isotopes, 8th ed. Update, John Wiley and Sons, New York, (1998).
[5]T. Kin *et. al*., *the 2009 NSS-MIC Conf. Rec.*, N24-2, (2009).
[6] K. Kino *et al*., NIM-A, **626**, pp. 58 -66 (2011).
[7] T. Nakao *et al.*, ND2016, **R130**, (2016).

This is a blank page.

35 Analysis of $^{135}Cs/^{137}Cs$ isotopic ratio for samples used for neutron capture cross section measurement project by thermal ionization mass spectrometry

Yuji Shibahara[1)*], Akihiro Uehara[1)], Toshiyuki Fujii[2)],
Shoji Nakamura[3)], Atsushi Kimura[3)], Brian Hales[3)], Osamu Iwamoto[3)]

1) Research Reactor Institute, Kyoto University,
2-1010 Asashiro Nishi, Kumatori, Sennan, Osaka, Japan, 590-0494
2) Graduate School of Engineering, Osaka University,
2-1 Yamadaoka, Suita, Osaka, Japan, 565-0871
3) Japan Atomic Energy Agency,
2-4, Shirakata, Tokai, Naka, Ibaraki, Japan, 319-1195
*e-mail: y-shibahara@rri.kyoto-u.ac.jp

The measurement of the isotopic composition of Cs by thermal ionization mass spectrometry was performed on the nuclear cross-section measurement project of ImPACT program. It was found that *ca*. 1×10^{-12} g of ^{137}Cs would be the achievable lower limit for the target level of the measurement precision (0.5% in ±2 r.s.d.). The measurement condition discussed in this study was applied for the measurement of the $^{135}Cs/^{137}Cs$ isotopic ratio of ^{137}Cs standard solution sample purchased from Japan Radioisotope Association.

1. INTRODUCTION

The long-lived fission products (LLFPs) show long-term radiotoxicity because of their extremely long half-lives, and are important on the nuclear waste management. One project in the Impulsing PAradigm Change through disruptive Technologies (ImPACT) program [1] has been launched to realize a theme of "Reduction and Resource Recycling of High-level Radioactive Waste through Nuclear Transmutation". This project focuses on the LLFPs such as ^{107}Pd, ^{93}Zr, ^{135}Cs, ^{126}Sn and ^{79}Se, and has a topic of "Nuclear reaction data acquisition" for the effective nuclear transmutation of these nuclides.

To pursue the acquisition and accuracy/precision improvement of nuclear data of LLFPs, high quality data of the isotopic composition of samples are indispensable. Because it is difficult to obtain a pure ^{135}Cs sample, in the case of data acquisition of ^{135}Cs, ^{135}Cs existing in a ^{137}Cs sample as the impurity has been used as a target in our studies [2, 3]. Objective of our group in this project is to analyze the isotopic composition of Cs samples for the evaluation of the neutron nuclear

reaction data of ^{135}Cs.

The mass spectrometry is the most suitable method for measurement of the isotopic composition of Cs, since ^{135}Cs has a long half-life of 2.3×10^{6} yr [4] and is a pure β-emitter. We have studied the isotopic composition of Cs in the environmental samples contaminated at a nuclear accident [5-7] by the thermal ionization mass spectrometry (TIMS), which has an advantage among the mass spectrometry. Based on these previous studies, we studied the analysis of the isotopic composition of Cs samples which were used to evaluate the neutron nuclear reaction data of ^{135}Cs.

For the high accuracy/precision analysis of the isotopic composition, the performance check with using the standard reference material is important. There is no suitable standard reference material for the analysis of isotopic composition of Cs, meaning that the performance check including the statistical error check is difficult. There are several reports on the isotopic analysis of Cs in the environmental sample [8-11]. We analyzed the isotopic composition of Cs in the environmental samples for the performance check of the Cs sample analysis as the first step.

For the acquisition and accuracy/precision improvement of nuclear data of ^{135}Cs, we set the target level of the precision of the ^{135}Cs/^{137}Cs isotopic ratio data as 0.5% in ±2 relative standard deviation (r.s.d.). For the suppressing of contamination of the mass spectrometer from the radioactive nuclei of ^{137}Cs and ^{135}Cs, on the other hand, the sample usage was extremely limited. Thus, we discussed that the analytical condition of the mass spectrometry of Cs to achieve this analytical level and the isobaric interference by Ba which would be important error factor for the analysis of the ^{135}Cs/^{137}Cs isotopic ratio.

Based on these studies, we analyzed the isotopic ratio of ^{135}Cs/^{137}Cs of ^{137}Cs standard solution sample purchased from Japan Radioisotope Association (JRIA).

2. EXPERIMENT

2.1. Reagents and materials

Reagent grade of strontium nitrate, barium nitrate and cesium nitrate, and ultrapure grade of hydrochloric acid and nitric acid were purchased from Wako Pure Industry. Ultrapure grade of hydrogen peroxide was obtained from Tama Chemicals Corporate. They were used without further purification.

The environmental sample of JSAC-0765 was obtained from the Japan Society for Analytical Chemistry. After baking at 723 K in the furnace, Cs including radionuclides was recovered from *ca*. 2.5 g of the sample according to the chemical purification procedure reported in our previous studies [5-7].

The ^{137}Cs standard solution sample (1.2×10^{5} Bq/mL, 3 mL) was purchased from JRIA. A small portion of this sample was taken and was converted to the nitric acid solution, since this sample was the chloric acid solution originally.

As the standard reference material of uranium mass spectrometry, CRMU010 standard material [12] was used. Uranium solution in 1 M HNO_3 was prepared as the sample solution for mass spectrometry.

2.2. Analytical procedure

In the analysis of Cs by TIMS, a thermal ionization mass spectrometer (TRITON-T1^{TM}, Thermo

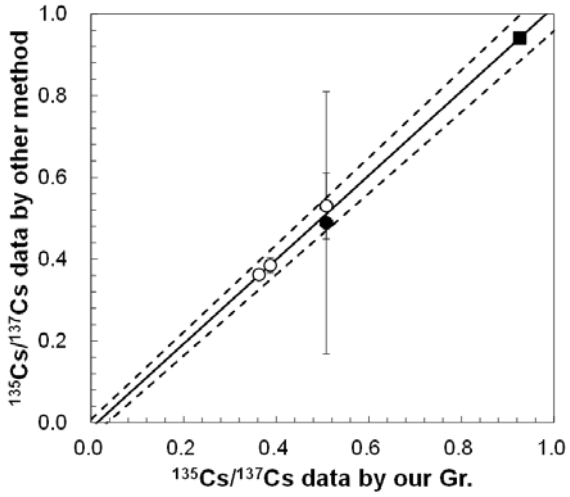

Fig. 1 Correlation of $^{135}Cs/^{137}Cs$ isotopic ratio data with results by other method
Open circle, closed circle and closed square show the data by TIMS[8-10], ICP-QMS[11] and calculated value using by ORIGEN-II code[14], respectively.

Fisher Scientific) with a rhenium single filament system was used. The sample solution prepared as 1 M HNO_3 was loaded onto a rhenium filament with a TaO activator. Because of the total amount of Cs loaded on the filament, the mass spectrometry of Cs was conducted with a secondary electron multiplier detector and the peak jump method [5-7].

A rhenium filament was heated until the Cs (^{135}Cs, ^{137}Cs and also ^{133}Cs) ion beam showed the enough intensity without the rapid increasing of the vacuum; the vacuum during the analytical procedure was kept less than 2.0×10^{-5} Pa around the ion source. After the optimization of the ion lens with the ion beam of Cs and the confirmation of the stability of the ion beam of Cs, the isotopic compositions of Cs samples were analyzed; the measurement procedure was based on our previous study [5-7], and the vacuum around the ion source during data acquisitions was better than 5.0×10^{-6} Pa. The isotopic compositions of Cs were evaluated from the isotopic ratio of $^{135}Cs/^{137}Cs$.

Analyses of Sr and Ba were conducted by TIMS with a rhenium single filament method using a TaO activator. The loading amounts of Sr and Ba were *ca*. 100 ng. Based on the procedure reported in our previous study [6], the isotopic compositions of Sr and Ba ($^{87}Sr/^{86}Sr$ for Sr, and $^{135}Ba/^{137}Ba$ for Ba) were measured at several levels of the ion beam current (from 9.2×10^{-16} A to 5.0×10^{-12} A). The Cs/Ba mixed solution was loaded onto a rhenium filament for the single filament method with a TaO activator, and the ion beams of Cs and Ba were observed for discuss of the isobaric interference effect of Ba.

Analysis of U was conducted by a rhenium double filament method of TIMS. The loading amount of U was *ca*. 1 ng. Based on the procedure reported in our previous study [13], the isotopic composition of U ($^{235}U/^{238}U$) was measured at several levels of the ion beam current (from 2.0×10^{-16} A to 2.0×10^{-13} A).

3. Results and discussion

3.1 Comparison of $^{135}Cs/^{137}Cs$ ratio by other method

The $^{135}Cs/^{137}Cs$ isotopic ratios obtained in our study were compared with literature data is shown in Fig. 1. The isotopic ratios of Cs in environmental samples contaminated by radioactive Cs at the Chernobyl nuclear accident (IAEA-156 [7]) and the Fukushima Daiichi nuclear accident (JSAC-0765 observed in this study, and the environmental sample obtained in Iitate village [5]) were compared with the results obtained by the other group [8-11]. In this study, the $^{135}Cs/^{137}Cs$ isotopic ratio obtained by the neutron irradiation of natural uranium at the KURRI [6] was also compared with the calculation results by using the ORIGEN-II code [14]. Although the statistical

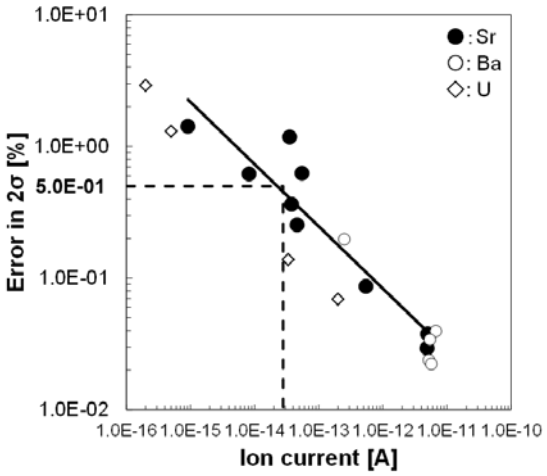

Fig. 2 Correlation of relative standard deviation with ion beam current of Sr, Ba and U (left).

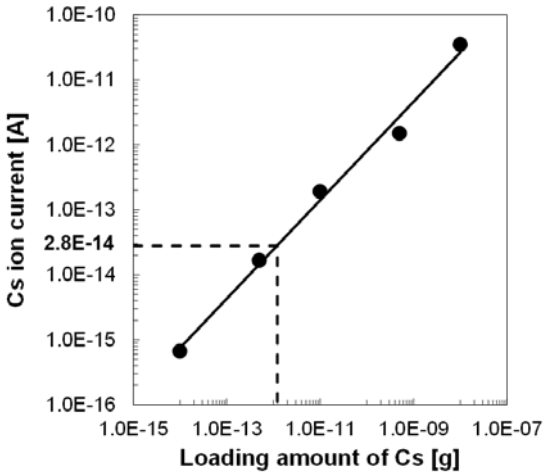

Fig. 3 Correlation of Cs ion beam current with loading amount of Cs (right).

precision was not excellent because of the low concentration of the radioactive Cs in the environmental sample, it was found that the isotopic ratio observed in our study showed the statistical agreement with the report of other group and the 1:1 linear correlation as follows;

$Y = (1.002 \pm 0.012) \times X$, $R^2 = 0.993$, or

$Y = (-0.013 \pm 0.021) + (1.030 \pm 0.037) \times X$, $R^2 = 0.996$,

where X and Y mean the analytical data of our group and that reported by the other group, respectively. The more detailed study on the systematic error of the analysis of the isotopic composition of Cs is under examination.

3.2 Loading amount of radioactive Cs and isobaric effect of Ba

Figure 2 shows the effect of ion beam current on the precision of isotopic ratio measurement in ±2 r.s.d. The analytical precision showed an inverse correlation with the ion beam current regardless of elements ($R^2 = 0.915$). In this study, the target level of the precision of the $^{135}Cs/^{137}Cs$

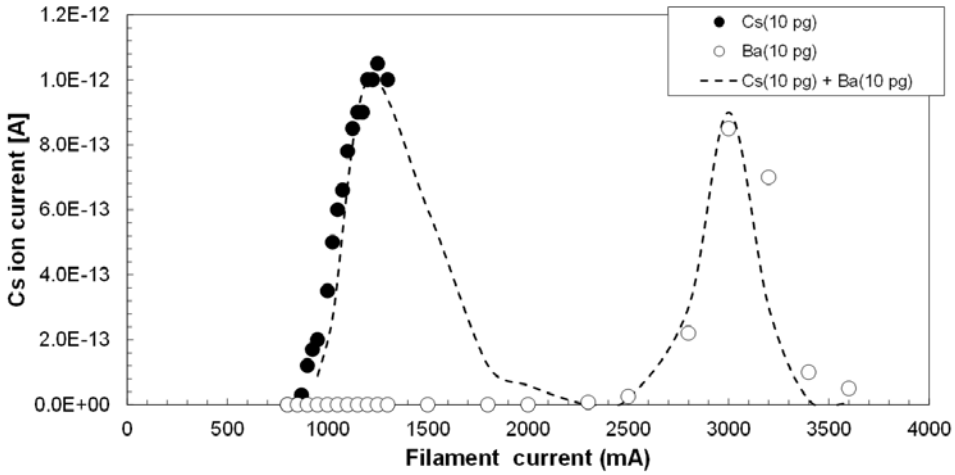

Fig. 4 Intensities of Cs and Ba ion beam as a function of filament current.
Dotted line shows result of mix sample of Cs and Ba.

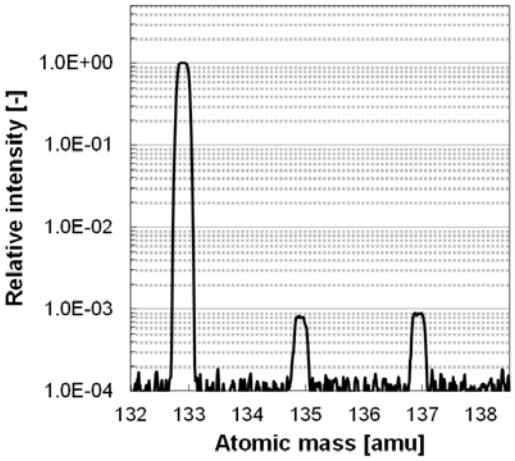

Fig. 5 Mass spectrum of ^{137}Cs standard solution sample-1.

isotopic ratio data was set to be 0.5% in ±2 r.s.d. Figure 2 shows that the ion beam current of *ca*. 2.8×10^{-14} A would show the analytical precision of 0.5% in 2 r.s.d.

Figure 3 shows the loading amount dependency on the ion beam current of Cs. The ion beam current of Cs showed the correlation with the loading amount of Cs (R^2 = 0.992). Figure 3 suggests that *ca*. 1.2×10^{-12} g of Cs would show the Cs ion beam current of *ca*. 2.8×10^{-14} A and also the analytical precision of the ^{135}Cs/^{137}Cs isotopic ratio of 0.5% in ±2 r.s.d.

For the isotopic composition analysis, it is important to evaluate isobaric interference. For the analysis of the isotopic composition of Cs by TIMS, Ba is the most important (other method such as ICP-MS, Mo and Sn would also influence to the isotopic composition data of Cs). The ion beam current profiles of ^{133}Cs and ^{138}Ba in both of the individual solutions of Cs and Ba and the Cs/Ba mixture solution are shown in Fig. 4. Figure 4 shows that the effect of isobaric interference of Ba on the isotopic composition analysis of Cs would be negligible in this study.

3.3 Analysis of isotopic composition of Cs

Figure 5 shows the mass spectrum of ^{137}Cs standard solution sample obtained from JRIA without further purification. Based on the study on the loading amount of Cs as above mentioned, *ca*. 3×10^{-12} g of ^{137}Cs (*ca*. 10 Bq) was loaded onto a rhenium filament. The ion beams of ^{135}Cs, ^{137}Cs and ^{133}Cs were observed. By the analysis of the isotopic composition of Cs, the isotopic ratio of ^{135}Cs/^{137}Cs was obtained as 0.868±0.004 (number of repetitions = 3). This analytical precision of 0.46% in ±2 r.s.d. including the reproducibility was better than the target level of 0.5% in ±2 r.s.d. However, the very small shoulder peaks were observed at the high mass side of atomic mass as shown in Fig. 6 (a).

Since these shoulder peaks would be originated by the polyatomic molecules, the chemical purification with the cation-exchange chromatography (a part

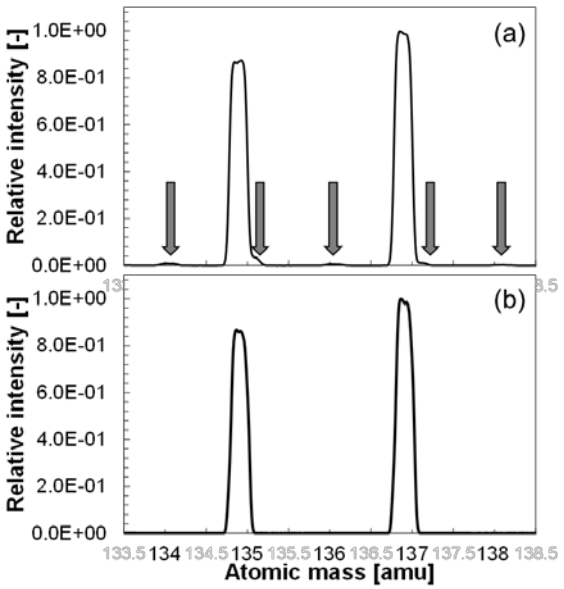

Fig. 6 Mass spectrum of ^{137}Cs standard solution sample-2.

of the chemical purification procedure of the environmental sample) was conducted. The mass spectrum of Cs after the cation-exchange chromatography was illustrated in Fig. 6 (b). There are no shoulder peaks in Fig. 6 (b), suggesting the very small amount of impurities in stock solution might be reason of them. The improved isotopic ratio of $^{135}Cs/^{137}Cs$ was obtained as 0.865±0.003, showing the agreement with the without chemical purification case and the achievement of the target level of the analytical precision of 0.5% in ±2r.s.d.

In this project, preparing the other Cs samples is ongoing. We are planning to further study for the improvement of the method of the analysis of the Cs isotopic composition by TIMS and analysis of the upcoming Cs sample.

4. Conclusions

The isotopic compositions of Cs samples used for nuclear cross-section measurement in ImPACT program were analyzed by TIMS. For the analysis of the isotopic composition of Cs, the analytical condition was discussed. It was found that *ca*. 1×10^{-12} g of ^{137}Cs was achievable lower limit for this target level. The ^{137}Cs standard solution sample purchased from JRIA was analyzed. Although the very small shoulder peaks were observed in the case of without further chemical purification, the analytical precision of $^{135}Cs/^{137}Cs$ ratio measurement met quality requirements of 0.5% in 2 r.s.d, and $^{135}Cs/^{137}Cs$ ratio was measured as 0.868±0.004. The chemical purification with the cation-exchange chromatography brought the elimination of shoulder peaks, and the $^{135}Cs/^{137}Cs$ ratio was observed as 0.865±0.003 showing agreement with the without chemical purification case.

Acknowledgements

This work was funded by ImPACT Program of Council for Science, Technology and Innovation (Cabinet Office, Government of Japan).

References

[1] http://www.jst.go.jp/impact/index.html.
[2] S. Nakamura et al. JAEA-Conf 2017-001. JAEA. 2017. 15-22.
[3] S. Nakamura et al. *Submitted to JAEA-Conf*.
[4] J. Magill et al. Karlsruhe Chart of the Nuclides 8th Edition. 2012.
[5] Y. Shibahara et al. J. Nucl. Sci. Technol. 2014, 51, 575-579.
[6] Y. Shibahara et al. Radiological issues for Fukushima's revitalized future. Springer. 2016. 33-46.
[7] Y. Shibahara et al. J. Nucl Sci. Technol. 2017, 54, 158-166.
[8] M. S. Snow et al. J. Environ. Radioact. 2016, 151, 258-263.
[9] M. S. Snow et al. Rapid Commun. Mass Spectrom. 2016, 30, 523-532.
[10] J. A. Dunne et al. Talanta. 2017, 174, 347-356.
[11] J. Zheng et al. Anal. Chem. 2016, 88, 8772-8779.
[12] S. Richter et al. Int. J. Mass Spectrom. 2003, 229, 181-197.
[13] Y. Shibahara et al. J. Radioanal. Nucl. Chem. 2016, 307, 2281-2287.
[14] S. B. Ludwig et al. ORNL/TM-11018. ORNL. 1989.

36 Measurement of interaction cross-section for ^{90}Sr, ^{88}Kr, ^{89}Rb, and ^{91}Y

K. Chikaato[A], M. Takechi[A], T. Otsubo[A], H. Wang[B], H. Otsu[B], H. Sakurai[B], D.S. Ahn[B], M. Aikawa[C], P. Doornenbal[B], N. Fukuda[B], T. Isobe[B], S. Kawakami[D], S. Koyama[E], T. Kubo[B], S. Kubono[B], G. Lorusso[B], Y. Maeda[D], A. Makinaga[C], S. Momiyama[E], K. Nakano[F], M. Niikura[E], Y. Shiga[G], P.-A. Söderström[B], H. Suzuki[B], H. Takeda[B], S. Takeuchi[B], R. Taniuchi[B,E], Ya. Watanabe[B], Yu. Watanabe[F], H. Yamasaki[E], K. Yoshida[B]

[A] *Department of Physics, Niigata University, Niigata 950-2102, Japan*
[B] *RIKEN., Nishina Center, Wako, Saitama 338-8570, Japan*
[C] *Department of Physics, Hokkaido University, Hokkaido 060-0809, Japan*
[D] *Department of Technology, Miyazaki University, Miyazaki 889−2192, Japan*
[E] *Department of Physics, the University of Tokyo, Tokyo 113-0033, Japan*
[F] *Interdisciplinary Graduate School of Engineering Sciences, Kyusyu University, Fukuoka 816-0811, Japan*
[G] *Department of Physics, Rikkyo University, Tokyo 171-8501, Japan*

email : chikaato@np.gs.niigata-u.ac.jp

Interaction cross sections (σ_I) for the fission products (FP) ^{90}Sr on C and CH_2 targets have been measured for the purpose of nuclear waste transmutation. The σ_I data for ^{90}Sr and neighboring nuclides have been obtained in inverse kinematics using fast radioactive beams at RIBF, RIKEN. Secondary beams of ~185 MeV/nucleon were produced from in-flight fission of a ^{238}U primary beam of 345 MeV/nucleon using the superconducting RI beam separator, BigRIPS. Measured σ_I for ^{90}Sr, ^{88}Kr, ^{89}Rb, and ^{91}Y on carbon targets have been compared with the Glauber model, the optical-limit approximation of the Glauber theory, a model which can uniquely calculate cross sections from the nuclear matter radii. The Glauber model reproduces the data when values larger by 1-4% than known root-mean-square radii of proton distributions for ^{90}Sr, ^{88}Kr, ^{89}Rb, and ^{91}Y are assumed as matter radii of those nuclei.

1. Introduction

One of the most important issues in the current society is to establish a safer method for the disposal of high-level radioactive wastes, produced after spent fuel from nuclear power plants is reprocessed. The transmutation is the technology which has a possibility to drastically shorten this period by converting fission products (FP) in wastes to shorter-lived particles through nuclear reactions [1]. In order to develop the transmutation technology, reliable reaction data are necessary. Especially, the utilization of proton induced reactions could be efficient for the transmutation of medium-life fission products such as ^{90}Sr and ^{137}Cs, of which thermal neutron capture cross sections are rather small. However, there is lack of data for proton induced spallation reactions on FP.

The interaction cross sections (σ_I : the sum of all reaction channels excluding the inelastic scattering channel) for ^{90}Sr and neighboring nuclei on carbon and CH_2 targets have been measured to fill the lack of data for proton induced reactions. The inverse reaction technique was adopted to obtain the data, using the fast radioactive beam of ^{90}Sr produced at the in-flight separator BigRIPS of the RIKEN Radioactive Isotope Beam Factory (RIBF) [2, 3]. In this paper, we report the preliminary results of σ_I for ^{90}Sr, ^{88}Kr, ^{89}Rb, and ^{91}Y on carbon targets. The comparison of the present data with the Glauber model (the optical-limit approximation of the Glauber theory) will be also shown, which allows us also to discuss sizes of nuclear matter radii of those nuclei.

2. Experiment

The experiment was performed at RIBF, operated by RIKEN Nishina Center and the Center for Nuclear Study, University of Tokyo. The transmission method [4, 5] was employed to measure σ_I data. The secondary beams of ^{90}Sr and other neighboring nuclides were produced by in-flight fission of a ^{238}U primary beam of 345 MeV/nucleon on a 1-mm-thick Be target located at the object point of the BigRIPS fragment separator. The average primary beam intensity was about 12 particle nA. The beam energies were ~185 MeV/nucleon in front of the secondary targets. The schematic view of the experimental setup is shown in Fig.1. The secondary reaction target (180.6-mg/cm^2 CH_2 or 224.1-mg/cm^2 C) was located at the F8 focal plane. Particles in the secondary beams were identified event-by-event via the *Bρ* - *TOF* - *ΔE* method using BigRIPS separator. The time of flight (*TOF*) of the particles were determined by the timing information from plastic scintillation counters (PL) at F3 and F7. The magnetic rigidity (*Bρ*) is reconstructed from the position information obtained by Parallel Plate Avalanche Counters (PPACs) installed at F3, F5 and F7 focal planes. For the measurements of the energy loss (ΔE) of particles, an ion chamber (IC) located at F7 was used. The identification of the beam and reaction products after the secondary reaction target is also based on *Bρ* - *TOF* - *ΔE* method, using ZeroDegree spectrometer (ZDS). *TOF* of each particles was measured using F8PL and F11PL, *Bρ* was determined from the F9 and F11 PPACs, and ΔE was measured by F11IC.

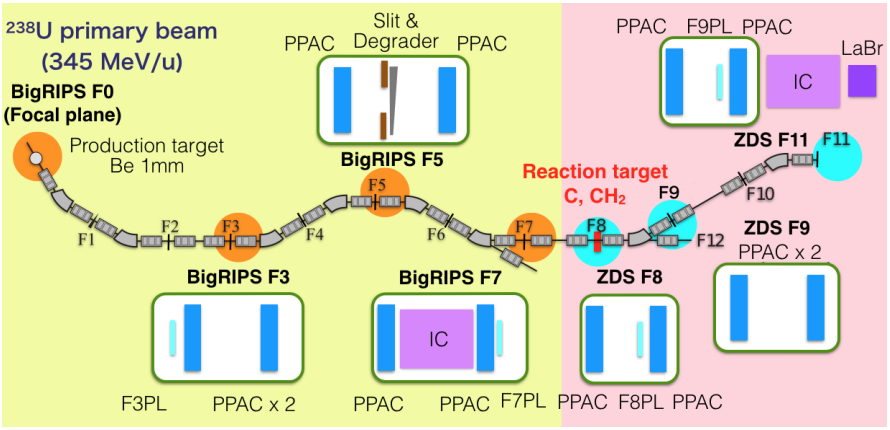

Fig. 1. The schematic view of the experimental setup based on the BigRIPS fragment separator and ZDS.

3. Result

In Fig. 2, preliminary results of σ_I for ^{90}Sr, ^{88}Kr, ^{89}Rb, and ^{91}Y on carbon targets are plotted as a function of the beam energy. Results are compared with Glauber-model calculations. The Glauber model is the optical limit approximation of the multiple scattering theory of Glauber [6], with which one can uniquely calculate cross sections using experimental nucleon-nucleon total scattering cross sections and by assuming certain sizes of nuclear matter radii (R_m) for projectile and target nuclei. In order to calculate the cross sections for ^{90}Sr, ^{88}Kr, ^{89}Rb, and ^{91}Y on carbon target, we used matter radius of carbon target which can be determined from experimental data [3]. As matter radii of projectiles, we used the known root-mean-square radii of proton distributions (R_p) of ^{90}Sr, ^{88}Kr, and ^{89}Rb obtained by isotope-shift measurements [7]. As there is no experimental data available for ^{91}Y, we used the average of R_p for ^{90}Y and ^{92}Y measured by isotope-shift measurements. In Fig. 2, the results of Glauber calculation for ^{90}Sr, ^{88}Kr, ^{89}Rb and ^{91}Y are shown with dot-dashed curves. Those curves were obtained by assuming that R_m are equal to R_p for those nuclei (with this assumption, we consequently assumed that the root-mean-square radii of neutron distributions (R_n) should be also equal to R_p). The dot-dashed curves underestimate cross sections by 3-8% for all nuclei. Instead of the assumption that R_m are equal to R_p, we tried another assumption in which R_m is larger than R_p by 1-4%. The result is shown with solid curves. It seems that present experimental data support the assumption that R_m is larger than R_p by 1-4%. This assumption consequently means that those nuclei have neutron skin structures. The further analysis is undergoing, including the deduction of proton induced σ_I for ^{90}Sr, ^{88}Kr, ^{89}Rb, and ^{91}Y.

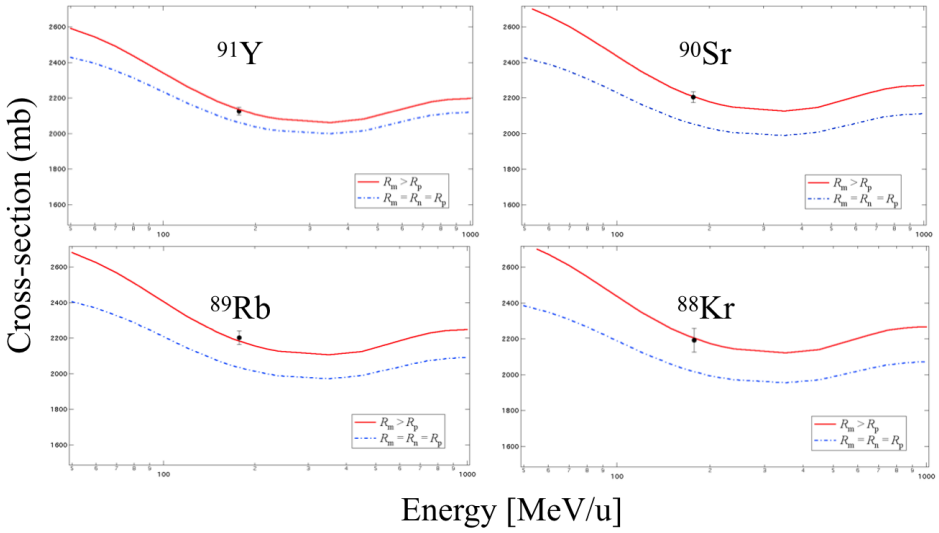

Fig. 2. Measured σ_I for ^{90}Sr, ^{88}Kr, ^{89}Rb, and ^{91}Y on carbon target are shown with solid symbols as a function of the beam energy. Glauber model calculations are also shown for the comparison with dot-dashed curves and solid curves (See text for the detailed explanation of Glauber model calculations shown in this figure.).

Acknowledgements

We thank the accelerator staff of the RIKEN Nishina center for providing high-quality ^{238}U primary beam. This work was supported by ImPACT Program of Council for Science, Technology and Innovation (Cabinet Office, Government of Japan).

References

[1] H. Wang et al., Phys. Lett. B 754, 104 (2016).
[2] T. Kubo, Nucl. Instrum. Methods B 204, 97 (2003).
[3] T. Kubo, *et al*., Prog. Theor. Exp. Phys. 2012, 03C003 (2012).
[4] M. Takechi *et al*., Phys. Rev. C 79, 061601(R) (2009).
[5] M. Takechi *et al*., Phys. Rev. C 91, 014614(R) (2014).
[6] R. Glauber, in Lectures in Theoretical Physics, edited by W. Brittin and L. Dunham (Inter science, New York, 1959).
[7] I. Angeli et al., Atomic Data and Nucl. Data tables 99, 69-95 (2013).

This is a blank page.

37 Microscopic effective reaction theory for deuteron-nucleus reactions and its applications

Kosho Minomo[1], Kouhei Washiyama[2], and Kazuyuki Ogata[1]

[1]*Research Center for Nuclear Physics, Osaka University, Ibaraki 567-0047, Japan*

[2]*Center for Computational Sciences, University of Tsukuba, Tsukuba 305-8577, Japan*

e-mail: minomo@rcnp.osaka-u.ac.jp

Total reaction cross sections of deuteron-nucleus reactions are calculated by a microscopic reaction theory. The framework has no free adjustable parameter and is applicable to deuteron-induced reactions for both stable and unstable spherical nuclei in a wide range of the deuteron incident energies E_d. The calculated cross sections are consistent with those evaluated by a phenomenological optical potential for $E_d < 200$ MeV in which the potential has been parametrized. We propose a simple formula of the total reaction cross sections for spherical nuclei up to 1 GeV, as a function of E_d, the target mass number A and its atomic number Z.

1. Introduction

The total reaction cross section is one of the most important reaction observables for nuclear data studies. For proton-nucleus reactions, $\sigma^{\rm R}$ has been investigated in many experiments, and a simple formula of practical use for the proton-nucleus total reaction cross sections was proposed on the basis of the rich data [1]. On the other hand, for deuteron-nucleus reactions, such systematic studies on total reaction cross sections have not been performed. This is mainly because of the lack of experimental data in comparison with those for the proton-nucleus reactions. Some global parametrizations of the deuteron-nucleus optical potential were highly successful but limited up to around 200 MeV of the deuteron incident energy E_d. [2, 3, 4] Furthermore, it should be kept in mind that, in general, deuteron optical potentials are more ambiguous than those for nucleon scattering, since deuteron is a weakly-bound system and the coupling

to its breakup channels can affect the elastic scattering. It is not trivial whether one can describe the dynamical polarization potential corresponding to the breakup channels by a standard parametrization of the optical potential, e.g., the Woods-Saxon form and its derivative, or not.

In this study [5], we describe deuteron-nucleus reactions within a microscopic framework. According to a $p + n + \mathrm{A}$ three-body model, where A stands for the target nucleus, we adopt the continuum-discretized coupled-channels method (CDCC) [6, 7, 8] that has successfully been applied to deuteron-nucleus reactions in a wide range of energies. As for $p(n)$-A optical potential, which is an input for CDCC calculations, we adopt a microscopic optical potential so as to calculate potentials for not only stable but also unstable nuclei. This framework is based on the nucleus-nucleus multiple scattering theory [9] and referred to the microscopic effective reaction theory for deuteron-induced reactions. Thus, we calculate the deuteron-nucleus total reaction cross sections for various target nuclei up to 1 GeV. Finally, a simple formula of the total reaction cross sections, as a function of E_d, the target mass number A and its atomic number Z, is proposed.

2. Theoretical Framework

CDCC is a non-perturbative reaction model that treats the couplings to projectile breakup channels explicitly. In CDCC the total wave function Ψ of the $p + n + \mathrm{A}$ three-body system is expanded in terms of the set $\{\phi_i\}$ of the eigenstates of the internal Hamiltonian h_d of the deuteron (p-n system):

$$\Psi(\boldsymbol{r}, \boldsymbol{R}) = \sum_{i=0}^{i_{\max}} \phi_i(\boldsymbol{r}) \chi_i(\boldsymbol{R}), \tag{1}$$

where R is the coordinate of the center-of-mass of the p-n system relative to the target nucleus A and r is that of p to n. The index i specifies the p-n eigenstate; $i = 0$ corresponds to the deuteron ground state and $i > 0$ to the discretized-continuum states of the p-n system. The expansion coefficient denoted by χ_i describes the scattering wave function between the p-n system in the i-th state and A. The three-body Schrödinger equation to be solved is given by

$$\left[K_{\boldsymbol{R}} + U_{p\mathrm{A}} + U_{n\mathrm{A}} + h_d - E\right] \Psi(\boldsymbol{r}, \boldsymbol{R}) = 0, \tag{2}$$

where $K_{\boldsymbol{R}}$ is the kinetic energy operator regarding R and E is the total energy of the three-body system.

In Equation (2), $U_{p(n)\mathrm{A}}$ is the $p(n)$-A scattering potential consisting of nuclear and Coulomb parts. In calculation of the nuclear part, we adopt the single folding model with the Melbourne nucleon-nucleon g-matrix interaction [10] and the proton and neutron densities of the nucleus A. The densities are obtained by solving Hartree-Fock-Bogoliubov (HFB) equations in coordinate space with SLy4 Skyrme energy density functionals [12]. We use the computer code LENTEUR [13], which enforces time-reversal and spherical symmetries. For odd nuclei, the so-called filling approximation is adopted.

In general, the present framework would be much reliable for heavier targets, where the g-matrix interaction and the HFB method work well, but becomes less reliable for light targets. In addition, the coupling effects due to collective excitations of the target, which may significant at low energy, are not included although single-particle excitation effects are approximately included by means of the g-matrix. We should be careful of the validity of the framework by comparing the calculated results with the measured data. Fortunately, as for the nucleon-nucleus total reaction cross sections for stable nuclei, the agreement between the theoretical results and the data is fairly well for both light and heavy targets in a wide incident-energy range, including no free adjustable parameters [11].

We have predicted $\sigma_d^{\rm R}$ for ^{9}Be, ^{12}C, ^{16}O, ^{28}Si, ^{40}Ca, ^{56}Fe, ^{58}Ni, ^{79}Se, ^{90}Zr, ^{93}Zr, ^{107}Pd, ^{116}Sn, ^{120}Sn, ^{135}Cs and ^{208}Pb targets at incident energies E_d from 10 MeV to 1000 MeV.

3. Results

In Figure 1, we show the calculated $\sigma_d^{\rm R}$ for ^{12}C, ^{58}Ni, ^{120}Sn, and ^{208}Pb by the thick solid, dashed, dotted and dash-dotted lines, respectively, as a function of E_d. The experimental data taken from Auce *et al.* [14] (squares), Matsuoka *et al.* [15] (triangles) and Millburn *et al.* [16] (inverted triangles) are shown by closed symbols. The open circles represent the results calculated with the An-Cai global potential [4]. The result of the microscopic CDCC calculation agrees well with the experimental data except for the data measured at 160 MeV [16], at almost the same level as that of the global optical potential [4]. One sees from Fig. 1 that the $\sigma_d^{\rm R}$ for ^{12}C measured at 160 MeV seems to deviate from the energy dependence of the data at lower energies, and that of the result of the An-Cai potential. Systematic measurement of $\sigma_d^{\rm R}$ at around 200 MeV with high precision will be of great importance. The four thin lines shown in Fig. 1 correspond to the results of NASA's formula [17, 18, 19] implemented in the particle and heavy ion transport code system (PHITS) [20]. They seriously undershoot the experimental data as well as the prediction of the CDCC calculation.

We parametrized the $\sigma_d^{\rm R}$ calculated for the 15 nuclei mentioned above at $10 \leq E_d \leq 1000$ MeV by using a simple functional form. The simple formula, which well reproduce the results of CDCC, is shown in Ref. [5].

4. Summary

We have calculated the deuteron-nucleus total reaction cross sections for various target nuclei at deuteron incident energies up to 1 GeV, by means of the three-body reaction model, i.e., CDCC. The nucleon-nucleus optical potential, which is the input of CDCC, was evaluated by the single-folding model with the Melbourne g-matrix interaction and the nuclear one-body density obtained by the Hartree-Fock-

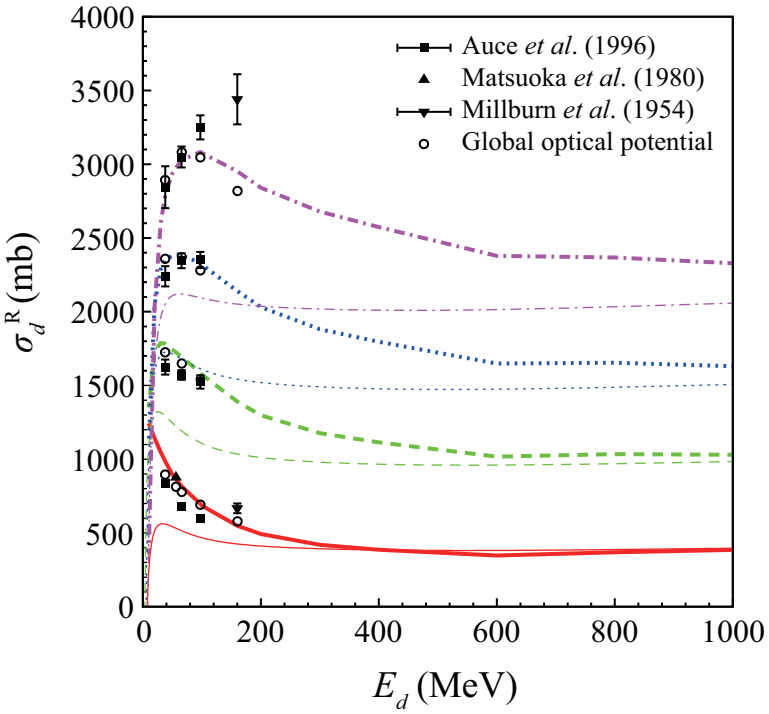

Figure 1: The calculated σ_d^{R} for ^{12}C (thick solid line), ^{58}Ni (thick dashed line), ^{120}Sn (thick dotted line) and ^{208}Pb (thick dash-dotted line) as a function of E_d. The closed squares, triangles and inverted triangles are the experimental data taken from Refs. [14], [15] and [16], respectively. The open circles represent the results calculated with the An-Cai global potential [4]. The four thin lines represent the results of NASA's formula [17, 18, 19] implemented in PHITS [20].

Bogoliubov method. The results of microscopic framework agree well with the experimental data and the results of the An-Cai global optical potential. NASA's formula for the total reaction cross sections implemented in PHITS was found to severely undershoot the results of CDCC, at low energies in particular. We have parametrized our results of σ_d^{R} by a simple functional form.

Acknowledgements

This work is supported in part by Grant-in-Aid for Scientific Research (Nos. 16K05352 and 16K17698) from the Japan Society for the Promotion of Science (JSPS) and by the ImPACT Program of Council for Science, Technology and Innovation (Cabinet Office, Government of Japan).

References

[1] R. F. Carlson: "PROTON-NUCLEUS TOTAL REACTION CROSS SECTIONS AND TOTAL CROSS SECTIONS UP TO 1 GeV", At. Data Nucl. Data Tables 1996 May; 63: 93-116.

[2] W. W. Daehnick, J. D. Childs and Z. Vrcelj: "Global optical model potential for elastic deuteron scattering from 12 to 90 Mev", Phys. Rev. C 1980 June; 21: 2253-2274.

[3] J. Bojowald, H. Machner, H. Nann, W. Oelert, M. Rogge and P. Turek: "Elastic deuteron scattering and optical model parameters at energies up to 100 MeV", Phys. Rev. C 1988 Sep; 38: 1153-1163.

[4] H. An and C. Cai: "Global deuteron optical model potential for the energy range up to 183 MeV", Phys. Rev. C 2006 May; 73: 054605.

[5] K. Minomo, K. Washiyama and K. Ogata: "Deuteronnucleus total reaction cross sections up to 1 GeV", J. Nucl. Sci. Technol. 2017 Jan; 54: 127-130.

[6] M. Kamimura, M. Yahiro, Y. Iseri, Y. Sakuragi, H. Kameyama and M. Kawai: "Chapter I Projectile Breakup Processes in Nuclear Reactions", Prog. Theor. Phys. Suppl. 1986 Jan; 89: 1-10.

[7] N. Austern, Y. Iseri, M. Kamimura, M. Kawai, G. Rawitcher and M. Yahiro: "Continuum-Discretized Coupled-Channels Calculations For Three-Body Models Of Deuteron-Nucleus Reactions", Phys. Rep. 1987 Oct; 154: 125-204.

[8] M. Yahiro, K. Ogata, T. Matsumoto and K. Minomo: "The continuum discretized coupled-channels method and its applications", Prog. Theor. Exp. Phys. 2012 Sep; 2012: 01A206.

[9] M. Yahiro, K. Minomo, K. Ogata and M. Kawai: "A New Glauber Theory Based on Multiple Scattering Theory", Prog. Theor. Phys. 2008 Oct; 120: 767-783.

[10] K. Amos, P. J. Dortmans, H. V. Von Geramb, S. Karataglidis and J. Raynal: Advances in Nuclear Physics, Vol. 25. Plenum, New York: J. W. Negele and E. Vogt; 2000. p.275-536.

[11] K. Minomo, K. Washiyama and K. Ogata: "Reexamination of microscopic optical potentials based on multiple scattering theory", arXiv[nucl-th] 2017 Dec; 1712.10121.

[12] M. Bender, P. H. Heenen and P. G. Reinhard: "Self-consistent mean-field models for nuclear structure", Rev. Mod. Phys. 2003 Jan; 75: 121-180.

[13] K. Bennaceur (unpublished).

[14] A. Auce, R. F. Carlson, A. J. Cox, A. Ingemarsson, R. Johansson, P. U. Renberg, O. Sundberg and G. Tibell: "Reaction cross sections for 38, 65, and 97 MeV deuterons on targets from ^{9}Be to ^{208}Pb", Phys. Rev. C 1996 June; 53: 2919-2925.

[15] N. Matsuoka, M. Kondo, A. Shimizu, T. Saito, S. Nagamachi, H. Sakaguchi, A. Goto and F. Ohtani: "DEUTERON BREAK-UP IN THE FIELDS OF NUCLEI AT 56 MeV", Nucl. Phys. A 1980 Aug; 345: 1-12.

[16] G. P. Millburn, W. Birnbaum, W. E. Crandall and L. Schecter: "Nuclear Radii from Inelastic Cross-Section Measurements", Phys. Rev. 1954 Sep; 95: 1268-1278.

[17] R. K. Tripathi, F. A. Cucinotta and J. W. Wilson: "Accurate universal parameterization of absorption cross sections", Nucl. Instru. Meth. B 1996 Oct; 117: 347-349.

[18] R. K. Tripathi, J. W. Wilson and F. A. Cucinotta: "Accurate universal parameterization of absorption cross sections II - neutron absorption cross sections", Nucl. Instru. Meth. B 1997 June; 129: 11-15.

[19] R. K. Tripathi, F. A. Cucinotta and J. W. Wilson: "Accurate universal parameterization of absorption cross sections III - light systems", Nucl. Instru. Meth. B 1999 Sep; 155: 349-356.

[20] T. Sato, K. Niita, N. Matsuda, S. Hashimoto, Y. Iwamoto, S. Noda, T. Ogawa, H. Iwase, H. Nakashima, T. Fukahori, K. Okumura, T. Kai, S. Chiba, T. Furuta, L. Sihver: "Particle and Heavy Ion Transport Code System PHITS, version 2.52", J. Nucl. Sci. Technol. 2013 Sep; 50: 913-923.

38 Studies on Calculations of Prompt Neutron Multiplicities, Fission Product Yields and Isomeric Yields by Hauser-Feshbach Statistical Decay Theory

Shin Okumura[1], Toshihiko Kawano[2], and Satoshi Chiba[1]

[1]Laboratory for Advanced Nuclear Energy, Tokyo Institute of Technology, 2-12-1 Ookayama, Meguro-ku, Tokyo 152-8550, Japan
[2]Theoretical Division, Los Alamos National Laboratory, Los Alamos, NM 87545, USA
e-mail: *okumura.s.aa@m.titech.ac.jp*

Abstract

We applied Hauser-Feshbach statistical decay calculations to the primary fission fragment distributions $Y(A, Z, TKE)$ produced by two theoretical model calculations, namely the Langevin 4D and Monte Calro CGMF codes. The fission observables such as post-neutron fission product yields (i.e. independent yield $Y_{ind}(Z, A)$), mass-dependent neutron multiplicities $\overline{\nu}(A)$ and isomeric ratios for neutron-induced fission of ^{235}U(n_{th},f) were calculated simultaneously for each fission fragments and the results were compared with experimental data. We found that a realistic distribution of $Y(A, Z, TKE)$ is important to reproduce the experimental fission observables reasonably and our model has a greater potential for predicting more reliable fission observables based on the theoretical fission theory and statistical decay theory.

1. Introduction

The nature of the primary fission fragments that are formed just after scission plays an important role to understand the nuclear fission process. These fragments are characterized by mass (A), charge (Z), total kinetic energy (TKE), total excitation energy (TXE) and spin/parity (J^{π}) as well as their production probabilities (yields) $Y(Z, A, TKE, TXE)$. These fragments de-excite from the excited states to its ground state by emitting prompt particles, mostly neutrons and/or gamma-rays. The prompt neutron multiplicity ν_P and its mass dependency $\overline{\nu}(A)$ therefore depend on their TKE and TXE.

The thermal neutron induced fission produces roughly 1,000 primary fission fragments (500 primary fission fragment pairs). In order to predict the accurate independent fission product yields ($Y_I(Z, A)$, post-neutron distributions), one must consider the decay process for all the 1,000 primary fission fragments individually. The precise prediction of the fission observables by means of theoretical simulation is desired, because fission fragments with an extremely small yield are very difficult to measure experimentally.

At present, nuclear data libraries such as ENDF/B-VIII and JENDL 4.0/FPY-2011 that contain the fission product yield data are compiled based mainly on experimental data. However the experimental basis is not enough for the system other than thermal neutron induced fission of ^{235}U. Therefore, it is necessary to rely on some model estimations such as Wahl's systematics [1]. Especially for the isomeric ratio, because most of the short-lived neutron rich nuclei are formed in fission, the isomeric ratios of these nuclei are difficult to measure and thus the experimental data are scarce. For this purpose, a model proposed by Madland and England [2] is widely used.

Recently, a 4D Langevin model that treats the deformation of each fragment independently has been developed[3]. Such theoretical simulation provides information on the primary fission fragment such as the mass A, charge Z, and total kinetic energy (TKE) distributions $Y(Z, A, TKE)$. However, this fragment yield cannot be compared directly with

experimental data. The Hauser-Feshbach theory has been utilized for describing the nuclear reaction and compiling the nuclear data. The CoH_3 Hauser-Feshbach code has been upgraded recently [4] and applied to calculate fission observables [5] by paying attention to the neutron and γ ray emissions in fission.

In this study, we combined the primary fission fragment distributions determined by the Langevin approach [6, 7] and the Monte Carlo CGMF code [8] with the de-excitation of fragments based on the Hauser-Feshbach statistical decay theory. Use of theoretical models to calculate the primary fission fragment distributions $Y(Z, A, TKE, TXE)$ is attractive because of difficulty in an experimental setup for such measurements, limitation on the actinide target preparation, and the incident neutron energy range. By connecting theoretical calculations of the primary fission fragment with the statistical decay model, an accuracy of each primary fission fragment $\underline{Y}(Z, A, TKE)$ generated by the theoretical model can be verified by comparing with the experimental $Y_I(Z, A)$, ν_P, and $\nu(A)$.

The present work shows an attempt to develop a connection between the model-calculated primary fission fragments and the Hauser-Feshbach statistical decay theory, which reproduces $Y_I(Z, A)$ and isomeric ratios together with ν_p and $\overline{\nu}(A)$ for ^{235}U(n_{th}, f). We employ two sets of models, namely the Langevin model [7] and the Monte Calro CGMF code [8].

2. Calculation Method

2.1 Primary Fission Fragment Calculation

The specifications of the primary fission fragment calculation used in this study are the Langevin 4D with microscopic transport coefficients [7] and Monte Carlo CGMF code [8]. The Langevin model produced 85,000 fission events including 150 fission fragments (i.e. 150 nuclides) and the CGMS code produced 200,000 fission events including 400 fission fragments (i.e. 400 nuclides). The 4D Langevin model can treat the deformation of each fragment independently. The Langevin trajectories start from inside of the saddle point along with the potential energy surface. The fission events occur when the nucleus elongates enough and the neck size is close to 0. The mass asymmetry parameter α obtained at each fission simulation allows us to determine the mass of the primary fission fragment pair by the simple assumption of (A_C/2.0 × (1+α)+0.5), where A_C is the mass of the compound nucleus. In this study, the charge distribution of the fission fragment pair was not taken into account, and the charge was assumed by just subtracting the mass number from the compound nucleus. The resulting input set for the Hauser-Feshbach calculation is $Y(Z, A, TKE)$. The CGMF method samples the primary fission fragment in several steps by the Monte Carlo technique. The calculated result of the set of primary fission fragment yield distribution $Y(Z, A, TKE)$ is used. In this set, the mass and TKE dependent fragment yield was introduced based on experimental data.

2.2 Statistical Decay Calculation

Recently updated CoH Hauser-Feshbach code version 3.0, CoH_3/BeoH [4], was used for the statistical decay calculations. The total excitation energy (TXE) are calculated from the energy balance of the reaction.

$$\begin{aligned} \mathrm{TXE}(Z_l, A_l, Z_h, A_h) &= Q - E_{inc} - \mathrm{TKE}(Z_l, A_l, Z_h, A_h) \\ &= E_{inc} + B_n(Z_c, A_c) \\ &+ [M_n(0,1) + M_n(Z_c, A_c) - M_n(Z_l, A_l) - M_n(Z_h, A_h)] - \mathrm{TKE}(Z_l, A_l, Z_h, A_h)\,, \end{aligned} \tag{1}$$

where l, h and c denote the light, heavy fragments and compound nucleus, respectively. Q is the Q-value of the fission reaction, and M_n represents the nuclear masses in the energy unit. The Q-value was calculated by using the values of mass excess in the updated mass table. E_{inc} is the incident neutron energy and B_n is the neutron binding energy. The TXE will be shared between the two fragments, light and heavy. We estimate the average excitation energy by using the anisothermal model parameter R_T which is defined as the ratio of effective temperatures of both fragments.

$$R_T = \frac{T_l}{T_h} = \sqrt{\frac{U_l}{U_h}\frac{a_h(U_h)}{a_l(U_l)}}\,, \tag{2}$$

where $a(U)$ is the level density parameter at excitation energy of U. The level density systematics based on KTUY05 mass model and the neutron optical potential by Koning and Delaroche were used for the parameters in the Hauser-Feshbach model.

2.3 Isomeric Ratio Calculation

The isomeric ratio is an important quantity for which no direct measurement is available. The isomeric state productions for some selected nuclides in the primary fission fragments were calculated by searching for metastable states from the discrete levels in Reference Input Parameter Library, RIPL-3 files [9]. The isomeric ratio is defined as

$$\mathrm{IR} = \frac{Y_m}{Y_m + Y_g}, \tag{3}$$

where Y_g and Y_m are the partial independent fission product yield of ground and isomeric states in a specific nuclide.

3. Results and Discussion

We conducted the Hauser-Feshbach statistical decay calculation using two different primary fission fragment $Y(Z, A, TKE)$ as inputs for ^{235}U(n$_{\mathrm{th}}$,f) system to reproduce the fission observables such as the probability of neutron

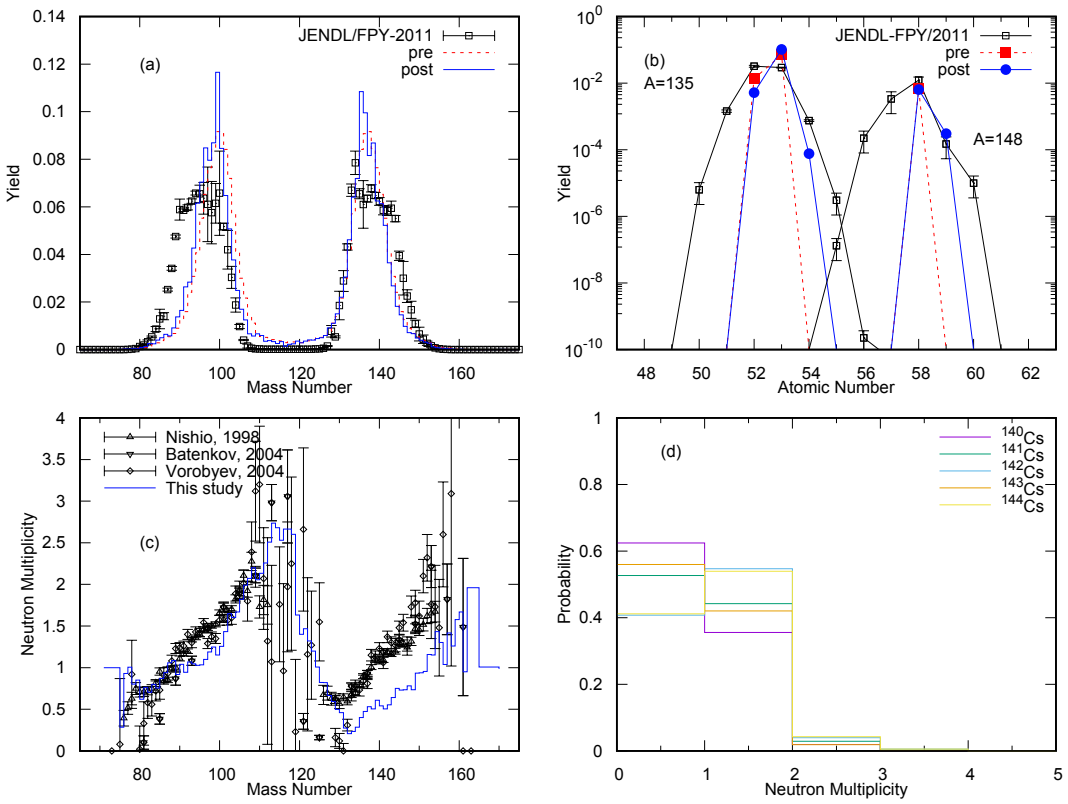

Figure 1: (a) Mass distribution of primary fission fragment yield generated by the Langevin model (pre-neutron emission in red dotted histogram) and that of the fission product yield (post-neutron emission in blue histogram). (b) Charge distributions at A = 135 and 148. (c) the mass dependence of neutron multiplicity $\overline{\nu}(A)$ (d) the probability of the neutron multiplicity of Cs isotopes.

multiplicity $P(\nu)$, the mass dependence of neutron multiplicity $\overline{\nu}(A)$, as well as the independent fission product yield $Y_I(Z, A)$.

Figure 1 (a) shows the calculated $Y_I(A)$ (post-neutron) together with the fission fragment (pre-neutron) yield generated by the Langevin model. We compare our calculated result with the JENDL/FPY-2011 data. This is simply because the large number of experimental data of $Y_I(A)$ for ^{235}U(n_{th},f) system are available and the evaluated nuclear data library represents them. The width of pre-neutron $Y(A)$ by the Langevin model used in this study was slightly thinner than $Y_I(A)$ in JENDL/FPY-2011. The peak position and the width of heavy fragments agree somewhat except for above the mass number 140. The mass distribution changes from the pre-neutron $Y(A)$ fragment to the post-neutron $Y_I(A)$ distributions, which are connected by the prompt neutron emission calculated with the Hauser-Feshbach theory. After neutron emission, post-neutron distribution does not shift pronouncedly. Compared to the heavy fragment distribution, the light one shifts larger toward the lower mass number, due to increase in the number of neutrons emitted from the pre-neutron fragments. The mass distribution of pre-neutron $Y(A)$ is no longer mirror symmetric after neutron emission, $Y_I(A)$.

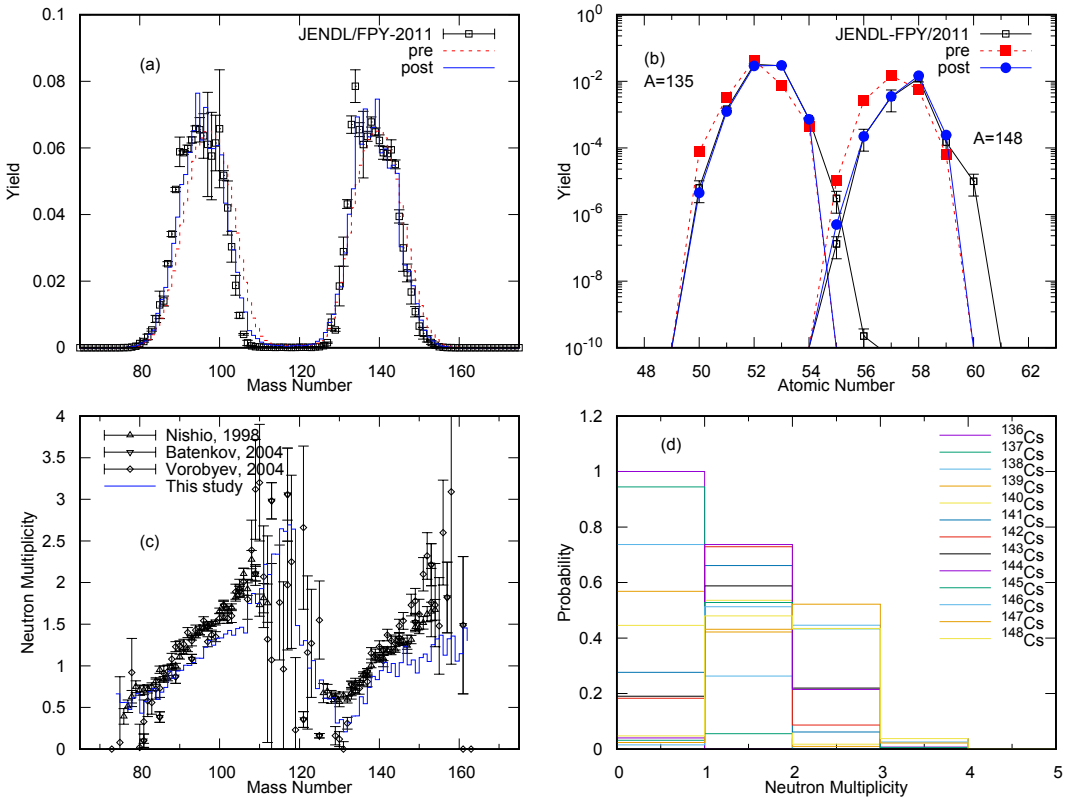

Figure 2: (a) Mass distribution of primary fission fragment yield generated by the Monte Carlo CGMF code (pre-neutron emission in red dotted histogram) and that of the fission product yield (post-neutron emission in blue histogram). (b) Charge distributions at $A = 135$ and 148. (c) the mass dependence of neutron multiplicity $\overline{\nu}(A)$ (d) the probability of the neutron multiplicity of Cs isotopes.

Figure 1 (c) shows the calculated $\overline{\nu}(A)$ plotted with some experimental data[10, 11, 12]. Obviously $\overline{\nu}(A)$ in the heavy fragment region is considerably lower compared with the experimental data, while that in the light fragment region well reproduces the experimental data. The reason for the low $\overline{\nu}(A)$ of heavy fragments was briefly confirmed by checking the probability of the neutron multiplicity and the charge distribution of fission fragment. Figure 1 (d) shows the probability of neutron multiplicity for the Cs isotopes. Probabilities of emitting more than two neutrons (i.e. $\nu \geq 2$) for $^{140-144}$Cs are low, although the experimental $\overline{\nu}(A)$ exhibits more than 1 in this mass region as shown in Fig. 1 (c).

The calculated $\overline{\nu}$ of 1.84 is significantly lower than the evaluated $\overline{\nu}$ in JENDL-4 of 2.42 at the thermal energy. In this study the charge distribution was not considered in the Langevin calculation. Therefore, the charge on a certain mass number is not distributed as shown in Fig. 1 (b), where the charge distributions for $A = 135$ and 148 are demonstrated. The isobars exist only around the most-probable position of charge. Due to this, nuclides which emit a large number of neutrons are not produced and the prediction of $\overline{\nu}(A)$ tends to be low.

The same calculation was performed for the primary fission fragment $Y(Z, A, TKE)$ generated by the Monte Carlo CGMF code [8]. The results are shown in Fig. 2 (a)-(d). As shown in Fig. 2 (a), the widths of the mass distribution of both the pre-neutron fission fragment yield $Y(A)$ and the post-neutron fission product yield $Y_I(A)$ well reproduce the JENDL/FPY-2011 data. The post-neutron distribution $Y_I(A)$ shifts toward the lower mass side in both the light and heavy fragments compared to the pre-neutron distribution $Y(A)$. The calculation also reproduces the small yield peaks at $A = 134$. The model produces wider ranges of charge for the same mass as shown in Fig. 2 (b). From Fig. 2 (c), the Hauser-Feshbach statistical decay calculation well reproduces the $\overline{\nu}(A)$ in the wide range of mass numbers. As evidently shown in Fig. 2 (d) as an example of the Cs isotopes, the number of isotopes is abundant compared to the case of using Langevin model. Owing to the contribution from the wider variation in $Y(Z, A, TKE)$, the calculated $\overline{\nu}$ of 2.35 is well reproduced that of 2.42 in JENDL-4.

Calculations of the isomeric ratio by using the primary fission fragment $Y(Z, A, TKE)$ by Monte Carlo CGMF were performed. Figure 3 shows the calculated isomeric ratios of some fission product nuclides together with JENDL and some experimental data[13] against Z^2/A. The isomeric ratio in JENDL/FPY-2011 is compiled by using the Madland and England (ME) model [2]. The ME model gives isomeric ratio by defining eight patterns whether the mass number of fission product is even or odd, whether the spin difference between metastable and ground state is even or odd, and whether the metastable state spin is greater or less than ground state one. Therefore, nuclides that have the same condition will have the same isomeric ratio in the ME model. We found that neither our calculation nor ME model perfectly reproduces the experimental data.

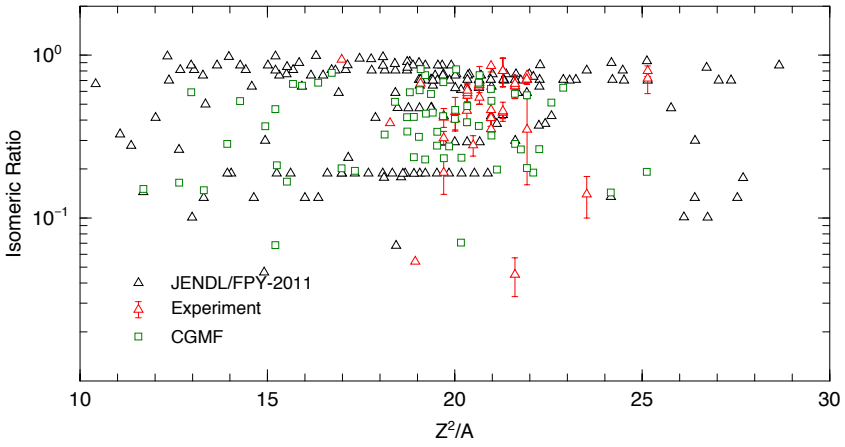

Figure 3: The calculated isomeric ratios of selected nuclides by comparison with the JENDL/FPY-2011 and some experimental data.

4. Conclusion

We successfully connected the fission theory and the Hauser-Feshbach statistical decay theory in order to calculate typical fission observables such as post-neutron fission products yield (independent fission product yield $Y_{ind}(Z, A)$, mass-dependent neutron multiplicities $\overline{\nu}(A)$ and isomeric ratios by starting with the primary fission fragment produced by the theoretical calculations. Our new method can demonstrate that the shift of pre-neutron yield mass distribution to the lower mass side and the break in the mirror symmetric with respect to the center of the mass distribution. The

calculated $\overline{\nu}(A)$ well reproduces the experimental data. We successfully calculated the isomeric ratio for many nuclides and compared with JENDL and experimental data. We found that $Y(A, Z, TKE)$ is the crucial parameter to obtain the reasonable reproduction of experimental fission observables. Development of our model has a greater potential for predicting more reliable fission observables based on the theoretical fission theory and statistical decay theory.

Acknowledgements

Present study includes the result of "Development of prompt-neutron measurement in fission by surrogate reaction method and evaluation of neutron-energy spectra" entrusted to Japan Atomic Energy Agency by Ministry of Education, Culture, Sports, Science and Technology.

References

[1] Wahl AC. Systematics of Fission-Product Yields. Los Alamos National Laboratory; 2002. LA-13928.

[2] Madland DG, England TR. The Influence of Isomeric States on Independent Fission Product Yields. Nuclear Science and Engineering. 1977;64(4):859–865.

[3] Ishizuka C, Usang MD, Ivanyuk FA, Maruhn JA, Nishio K, Chiba S. Four-dimensional Langevin approach to low-energy nuclear fission of ^{236}U. Phys Rev C. 2017;96:064616.

[4] Kawano T, Talou P, Chadwick MB, Watanabe T. Monte Carlo Simulation for Particle and γ-Ray Emissions in Statistical Hauser-Feshbach Model. Journal of Nuclear Science and Technology. 2010;47(5):462–469.

[5] Kawano T, Talou P, Stetcu I, Chadwick MB. Statistical and evaporation models for the neutron emission energy spectrum in the center-of-mass system from fission fragments. Nuclear Physics A. 2013;913(2):51 – 70.

[6] Usang MD, Ivanyuk FA, Ishizuka C, Chiba S. Effects of microscopic transport coefficients on fission observables calculated by the Langevin equation. Phys Rev C. 2016;94:044602.

[7] Usang MD, Ivanyuk FA, Ishizuka C, Chiba S. Analysis of the total kinetic energy of fission fragments with the Langevin equation. Phys Rev C. 2017;96:064617.

[8] Becker B, Talou P, Kawano T, Danon Y, Stetcu I. Monte Carlo Hauser-Feshbach predictions of prompt fission γ rays: Application to n_{th} + ^{235}U, n_{th} + ^{239}Pu, and ^{252}Cf (sf). Phys Rev C. 2013 Jan;87:014617.

[9] Capote R, Herman M, Obložinský P, Young PG, Goriely S, Belgya T, et al. RIPL - Reference Input Parameter Library for Calculation of Nuclear Reactions and Nuclear Data Evaluations. Nuclear Data Sheets. 2009;110(12):3107 – 3214. Special Issue on Nuclear Reaction Data.

[10] Nishio K, Nakagome Y, Yamamoto H, Kimura I. Multiplicity and energy of neutrons from ^{235}U(n_{th},f) fission fragments. Nuclear Physics A. 1998;632(4):540 – 558.

[11] Batenkov OA, Boykov GA, Hambsch FJ, Hamilton JH, Jakovlev VA, Kalinin VA, et al. Prompt Neutron Emission in the Neutron-Induced Fission of ^{239}Pu and ^{235}U. AIP Conference Proceedings. 2005;769(1):1003–1006.

[12] Vorobyev A, Shcherbakov O, Pleve YS, Gagarski A, Val'ski G, Petrov G, et al. Angular and energy distributions of prompt neutrons from thermal neutron-induced fission of U-233, U-235 (N, F). In: International Seminar on Interaction of Neutrons with Nuclei; 2009. p. 60.

[13] Naik H, Dange SP, Singh RJ, Datta T. Systematics of fragment angular momentum in low-energy fission of actinides. Nuclear Physics A. 1995;587(2):273 – 290.

国際単位系（SI）

表１．SI 基本単位

基本量	SI 基本単位	
	名称	記号
長さ	メートル	m
質量	キログラム	kg
時間	秒	s
電流	アンペア	A
熱力学温度	ケルビン	K
物質量	モル	mol
光度	カンデラ	cd

表２．基本単位を用いて表されるSI組立単位の例

組立量	SI 組立単位	
	名称	記号
面積	平方メートル	m^2
体積	立方メートル	m^3
速さ，速度	メートル毎秒	m/s
加速度	メートル毎秒毎秒	m/s^2
波数	毎メートル	m^{-1}
密度，質量密度	キログラム毎立方メートル	kg/m^3
面積密度	キログラム毎平方メートル	kg/m^2
比体積	立方メートル毎キログラム	m^3/kg
電流密度	アンペア毎平方メートル	A/m^2
磁界の強さ	アンペア毎メートル	A/m
量濃度(a)，濃度	モル毎立方メートル	mol/m^3
質量濃度	キログラム毎立方メートル	kg/m^3
輝度	カンデラ毎平方メートル	cd/m^2
屈折率(b)	（数字の） 1	1
比透磁率(b)	（数字の） 1	1

(a) 量濃度（amount concentration）は臨床化学の分野では物質濃度（substance concentration）ともよばれる。
(b) これらは無次元量あるいは次元１をもつ量であるが、そのことを表す単位記号である数字の１は通常は表記しない。

表３．固有の名称と記号で表されるSI組立単位

組立量	SI 組立単位			
	名称	記号	他のSI単位による表し方	SI基本単位による表し方
平面角	ラジアン(b)	rad	1 (b)	m/m
立体角	ステラジアン(b)	sr(c)	1 (b)	m^2/m^2
周波数	ヘルツ(d)	Hz		s^{-1}
力	ニュートン	N		m kg s^{-2}
圧力，応力	パスカル	Pa	N/m^2	m^{-1} kg s^{-2}
エネルギー，仕事，熱量	ジュール	J	N m	m^2 kg s^{-2}
仕事率，工率，放射束	ワット	W	J/s	m^2 kg s^{-3}
電荷，電気量	クーロン	C		s A
電位差（電圧），起電力	ボルト	V	W/A	m^2 kg s^{-3} A^{-1}
静電容量	ファラド	F	C/V	m^{-2} kg^{-1} s^4 A^2
電気抵抗	オーム	Ω	V/A	m^2 kg s^{-3} A^{-2}
コンダクタンス	ジーメンス	S	A/V	m^{-2} kg^{-1} s^3 A^2
磁束	ウエーバ	Wb	Vs	m^2 kg s^{-2} A^{-1}
磁束密度	テスラ	T	Wb/m^2	kg s^{-2} A^{-1}
インダクタンス	ヘンリー	H	Wb/A	m^2 kg s^{-2} A^{-2}
セルシウス温度	セルシウス度(e)	℃		K
光束	ルーメン	lm	cd sr(c)	cd
照度	ルクス	lx	lm/m^2	m^{-2} cd
放射性核種の放射能(f)	ベクレル(d)	Bq		s^{-1}
吸収線量，比エネルギー分与，カーマ	グレイ	Gy	J/kg	m^2 s^{-2}
線量当量，周辺線量当量，方向性線量当量，個人線量当量	シーベルト(g)	Sv	J/kg	m^2 s^{-2}
酸素活性	カタール	kat		s^{-1} mol

(a)SI接頭語は固有の名称と記号を持つ組立単位と組み合わせても使用できる。しかし接頭語を付した単位はもはやコヒーレントではない。
(b)ラジアンとステラジアンは数字の１に対する単位の特別な名称で、量についての情報をつたえるために使われる。実際には、使用する時には記号radおよびsrが用いられるが、習慣として組立単位としての記号である数字の１は明示されない。
(c)測光学ではステラジアンという名称と記号srを単位の表し方の中に、そのまま維持している。
(d)ヘルツは周期現象についてのみ、ベクレルは放射性核種の統計的過程についてのみ使用される。
(e)セルシウス度はケルビンの特別な名称で、セルシウス温度を表すために使用される。セルシウス度とケルビンの単位の大きさは同一である。したがって、温度差や温度間隔を表す数値はどちらの単位で表しても同じである。
(f)放射性核種の放射能（activity referred to a radionuclide）は、しばしば誤った用語で"radioactivity"と記される。
(g)単位シーベルト（PV,2002,70,205）についてはCIPM勧告2（CI-2002）を参照。

表４．単位の中に固有の名称と記号を含むSI組立単位の例

組立量	SI 組立単位		
	名称	記号	SI 基本単位による表し方
粘度	パスカル秒	Pa s	m^{-1} kg s^{-1}
力のモーメント	ニュートンメートル	N m	m^2 kg s^{-2}
表面張力	ニュートン毎メートル	N/m	kg s^{-2}
角速度	ラジアン毎秒	rad/s	m m^{-1} s^{-1}=s^{-1}
角加速度	ラジアン毎秒毎秒	rad/s^2	m m^{-1} s^{-2}=s^{-2}
熱流密度，放射照度	ワット毎平方メートル	W/m^2	kg s^{-3}
熱容量，エントロピー	ジュール毎ケルビン	J/K	m^2 kg s^{-2} K^{-1}
比熱容量，比エントロピー	ジュール毎キログラム毎ケルビン	J/(kg K)	m^2 s^{-2} K^{-1}
比エネルギー	ジュール毎キログラム	J/kg	m^2 s^{-2}
熱伝導率	ワット毎メートル毎ケルビン	W/(m K)	m kg s^{-3} K^{-1}
体積エネルギー	ジュール毎立方メートル	J/m^3	m^{-1} kg s^{-2}
電界の強さ	ボルト毎メートル	V/m	m kg s^{-3} A^{-1}
電荷密度	クーロン毎立方メートル	C/m^3	m^{-3} s A
表面電荷	クーロン毎平方メートル	C/m^2	m^{-2} s A
電束密度，電気変位	クーロン毎平方メートル	C/m^2	m^{-2} s A
誘電率	ファラド毎メートル	F/m	m^{-3} kg^{-1} s^4 A^2
透磁率	ヘンリー毎メートル	H/m	m kg s^{-2} A^{-2}
モルエネルギー	ジュール毎モル	J/mol	m^2 kg s^{-2} mol^{-1}
モルエントロピー，モル熱容量	ジュール毎モル毎ケルビン	J/(mol K)	m^2 kg s^{-2} K^{-1} mol^{-1}
照射線量（X線及びγ線）	クーロン毎キログラム	C/kg	kg^{-1} s A
吸収線量率	グレイ毎秒	Gy/s	m^2 s^{-3}
放射強度	ワット毎ステラジアン	W/sr	m^4 m^{-2} kg s^{-3}=m^2 kg s^{-3}
放射輝度	ワット毎平方メートル毎ステラジアン	$W/(m^2$ sr)	m^2 m^{-2} kg s^{-3}=kg s^{-3}
酵素活性濃度	カタール毎立方メートル	kat/m^3	m^{-3} s^{-1} mol

表５．SI 接頭語

乗数	名称	記号	乗数	名称	記号
10^{24}	ヨタ	Y	10^{-1}	デシ	d
10^{21}	ゼタ	Z	10^{-2}	センチ	c
10^{18}	エクサ	E	10^{-3}	ミリ	m
10^{15}	ペタ	P	10^{-6}	マイクロ	μ
10^{12}	テラ	T	10^{-9}	ナノ	n
10^{9}	ギガ	G	10^{-12}	ピコ	p
10^{6}	メガ	M	10^{-15}	フェムト	f
10^{3}	キロ	k	10^{-18}	アト	a
10^{2}	ヘクト	h	10^{-21}	ゼプト	z
10^{1}	デカ	da	10^{-24}	ヨクト	y

表６．SIに属さないが、SIと併用される単位

名称	記号	SI 単位による値
分	min	1 min=60 s
時	h	1 h =60 min=3600 s
日	d	1 d=24 h=86 400 s
度	°	1°=(π/180) rad
分	’	1’=(1/60)°=(π/10 800) rad
秒	”	1”=(1/60)’=(π/648 000) rad
ヘクタール	ha	1 ha=1 hm^2=10^4m^2
リットル	L, l	1 L=1 l=1 dm^3=10^3cm^3=$10^{-3}m^3$
トン	t	1 t=10^3 kg

表７．SIに属さないが、SIと併用される単位で、SI単位で表される数値が実験的に得られるもの

名称	記号	SI 単位で表される数値
電子ボルト	eV	1 eV=1.602 176 53(14)×10^{-19}J
ダルトン	Da	1 Da=1.660 538 86(28)×10^{-27}kg
統一原子質量単位	u	1 u=1 Da
天文単位	ua	1 ua=1.495 978 706 91(6)×10^{11}m

表８．SIに属さないが、SIと併用されるその他の単位

名称	記号	SI 単位で表される数値
バール	bar	1 bar=0.1MPa=100 kPa=10^5Pa
水銀柱ミリメートル	mmHg	1 mmHg≈133.322Pa
オングストローム	Å	1 Å=0.1nm=100pm=10^{-10}m
海里	M	1 M=1852m
バーン	b	1 b=100fm^2=(10^{-12}cm)^2=$10^{-28}m^2$
ノット	kn	1 kn=(1852/3600)m/s
ネーパ	Np	SI単位との数値的な関係は、対数量の定義に依存。
ベル	B	
デシベル	dB	

表９．固有の名称をもつCGS組立単位

名称	記号	SI 単位で表される数値
エルグ	erg	1 erg=10^{-7} J
ダイン	dyn	1 dyn=10^{-5}N
ポアズ	P	1 P=1 dyn s cm^{-2}=0.1Pa s
ストークス	St	1 St =1cm^2 s^{-1}=$10^{-4}m^2$ s^{-1}
スチルブ	sb	1 sb =1cd cm^{-2}=10^4cd m^{-2}
フォト	ph	1 ph=1cd sr cm^{-2} =10^4lx
ガル	Gal	1 Gal =1cm s^{-2}=$10^{-2}ms^{-2}$
マクスウエル	Mx	1 Mx = 1G cm^2=10^{-8}Wb
ガウス	G	1 G =1Mx cm^{-2} =10^{-4}T
エルステッド(a)	Oe	1 Oe ≙ (10^3/4π)A m^{-1}

(a) ３元系のCGS単位系とSIでは直接比較できないため、等号「 ≙ 」は対応関係を示すものである。

表10．SIに属さないその他の単位の例

名称	記号	SI 単位で表される数値
キュリー	Ci	1 Ci=3.7×10^{10}Bq
レントゲン	R	1 R = 2.58×10^{-4}C/kg
ラド	rad	1 rad=1cGy=10^{-2}Gy
レム	rem	1 rem=1 cSv=10^{-2}Sv
ガンマ	γ	1 γ=1 nT=10^{-9}T
フェルミ		1 フェルミ=1 fm=10^{-15}m
メートル系カラット		1 メートル系カラット= 0.2 g = 2×10^{-4}kg
トル	Torr	1 Torr = (101 325/760) Pa
標準大気圧	atm	1 atm = 101 325 Pa
カロリー	cal	1 cal=4.1858J（「15℃」カロリー），4.1868J（「IT」カロリー），4.184J（「熱化学」カロリー）
ミクロン	μ	1 μ =1μm=10^{-6}m

（第8版，2006年）